

Synthesis and Modification of Graphene Nanowalls using Plasma Immersion Ion Implantation and Deposition Facility

by

P. A. Manojkumar

Enrolment No.: ENGG 02 2012 04 016

Indira Gandhi Centre for Atomic Research, Kalpakkam, India.

*A thesis submitted to the
Board of Studies in Engineering Sciences*

*In partial fulfillment of requirements
for the Degree of*

DOCTOR OF PHILOSOPHY

of

HOMI BHABHA NATIONAL INSTITUTE

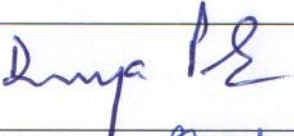
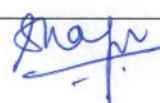
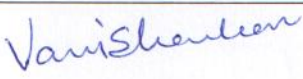
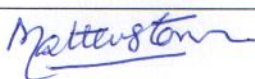


August, 2019

Homi Bhabha National Institute

Recommendations of the Viva Voce Committee

As members of the Viva Voce Committee, we certify that we have read the dissertation prepared by P.A. Manojkumar entitled "Synthesis and Modification of Graphene Nanowalls using Plasma Immersion Ion Implantation Facility" and recommend that it may be accepted as fulfilling the thesis requirement for the award of Degree of Doctor of Philosophy

Chairman - Dr. B. K. Panigrahi		Date: 17/06/2020
Guide & Convener - Dr. Shaju K Albert		Date: 17/06/2020
Co-guide - Dr. M. Kamruddin		Date: 17/6/20
Examiner - Dr. Chinnakonda S. Gopinath		Date: 17/6/2020
Member 1- Dr. G. Mangamma		Date: 17.06.2020.
Member 2- Dr. S. Vani Shankar		Date: 17.6.2020
Member 3- Dr. Tom Mathews		Date: 17-06-2020

Final approval and acceptance of this thesis is contingent upon the candidate's submission of the final copies of the thesis to HBNI.

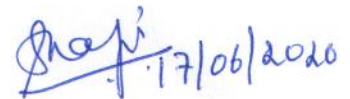
I/We hereby certify that I/we have read this thesis prepared under my/our direction and recommend that it may be accepted as fulfilling the thesis requirement.

Date: 17-06-2020

Place: IGCDR

Co-guide

Guide



STATEMENT BY AUTHOR

This dissertation has been submitted in partial fulfillment of requirements for an advanced degree at Homi Bhabha National Institute (HBNI) and is deposited in the Library to be made available to borrowers under rules of the HBNI.

Brief quotations from this dissertation are allowable without special permission, provided that accurate acknowledgement of source is made. Requests for permission for extended quotation from or reproduction of this manuscript in whole or in part may be granted by the Competent Authority of HBNI when in his or her judgment the proposed use of the material is in the interests of scholarship. In all other instances, however, permission must be obtained from the author.

Signature :  17/06/2020

Name of the student : P. A. Manojkumar

DECLARATION

I, hereby declare that the investigation presented in the thesis has been carried out by me.

The work is original and has not been submitted earlier as a whole or in part for a degree / diploma at this or any other Institution / University.

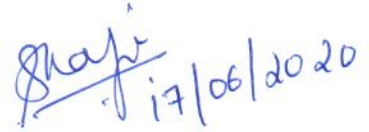
Signature :



17/06/2020

Name of the student : P. A. Manojkumar

Signature :



17/06/2020

Name of guide : Prof. (Dr.) Shaju K Albert

List of Publications

Publications in Journal:

- [1] “Shallow nitrogen ion implantation: Evolution of chemical state and defect structure in titanium”, **P.A. Manojkumar**, V.A. Chirayath, A.K. Balamurugan, Nanda Gopala Krishna, S. Ilango, M. Kamruddin, G. Amarendra, A.K. Tyagi, Baldev Raj, *Nuclear Instruments and Methods in Physics Research B*, **2016**, 383, 6-13.
- [2] “Understanding the structural and chemical changes in vertical graphene nanowalls upon plasma nitrogen ion implantation”, **P. A. Manojkumar**, Nanda Gopala Krishna, G. Mangamma, S. K. Albert, *Physical Chemistry Chemical Physics*, **2019**, 21, 10773-10783.
- [3] “Role of process gas ratio on the structural and plasmonic properties of graphene nanowalls”, **P. A. Manojkumar**, G. Mangamma, S. Amirthapandian, Ramanathaswamy Pandian, T.N. Sairam, S. K. Albert, *Diamond & Related Materials*, **2019**, 97, 107452.

Conferences:

- [1] **P. A. Manojkumar**, G. Mangamma, R. Pandian, S. Bera, M. Kamruddin, A.K. Tyagi “Formation of fullerene like CN_x in vertically grown graphene nanowalls” International conference on Nanoscience and Technology (**ICONSAT 2016**), IISER, Pune, India, 29th Feb to 2nd March 2016.
- [2] **P. A. Manojkumar**, G. Mangamma, R. Pandian, A. Pandian, S. K. Dhara “Tuning the morphology and structure of vertical graphene nanowalls: Raman and EELS study”. National Symposium on Advances in Functional and Exotic Materials, MRSI Trichy & Bharathidasan University, Tiruchirapally, TN, 14th-16th, Feb. **2018**.
- [3] **P. A. Manojkumar**, G. Mangamma, R. Renjith, Nanda Gopala Krishna, P. Magudapathy, S. Ilango, S. K. Dhara, M. Kamruddin, Shaju. K. Albert “Probing the evolution of chemical state and defect structure in N⁺ and N₂⁺ ion implantation on Zirconium thin film”. International conference on Nanoscience and Technology (**ICONSAT 2018**), CeNS, Bangalore, India, March 21-23, 2018.
- [4] **P. A. Manojkumar**, T. Manovah David, G. Mangamma, Tom Mathews “Massive enhancement of charge storage in plasma nitrogen implanted graphene nanowalls” International conference on Nanoscience and Nanotechnology (**ICNAN 2019**), VIT, Vellore, T.N., India, 29th Nov. to 1st Dec., 2019.

Other Journal Publications not included in the thesis

- [1] “Role of nanocrystalline feedstock in the tribological behaviour of alumina coatings deposited by detonation gun”, **P. A. Manojkumar**, A. S. Gandhi, M. Kamaraj, V. Thomas Paul, N. Kumar, A.K. Tyagi, *Int. Journal of Refractory Metals and Hard Materials*, **2012**, 35, 108-114.

- [2] "Sliding wear behaviour of alumina coatings prepared from mechanically milled powders", **P. A. Manojkumar**, A. S. Gandhi, M. Kamaraj, A. K. Tyagi, WEAR, **2014**, 313, 11-18.
- [3] "Atomic scale study of ball milled Ni-Fe₂O₃ using Mössbauer spectroscopy", Ravi Kumar Yadav, R. Govindaraj, K. Vinod, **P. A. Manojkumar**, G. Amarendra, AIP Conference Proceedings, **2016**, 1730, 050137, doi: 10.1063/1.4947791.
- [4] "Enhanced tribochemical properties of oxygen functionalized mechanically exfoliated hexagonal boron nitride nanolubricant additives", Jayakrushna Sahu, Kalpataru Panda, Bhavana Gupta, Niranjana Kumar, **P.A. Manojkumar**, T. Mathews, M. Kamruddin, Materials Chemistry and Physics, **2018**, 207, 412-422.

Other Conferences not included in the thesis

- [1] **P. A. Manojkumar**, A. S. Gandhi, M. Kamaraj, N. Kumar, M. Kamruddin, A.K. Tyagi, "Tribological properties of nanocrystalline alumina coating deposited by D-gun" Heat Treatment and Surface Engineering Conference and Expo 2013, (**HT&SE -2013**), 27th Surface Modification Technologies (**SMT-27**), Chennai Trading Centre, Chennai.
- [2] G. Mangamma, **P. A. Manojkumar**, "Colossal Piezoelectric effect in vertical graphene nanowalls" International Conference on Laser Deposition (**iCOLD-2017**), Nov 20-22, 2017, IITM, Chennai.
- [3] G. Mangamma, **P. A. Manojkumar**, A. Rajesh "Evidence for Charge Transfer in BaTiO₃-VGN nano-composite" National Conference on Light Matter Interaction at Nanoscale (**LMIN-2019**), July 15-17, 2019, Sarabhai Auditorium, IGCAR, Kalpakkam.
- [4] K. Ganesan, **P.A. Manojkumar**, A. K. Balamurugan and P. K. Ajikumar, "Studies on shallow nitrogen ion implantation in micro- and nanocrystalline diamonds by plasma immersion ion implantation" 5th International Conference on Nanostructuring by Ion Beams (**ICNIB-2019**), 6-8 November, **2019**, IGCAR, Tamil Nadu.

Signature :

Name of the student : P. A. Manojkumar

Acknowledgements

*I enjoy immense pleasure in presenting my hard work, dedication and continuous pursuit of knowledge in front of the scientific community and those who helped and supported me directly and indirectly, in this long journey. In this context, I express my sincere gratitude to my guide **Prof: Shaju K. Albert**, Homi Bhaba National Institute and Director, Materials Science Group & Metallurgy and Materials Group, IGCAR for providing me splendid support, encouragement and guidance throughout my Ph. D tenure. In spite of his busy schedule, he found time to listen, analyse and direct me towards the fruitful completion of this work. I use this opportunity to thankfully acknowledge his personal care and affection to me.*

*Besides my guide, I am extremely thankful to the Chairman of Doctoral Committee: **Prof: B. K. Panigrahi**, a doyen of physics and vibrant face of physics research at MSG, who given technical and moral support to my research and subsequent submission of thesis. I thank co-guide **Prof: M. Kamruddin**, DC members **Dr. S. Vani Shankar** and **Dr. Saroja SaiBaba** for their support.*

*I am very thankful to **Dr. G. Mangamma**, DC member and Head NCSS for the moral and technical support to my Ph D work and AFAM measurements of GNWs. I am extremely grateful to **Dr. Tom Mathews**, D C member, for his interest in my work and commitment towards the submission of thesis. I'll always cherish my association with him.*

*With extreme reverence, I thankfully acknowledge Late **Dr. Baldev Raj**, former Director-IGCAR for his care and affection to me and for the pragmatic support to my pursuit of knowledge. I thank **Dr. A. K. Bhaduri**, Director-IGCAR for his support to my research programme.*

*I thank **Dr. S. K. Dhara**, Head-SND for his interest and support, **Dr. R. Govinda Raj**, Head-MPD and **Dr. N. V. Chandrasekhar**, Head-CMPD for their appreciation and support to my programmes.*

*My sincere thanks goes to my lab-mates **Dr. P.K. Ajikumar** and **Dr. K. Ganesan** for technical discussions and other supports in conducting experiments. I am very grateful to **Sri. A.K. Balamurugan** for all his technical supports, especially in SIMS related studies. I thank my other colleagues **Sri. P. Magudapathy**, **Dr. R. Pandian**, **Dr. Arindam Das**, **Dr. P. Syamala Rao**, **Sri. Nandagopala Krishna** and **Sri. U.K. Gautam (RRCAT)** for their support in experimental analysis or technical discussions. My thanks are due to other SND colleagues **Dr. S. Ilango**, **Dr. R. Krishnan**, **Dr. Gomathi Natarajan**, **Dr. K. Arun Prasad**,*

Dr. D.K. Baisnab and Dr. R. Ramaseshan for their well wishes and support. I thank Dr. Manovah David, Dr. T. R. Ravindran, Dr. T. N. Sairam, Dr. Amirtha Pandian and Sri.R. Renjith for supporting me with various characterisation techniques. Mr. P. Jagadeesan owe my special thanks for providing me the word template for thesis preparation and Mrs. Sruthi Mohan for technical discussions, Dr. Rajini P Antony and Sri. Sinu Chandran for providing some useful literature. I would like to acknowledge Dr. R. Rajagopal, Dr. A. K. Tyagi and Dr. Sitaram Dash my previous senior colleague and Dr. T. Jayakumar for their support. I thankfully acknowledge Dr. P. Shankar, my previous colleague, for his efforts in setting up the PIII&D facility. I thank other members of SND, MSG and MMG who supported and helped me during my PhD tenure.

*My thanks are also due to my friends and colleagues at Kalpakkam for their support. I thank my cousins and in-laws for their care, concern and support. I express my deep sense of love and gratitude to **my parents and siblings** for their supreme support, sacrifice and solicitude which shaped my early years and career. The acknowledgement part of this thesis will be largely incomplete without the mention of my wife **Rashmi**, my daughter **Tejal** and my son **Thanish** who suffered the real heat of my absence in long working hours at lab eating up their private time; still they consoled, encouraged and supported my journey with their love, care and affection.*

P. A. Manojkumar

Abstract

KEYWORDS: *Plasma enhanced chemical vapour deposition, graphene nanowalls, plasma ion implantation, electron microscopy, Raman spectroscopy, FTIR-spectroscopy, X-ray photoelectron spectroscopy, electron energy loss spectroscopy, electrochemical studies.*

A few layer graphene grown upright to the surface having self-standing mechanical stability is called vertical graphene nanowalls (VGNs) or simply, graphene nanowalls (GNWs). GNWs attract the attention of scientific community due to its conducting nature, large specific surface area and high edge density. Consequently, GNWs are demonstrated as excellent electrode material for several electrochemical devices, such as fuel cell, supercapacitor, etc. However, there is a continuous demand for exploring and improving the performance by modifying the surface properties. The present study describes one such full spectrum approach. A custom made plasma immersion ion implantation and deposition (PIII&D) facility is benchmarked and used for synthesis (of GNWs) and its nitrogen modification (N-GNWs). One of the potential applications of N-GNWs, the electrode material for supercapacitors is briefly studied.

Towards benchmarking the PIII&D system, nitrogen plasma ion implantation is carried out on Si and Ti at 10 kV pulsed dc bias. SIMS and depth resolved XPS analysis were used to obtain the range of nitrogen ions and chemical nature of the implanted regions. The study reveals that N^+ ions and N_2^+ ions are preferentially implanted at high and low plasma power, respectively. N^+ ions are found to be chemically more active than N_2^+ ions. Nitrogen ions were implanted at 10 keV/ion energy on Zr thin films using particle accelerator to generate data on the profile variation due to mono and di – atomic nature of ions. Based on the results, general operating conditions for plasma ion implantation is deduced.

Ar-CH₄ gas mixture is found to give high growth rate for plasma enhanced chemical vapour deposition (PECVD) of GNWs. However, the utility of GNWs is fundamentally related to its morphology and electronic structure. Hence, the influence of process gas ratio on morphology and the electronic structure is studied. Basic characterisation is done using SEM and Raman spectroscopic techniques. HR-TEM and electron diffraction studies show that the *d*-spacing of GNWs are higher than that of highly oriented pyrolytic graphite (HOPG). The characteristic huge secondary growth observed in RF plasma deposited GNWs is correlated to the presence of bridging methylene group by FTIR spectroscopic studies. The influence of peculiar morphology; possibly, an after effect of edge groups is correlated to the plasmonic peak values obtained from EELS studies. It is found that the

C *K-edge* energy of GNWs is less than that of HOPG by $\sim 1\text{eV}$. The study shows that gas composition influence the morphology and the plasmonic properties of GNWs.

The GNWs were nitrogen plasma ion implanted at low energy (-2kV) for 10, 20 and 30 minutes. Due to structural defects and preference of nitrogen to occupy various locations in the 2D layered structure, a large overlap of several N_{1s} energy levels are reported in literature. In order to simplify the analysis, the binding energy of N_{1s} electron is correlated with the chemical state of nitrogen as lone pair localised (N1), lone pair delocalised (N2) and quaternary nitrogen (N3). This new approach helps to understand the electronic nature of implanted GNWs, based on the occupancy of structural locations by nitrogen as *p*-type (N1), *n*-type (N2) and polar (N3). Further, the increase in relative stiffness as observed in AFAM studies is correlated with the formation of graphitic CN_x (N2), cross linking of layers by quaternary nitrogen (N3) and interlayer sp^3C . It is found that increasing the implantation duration beyond 10 minutes does not yield high nitrogen fraction or stiffness; but, leads to more defects and sputter removal of material. Hence, the experiment was directed to low energy and low dose plasma ion implantation of GNWs.

Towards the synthesis of N-doped GNWs with minimum damage to morphology and hexagonal structure, low energy ($\sim 1\text{kV}$) and low dose (4-6 at%) nitrogen implantation were carried out. The samples were nitrogen plasma ion implanted for 2, 4 and 8 minutes and characterised using SEM, water contact angle, Raman and IR spectroscopy, XPS and electrochemical methods. The sample implanted for 2 min. has shown more than 100 times increase in supercapacitance as compared to the pristine sample. The increase in capacitance value is attributed to the presence of N1 type nitrogen, super hydrophilicity and possibly due to hydroxyl and carbonyl ($-\text{C}=\text{O}$) group in GNWs.

The plasma ion implantation of GNWs using nitrogen is reported for the first time in literature. The analysis of implanted samples are simplified with an engineering perspective such as the G-peak normalised intensity for Raman spectra and limiting the number of XPS N_{1s} peak into three configurations (N1, N2 and N3) for correlating it with the electronic nature of GNWs as *p*-type, *n*-type, or polar. By normalizing the EELS data with zero loss peak intensity, the issues related to intensity variation is circumvented. Additionally, the conditions enhancing secondary growth and thus increased surface area is revealed. In a nutshell, the work describes, a systematic approach towards tuning the facility, synthesis and modification of samples, analysis of data using simple and novel approach for the prime objective, study the effects of shallow nitrogen ion implantation of GNWs for advanced applications.

Table of Contents

List of Publications	v
Acknowledgements	vii
Abstract	ix
Table of Contents	xi
List of Figures	xiv
List of Tables.....	xxii
Abbreviations	xxiii
Notations and Symbols	xxiv
Chapter 1 Graphene nanowalls and its nitrogen modification-An overview	1
1.1. Introduction.....	1
1.2. Synthesis of Graphene nanowalls	4
1.2.1. Growth mechanism of graphene nanowalls	7
1.3. Characteristics of Graphene nanowalls.....	10
1.3.1. Morphology and Microstructure.....	10
1.3.2. Electronic properties.....	12
1.3.3. Mechanical properties	13
1.3.4. Applications of graphene nanowalls	14
1.4. Nitrogen modification of Graphene nanowalls: techniques and characteristics.....	16
1.4.1. Techniques for nitrogen incorporation into GNWs.....	16
1.4.1.1. CVD Methods for nitrogen doping	17
1.4.1.2. Plasma based processes.....	17
1.4.1.3. Ion implantation.....	19
1.4.2. Structural effects of nitrogen implantation in graphitic layers	20
1.4.2.1. Morphological studies.....	21
1.4.3. X-Ray photo electron spectroscopic studies.....	21
1.4.4. Raman spectroscopic studies	23
1.4.5. Fourier Transform Infra-Red spectroscopic studies	25
1.4.6. Atomic force acoustic microscopic studies	27
1.5. Electrochemical characterisation of GNWs and N-GNWs.....	28
1.6. Literature review on supercapacitor application of GNWs and N-GNWs	28
1.7. Objective and Scope of the study.....	32
1.8. Organisation of the thesis.....	32
Chapter 2 Experimental Procedures	33
2.1. Research Methodology	33

2.2. Equipment and materials	37
2.2.1. Plasma Immersion Ion Implantation and Deposition (PIII&D) Facility.....	38
2.2.1.1. Plasma Enhanced Chemical Vapour Deposition (PECVD)	38
2.2.1.2. Physical Vapour Deposition.....	40
2.2.1.3. Plasma Immersion Ion Implantation	41
2.2.2. FESEM	44
2.2.3. TEM	44
2.2.4. EELS	45
2.2.5. Raman spectroscopy.....	47
2.2.6. Infrared spectroscopy	50
2.2.7. Secondary Ion Mass Spectroscopy (SIMS).....	52
2.2.8. X-ray Photo-electron Spectroscopy (XPS)	54
2.2.9. Atomic Force Acoustic Microscopy (AFAM)	58
2.2.10. Water contact angle measurement.....	59
2.2.11. Electrochemical studies.....	61
2.3. Summary	65
Chapter 3 Facility benchmarking	67
3.1. Introduction.....	67
3.2. Nitrogen plasma ion implantation of Titanium.....	68
3.3. Nitrogen plasma ion implantation of Silicon.....	72
3.4. Nitrogen ion implantation of Zirconium thin films	74
3.5. Parameters derived for plasma ion implantation	76
3.6. Summary.....	77
Chapter 4 Effect of gas composition on PECVD synthesis of graphene nanowalls	79
4.1. Introduction.....	79
4.2. Synthesis of GNWs.....	79
4.2.1. PECVD of GNWs using Hydrogen–Methane gas mixture	81
4.2.2. PECVD of GNWs using Argon–Methane gas mixture.....	84
4.2.2.1. Results and discussion.....	86
4.3. Summary	101
Chapter 5 High dose nitrogen plasma ion implantation of graphene nanowalls	103
5.1. Process, Materials and Methods	103
5.2. Results	105
5.2.1. Raman spectroscopic studies.....	106
5.2.2. XPS studies	110

5.2.3. Atomic Force Acoustic Microscopic studies.....	119
5.3. Discussion	120
Chapter 6 Low dose nitrogen plasma ion implantation of graphene nanowalls	127
6.1. Introduction.....	127
6.2. Process, Materials and Methods	127
6.3. Results	128
6.3.1. Raman spectroscopic studies	131
6.3.2. FTIR spectroscopic studies.....	134
6.3.3. X-ray photoelectron spectroscopic studies	137
6.3.4. Water contact angle measurement.....	144
6.3.5. Electrochemical studies	145
6.3.5.1. Cyclic voltammetry.....	145
6.3.5.2. Galvanostatic Charge-Discharge.....	148
6.4. Discussion	150
Chapter 7 Summary, Conclusion and Future prospects	155
7.1. Summary	155
7.2. Conclusion	159
7.3. Scope for future works	159
References	163

List of Figures

Fig. 1.1	Over view of carbon allotropes and their atomic arrangements in space	2
Fig. 1.2	First report on GNWs synthesised during the growth of CNTs. (a) CNTs, (b) GNWs [32]	5
Fig. 1.3	Schematic representation of GNWs (VGNs) growth model. (a) Shows the nanocrystalline a few layer graphene deposited over amorphous carbon layer formed on the substrate. (b) At the junctions, horizontal growth changes direction due to stress and the directionality of electric field. Possible plasma species also shown.	8
Fig. 1.4	The influence of nitrogen in the synthesis of GNWs deposited using ECR-CVD. S1 and S3 use high pure Ar (5N) and S2 and S4 use commercial pure Ar (3N). Nitrogen induces etching of GNWs and facilitate graphitic nano island formation at high concentration. Only S5 shown the presence of nitrogen in XPS studies [123].	18
Fig. 1.5	Typical XPS C 1s spectrum of graphene nanowalls (a) As-prepared and (b) argon ion irradiated. Increase in FWHM and increase in sp ³ fraction due to Ar ion irradiation is evident from the image [141].	22
Fig. 1.6	(a) Typical C 1s XPS spectrum showing various peak assignments including vacancy induced broadening of sp ² C peak [140]. and (b) possible C-Si peak at 283.5 eV [116].	22
Fig. 1.7	Typical nitrogen configuration in hexagonal carbon ring of graphene, respective names are given above each [116].	23
Fig. 1.8	Typical Raman spectrum of vertical graphene nanowalls. Respective peak designations are given. The 2D peak is also referred to as G' peak in literature [153].	24
Fig. 1.9	Infrared absorption range of compounds containing Carbon, Oxygen and Nitrogen. [156].	25
Fig. 1.10	Typical IR transmission spectrum of graphene showing peak positions of relevance to graphene nanowalls. (a) Graphene Oxide [157] and (b) conductive polymer functionalised graphene oxide (FGO) and functionalised reduced graphene oxide (FR-GO) [158].	26
Fig. 2.1	Research methodology for the experimental study.	34
Fig. 2.2	Flow chart of the experiments.	36
Fig. 2.3	Photograph of the PIII&D system.	37
Fig. 2.4	PECVD system used for the synthesis of graphene nanowalls.	40
Fig. 2.5	Schematic of PIII process. The specimen placed at the centre experience ion implantation upon (–) ve pulse bias.	42
Fig. 2.6	(a) Schematic of TEM line diagram with the Ω -energy filter after the specimen stage. (b) Typical EELS spectrum showing Zero-loss peak, Plasmon peak and ionization edges for different elements [204].	46

Fig. 2.7	Schematic of energy level diagram of Raman scattering.	48
Fig. 2.8	Raman bands corresponding to defective graphene or graphene nanowalls. Respective phonon modes acting on the excited electron at the high symmetry points of Brillouin zone is shown.	49
Fig. 2.9	Schematic of FTIR system.	51
Fig. 2.10	Schematic of Secondary Ion Mass Spectrometer.	54
Fig. 2.11	The schematic of photoelectron emission process.	55
Fig. 2.12	Schematic of XPS work function compensation. For conducting samples, the Fermi level (E_f) of both sample and instrument become equal upon earthing. Φ_s and Φ_I are work function of the sample and instrument. The total electron energy (TEE) measured is the sum of KE_2 and Φ_I . The difference between the X-ray energy ($h\nu$) and TEE will give the binding energy.	56
Fig. 2.13	Schematic of AFM and AFAM technique.	59
Fig. 2.14	Schematic of the liquid contact angle.	60
Fig. 2.15	Schematic representation of Wenzel and Cassie Baxter model of surface wetting due to variation in surface morphology.	61
Fig. 2.16	Theoretical cyclic voltammogram of a reversible electrochemical reaction. The US convention is shown at the left and IUPAC convention is at the right [219]. In India, IUPAC convention is followed.	63
Fig. 2.17	Theoretical voltammogram showing the respective current and voltage values.	63
Fig. 3.1	The oscilloscope out put of a single pulse of the high voltage pulsed dc modulator at 10 kV, 0.1 KHz, 45 μ s pulse width. The pulse is stabilised within a few microseconds.	69
Fig. 3.2	SIMS profile of nitrogen plasma ion implanted titanium. The figure shows bimodal distribution of nitrogen and the intensity is high at low depth due to large fraction of N_2^+ ions in the plasma.	69
Fig. 3.3	SRIM simulation of nitrogen ions in titanium. The energy 10.5 k eV represent N^+ ions; whereas, 5.25 k eV represent N_2^+ ions. The vacancy peak of N^+ ions falls in the range peak of N_2^+ ions.	71
Fig. 3.4	Depth resolved XPS data of ion implanted titanium. The binding energy shift in $2P^{3/2}$ bonding state of titanium from higher energy (TiO_2) to lower energy (TiN) with corresponding time in minute is shown. (a) for sample S1 (45 minutes) and (b) for sample S2 (90 minutes) .	71
Fig. 3.5	XPS data of S1 and S2 after 0.5 minute to 20 minute of surface sputtering. The binding energy corresponding to $N1s$ bonding state of nitrogen at 403.7 eV shows N-N bonding and 397.2 eV shows Ti-N bonding.	71
Fig. 3.6	SIMS profile of silicon wafer implanted at 10kV using nitrogen plasma upto 30 minutes. Highest surface nitrogen is observed at 2 min. implanted sample.	74

- Fig. 3.7 SIMS data of Zr thin film samples. N^+ ions are implanted using particle accelerator. The peak shape is similar to SRIM simulated data as shown in Fig. 3.3. The range is almost double that of SRIM simulation. 75
- Fig. 3.8 SIMS data of Zr thin film samples. N_2^+ ion implanted using particle accelerator showing bi-modal distribution of ions. High dose implantation of N_2^+ ions gives a broad peak. The peak range is higher than SRIM simulated value as shown in Fig. 3.3. 76
- Fig. 4.1 SEM images of GNWs. (a) surface image, showing corrugated surface morphology. (b) Cross-sectional image, showing the vertical nature of growth. 80
- Fig. 4.2 Raman spectra of GNWs. General quality parameters are given at the right corner. 80
- Fig. 4.3 SEM images of GNWs synthesised at different $H_2:CH_4$ ratios. At 7:1 ratio, a semi-cross sectional image is given to show the etch removal effect of hydrogen at higher concentrations. At 1:1 and 1:7 ratios, the morphology is identical. At 1:1 ratio, more dense GNWs are formed. 81
- Fig. 4.4 Deconvoluted Raman spectrum of GNWs deposited at hydrogen to methane ratio 1:7. Peak positions and FWHM (in bracket) are given. General quality parameters are given at the right corner. 82
- Fig. 4.5 Deconvoluted Raman spectrum of GNWs deposited at hydrogen to methane ratio 1:1. Peak positions and FWHM (in bracket) are given. General quality parameters are given at the right corner. 82
- Fig. 4.6 Deconvoluted Raman spectrum of GNWs deposited at hydrogen to methane ratio 7:1. Peak positions and FWHM (in bracket) are given. General quality parameters are given at right corner. 83
- Fig. 4.7 The Raman spectrum is plotted after normalizing the G-peak intensity of all samples. With increase in hydrogen volume fraction, the graphite like nature is increasing and intensity of G' peak reduces. 83
- Fig. 4.8 SEM images of GNWs deposited at various $Ar:CH_4$ ratios. With increasing Ar volume fraction, secondary growth reduces. 85
- Fig. 4.9 SEM images of GNWs showing variation of morphology with change in $Ar:CH_4$ ratios. With decreasing Ar volume fraction, secondary growth increases. 85
- Fig. 4.10 Optimization of gas ratio for deposition. Highest deposition rate at 3:1 ($Ar:CH_4$) gas ratio. 86
- Fig. 4.11 SEM images of GNWs deposited with three different ratios. At 7:1(S1), $Ar:CH_4$ ratio; open channel morphology is developed. With decreasing Ar fraction, secondary growth with high corrugation is observed in S4 and S7. 87
- Fig. 4.12 Deconvoluted Raman spectrum of GNWs deposited at 7:1 (S1) $Ar:CH_4$ gas ratio. Results of analysis are given in Table 4.3. 90

- Fig. 4.13 Deconvoluted Raman spectrum of GNWs deposited at 1:1(S4), Ar:CH₄ gas ratio. Results of analysis are given in Table 4.3. 90
- Fig. 4.14 Deconvoluted Raman spectrum of GNWs deposited at 1:7(S7), Ar:CH₄ gas ratio. Results of analysis are given in Table 4.3. 91
- Fig. 4.15 The Raman spectrum of the three samples are plotted with G peak normalised intensity in Y-axis. The major difference is seen only in D band intensity. 91
- Fig. 4.16 FTIR spectrum of GNWs, (a) Absorption coefficient is used in the Y-axis to show the lower background of S4 due to better long range order. Relevant peaks in the finger print regions are marked. The sp³C-H region in Fig. 4.16 (a) is blown up and plotted in Fig.4.16 (b), (c) and (d) to compare the methine, methylene and methyl group of sp³carbon – hydrogen stretching vibrations. Peak positions and its relative intensity is summarised in Table 4.4. 93
- Fig. 4.17 Schematic of proposed geometrical arrangement of methine, methylene and methyl groups in GNWs. Methine group is formed by attaching hydrogen to a tertiary carbon on the surface. Methylene group is attached to the sp³carbon in the graphene ring or connected to sp²carbon in the ring as bridging methylene. Methyl group is attached to sp² carbon and protrude out of the graphene system. 94
- Fig. 4.18 TEM images of S1, S4, S7 and HOPG. Typical regions where inter-planar spacing measured using image J software is highlighted. Images are taken in the direction perpendicular to (001) plane. The electron diffraction pattern of S1, S4 and S7 are shown below. Diffused ring pattern indicate lack of long range order (of S1 and S7) and spotty ring pattern (of S4) indicate nanocrystalline nature. 96
- Fig. 4.19 ZL peak normalised low loss region of electron energy loss spectroscopy (EELS) data of S1, S4, S7 and HOPG showing typical π - π^* transition region of sp² type bonding. By convention the shaded portion is considered as zero loss region. Actual zero loss peak is at 0 eV. Because of no π bonding in diamond, π - π^* peak is absent. Individual curve fit is given in Fig. 4.20. 97
- Fig. 4.20 Gaussian fitting of π - π^* plasmonic peak of S1, S4, S7 and HOPG. ZL-peak normalised intensity was used to compare the area under the curve. 98
- Fig. 4.21 The deconvoluted high loss region of electron energy loss spectroscopy (EELS) of GNWs and HOPG. The area under the curve (A1) was used for estimating the sp² fraction of respective samples along with the EELS spectrum of HOPG. The ratio A2/A1 was used for analyzing the c-axis mixing in GNWs. The curve A3 was generated to determine π^* + σ^* peak and to fit A1 and A2. 99
- Fig. 5.1 FESEM image showing the surface and cross-section of GNWs, pristine (S0), nitrogen plasma implanted for 10 min.(S1), 20 min.(S2) and 30 min.(S3). The sputter removal of material due to implantation is seen in S3. 104

- Fig. 5.2 SRIM simulation of N⁺ ion implanted at 2 kV bias. Peak range is at 5.7 nm and peak vacancy generation is at 2.5 nm deep from surface. At half the energy ion implantation (N₂⁺ ions), the above values can be reduced by half and hence, the collision cascade intercepts the surface and cause excessive sputtering of material. 105
- Fig. 5.3 Variation in sample thickness of pristine (S0) and implanted for 10, 20 and 30 min. (S1, S2 and S3, respectively), showing reduction in thickness due to sputter removal of material. 106
- Fig. 5.4 Raman spectrum of pristine sample showing the typical peaks corresponding to graphene nanowalls. 107
- Fig. 5.5 Deconvolution of Raman spectrum of S1. The G-peak shown is formed by the merger of G and D' peaks of pristine. The peaks at ~1441 cm⁻¹ and ~1517cm⁻¹ (A- peaks) are due to fullerene and other structural defects. The peaks at ~1217 and ~1290 (T-peaks) are due to high density of edges, disordered hydrogenated sp³ carbon and olefinic structure similar to trans polyacetylene. The G' and D+G peaks are also shown. 108
- Fig. 5.6 Deconvolution of Raman spectrum of S2 and S3. The peak positions are shown. The G-peak is formed by the merger of G and D' peaks. The peaks at ~1460 cm⁻¹ and ~1520cm⁻¹ (A- peaks) are due to fullerene and other structural defects. The peaks at ~1257 and ~1283 (T-peaks) are due to high density of edges, disordered hydrogenated sp³ carbon and olefinic structure similar to trans polyacetylene. 109
- Fig. 5.7 Raman spectrograph of pristine and nitrogen plasma ion implanted samples. The variation in intensity is shown against G-peak. The respective GNWs peaks and -C≡N are identified. The C≡N peak is highlighted in the inset. 109
- Fig. 5.8 The survey spectrum of photo-electron spectra of pristine GNWs. The peaks are labelled. No peak corresponding to N 1s is seen. 110
- Fig. 5.9 Carbon 1s photo-electron spectra of pristine GNWs. The peaks are labelled. 111
- Fig. 5.10 The survey spectrum of S1-Peaks corresponding to carbon, nitrogen and oxygen is given. 111
- Fig. 5.11 The survey spectrum of S2-Peaks corresponding to carbon, nitrogen and oxygen is given. 111
- Fig. 5.12 The survey spectrum of S3-Peaks corresponding to carbon, nitrogen and oxygen is given. 112
- Fig. 5.13 C_{1s}-XP spectrum of S1, S2 and S3. Significant increase in sp³ C was due to structural disorder and destruction of crystalline nature of the sp² C structure at the surface. 113
- Fig. 5.14 N_{1s}-XP spectrum of nitrogen implanted GNWs (S1) sample. Based on the binding energy of N_{1s} electron, the nitrogen is categorised as lone pair localised (N1), lone pair delocalised (N2) and quaternary and trapped

- nitrogen (N3). Respective location of nitrogen in implanted GNWs is shown at the right. 116
- Fig. 5.15 N_{1s}-XP spectrum of nitrogen implanted GNWs (S2 and S3) sample. Based on the binding energy of N_{1s} electron, the nitrogen is categorised as lone pair localised (N1), lone pair delocalised (N2) and quaternary and trapped nitrogen (N3). 116
- Fig.5.16 Survey spectrum of S1: As-received and after 1 min. Ar- ion sputtering. The O1s peak shows a reduction in photoelectron intensity by 20-30 % after sputtering. 117
- Fig. 5.17 O_{1s}-XP spectra of nitrogen implanted GNWs (S1, S2 and S3) sample. Oxygen is attached or deposited to the GNWs inadvertently due to exposure of the sample to atmosphere (O₂ and H₂O). 118
- Fig. 5.18 AFM (figures (a) and (c)) and AFAM (figures (b) and (d)) images of S0 and S1, respectively. The scan area is 2.5 μm² in all the images. The scale bar for topography (AFM) and AFAM feedback signal in nano ampere are given just below the respective images. The acoustic force feedback signal in S1 is more than 2 times the value of S0. The stiffness constant derived from the AFAM of S1 (as seen from fig. (d)) is ~2 times higher than stiffness constant of S0 (fig. (b)). 121
- Fig. 5.19 Relative stiffness calculated against standard Silicon. Highest change in stiffness was observed in S1. 123
- Fig. 6.1 SEM images showing the surface morphology of GNWs on SiO₂/Si substrate. No visible change in morphology could be seen with implantation duration (as shown in the right corner of the images). 129
- Fig. 6.2 SEM image of carbon paper reveals the fibrous nature and thus large surface area. 129
- Fig. 6.3 SEM image shows the full coverage of surface area of carbon fibre by GNWs at different magnifications. 130
- Fig. 6.4 GNWs on carbon paper pristine and nitrogen plasma implanted for 2, 4 and 8 minutes. With increase in implantation duration etch removal of material increases. 130
- Fig. 6.5 Deconvoluted Raman spectrum of GNWs. Respective nitrogen plasma implantation duration is given in each figure. 132
- Fig. 6.6 The G-normalised full spectrum comparison of Raman spectrum of implanted GNWs. The inset shows the increase in background intensity in between D and G peaks due to implantation. The 'A' peak falls in this region. 133
- Fig. 6.7 FTIR spectrum of GNWs in the mid IR range. IR transparent Si is used as the substrate. The background intensity decreases with implantation duration. 135
- Fig. 6.8 FTIR spectrum of GNWs in 1000 -1800 (cm⁻¹) range. The respective peaks are identified. Pristine and 2 min. samples show identical graphical pattern indicating definite functional groups are not formed in 2 minutes of

- nitrogen plasma implantation. Functional groups are generated only after 4 min. of implantation. 136
- Fig. 6.9 FTIR spectrum of GNWs in 2700-3700 (cm^{-1}) range. The spectrum shows change in the sp^3C bonding pattern. The peak 2852 and 2921 (cm^{-1}) are due to methylene ($\text{sp}^3\text{C}-2\text{H}$) symmetric and asymmetric stretch vibration. The peaks 2868 and 2953 (cm^{-1}) are due to methyl group ($\text{sp}^3\text{C}-3\text{H}$) symmetric and asymmetric stretch vibrations. 136
- Fig. 6.10 Survey spectrum of GNWs. Peaks corresponding to C 1s and O 1s can be observed in pristine GNWs. Survey spectrum of 2 min., 4 min. and 8 min. implanted GNWs show the peaks corresponding to C 1s, N 1s and O 1s. 138
- Fig. 6.11 The C 1s and O 1s X-ray photo electron spectrum of pristine GNWs. Respective peaks are identified. The D peak in C1s pristine stands for hydrogen terminated defect peak. 139
- Fig. 6.12 C 1s spectrum of GNWs nitrogen plasma implanted for 2 min. The C 1s BE variation due to defect and bonding is shown. 140
- Fig. 6.13 C 1s spectrum of GNWs, nitrogen plasma implanted for 4 min. and 8 minutes. 140
- Fig. 6.14 N 1s spectrum of GNWs nitrogen plasma implanted for 2 min. The nitrogen is categorised as N1, N2 and N3 based on the binding energy of N 1s electron. More details are this categorization is discussed in chapter 5. 141
- Fig. 6.15 N 1s spectrum of GNWs, nitrogen plasma ion implanted for 4 and 8 minutes. The peaks corresponding to N1, N2 and N3 are marked. The area fraction is given in table 6.4. 142
- Fig. 6.16 The O 1s XPS spectrum of GNWs. The oxygen is assumed to be in surface adsorbed state. 142
- Fig. 6.17 O 1s spectrum of GNWs, nitrogen plasma ion implanted for 4 and 8 minutes. The peaks corresponding to O1, O2 and O3 are marked. The area fraction is given in table 6.5. 143
- Fig. 6.18 Typical water contact angle measurement of GNWs on carbon paper 144
- Fig. 6.19 Cyclic voltammogram of pristine GNWs at different scan rate. With increase in scan rate the area enclosed by the curve also increases. 145
- Fig. 6.20 Cyclic voltammogram of GNWs on CP nitrogen plasma implanted for 2 minutes. The area enclosed by the curve increases with scan rate. Near square like pattern indicate charge storage. 146
- Fig. 6.21 Cyclic voltammogram of GNWs on CP, nitrogen plasma implanted for 4 minutes and 8 minutes. The area enclosed by the curve increases with scan rate in both cases. Near square like pattern indicate charge storage. 146
- Fig. 6.22 Comparison of Cyclic voltammogram of VGNs on CP pristine and nitrogen plasma implanted samples at 100mV/s scan rate. All the implanted samples show increase in area enclosed by the curve as compared to the pristine. The 2 min. implanted sample show highest area. 148

Fig. 6.23 The charge-discharge curve of GNWs pristine and implanted for 2, 4 and 8 min. The 2 min. implanted GNWs show improved charge- discharge behaviour. 149

List of Tables

Table 1.1	Various methods and process condition of synthesis of GNWs.	9
Table 1.2	Raman spectroscopic features applicable to both monolayer graphene and graphene nanowalls [149]. The peak values given are for monolayer graphene. The term ‘blue shift’ and ‘red shift’ used by the author (Ado Jorio) is maintained in the table below.	24
Table 1.3	Some common functional groups in FTIR spectrum of Graphene materials.	26
Table 2.1	Technical details of PIII&D System.	42
Table 4.1	Process parameters used GNWs synthesis using H ₂ -CH ₄ mixture.	81
Table 4.2	Deposition parameters used for Ar-CH ₄ mixture.	87
Table 4.3	Comparison of Raman spectra.	91
Table 4.4	FTIR spectroscopic study of GNWs.	94
Table 4.5	Results of TEM images, diffraction pattern and EELS analysis.	100
Table 5.1	Raman spectroscopic analysis of GNWs (S1, S2 and S3).	108
Table 5.2	Carbon 1s photoelectron analysis of S1, S2 and S3.	114
Table 5.3	Nitrogen 1s photoelectron analysis of S1, S2 and S3.	116
Table 5.4	Oxygen 1s photoelectron analysis of S1, S2 and S3.	119
Table 6.1	Results of deconvolution of Raman spectra.	131
Table 6.2	Elemental composition of pristine and implanted GNWs.	138
Table 6.3	Results of C1s analysis of samples.	141
Table 6.4	Results of N1s analysis of samples.	142
Table 6.5	Results of O1s analysis of samples.	143
Table 6.6	Water contact angle measurements on GNWs.	145
Table 6.7	Capacitance calculated from cyclic voltammetry. The 2 min. sample show highest capacitance improvement.	147
Table 6.8	The charge / discharge characteristics of GNWs.	150

Abbreviations

2D	Two dimensional
AFAM	Atomic Force Acoustic Microscopy
AFM	Atomic Force Microscopy
BWF	Breit Winger Fano
BZ	Brillouin zone
CA	Contact Angle
CD	Charge-Discharge
CNTs	Carbon Nanotubes
CP	Carbon Paper
CV	Cyclic Voltammetry
CVD	Chemical Vapour Deposition
DFT	Density Functional Theory
ECR-CVD	Electron Cyclotron Resonance Chemical Vapour Deposition
EELS	Electron Energy Loss Spectroscopy
FESEM	Field Emission Gun Scanning Electron Microscope
FTIR	Fourier Transform Infra-Red Spectroscopy
FWHM	Full Width at Half Maximum
GNWs	Graphene Nanowalls
GO	Graphene Oxide
H-BN	Hexagonal Boron Nitride
HFCVD	Hot Filament Chemical Vapour Deposition
ICDD	International Crystal Diffraction Data
MWNTs	Multi Walled Carbon Nano Tubes
N-VGNs	Nitrogenised Vertical Graphene Nanowalls
PCV	Physical Vapour Deposition
PECVD	Plasma Enhanced Chemical Vapour Deposition
PIII&D	Plasma Immersion Ion Implantation and Deposition
RF	Radio Frequency
SC	Supercapacitor
SIMS	Secondary Ion Mass Spectroscopy
SRIM	Stopping and Range of Ions in Matter
SWNTs	Single Walled Carbon Nano Tubes
VGNs	Vertical Graphene Nanowalls
XPS	X-Ray Photoelectron Spectroscopy
ZL	Zero Loss

Notations and Symbols

θ	Diffraction angle (Degree)
λ	Wavelength (nm)
ν	Frequency(Hz)
C_s	Specific Capacitance
V_0	Voltage across sheath (V)
j_c	Current density (A.m-2)
k_c	Spring constant (Nm-1)
n_0	Plasma density (m-3)
γ_{SL}	Surface energy (Jm-2)
ϵ_0	Permittivity of free space (F.m-1)
ω_{pi}	Ion Plasma frequency (Hz)
$\sigma(\nu)$	Raman cross section (cm2)
e	Electronic charge (C)
E_b	Binding energy (eV)
h	Planks constant(Js)
i	Current (A)
k	Boltzmann constant(JK-1)
M	Mass (Kg)
Q	Charge (C)
α	IR absorption coefficient
ϕ	Work function (eV)
S	Sheath thickness (m)
d	Interplanar spacing (nm)

Graphene nanowalls and its nitrogen modification-An overview

1.1. Introduction

In nature, carbon exists in sp^2 hybridised (graphite) and sp^3 hybridised states (diamond and amorphous carbon). Graphite is three dimensional (3D) crystalline assembly of sp^2 hybridised two dimensional (2D) crystal, graphene. Other allotropes such as fullerene (C_{60} , C_{70} , etc.) and carbon nanotubes (CNTs) are spherical and tubular manifestation of graphene, respectively.

Graphene exhibit a variety of exotic properties in comparison to other familiar materials in the respective categories. Graphene has a surface area of $2630 \text{ m}^2/\text{g}$ [1], high thermal conductivity ($\sim 5000 \text{ W/mK}$) [2], fast carrier mobility ($\sim 200000 \text{ cm}^2/\text{Vs}$) [2] and high Young's modulus ($\sim 1 \text{ TPa}$) [3]. The above values are much higher than their commonly used counter parts. For example, suspended graphene exhibit fascinating electrical (current density 1×10^6 times better than copper), mechanical (harder than diamond, more than 300 times stronger than the strongest steel) optical (98% transmittance), thermal (best thermal conductor) and chemical (π –electron doping and 2D crystal) properties. However, making use of the above properties of monolayer graphene is not trivial. For example, the thermal conductivity of monolayer suspended graphene is $\sim 5000 \text{ W/m K}$ whereas; graphene on SiO_2 support surface has a reduced value of 600 W/m K . This is because, the phonon propagation in an atomically thin graphene sheet is very sensitive to surfaces, edges and defects that coupling and scattering of phonon modes of graphene with vibrational modes of substrate takes place [4]. Similar situation arises for other properties also. Even then, graphene is used in a variety of applications.

Graphene exhibit extraordinary strength, stiffness combined with lightness; it has generated great expectations in the application in flexible electronics and as mechanical reinforcement agent of various high stiffness gadgets [5,6]. Additionally, the superior mechanical properties make graphene a materials for nano electromechanical systems and gadgets [7]. High Young's modulus, extremely low mass, large surface area make these materials suitable for sensing mass, force and charge at low (nano) dimensions [7]. Though extreme properties cannot be achieved to the maximum, few layer graphene and other graphene derivatives are finding lots of applications as graphene-enhanced composites for light weight high strength materials for sports, electronics, sensor and energy applications.

To mention a few, graphene has been used for solar cell [8–10], ultra capacitor [1,11], hydrogen storage [12,13] and re-chargeable battery [14].

Instead of opting for horizontal or random arrangement, if monolayer graphene is stacked vertically, the extreme properties can be largely extracted with enormous release of surface area and active edges. Being a 2D material, monolayer graphene do not have

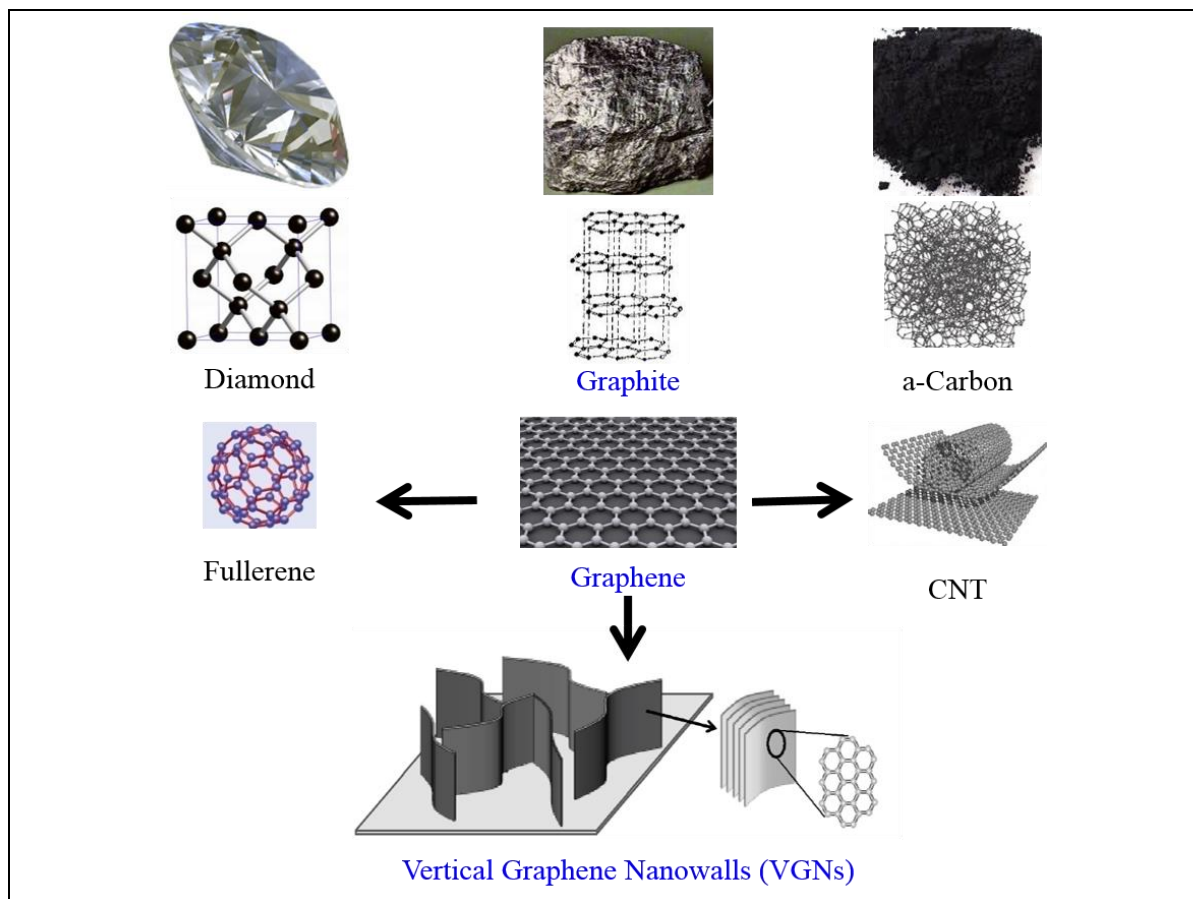


Fig. 1.1 Over view of carbon allotropes and their atomic arrangements in space

self-standing mechanical stability. However, if two or more layers are stacked together vertically, mechanical stability can be achieved. In this context, graphene nanowalls (GNWs) also called as vertical graphene nanowalls (VGNs) is a promising material which offers self-standing mechanical stability. GNWs exhibit electrical conductivity, large surface area and high edge density. GNWs are synthesised using a variety of chemical vapour deposition (CVD) methods on different substrate materials at ease [15]. Consequently, application of GNWs as an excellent choice for electrode material in areas of supercapacitor, photovoltaic, field emission and fuel cell has been successfully demonstrated [16]. A similar technological advantage has been described for vertically aligned CNTs over randomly oriented ones in field emitters, electromechanical actuators,

gas sensors and catalysis [17]. Though these applications offer great potential for GNWs as electrode material, there is continuous demand for improving the performance and exploring new avenues of applications, by modifying the surface properties. Advanced engineering design demands materials tailored to obtain the best achievable combination of properties. However, for the most demanding applications, it is difficult or even impossible to select a pristine suitable material which exhibits the critical properties required to meet the most demanding applications. Hence, the strategy is to synthesis the best possible material and modify/dope it suitably for achieving the required properties. Among the numerous potential doping elements of graphene, nitrogen is considered to be an excellent choice, because of its comparable atomic size/weight to carbon and availability of five valence electrons to form bonds with carbon atoms [18]. Since graphene is the building block of GNWs, deposition and modifications are fundamentally taking place at the hexagonal carbon structure of graphene. Hence, the discussions on modifying /doping of GNWs are usually flip-flopped between graphene and graphitic layers. In this thesis, the synthesis of GNWs and its nitrogen incorporation by plasma nitrogen ion implantation technique are discussed.

Nitrogen doping has been successfully applied to graphene to improve the electrochemical properties. For example, in fuel cells, CO poisoning of Pd, Pt catalysts supported on graphene is an issue and studies have shown that nitrogen doped graphene can replace the costly and scarcely available metal catalyst [19]. Several reviews and other reports shows the importance of N doped graphene in H₂ storage [20] supercapacitors [21], Bio-sensing [22] and solar [10] applications.

Nitrogen doping of graphene can be carried out by different methods such as CVD, arc discharge, solvothermal growth, thermal, plasma treatment etc. [23]. GNWs have been synthesised mostly by plasma based methods termed as plasma assisted chemical vapour deposition (PACVD) or plasma enhanced chemical vapour deposition (PECVD) technique [24–26]. Since, gaseous precursors are used for the generation of plasma, nitrogen doping during synthesis become a subject of interest. However, synthesis of nitrogen doped GNWs are not trivial, especially because of the difficulty in optimizing the feed gas ratio to get the required growth rate and fraction of possible N-doped phase selection. In any CVD synthesis technique, the deposition and doping aspects are basically controlled by the chemical energetics and preference of the doping centres to bond with the dopant. The thermodynamic stability of the doped phase determine the final location of doping in the graphene/GNWs. Hence, in a CVD process, the doping concentration and doping centre selection are largely controlled by the local chemistry. Further, in a

PECVD/PACVD process slight enhancement of dopant concentration by plasma activation is possible. However, the chemical preference of doping centres can be avoided by physical bombardment of energetic nitrogen ions (N-ions) into the GNWs. Consequently, strong efforts have been made to make N-doped graphene by ion bombardment of the target using an ion gun [27,28] and nitrogen plasma ion implantation [29].

With reference to GNWs, they offer large surface area in the vertical plane towards tuning the electronic and mechanical properties. Hence, surface modification by nitrogen is used to improve specific properties for several applications [15,30,31]. Therefore, understanding and controlling implantation/doping in GNWs are important both in terms of fundamental and technological aspects. The present study describes one such new approach; exploring the PECVD versatility on morphological control in synthesis and high density, less defective nitrogen surface modification by plasma ion implantation in a plasma immersion ion implantation and deposition (PIII&D) facility. Though there are encouraging reports on N-GNWs, literature lacks clarity on control of morphology, crystallinity, secondary growth and electronic nature as a function of process parameters during synthesis, and effect of energy, ions and dose on doping.

In the present work, the entire process of GNWs synthesis, modification and a possible application have been studied along with preliminary studies on synthesis, PIII&D facility optimization and functioning. To start with, the literature on synthesis of GNWs is discussed to understand the influence of process parameters, importance of morphological, structural and electronic properties to understand the base materials response to improved mechanical and electro-chemical properties upon nitrogen modification/doping. The nitrogen modification process, characteristics and application of GNWs and N-GNWs are discussed, next. Literature on supercapacitor application of GNWs / N-GNWs as electrodes is reviewed. Finally, the objectives and scope of the work is presented.

1.2. Synthesis of Graphene nanowalls

The first vertical sheet like carbon structure, graphene nanowalls were accidentally discovered in a PECVD (microwave) chamber during the synthesis of carbon nanotube on NiFe coated sapphire substrate using CH₄-H₂ gas in 2002 as shown in Fig. 1.2 [32]. Earlier, zero dimensional (0D) manifestation of graphene, buckminsterfullerene (C₆₀) was discovered in early 1980s [33] and Fullerene became an active topic of research in 80s and 90s, later (2D) petal like graphite sheet was discovered in 1997 [34]. Monolayer graphene was separated for the first time in 2004 from graphite sheet [35], which unleashed a boom

in 2D materials research including graphene nanowalls. Since then, large prospects of applications were linked to graphene and graphene nanowalls in scientific reports.

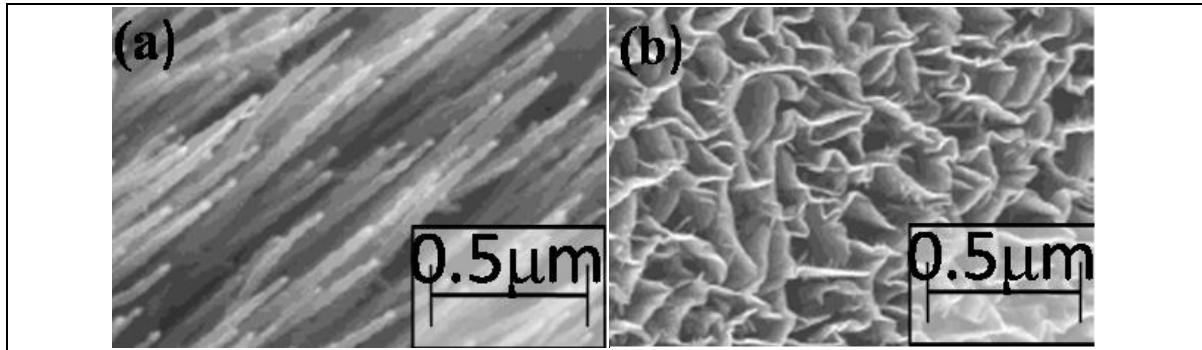


Fig. 1.2 First report on GNWs synthesised during the growth of CNTs. (a) CNTs, (b) GNWs [32]

Very often, literature finds a mention of graphene nanowalls and graphene nanosheets, in applications related to graphene based materials. This induce some confusion in readers on the type of material discussed. Basically, these two type of material are the outcome of two school of thoughts that have been developed based on the much familiar synthesis methods; top down and bottom up approaches for nanomaterials synthesis. Graphene nanowalls are grown unparallel to the substrate surface with large amount of corrugation and secondary growth in an atom by atom deposition process. In this thesis, graphene nanowalls (GNWs)/vertical graphene nanowalls (VGNs) are deposited by bottom up approach is described. On the other hand, graphene nanosheets are random oriented graphene / a few layer graphene sheets with modified surfaces produced by breaking down of bulk material (Graphite) by chemical (e.g. H_2SO_4) and mechanical (e.g. Ultrasonic, Ball mill) methods [36–39]. Modified Hummers method is one such high yielding and popular graphene oxide (GO) or reduced GO synthesis technique [40]. In comparison to the conventional randomly oriented graphene nanosheets, graphene nanowalls (GNWs) exhibit vertical orientation to the substrate, non-agglomerated morphology, controlled inter-sheet connectivity, and sharp-open edges that make them different [16].

Vertical graphene nanowalls are usually synthesised by plasma enhanced /assisted chemical vapour deposition (PE/PA CVD) on various substrates using gas (CH_4 , C_2H_2 , C_2F_6 , etc.), liquid (Honey) [41]. or solid (magnetron sputtering of carbon) [42] precursors. GNWs can be synthesised on any substrate which can withstand the deposition temperature. PECVD method for deposition of GNWs do not require any catalyst for deposition. In addition to PECVD, chemical vapour deposition (CVD) [43] and hot filament CVD (HFCVD) [15,44] methods have also been reported in literature. In CVD process, the

growth is done at a hot zone measuring $\sim 1130^{\circ}\text{C}$ whereas in HF CVD, the substrate is heated to $\sim 700^{\circ}\text{C}$ and the filament which is used to decompose the precursor gases ranges up to $\sim 2200^{\circ}\text{C}$. In both the above cases, the process temperature is much higher than plasma based processes. However, in PECVD synthesis, substrate temperature as low as 500°C is reported for VGN growth [45]. Additionally, the deposition temperature can be lowered and deposition rate is improved by using higher hydrocarbons (such as C_2H_2) in place of methane or using diluting gases such as CO_2 in place of Ar [46,47]. Additionally, PECVD offers large scope for synthesis and in-situ modification of GNWs. Hence, PECVD technique is used for the synthesis of GNWs in the present study.

The process parameters influence the deposition process. The essential requirements for PECVD of GNWs are precursor carbonaceous gas and a diluting gas, plasma generating system, the substrate and substrate heater. The operating parameters of each influence the deposition process. Hydrocarbons (CH_4 , C_2H_2 , etc.) are used as the carbon source and Ar, H_2 , N_2 , etc., are the common diluting or plasma generating or doping gases. High plasma power induces ionization and generation of directed electric field and magnetic field in the plasma. The gas molecules are broken down into ions, and with increases in plasma power, the energy of plasma constituents are also increased. Almost all carbonaceous gases constitute hydrogen; the hydrogen ions etch away the unstable carbon into gaseous phase leading to reduction in edge density of GNWs. Similarly, Ar is another important constituent in the precursor gases which increases the energy of plasma constituents and electrons to influence the deposition process. The scattered literature in these aspects has been brought together and a consolidated view is brought-in, with respect to the influence of process gases (CH_4 , H_2 and Ar) and its ratio on the structure and morphology of GNWs. This aspect is discussed in chapter 4.

If the precursor gas flow is less and pressure is low, the ions mean free-path increases and it acquire more energy for a given plasma power. Increase in pressure, increases the available number of ions and its collision and recombination rate. Thus, high pressure reduces the ion density and energy of plasma constituents. As a result, the specific plasma species facilitating certain deposition can be reduced. Hence, there exist an optimum plasma power and pressure for growth keeping all other (temperature, substrate type and its position, etc.,) parameters unchanged [48]. There are several studies in this topic and each one of them is not conclusive because several parameters (*gases and gas ratio, forward and reflected power of the plasma system, substrate proximity to plasma source, type of plasma*

-dc, capacitive, inductive, RF, microwave, ECR-Microwave, heater temperature, substrate and its pretreatment, pretreatment before deposition , etc.) are involved in the process. Hence, even after several detailed in-depth studies mechanism behind the deposition of GNWs is inconclusive and one has to explain and correlate the process condition with the characteristics of GNWs with respect to the specific system used for synthesis. Additionally, when doping is performed extra complexity is introduced. Though plasma process offers the flexibility in growth with different properties, it is a challenge to find suitable parameters for the optimal growth for a specific need [49]. Hence, a separate study is taken up to understand the working of the custom made system (Chapter 3) and literature back up is used to select the initial precursor gas parameters for GNWs growth (Chapters 4).

1.2.1. Growth mechanism of graphene nanowalls

Even after extensive studies on synthesis and applications of GNWs, the plasma based growth mechanism of GNWs is not fully understood particularly the initial stages (nucleation and further development). Bo et al., describe that the growth mechanism involve the formation of a structurally defective buffer layer of carbon. This is followed by vertical growth due to the stress and/or electric field direction and the growth saturates when material deposition and etching rate equilibrates [16]. Baranov et al consider the ion bombardment and surface diffusion as the key factor in the generation GNWs [50]. There are postulates that the GNWs grow on amorphous or graphitic layers randomly on surface defects [51], and defective nano diamond and nano graphite layers [51,52]. Considering different substrates, there were postulates on substrate thermal conductivity and hot spot formation due to plasma–solid interaction, as the reason for GNWs nucleation and variation in morphology [53]. However, the above reports are inadequate to explain the nucleation and growth completely. For example, it has been well established that GNWs can be deposited in any surface and the incoming carbon containing radical do not require any extra energy to attach to the substrate; rather it requires a suitable *active* site for shedding its extra kinetic energy. As a result, crystalline SiO₂ (quartz) show poor deposition rate as against oxidised Silicon surface (defective and amorphous) under same process conditions [53]. However, it is logical to assume the first layer of carbon can be amorphous due to large mismatch of lattice parameters between the substrate and the carbon /graphite layer. Vitchev *et al.*, did not observe the formation of amorphous layer on platinum substrate; whereas, an amorphous carbon layer is observed on quartz and Si substrate whose surface is converted

into SiC [51]. This indicates that depending on the substrate surface there can be a carbon buffer layer or a compound like SiC.

GNWs can be deposited in a variety of processes. In all the processes (even in HFCVD) plasma of the precursor gases/material is present. Plasma is an aggregate of high energy ions, radicals and electrons having net positive charge with respect to the surroundings due to the higher velocity of electrons as compared to positive ions. As a result, an electric field is generated. With respect to plasma, the substrate surface is at a negative potential and so, the ions are attracted and electrons are repelled. Fig. 1.3 shows the schematic of GNWs deposition. The region in between the plasma and substrate where incoming ions and expelled electrons interact is called 'sheath'.

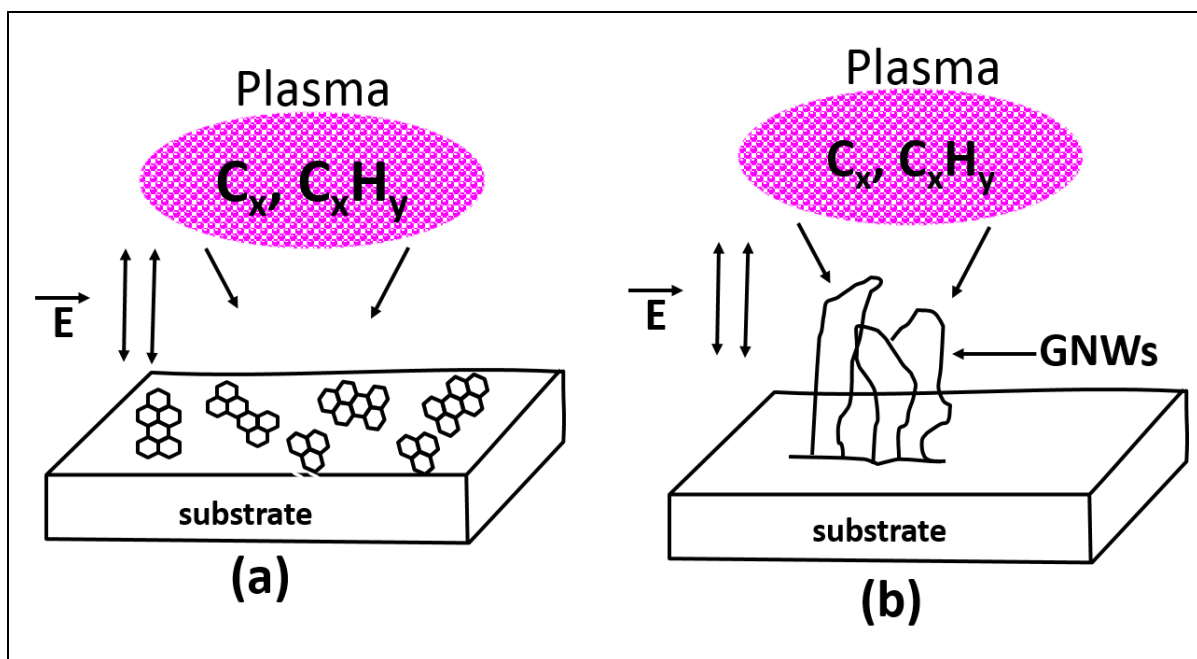


Fig. 1.3 Schematic representation of GNWs (VGNs) growth model. (a) Shows the nanocrystalline a few layer graphene deposited over amorphous carbon layer formed on the substrate. (b) At the junctions, horizontal growth changes direction due to stress and the directionality of electric field. Possible plasma species also shown.

The sheath above the substrate surface attracts the ions and repels the electrons even in an unbiased condition. The energetic ions impinge on the substrate surface and produce dangling bonds. The high energy and chemically active plasma species attach with these dangling bonds to stay on the surface. Addition of new plasma species induces growth and the direction of electric field aligns the growth parallel to its direction. However, initial nucleation and growth takes place parallel to the substrate surface due to the geometrical

Table 1.1 Various methods and process condition of synthesis of GNWs.

Plasma source	Source Gas	Ratio / Flow rate (sccm)	Process Parameters			Nanostructure and characteristics	Ref.
			Temp. (°C)	Press. (mbar)	Plasma power (W)		
RF excitation of plasma (13.56 MHz)	CH ₄ :H ₂ :Ar	0.9:9:90	1000	1.3	600	Graphene layers	[54]
	CH ₄ :H ₂	10:200	680	0.12	900	Free standing graphite sheets	[55]
	CH ₄ :Ar	7:1.4	700-850	0.08	500	Graphene nanowalls	[45]
	CH ₄ :H ₂	1:4	400	0.2	200	Pt support GNWs	[56]
	CH ₄	6	650	1.3	550	Both few layer and monolayer graphene	[52]
	C ₂ F ₆ , H ₂	50:100	580	1.6	270	GNWs	[57]
	Ar, H ₂ , C ₂ H ₂	1050:25:1	700	1.3	300	GNWs and nanostructures	[58]
Microwave (2.45GHz)	CH ₄ :H ₂	40:10	700	1.3	500	Uniformly oriented GNWs	[32]
	CH ₄ :H ₂	1:8	700	53	2000	A few layer graphene with 4-6 atomic sheets	[59]
	C ₂ H ₂ :Ar	10:200	240	<1.3	1200	A few layer graphene d spacing 0.345 nm	[60]
	CH ₄ :N ₂	1:4	1250	2.7 × 10 ⁻³	800	GNWs	[61,62]
DC plasma	Ar:H ₂ :C H ₄	1000:0.15:1.35	700	1000	10kV	GNWs	[63]
Hot filament CVD	CH ₄ :H ₂	10:50	1000	0.37	1750 (°C) Filament temp.	Corrugated graphene patches on Cu	[64]
	CH ₄ :He	2:98	700	30	2000 (°C) Filament temp.	GNWs on carbon fibre	[15]

instability of vertical monolayer. The horizontal growth on the surface continues until different planar nanographitic layers meet. The stress at the point of contact and direction of electric field induces the vertical growth. Since the electric flux density is high at the tip, more and more radicals are directed from the plasma and get deposited on the tip and the tip grows [49]. The corrugation of the GNWs is associated to different growth orientation of the individual ionic species and stresses associated with constrained growth. In all the above processes the energy, ionization species and plasma sheath above the GNWs play a crucial role. Table 1.1 summarizes the GNWs deposition process and other characteristics. The flow rate, gas pressure, and ratio of the above gases also influence the deposition process.

Plasma power is an important parameter in the formation of GNWs. Plasma power increase the ionization and ionic species density. Since, different ionic species have varying sticking coefficient and etching capabilities, it affects the GNWs growth. Additionally, in a plasma system, the extent of ionization of a mixture of gas depends on the reflected power also. It has been shown that high plasma power induced strong electric field influence the microstructure [65]. The electric field strength helps to increase the height of GNWs [50]. The neutral species developed in the plasma influence the growth process and defect generation [66]. These aspects are not exclusively discussed in literature systematically for a given sample. However, the above aspects may be taken as a directive and one has to formulate system specific plasma parameters.

Substrate temperature is another important parameter in the formation of GNWs. In a plasma process like ECR-CVD, under similar conditions, when the temperature is in the range of 800 °C, GNWs can be prepared; whereas, if the no heating is provided DLC (with bias) or amorphous carbon can be deposited. The substrate temperature provides sufficient energy to the deposited carbon atoms to diffuse and occupy the equilibrium graphitic positions in GNWs. However, high temperature is found to have adverse effect in CH₄/H₂ microwave plasma [67]. Our own experience shows that a temperature up to 850 °C helps to improve the quality of graphitised layers and no adverse effect is noticed..

1.3. Characteristics of Graphene nanowalls

Graphene nanowalls or vertical graphene/carbon nanowalls are a few layer aggregate of graphene arranged unparallel to the substrate surface.

1.3.1. Morphology and Microstructure

In the present study, GNWs are deposited in SiO₂/Si substrate and hence, we assume amorphous layer in between the GNWs and the substrate. Bo et al. indicated that GNWs, no

longer show any substrate-dependent features [16]. However, Ghosh et al. airs a contrary view [53]. Our own experience also shows that GNWs structure and morphology vary with different substrates that even same material of different crystal orientation viz. $\text{Si}_{\langle 100 \rangle} \text{O}_2$ or $\text{Si}_{\langle 111 \rangle} \text{O}_2$, can give different morphology at least in the initial stages of growth. This indicates that even the intermediate amorphous layer holds the morphological signature/feature of the substrate below, and its influence percolate into the GNWs morphology.

However, once the GNWs is grown sufficiently large, the substrate surface effects can be less influential. Keeping aside the substrate surface inequality, there are other process parameters influence the morphology for identical substrate material. The GNWs prepared using thermal, RF, DC and microwave plasma assisted CVD techniques slightly differs in their fine morphology. This is due to the difference in the energy of the plasma species and the defects it produce on the growth. Microwave synthesised GNWs indicated highly graphitised a few layer (3) graphene like GNWs [62]. RF synthesised GNWs are more defective than microwave or ECR-CVD synthesised GNWs owing to the higher energy of plasma species. The secondary growth is more pronounced in RF synthesised GNWs and are beneficial for a variety of electrochemical applications such as supercapacitor electrodes.

The essential attraction of GNWs is its vertical growth. Of course, CNTs or other nanotubular structures (e.g. TiO_2 nanotubes) also grow vertically. But, such growth is taking place under geometric restriction of catalyst size or the electrode. Bo *et al.* associated three factors influencing the vertical growth of GNWs, viz. the electric field, the internal stress, and the anisotropic growth effects [16]. Each of these will be discussed.

With respect to the orientation of electric field to the substrate surface, the density and orientation of the GNWs networks can be controlled [68,69]. The stresses are developed at the nucleation site due to temperature gradients, ion bombardment and lattice mismatch between the substrate material and the graphitic material. The stresses accumulated on the growing planar graphitic sheet can be released upon growth in the vertical direction. Jiong Zhao *et al.*, brought out a reasonable growth model for GNWs [70]. In this model, the initial nucleation and planar growth of graphitic layers takes place on the substrate followed by vertical growth at the numerous junctions. However, the junctions are not open but closed and the addition of further elementary carbon species takes place on all over the graphitic layer. Hence, the GNWs exhibit a corrugated morphology with a few vertical graphitic layers.

The GI XRD studies of GNWs indicate that fully grown carbon nanowalls has a single phase of hexagonal graphitic structure with high degree of graphitisation similar to graphite powder. The preferred orientation of fully developed /grown graphene layers is perpendicular to substrate surface. However, some peaks which cannot be assigned to hexagonal system indicate horizontal to vertical transition of graphene layers [71]. XRD studies shows increased crystallinity and reduction in the d -spacing of (002) plane of GNWs with increase in time of growth [61]. The electron diffraction studies of GNWs, identifies three major peaks, viz. (002), (101) and (112) that corresponds to ICDD database no 75-1621. The d -spacing of graphitic carbon systems measures ~ 0.34 nm to 0.42 nm depending on the synthesis route [17]. After analysing the HR-TEM images, Ghosh et al., indicates that higher d -spacing (0.356 and 0.364 nm) in GNWs is due to stacking fault disorder induced generation of turbo static graphite in GNWs prepared under CH₄:Ar:H₂ ratio 1:7:0 and 1:0:5, respectively [70,71]. However, there is lack of systematic study with respect to the d -spacing change in specific conditions. Hence, a systematic study on the effect of change in Ar: CH₄ ratio on GNWs growth is taken up and is discussed in chapter 4.

1.3.2. Electronic properties

The basic building block of GNWs is graphene. Graphene is a zero band gap semi-metal; i.e., it exhibit metallic behaviour in current transport because of the unique band structure that both electrons and holes move as massless Fermions with $1/100^{\text{th}}$ velocity of light at Brillouin zone corners (Dirac points) [74]. If substitutional defects are preserved with D_{6h} symmetry, the Dirac cones are unaffected, otherwise band gap is generated [23]. The substrates (SiO₂, HfO₂ and H-BN) also influence graphene electronic state, because of potential undulations, structural distortion and hybridization. A few layer graphene exhibit quadratic dispersion of electronic energy state with small and finite energy gaps instead of linear dispersion for monolayer suspended graphene [75,76]. This poses a serious problem in utilizing graphene for conventional electronic application at nano scale where a substrate is required to give mechanical support to graphene and normal metals for electrical contact.

The metallic character of graphene is due to vanishing density of states at the Fermi level due to the presence of two linear dispersion bands [77]. GNWs consists of bundled corrugated graphene sheets [55,78] and DFT studies shows corrugated graphene have semiconducting properties with tiny (a few meV) band gap [76]. Electronic properties are sensitive to structural undulations and shows with a difference in directions parallel and perpendicular to the undulation [76]. The graphene sheet with defects are semiconductors

that the dangling bond states and non-bonding π states form flat dispersion throughout the entire Brillouin zone [79,80]. Thinning the GNWs induce semiconductor to metallic transition [81].

The atoms and molecule adsorbed to graphene also influence the electronic properties. The adsorption of fluorine convert metallic graphene to semiconducting depending on the location of fluorine [76]. DFT simulation of B and N doped graphene shows that isomers formed differ significantly in stability, bond length and band gap. The band gap is maximum when dopants are placed at same sub-lattice points and the band gap is closed when dopants are placed at adjacent positions (alternate sublattice positions). These interesting results provide the possibility of tuning the band gap of graphene required for electronic devices such as replacements to Pt based catalysts in Polymer Electrolytic Fuel Cell (PEFC) [30].

1.3.3. Mechanical properties

Monolayer defect free graphene exhibit extraordinary mechanical properties [3]. However, generation of lattice defects (vacancy, sp^3) are unavoidable in bulk fabrication of graphene and graphene related materials such as GNWs. Studies indicate that the in-plane Young's modulus increases with increasing defect density up to two times the initial value for ~0.2% vacancy content. This is a very encouraging result, that graphene with some amount of vacancy defects make it the stiffest material ever reported [82]. The initial increase in Young's modulus is explained in terms of a dependence of the elastic coefficients with the momentum of flexural modes predicted for 2D membranes [83,84]. However, with increase in defect density (vacancies), the elastic modulus decreases. The reduction in fracture strength with increasing defect density is in line with standard fracture continuum models. There are reports that large area graphene synthesised using CVD technique, largely maintain its mechanical properties even with the existence of grain boundaries, if post processing steps can avoid damage or rippling [85]. Additionally, high density of sp^3 defect in graphene has only reduced the breaking strength by 14 % of its pristine counterpart. However, it is well accepted that the increased density of vacancy defect reduces the mechanical properties [86]. These quantitative structure-property relationships are of fundamental and technological relevance to provide guidance for applications of GNWs; because, GNWs are inherently defective (vacancy, sp^3 , etc.).

GNWs subjected to Gallium (Ga) implantation in FIB chamber showed an increase in elastic moduli from ~4.9 MPa for pristine to 10 MPa for implanted one. Further, it is

shown that by exposing the GNWs to XeF₂, fluorination of GNWs is achieved and the resulting sample show an increase in the elastic modulus (18.4 MPa). Hence, the combined treatment of Ga irradiation and fluorination yielded GNWs of modulus 32.4 MPa [87]. Similarly, atomic layer deposition of alumina (5 nm) on GNWs synthesised by PECVD techniques yielded 3 fold increase in effective elastic constant than pristine GNWs measured using Nano indentation technique [88].

The mechanical properties of graphene nanowalls (GNWs) is not discussed in literature much. Though individual graphene sheets register highest strength and hardness, when a few layers are combined, the mechanical strength reduces. However, theoretical study of graphene sheet indicate that simultaneously tuning the graphene sheet size and cross link mechanisms for improved mechanical properties [89].

In the present study, the mechanical property evaluation of graphene is attempted. Atomic force acoustic microscopy (AFAM) technique is employed for the comparison of mechanical properties of pristine and implanted GNWs for the first time. The AFAM study reveal the mechanical property variation at microscopic dimensions. This aspect is discussed in chapter 5.

1.3.4. Applications of graphene nanowalls

Graphene nanowalls are reported to have several unique properties to be used in a variety of applications. In order to provide the potential of GNWs, a few applications are summarised.

GNWs are used in a variety of energy related applications. GNWs has been used for rechargeable Li batteries anode materials; the peculiar morphology and structure provide numerous sites to capture Li ions [16,90]. Graphene based Li batteries showed very reversible lithium storage capacity and good cyclic stability [91]. GNWs are used to capture solar energy in Si based solar cells [88]. Graphene nanowalls are used in double layer capacitor and it can be used as better ac filter in place of conventional RC circuits with better performance and lower response time [16,93]. GNWs deposited on nickel substrates are used as electric double layer capacitors. High growth rate was observed on GNWs grown on nickel film 70-80 nm per minute and a maximum capacitance of 120 $\mu\text{F}/\text{cm}^2$ is reported. The mechanism is suggestive of not simple double layer capacitance [94]. The graphene nanowalls show excellent resistance to acid (H₂SO₄, HNO₃, HCL and HF) attacks [95]. This aspect is used to separate free standing GNWs from metallic substrate to be used with flexible or low melting point electrode materials for supercapacitor applications [96].

GNWs have shown excellent electrochemical response in cyclic voltammetry (CV) and impedance spectroscopy [97]. This aspect have been used for several electrochemical applications of GNWs. CV measurements show that the Pt/CNWs (GNWs) electrode has a better electrochemical activity and methanol oxidation property than Pt/ vertically aligned carbon nanofibre electrode. The unique structure of GNWs ensures that Pt/CNW electrode has a faster electron transport rate and shorter electron transport path, which lead to improvement in electro-catalysis activity compared to the Pt/VACNF electrode and shows further potential for application in direct alcohol fuel cells [56]. Graphene and its derivatives are used for carbon/ (CO₂) capture and conversion in green energy application [98].

Field emission is another area where several reports on low turn-on voltage and high intensity are reported. A few layer graphene (GNWs) synthesised by microwave PECVD has been shown to have low turn-on voltage (1 V/ μ m) and several orders of field emission amplification. The same GNWs, when subjected to hydrogen etching is found to have improved the field emission [99] Similarly, the Ar-plasma treatment of GNWs form sharp edges which decreases turn-on voltage for field emission from 3.91 to 2.23V/ μ m [100]. Magnetron sputter deposited graphene nanosheets also shown to have good field emission turn-on voltage 2.522V / μ m and excellent stability [42].

GNWs are used in different types of sensors by utilizing the conductivity aspects or electrochemical selectivity. GNWs are used as gas sensors for toxic and gas like NO₂, CO and H₂, where the gas induced change in conductivity is used for detection of gases [16]. Field effect transistor (FET) based on GNWs sheet labelled with gold nanoparticles is used as bio sensor for the detection of anti-body coagulates. The biosensor shows high sensitivity (up to 2 ng/ ml or 13 pM) and selectivity towards specific proteins [101]. GNWs synthesised by plasma exposure to natural honey is reported to have reliable gas and bio-sensing performances [41]. Individual base strands of DNA (adenine, thymine guanine and cytosine) can be detected by graphene nanowalls based biosensors [102].

In the thermal energy management, GNWs are used as perfect black body coating with total reflectance of 0.13 %. This value is an order better than that of similar CNT forest [103].

In several applications, deposition of GNWs directly on the substrate helps to improve the contact with the supporting substrate. Hence, the substrate that withstand high temperature (\sim 800 °C) are necessary to get good quality GNWs. There are reports of low temperature growth to overcome this disadvantage. Growth of high quality large area

graphene by RF-PECVD on SiO₂/Si substrate is prepared at 650 °C [104] and nanocarbon structure on Si at 450 °C [105] are reported in literature. Ideally, GNWs should be able to maintain monolayer graphene like properties to utilize its full potential in practical applications. Hence, there is a need to improve the understanding on synthesis of vertically self-standing graphene nanowalls to bring down the temperature without compromising the quality.

1.4. Nitrogen modification of Graphene nanowalls: techniques and characteristics

Defect free mono layer graphene is zero band gap semiconductor. However, introduction of defects (pyridinic and pyrrolic) make the conduction *p*-type; whereas, the conductive behaviour of graphitic graphene is *n*-type [106,107]. Nitrogen doping of graphene can make it an *n*-type semiconductor with little addition of mass and minimum disturbance to the hexagonal lattice.

GNWs are inherently defective and exhibit *p*-type character. In this line, nitrogen doping of inherently *p*-type GNWs can be converted into *n*-type and the carrier concentration can be controlled by adjusting the concentration of nitrogen [106]. It has been reported that introduction of nitrogen in to graphene improves the catalytic activity of Pt loaded in GNWs in the oxygen reduction reaction of fuel cells [23]. Hence, studies of nitrogen doping is very important for several applications. In the following section the techniques for nitrogen incorporation into graphene /GNWs are discussed. Fundamentally, doping takes place at atomic /molecular level and hence, the discussion on both graphene nanowalls and graphitic nanosheets are presented.

1.4.1. Techniques for nitrogen incorporation into GNWs

Nitrogen may be incorporated into the graphene/GNWs by several physical and chemical techniques [21,23,108–110]. Some of the relevant and important methods suitable for GNWs are described. Additionally, a few soft chemistry methods are also used for nitrogen incorporation. The hydrothermal and solvothermal methods give high yield and are used for nitridation of graphene nanosheets [111,112]. Similarly, pyrolysis or annealing is also used for nitrogen doping [113–115]. However, these (soft chemistry) techniques are not discussed here owing to the pure chemical nature of the process and also its irrelevance to the nitridation of GNWs.

1.4.1.1. CVD Methods for nitrogen doping

Planar graphene is synthesised by catalytic CVD methods at very high ($>1000^{\circ}\text{C}$) temperatures [21]. It is often better to perform in-situ doping during synthesis to improve electron transfer and thus impart the required properties for certain applications. In-situ doping of nitrogen can be achieved using a gas mixture of H_2 , CH_4 , SiH_4 and N_2/NH_3 to deposit N-GNWs at 1300°C [116]. In this direction, nitrogen doped graphene (here, pyridinic-N) is synthesised on copper substrate by using ammonia gas as the source of nitrogen [117,118]. Ammonia is also an efficient nitrogen source that as much as 16 at% doping is achieved in planar graphene [119]. CVD methods usually employ very high temperature ($\sim 1000^{\circ}\text{C}$), however, there are a few reports of low temperature (300°C) CVD of pyridine on Cu to get ~ 16.7 at% nitrogen doped tetragonal -shaped single crystal graphene [118]. Relatively, less number of reports are available in the thermal CVD doping of GNWs, owing to the high temperature. Hence, plasma based techniques are considered better.

1.4.1.2. Plasma based processes

Plasma nitrogen doping processes are highly versatile and can be applied on graphene structures at ease. By exposing graphene to nitrogen plasma, up to 1.35 at% nitrogen is incorporated [120]. Since plasma is highly reactive even unintentional exposure lead to nitrogen incorporation. Unintentional nitrogen doping (5.2 at%) is reported on the GNWs synthesis at 100 Pa -RF plasma (300 W) using the gas mixture Ar: C_2H_2 : H_2 (at 1050:25:1 sccm ratio) at 600°C [121].

GNWs are deposited on flexible carbon cloths by microwave plasma-enhanced chemical vapor deposition and N doping is achieved by introducing NH_3 into the plasma, to form N-doped GNWs [116]. In another study, C_2H_2 and H_2 gas mixture is injected into Ar -RF plasma jet of 300W power (Ar: H_2 : C_2H_2 ::1400:25:1 sccm at 120 Pa), and GNWs of 4 μm thickness is deposited in 60 min. at 700°C . Into the same Ar jet, N_2 is injected at 100:10 (Ar: N_2) ratio to incorporate ~ 12 at% nitrogen in GNWs [122].

Ghosh et al. conducted a study on the effect of nitrogen on deposition and doping of GNWs in ECR-CVD reactor. It is demonstrated that addition of nitrogen gas along with a hydrocarbon precursor can enhance the nucleation and growth rate of graphitic base layer as well as vertical sheets depending on the process conditions. During the synthesis of GNWs, using CH_4 -with 3N and 5N purity, 3N purity sample showed no peak corresponding to nitrogen in XPS studies [123]. At low concentrations of nitrogen, the vertical sheet

nucleation and growth is enhanced and at high concentration, more etching or nitrogen inclusion occurred depending on the presence of oxygen (Fig. 1.4). Presence of oxygen as impurity appears to decrease the nitrogen incorporation into GNWs. Nitrogen ions exhibit both etching and doping character simultaneously.

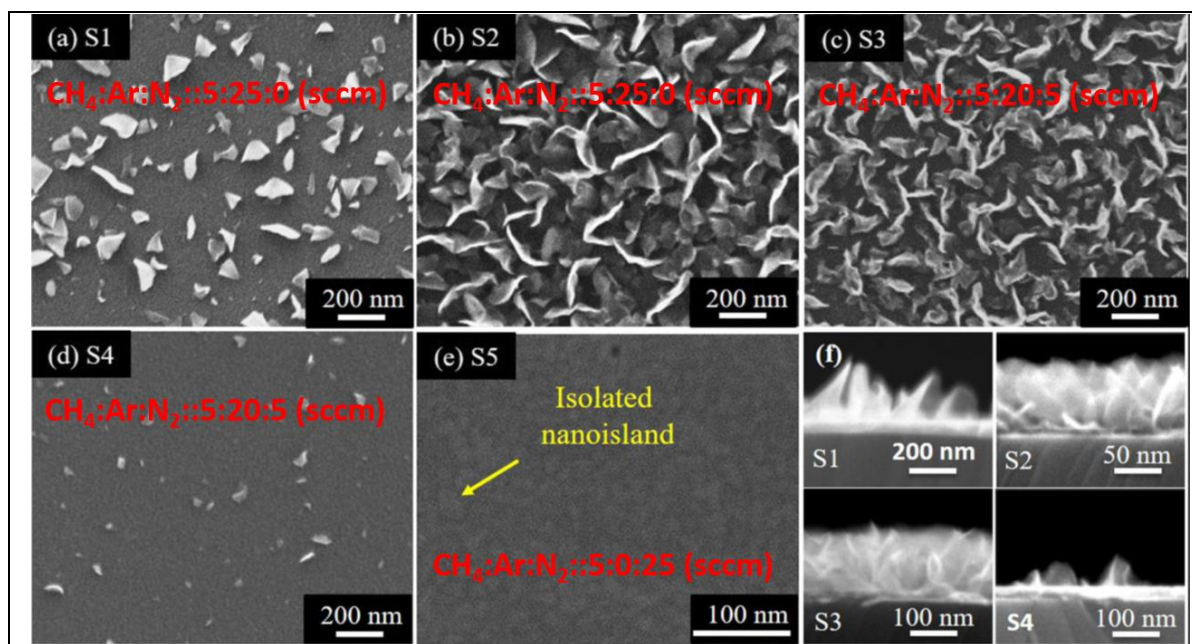


Fig. 1.4 The influence of nitrogen in the synthesis of GNWs deposited using ECR-CVD. S1 and S3 use high pure Ar (5N) and S2 and S4 use commercial pure Ar (3N). Nitrogen induces etching of GNWs and facilitate graphitic nano island formation at high concentration. Only S5 shown the presence of nitrogen in XPS studies [123].

Plasma synthesis of *n*-type GNWs is achieved by using Ar/N₂/C₂H₂ and Ar/N₂/CH₄ gases at 800W microwave power, 13.3 kPa pressure, 850-950 °C temperature [124]. Nitridation of GNWs have been carried out using ECR-CVD based microwave plasma (2.45 GHz, 280W) at 2×10⁻³ mbar under N₂ gas plasma at 340 °C for 3 min at 300W power and 1×10⁻³ mbar given a doping of 17at% N₂ fraction. [125]

GNWs synthesised using RF (13.56 MHz) inductively coupled plasma upon post synthesis Ar:N₂ (2:1) ratio mixture plasma treatment and same RF power at 200, 300, and 600 W have given nitrogen fraction up to 20at% [126]. In all the above processes nitrogen could be incorporated into graphene or GNWs. However, the mechanism of incorporation is controlled by the chemical energetics of the system with a little enhancement due to high reactivity of the plasma. The plasma process have relatively less control over the doping concentration. Better control over ion dose can be achieved by physical processes such as ion implantation.

1.4.1.3. Ion implantation

The basic advantage of ion implantation is that the process is not dependent on the chemical energetics and chemical kinetics of the nitridation reaction. It is purely a physical process and any amount of nitrogen can be incorporated into the GNWs by implanting the ions, provided the irradiation effects such as sputtering is controlled. Usually, an ion source which can accelerate the required ion of specific energy is required for this purpose.

Microwave (2.45 GHz) plasma ion torch is used to produce 25 eV nitrogen ions to implant nitrogen ions (20 at% N). Microwave plasma torch coupled PECVD synthesised GNWs obtained by mixing the N₂ gas along with CH₄ keeping the ratio 1:1 at a pressure 40 mTorr and 1000W power given 7.6 at% doping [127].

Beam line implantation has been used for ion implantation in carbon materials. At 1 kV bias, nitrogen is implanted on vertically aligned carbon nanotubes (CNTs), and upto 19.5 at % nitrogen obtained at the top surface [128]. Similarly, 3 keV, N₂⁺ ion implantation has generated an ion dose of upto 4×10^{15} ions/cm² in SWNTs [129]. Chemically prepared Graphene (Modified Hummers method) deposited on SiO₂ substrate is nitrogen implanted using BNU-400 kV implanter to get a dose of 5×10^{16} ions/cm² [130]. Scardamaglia et al. reported that the nitrogen inclusion in both chemical vapour deposited and exfoliated few-layer graphene flakes in ultra-high vacuum by nitrogen ion implantation in ultra-high vacuum to obtain ~ 20 at.% nitrogen maintaining the sp²-carbon network largely unaffected [131]. Low-energy N₂⁺ ion sputtering of graphene oxides (GO) reports simultaneous removal of oxygen and N-doping [132].

It should be noted that no work on shallow nitrogen ion implantation of GNWs is reported in literature. Since plasma immersion ion implantation is a versatile technique for doping, it is important to explore this avenue for nitrogen incorporation into GNWs.

Conventionally implantation induce defects (vacancy/interstitials) in the materials. Additionally, implantation process can induce sputtering of materials. The projectile ion penetrate the target materials and interact with it before being at rest. At low energies, the interaction with the substrate materials is nuclear that the target atoms get displaced from the mean position. The implanted region is expected to have change in its chemical nature with increase in dose. However, when plasma is used for low energy implantation, in addition to the above effects, plasma-surface chemical interaction also will be taking place. Hence, the process is quite complicated and experimental evaluation of implantation process become a necessity. In addition to that the above effects influence the mechanical properties of the material. The range of ions in materials is estimated by using SRIM simulation. The

above aspects are considered and discussed in the research methodology section in chapter 2.

1.4.2. Structural effects of nitrogen implantation in graphitic layers

Since plasma nitrogen ion implantation is used for nitrogen incorporation of GNWs, it is necessary to know the structural effects of nitrogen ion implantation on graphene/few layer graphitic layers. Molecular dynamics simulation of B or N bombardment on bilayer graphene shows maximum probabilities for perfect substitution of a carbon atom by an incident B or N atom at energies 70 eV (38%) and 110 eV (33%) [133]. This indicates the importance of using low energy ions for plasma ion implantations. The band gap can also be tuned with B or N substitution.

In another study, nitrogen doping in single walled carbon nanotubes by 300 eV N_2^+ ion implantation have shown 11.3 at.% nitrogen concentration. Nitrogen atoms are substitutionally inserted into the sp^2 hexagonal network (graphitic-most stable) or form a pyridine like configuration in a vacancy or bond with four or three neighbours (Quaternary nitrogen). These samples on annealing at 1000° C stabilises into stable graphitic configuration [134].

The nitrogen-doped graphite was prepared by nitrogen ion bombardment followed by thermal annealing. Two types of nitrogen species were identified at the atomic level: pyridinic-N (N bonded to two C nearest neighbours) and graphitic-N (N bonded to three C nearest neighbours) [135]. The pyridinic N in the above study is identified as nitrogen at a vacancy and is negatively charged. The nitrogen substitutionally occupy a carbon position in the hexagonal ring is called graphitic nitrogen. The position of the N atom in graphitic-N species is almost same as that of C atom in graphite (C-N bond shorter by 0.002 nm compared to C-C bond). The graphitic nitrogen is relatively positively charged and is expected to have the chemical shift in N 1s binding energy to higher energy (401.1 eV) in the XPS spectrum compared to that for the negatively charged pyridinic-N (398.5 eV). The difference of 2.6 eV is comparable with that for the pyridinium ion, $C_5H_5NH^+$ (401.2 eV), and the ammonium ion, NH_4^+ (401.5 eV), where N is positively charged in both cases [136], suggesting a positive charge of N for graphitic-N. If N is positively charged, the surrounding carbon atoms should be charged negatively because of the screening effect. Thus, nitrogen implantation can cause formation of pyridinic and graphitic nitrogen in graphene to form Lewis base and acid like character, respectively [135]. It is further indicated that by controlling the N concentration, the defect states population can be controlled. It has been

observed that for low nitrogen doses the nitrogen atoms is relatively positively charged and for high doses the defects become neutral i.e., the changeover occurs above defect concentration $\sim 1.8 \times 10^{13}$ defects/cm² [135]. A detailed XPS analysis of nitrogen implanted GNWs in high and low dose is discussed in chapter 5 and chapter 6 respectively.

The nitrogen incorporation influence the microstructure, morphology, electronic and mechanical properties of GNWs. The microstructure and morphology are macro-phenomenon and may be observed under electron microscope. The defect generation, doping and intercalation of nitrogen in between the graphitic layers are analysed in terms of chemical changes using XPS, Raman or FTIR. There are no literature reports of mechanical property evaluation of N-GNWs.

1.4.2.1. Morphological studies

Studies of nitrogen inclusion during synthesis of N-GNWs indicate that inclusion of slight amount of N₂ in the precursor gas promotes the growth of VGN, whereas, high volume fraction of nitrogen etch remove both the vertical walls as well as the base layer [123]. The above observation is attributed to increases in C₂ and CN radical density as described by Cheng and Teii [137]. However, further introduction of N₂ is observed to not favour GNWs growth, resulting in isolated nanographitic islands. Fig. 1.4 shows the influence of nitrogen on the morphology of GNWs [123]. S.Vizireanu et al., shows that, low temperature nitrogen plasma exposure to pre-synthesised GNWs shows a slight thinning effect. Also, the wetting contact angle of GNWs decreases from $121.988 \pm 3.7^\circ$ to 3.528 ± 0.7 after nitrogen plasma treatment [138]. The bombardment with nitrogen plasma constituents can sputter remove some materials from the tips of GNWs.

1.4.3. X-Ray photo electron spectroscopic studies

The XPS studies of GNWs are usually carried out of C 1s, N 1s and O 1s spectrum to identify the chemical state of nitrogen doped /implanted GNWs. The C 1s spectrum of GNWs peak at 284.5 eV for sp² bonded carbon. Depending on the local bonding and electronegativity of the bonded species a shift in energy is observed. The graphitic structures in GNWs exhibit vacancies and the region rearrange itself to have a pentagon and an unpaired spin giving rise to magnetic vacancy [139]. The unpaired spin is a high energy state and hence, the binding energy (283.5 eV) peak below 284.5 eV is assigned to vacancy defect in GNWs [140]. However, one has to check the 283.5 eV for C-Si peak before assigning it to defect peak [116]. Carbon in sp³ bonding state and bonded with other more electro negative elements show higher C 1s energy state (Fig. 1.5).

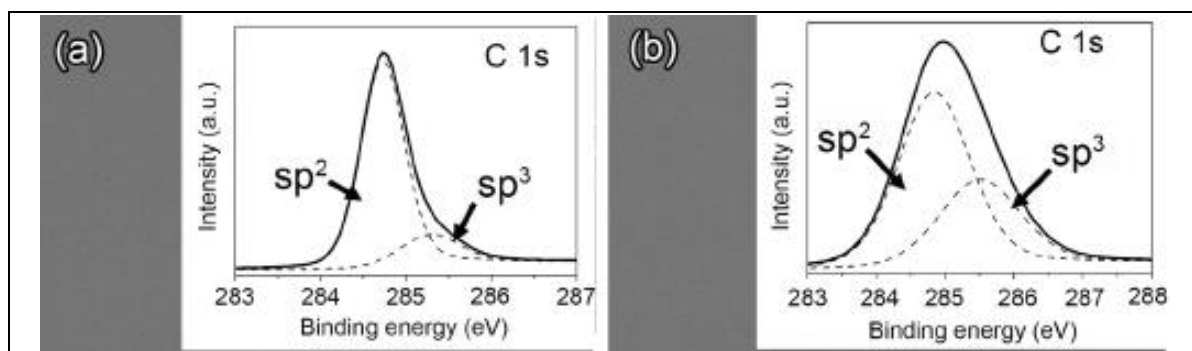


Fig. 1.5 Typical XPS C 1s spectrum of graphene nanowalls (a) As-prepared and (b) argon ion irradiated. Increase in FWHM and increase in sp^3 fraction due to Ar ion irradiation is evident from the image [141].

In the case of nitrogen, nitrogen can have pyridinic, pyrrolic, graphitic and quaternary /oxidised nitrogen configurations. Kondo et al. have analysed the nitrogen position and evolution of pyridinic and graphitic nitrogen for the N 1s binding energies [135]. The deconvolution of N1s spectrum of N-GNWs prepared by N plasma exposure shows the presence of three main peaks corresponding to pyrrolic (400.2 eV), pyridinic (399.0 eV) and graphitic (401.2 eV) nitrogen [125]. The nitrogen ion implanted rGO (Chemically prepared Graphene: Modified Hummers method) shows the presence of unique C=N bonding at 285.7 eV. Several spectral peaks: C–C and/or C=C at 284.7 eV, C=N at 285.7 eV and C=O 288.2 eV are also reported [130].

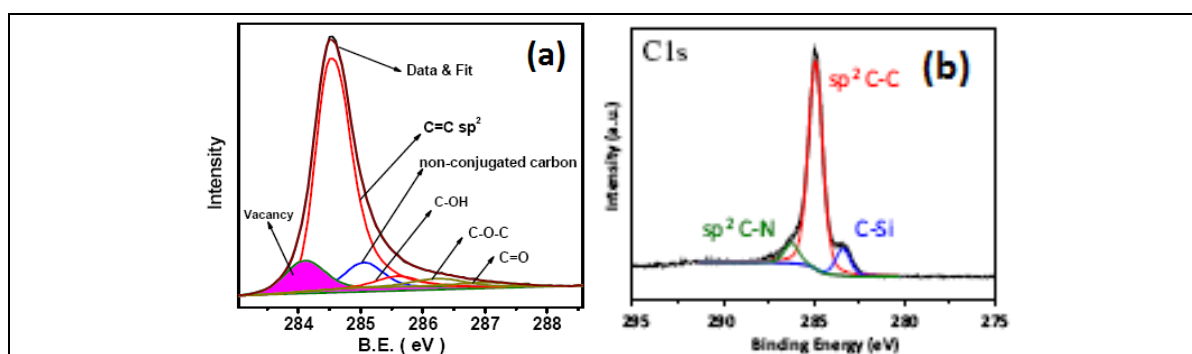


Fig. 1.6 (a) Typical C 1s XPS spectrum showing various peak assignments including vacancy induced broadening of sp^2C peak [140]. and (b) possible C-Si peak at 283.5 eV [116].

From the analysis of N 1s spectrum binding energy 398.5, 399.9 and 401.1 (eV) are assigned to pyridinic, pyrrolic and quaternary N, respectively [142,143]. Several nitrogen configuration are assigned to binding energy above 401 eV and one of them is quaternary nitrogen. Some of the nitrogen configuration from literature is given in Fig. 1.7. However, literature shows large overlap of binding energy values and designations. Similarly, O 1s binding energy also show large variation in values. There are very conflicting reports in

literature about the designation and the respective structure assigned to nitrogen in graphene [144–146]. Bertoti et al. has summarised the various 1s binding energy options for carbon, nitrogen and oxygen [146]. However these categorization and the designation of 1s energy state did not provide a comprehensive picture about the type of bonding and its chemical state of GNWs towards making process optimization. Hence, a comprehensive treatment useful for application of N-GNWs has been discussed in chapter 5.

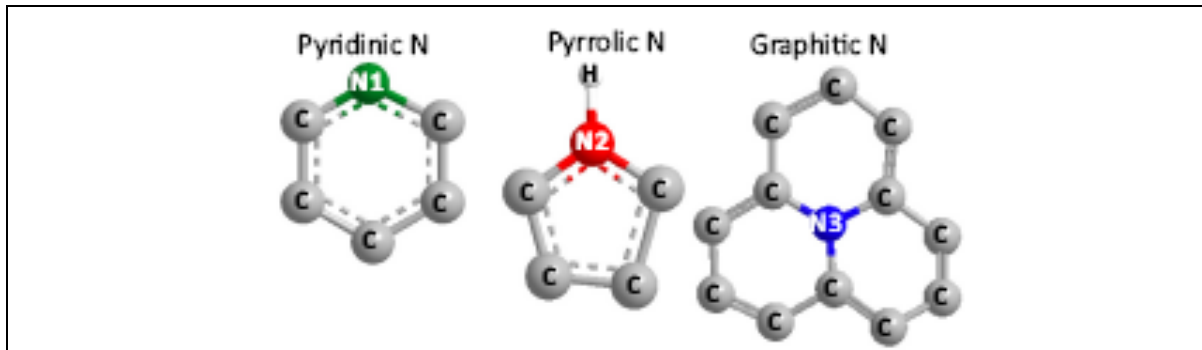


Fig. 1.7 Typical nitrogen configuration in hexagonal carbon ring of graphene, respective names are given above each [116].

1.4.4. Raman spectroscopic studies

GNWs have unique Raman spectra with features ranging from 800 to 3300 cm^{-1} . [147]. In general, the Raman spectra of carbon materials are dominated by sp^2 bonds, because visible excitation resonates with the π states [148]. The E_{2g} vibrational mode or the graphitic G band (1580–1590 cm^{-1}) is associated with bond-stretching of all pairs of sp^2 atoms in ring or chains. For sp^2 carbons, the G band is accompanied by a G' (2D) band (2500–2800 cm^{-1}). The A_{1g} breathing mode or D band (1250–1400 cm^{-1}) is a disorder-induced phonon mode. Additionally, for defective carbons, the D' band sometimes emerges as a shoulder near the G band via an intra-valley double resonance process [148]. A typical Raman spectrum of GNWs is given in Fig. 1.8.

Above 1650 cm^{-1} , the observed Raman features are all multiple-order combination modes and overtones, though some of the peaks observed below 1650 cm^{-1} are actually one phonon-bands activated by defects [149]. The intensity ratios $I_{\text{D}}/I_{\text{G}}$ and $I_{\text{G}}/I_{\text{G}'}$, the FWHM of the G band, and the G and G' band positions are used to characterise the disorder in carbon materials and doping type [126]. Some of the major effects are summarised in Table 1.2. If the $I_{\text{D}}/I_{\text{G}}$ ratio of GNWs are >1.0 and G band position $\geq 1579 \text{ cm}^{-1}$, it represent nanocrystalline or disordered graphite. Due to the defective nature of GNWs, $I_{\text{D}}/I_{\text{G}}$ ratio is higher than graphite [150] and pristine graphene [151]. Kurita et al. report that CNWs with wall lengths $\leq 1.0 \mu\text{m}$ had an $I_{\text{D}}/I_{\text{G}}$ of ~ 2.0 for a laser of $\lambda = 532 \text{ nm}$ [147]. Larger the

crystallite size, higher will be the change in I_D/I_G ratio [126]. Nitrogen doping induced blue shift in the G peak position is also reported in the literature [152].

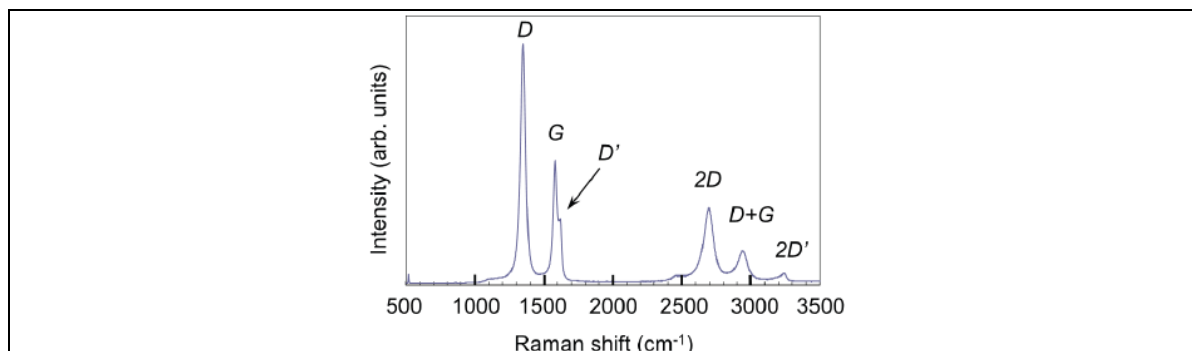


Fig. 1.8 Typical Raman spectrum of vertical graphene nanowalls. Respective peak designations are given. The 2D peak is also referred to as G' peak in literature [153].

Table 1.2 Raman spectroscopic features applicable to both monolayer graphene and graphene nanowalls [149]. The peak values given are for monolayer graphene. The term 'blue shift' and 'red shift' used by the author (Ado Jorio) is maintained in the table below.

G band (iTO-LO)		G' band (2iTO)		D Band (iTO)	
Effect	Cause	Effect	Cause	Effect	Cause
Blue shift	p-type doping	Blue shift	p-type doping	Shift	Dispersion 50 cm ⁻¹ /eV
Red shift	n-type doping	Red shift	n-type doping	Increase in FWHM	Increase in defect/disorder
Red shift	Increase in temperature	G' band intensity larger by 24 times than G band	Mono layer graphene	Low intensity	Lower defect/ Zigzag edges
Nominal value	FWHM=10-15 cm ⁻¹	Two peak G' feature	HOPG like structure	I_D/I_G	Measure of disorder
Split in G band	Bending	Single G' peak	Turbo static graphite	Activation only at a defect	Coherence length of 2 nm

Issac et al., indicate that for 532 nm laser, an increase in number of layers causes widening of FWHM of G' band (2690 cm⁻¹) and red shift of G peak as compared to mono layer graphene (1580 cm⁻¹). With increase in disorder D (1350 cm⁻¹), D'(1620 cm⁻¹) and D+G (2940 cm⁻¹) intensity increases in graphene. The position of defect peak, its overtones and combinations changes with the laser energy [154]. In the analysis of defects the I_D/I_G values shows dependence to two regimes, viz. the low defect density and high defect

density. The I_D/I_G ratio increases with increases in defect density in the low density case and decreases with increase in defect density in the high defect density case [155]. In this work Raman spectroscopy have been used extensively. In addition to the conventional peaks (D, G, D' and G'), a few additional peaks (T and A) and its significance and deconvolution aspects have been discussed in chapter 4, 5 and 6.

1.4.5. Fourier Transform Infra-Red spectroscopic studies

Fourier transform infrared (FTIR) spectroscopy is an ideal analytical tool to identify the functional groups present in graphene and related materials. FTIR spectroscopy is performed to analyse the changes taken place in various synthesis techniques and plasma nitrogen ion implantation of GNWs. The range of energy corresponding to various vibrations of carbon, oxygen and nitrogen is given in Fig. 1.9. Since peaks can form in a range of frequencies, the FTIR spectrum need to be analysed with utmost care by considering the sample synthesis history also. Typical absorption spectrum relevant to GNWs is shown in Fig. 1.10 and some of the peak values are summarised in Table 1.3.

In GNWs, carbon forms bonds with carbon, hydrogen, oxygen and upon nitrogen implantation, these bonds are disturbed. It is expected that the analysis of bonding characteristics reveal more details about the morphological changes. This aspect has been dealt in detail in chapter 4. The implantation induced effected are discussed in chapter 6.

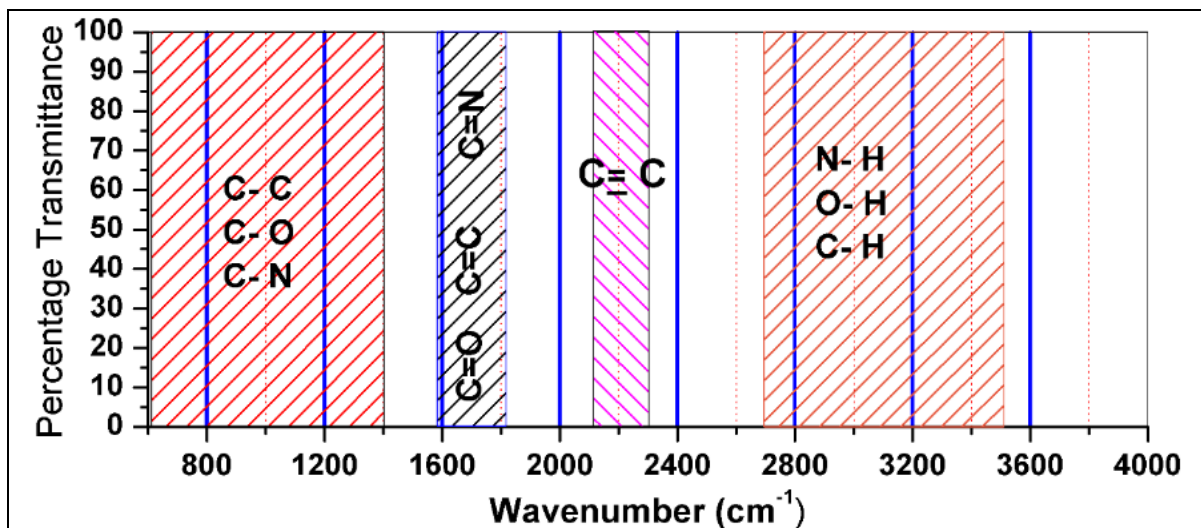


Fig. 1.9 Infrared absorption range of compounds containing Carbon, Oxygen and Nitrogen. [156].

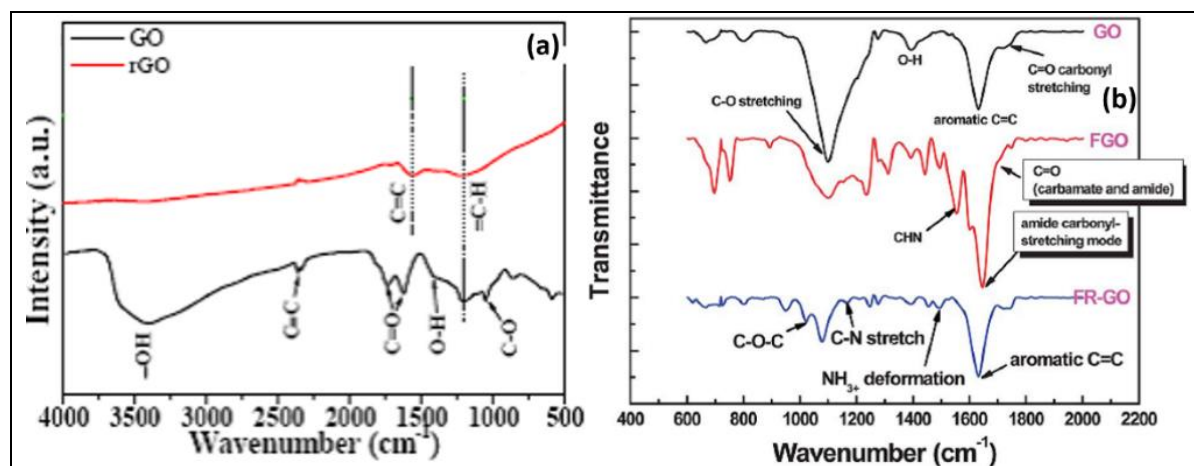


Fig. 1.10 Typical IR transmission spectrum of graphene showing peak positions of relevance to graphene nanowalls. (a) Graphene Oxide [157] and (b) conductive polymer functionalised graphene oxide (FGO) and functionalised reduced graphene oxide (FR-GO) [158].

Table 1.3 Some common functional groups in FTIR spectrum of Graphene materials.

No.	Functional group	Energy in cm ⁻¹ and [Ref]	Sample details
1	O-H in Carboxyl	3400 [159]	Ref. [160] is N-doped graphene.
2	O-H & N-H (stretch)	3425 [160],	Ref. [161] High quality graphene sheet.
3	Deformed O-H	1384 [160]	Ref. [159] Graphene by GO reduction.
4	C-O / C-N (Stretch)	1115 [160], 1101 [159] 1032 [162]	Ref. [163] Nitrogen doped reduced graphene oxide.
5	C=C (stretch)	1107 [160]	Ref. [164] Graphene TiO ₂ composite.
6	Un oxidised graphitic skeleton	1590-1620 [159]	Ref. [165] Nitrogen doped CNT.
7	Aromatic C-H deformation	685, 720 & 801 [163]	Ref. [166] Exfoliated Graphene oxide.
8	C-O (stretch)	1028 & 1308 [163] 1048 in N-rGo [163], 1052 [164] 2362 [165], 1100 alcoxy [159] 1242 epoxy [166], 1366 epoxy [167],	Ref. [167] Graphene metal nano-composite Ref. [168] Carbon nitride film Ref. [169] High temp. carbon
9	O=C-O (stretch)	1577 [163]	Ref. [170] Nitrogen doped CNT
10	C=O (Carbonyl stretch)	1706 [163], 1724 in N-rGo [163], 1726 in COOH [164] 1720-1740 in carbonyl/carboxyl [159]	Ref. [171] Nitrogen doped porous carbon
11	O-H stretch in C-OH	3119 [163], 1393 (tertiary C-OH stretch) [164]	Ref [162] In GO

12	C-H ₂ stretch	2879 [163] 2851,2925 [165]	
13	O-H in rGO	3400 [163]	
14	C-H in methylene	2806 [163]	
15	sp ³ C-N	1430-1480 [163]	
16	O-H stretch in GO due to adsorbed water	3400 [164] 3413 [161]	
17	O-H bending	1626 [161]	
18	Carbonyl (>C=O) stretch	1735 [161], 1730 [168]	
19	Si-O stretch	1026 [165]	
20	C-N stretch	1250 [165], 1270&1420 [168]	
21	N-CH ₃ stretch	1372 [165]	
22	CO ₂ stretch	2350 [168]	
23	C≡N	2160 [168], 2225 [170]	
24	sp ³ C	2850-2960 [169]	
25	N-H	3200 [171]	

1.4.6. Atomic force acoustic microscopic studies

GNWs in pristine and doped form need to be quantitatively analysed for its mechanical properties. With respect to GNWs, the main issue is the flexibility of individual walls of GNWs. The vertical walls deform upon the application of a load without being plastically deformed. Since GNWs has corrugated morphology, the surface mechanical properties are expected to be highly non-uniform and measurement with conventional indentation methods will be highly erratic. In order to avoid this issue epoxy composite can be used. However, nano mechanical properties expected to be different from what is measured in a composite. Hence, there is need for newer methods for evaluation.

The atomic force acoustic/ultrasonic microscopy has been demonstrated as a versatile tool for elastic property evaluation at microscopic levels. In this direction, excellent reviews on atomic force acoustic microscopy (AFAM) of thin film has been reported in literature [172]. Additionally, graphene based materials have already been evaluated with AFAM that Passeri et al., reports the characterisation of epoxy/SWNT composite using AFAM technique [173]. Different modes of AFAM can be used to detect and image defects in a few layer graphite and estimate elastic properties. The technique is so sensitive that a vacancy positioned in the second layer of graphite is observed to induce 2.2% elastic modulus difference [174]. In AFAM, the mechanical property evaluation is based on the resonant frequency of vibration of GNWs and the tip of AFM, together upon acoustic excitation from the bottom. The resonant frequency of vibration is a function of the elastic property. Hence, it is possible to compare the elastic properties of doped/implanted GNWs

against pristine or a known material to compare and evaluate the properties. More details of methodology are discussed in the experimental section.

1.5. Electrochemical characterisation of GNWs and N-GNWs

Electrochemical characterisation of a material is carried out to understand the performance of materials to an electric stimuli, possibly in presence of a given electrolyte. This is very important for the property evaluation of GNWs and N-GNWs for its application and further development. Graphene nanowalls consists of a few layers of graphene and large number density of edges and defects. In addition to the intrinsic property variation of graphene due to stacking of a few layers, the interfaces, edges and defects alter the properties. This situation become more complicated when the graphene is supported on a substrate or doped. Additionally, the crystallite size, pore and pore density also influence the property. Hence, electrochemical studies become an indispensable tool to explore the application and development of more advanced materials. However, full-fledged electrochemical characterisation study of GNWs and N-GNWs are beyond the scope of this thesis. Hence, only two fundamental measurements (Cyclic voltammetry and charge - discharge) useful for possible supercapacitor application is discussed. In CVs typical rectangular shape implies pure electrical double -layer capacitive behaviour [175]. In between the extremes some undulations are indicative of pseudocapacitance in CV studies. The charge discharge studies provide charging and discharging time for the half cell (electrode). Ideally, a supercapacitor requires quick charging time and long discharge time.

1.6. Literature review on supercapacitor application of GNWs and N-GNWs

Among several applications, nitrogen incorporated GNWs exhibit several possible characteristics required for electrochemical capacitor such as high surface area, corrugated porous structure with varying size distribution, conductivity, wettability and presence of electro active species. Hence, an introductory review is presented.

Supercapacitors (SCs) store huge electrical energy in comparison to conventional capacitors. They are called by different names as electrochemical (EC) capacitors, electric double layer capacitor (EDLC) and ultracapacitors (UC). The basic advantage of SCs are: their operation is largely temperature independent, very high cycle life and high power density. However, their energy density is low. SCs work under the principle that all the ions are distributed randomly in discharged state and in charging, the ions of the electrolyte

preferentially align to the appositively charged electrode. The semi-permeable membrane (SPM) act as necessary ionic charge transport conduit during charging and discharging.

The capacitance value of a capacitor is proportional to the area of the contact plates and the dielectric constant of the medium between the plates, and it is inversely proportional to the separation between the plates. High specific-area materials such as porous carbon, porous oxides of some metals and graphene based materials (e.g., graphene nanowalls) increases the surface area of electrodes and thus increase the available charge storage area. Tight packing of the highly ionised electrolytic solutions, such as KOH, H₂SO₄, etc., separated by SPM in between the electrodes address minimum separation and high dielectric constant. This is the basis of EDLC or space-charge capacitance.

While charging a negative plate, the electrons occupy higher-energy states in the band structure and the positive plates loses electrons, which leave it behind the electrons with lower –energy states in the band structure. Therefore, the voltage changes at a different rate during charge and discharge which is related to filling or emptying of the energy bands. The band-filling / band-emptying is a function of the density of states of the regions and hence, it is related to quantum wave function of electrons. For bulk materials this effect is insignificant whereas in the case of 2D materials with large density of edges, if the size of the region of consideration is a few nanometers; then, the kinetic energy of the stored electrons becomes dominant over the electrostatic stored energy purely due to quantum mechanical effects. Additionally, when the GNWs are doped with a heteroatom like nitrogen the electronic density of states also changes. So, the quantum effects due to size as well as hetero atoms influence the capacitance. Hence the size, chemical nature and density of small regions (edges) contribute to quantum capacitance of 2D materials [176,177].

In the development of supercapacitors, using double layer capacitance alone was not giving high energy density. Because, the applied electric field intensity is low and as a result the thickness of Helmholtz layer also become low. However, if the electrode undergo redox reaction by the application of a potential, more amount of energy can be stored. In fact, the energy storage become chemical and the resulting capacitance is called pseudocapacitance. Hence, total capacitance of the system is sum of the double layer capacitance, quantum capacitance and pseudocapacitance. Both EDLC and pseudo capacitance are technically more familiar owing to bulk systems as compared to quantum capacitance. However, the focus of current study is the effect of nitrogen implantation and not the mechanism. The value of pseudocapacitance is hundreds of times higher than double layer capacitance. Towards improving the pseudocapacitance, transition metal oxide such as RuO₂, MnO₂,. are

used along with porous carbon composite electrode [178,179]. The mechanism operating in pseudocapacitance is explained as: the metal oxide ($\text{Ru}^{\text{IV}} \text{O}_2$) upon charging reduced to lower ($\text{Ru}^{\text{IV}}_{1-x} \text{Ru}^{\text{III}}_x \text{O}_2\text{H}_x$) oxidation state by gaining H^+ ions and thus store +ve charge in the electrode and in the counter electrode, one -ve charge is deposited. This is occurring in addition to the Helmholtz double layer capacitance. The total capacitance is the sum of both and as a result, multi fold increase in capacitance is observed in such capacitors. Surface area enhancement of metal oxide particle takes place at its fine dispersion on the electrode (say carbon). Since the charge and discharge process involve faradic processes, these devices suffer from lack of stability and low power density. This may be due to physical (architectural stability and interface contact between particle and the electrode) or chemical (ease of transport of H^+ ions) effects. Eventually, the efficiency and cycle life of SCs reduces. Hence, there is a requirement of improving the scenario by finding alternatives to transition metal oxide in carbon nanostructures.

Towards avoiding costly metal oxide addition and interface between heteroatom and base electrode, modification of the electrode chemistry is a useful alternative. The preliminary step for this is the synthesis and usage of high surface area GNWs of suitable morphology and electronic properties followed by nitrogen doping. In this direction, the reports in literature are encouraging. The nanographitic (NG) films were coated on carbon fibres have shown 2 order high specific capacitance as compared to conventional smooth carbon electrode [180]. Chi et al., indicated that nitrogen incorporated GNWs have shown multifold increase in capacitance as compared to pristine samples [127]. Cho et.al., indicated that nitrogen doping significantly influence the electronic properties of graphene nanowalls [181]. Huang et al. have shown that the high electrochemical activity of graphene sheet embedded carbon film is originated from the nanosized graphene sheets, which offered faster electron transfer path and more active sites [182]. Recently, various nitrogen incorporation processes during the synthesis of graphene also demonstrated to have a positive effect on its specific capacitance [116]. The nitrogen modification of graphene is theoretically predicated to induce band gap in graphene [183,184]. Nitrogen incorporation (7.6 at%) of GNWs has increased the positive electrode potential limit from 0.1 V to 1.3-1.5 V and the negative electrode of EDLCs -2.0 to -2.5 V in electric double layer against Ag/AgNO₃ standard electrode. It is very encouraging to note that nitrogen plasma treatment have improved the capacitance tremendously [185,186]. The enhanced electro catalytic performance is mainly attributed to the structure, defects and nitrogen-oxygen-containing groups. Hence, N-graphene find several applications in electrochemical energy devices (fuel

cells, batteries, supercapacitors) and sensors [120]. The above reports also indicate high cycle life and stable charge –discharge performances. It appears that the N doped GNWs based electrodes are ideal substitutes to hybrid electrodes. It is interesting to look into the mechanism operating behind the high performance of such electrodes towards high charge storage.

Aradilla et al., indicate that doping influence morphological (surface defects and reactions, porosity) and structural (conductivity) properties, which caused the enhancement of the capacitive properties compared to undoped GNWs [125]. Yen et al attribute the ultra-high capacitance to high surface area of GNWs and unique specificity to the pyridinic N-doping configuration [116]. Hyung et.al., indicate the basal-plane pyridinic-N (N-6) has larger binding energy to accommodate more ions on the surface and the high power density is due to highly conducting graphitic nitrogen [187]. In the DC plasma nitrogen (3%) doped carbon nanowalls, increased electrochemical activity and increase in specific capacitance upto 6 times of the pristine one was observed. The XPS analysis of the tested samples indicate the disappearance of pyridinic sites and reduction in number density of pyrrolic sites and doubling the graphitic sites [188]. Additionally, in several other reports, the importance of pyridinic N sites and some O sites are accounted for the alteration of the GNWs specific capacitance and catalytic activity [185,186].

Theoretical studies shows that the nitrogen configurations (substitution: graphitic N) and trimerised pyridine type nitrogen (N₃V) significantly enhances the quantum capacitance (QC) as compared to the pristine sample [189]. It has been discussed in literature that the pyridinic-N and pyrrolic-N improve the pseudocapitance by the redox reactions whereas the quaternary-N contribute to the conductivity in nanographene [21]. Hence, GNWs with lower defect, microtextures, high secondary growth are fascinating materials for SCs.

It is summarised that both defects sites and its number density, and nitrogen doping fraction and chemical state influence the catalytic activity and supercapitance of GNWs. However, a specific treatment which generate defects and incorporate nitrogen are scarcely discussed in literature. In this context, nitrogen plasma implanted GNWs for different duration are studied and analysed for its supercapitance in chapter 5 and chapter 6. The detailed study in this area is further promising that Yu-Wen Chi, et al., have shown a new strategy to increase the potential window of supercapacitors by using GNWs (positive electrode) and N-GNWs (negative electrode) as asymmetric supercapacitor to have a cell voltage of 4V with high specific energy of 52 Wh kg⁻¹, and specific power of 8 kW kg⁻¹ and 100% retention after 10,000 charge-discharge cycles [127].

1.7. Objective and Scope of the study

The main objective of present investigation is to deposit GNWs using PECVD technique and modify the surface and sub-surface by nitrogen plasma ion implantation to study the evolution of physical, chemical and electro-chemical properties.

The work involves

- Establishing the PIII&D facility and its operating procedures for RF plasma generation and plasma ion implantation. Study the effects of plasma ion implantation on standard materials such as silicon and titanium towards benchmarking the plasma generation and implantation process.
- PECVD synthesis of GNWs at different H₂:CH₄ ratio and Ar:CH₄ ratio and its characterisation.
- Nitrogen plasma ion implantation of GNWs for different durations and its characterisation.
- Electro-chemical characterisation of pristine and ion implanted GNWs deposited on carbon paper towards supercapacitor application.

1.8. Organisation of the thesis

An introduction to graphene nanowalls, nitrogen modification, characterisation and applications has been presented. The remaining part of the thesis is organised in the following way. The experimental system and its operational details and characterisation techniques are explained in Chapter 2. Facility benchmarking experiments and the results are discussed in Chapter 3. Synthesis of graphene nanowalls and its characterisation are discussed in Chapter 4. Chapter 5 and Chapter 6 discuss the nitrogen plasma ion implantation of GNWs and its characterisation for high and low doses respectively. The summary, conclusions and future research prospects are given in Chapter 7.

Chapter 2

Experimental Procedures

This chapter provides a description of research methodology, materials, equipment and theories used in the present study. Research methodology describes the overall research approach, both qualitative and quantitative methods used in this study. Finer details and respective equipment and theories are separately described in the equipment's and materials section. The main experimental facility used for the synthesis and modification of GNWs, the Plasma Immersion Ion Implantation and Deposition (PIII&D) facility is introduced along with basic theories of plasma enhanced chemical vapour deposition (PECVD) and plasma immersion ion implantation (PIII). The experimental part of the thesis is divided into three parts viz. system benchmarking experiments, PECVD synthesis and PIII modification of GNWs. The techniques used for the characterisation of pristine and implanted graphene nanowalls are also discussed. A brief introduction to SEM and TEM has been given. Details of the Raman spectroscopy, Fourier transform infrared (FTIR) spectroscopy, X-ray photoelectron spectroscopy (XPS), electron energy loss spectroscopy (EELS), secondary ion mass spectroscopy (SIMS), atomic force microscopy (AFM), water contact angle measurement and the electrochemical analysis are also provided. A schematic of the research methodology is given Fig. 2.1 in experimental flow chart is given in Fig. 2.2.

2.1. Research Methodology

Plasma enhanced or plasma assisted CVD techniques have been used for the synthesis of GNWs. Several interlinked parameters are involved in plasma based synthesis techniques. For example, gas composition and pressure influence the entire plasma parameters and hence the process and the product. In this direction, the process parameter induced morphological changes are seldom analysed at finer (electronic state) level to explore whether the change in morphology has additional (apart from change in surface area) influence on the electronic nature of the material. Such material property evaluation provides a solid background for the evaluation of properties of modified materials. Hence, the initial studies focus on one of the fundamental process parameters, the plasma producing gas composition and its effect on the deposition rate of GNWs along with characterisation using SEM, Raman spectroscopy, TEM, electron diffraction and EELS techniques.

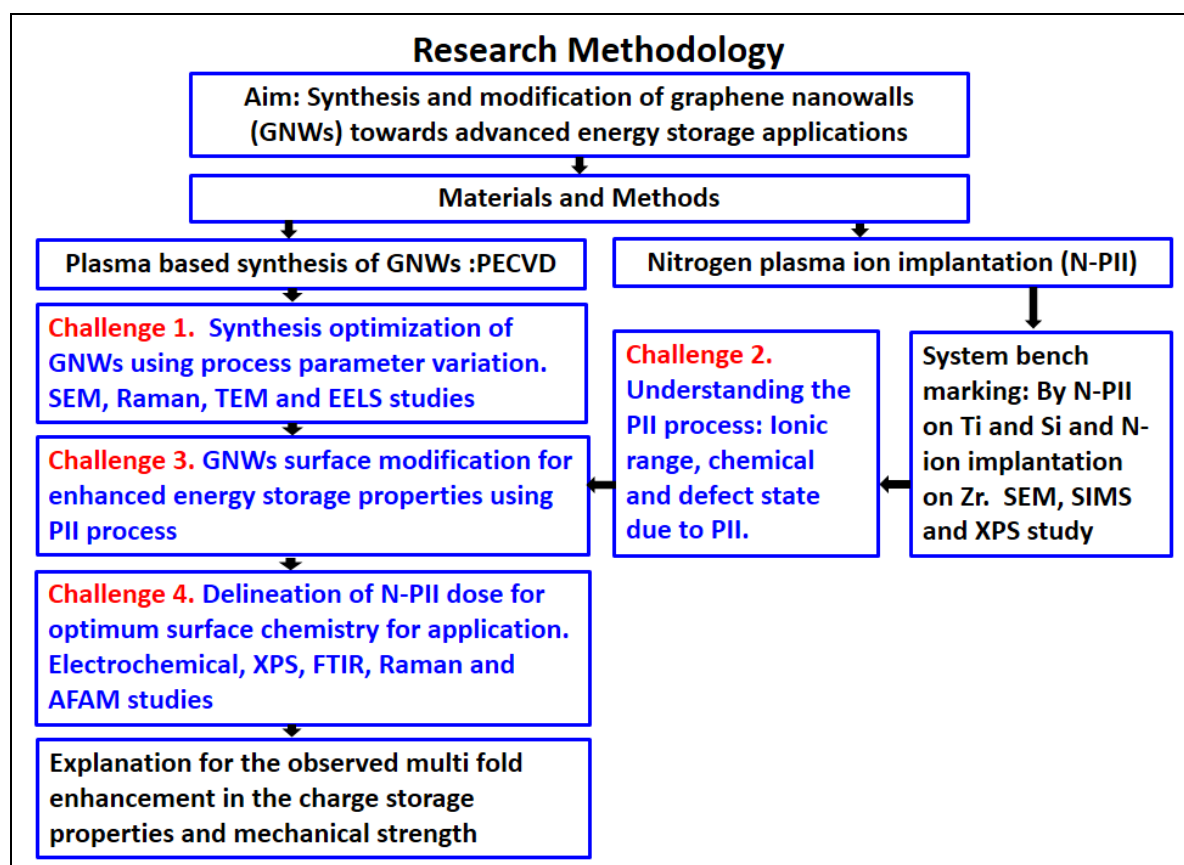


Fig. 2.1 Research methodology for the experimental study.

In the process of nitrogen modification of graphene nanowalls for advanced application, the possibility of plasma ion implantation has been seldom described in literature. Hence, the plasma ion implantation aspect on standard materials needs to be experimented to acquire confidence on the nitrogen plasma ion implantation of GNWs. Though instrumental plasma characterisation techniques and plasma theory will provide basic information of plasma parameters, the actual implantation process is complicated and experimental evaluation of properties of the implanted sample is required to reveal the actual state of sample. Hence, the benchmarking experiments have been performed to evaluate and generate confidence on the nitrogen implantation process. In this respect, nitrogen plasma ion implantations have been carried out on Ti and Si under different plasma power conditions. Because, plasma power is expected to play a role in the ionization of N_2 and generation of N^+ and N_2^+ ions, which is being used for ion implantation. However, an identical bias energy per ion is maintained in the experiments for a realistic comparison of the effect at similar depth in the specimen. There is no way to understand the individual effect of N^+ and N_2^+ ions in the plasma in PIII process. For this purpose, there is a need to implant individual N^+ and N_2^+ ions. Hence, separate N^+ and N_2^+ ion implantation studies

have been carried out on Zr thin films using accelerator. All samples have been examined using SIMS in common, for evaluating the range of ions. Other techniques such as Raman, XPS, AFAM, etc., have been used in respective experiments. SIMS being a high resolution elemental analysis technique, provide a clear picture of the plasma ion implantation process and also the behaviour of atomic and molecular ions in materials. Titanium and Zirconium samples have been analysed using XPS along the range after selectively sputter removing the material. However, the XPS data required to explain the chemical effect of nitrogen PIII on Ti is only discussed in this thesis.

For synthesis of GNWs, the approximate experimental conditions such as precursor gases and temperature was initially obtained from literature. Being a custom made system, several experiments were carried out to set the process parameters for the PECVD system (precursor gases and its ratio, plasma power, gas flow rate, substrate temperature, chamber pressure, substrate distance from the antenna, etc.). Since gas ratio is the most important parameter which influence the plasma and the GNWs characteristics, the gas ratio is changed. Being first of its kind study, the sputtering effect and extent of nitrogen incorporation into GNWs were not available in literature. Hence, the first set of PII experiments are carried at 10, 20 and 30 minutes at 2 kV bias and the second was at 2, 4 and 8 minutes at 1 kV bias. With this choice of process parameters, the basic experimental procedure for high dose and low dose nitrogen ion implantation of GNWs using PIII technique is understood.

The literature in Raman spectroscopic studies is dominated with elaborate analysis of monolayer graphene and its properties. However, the electronic density of states varies with addition of layers and the Dirac cones do not exhibit point contact at the high symmetry K and K' points in the reciprocal lattice. Hence, the G –peak is always deconvoluted with voigt function instead of BWF function and other peaks are fitted with Lorentzian function. After deconvoluting the Raman spectrum, the peaks ratio such as I_D/I_G , etc., is obtained from area under the curve and this values are given in tables. Fitting a curve is always tricky and involve optimization of several parameters and use of logical reasoning for material like GNWs and process like PII. Hence towards providing a basic comparison of Raman spectrum in between the pristine and processed samples, G-peak normalised intensity is used to provide a graphical comparison of whole spectrum. In this method, the intensity of G peaks of all samples is made equivalent to 1 and the spectrum is plotted. The selection criteria for area under the curve or intensity for I_D/I_G calculation is further

discussed in chapter 4. This new method for graphical representation (like *analog display*) provide additional comfort and feel while interpreting the Raman data.

Though nitrogenated graphene is said to have several applications, a comprehensive treatment for nitrogen chemical state in GNWs is not available in literature. In the nitrogen implanted graphene, the nitrogen state is generally described as pyrrolic, pyridinic, graphitic, oxidised, quaternary and molecular nitrogen. This description provide little engineering comfort towards process optimization and evaluation of the modified GNWs towards an application. Hence, a new methodology for categorization have been introduced to describe nitrogen state based on the status of lone pair of electron as localised or delocalised and the bonding state of (oxidised, quaternary and molecular) nitrogen. Being the GNWs a layered compound and oxygen is mostly surface bounded, higher binding energy of nitrogen is assigned to interstitial nitrogen in quaternary form. This methodology of categorizing nitrogen in GNWs, can be directly linked to the electronic nature of N-GNWs towards its application as electrode materials.

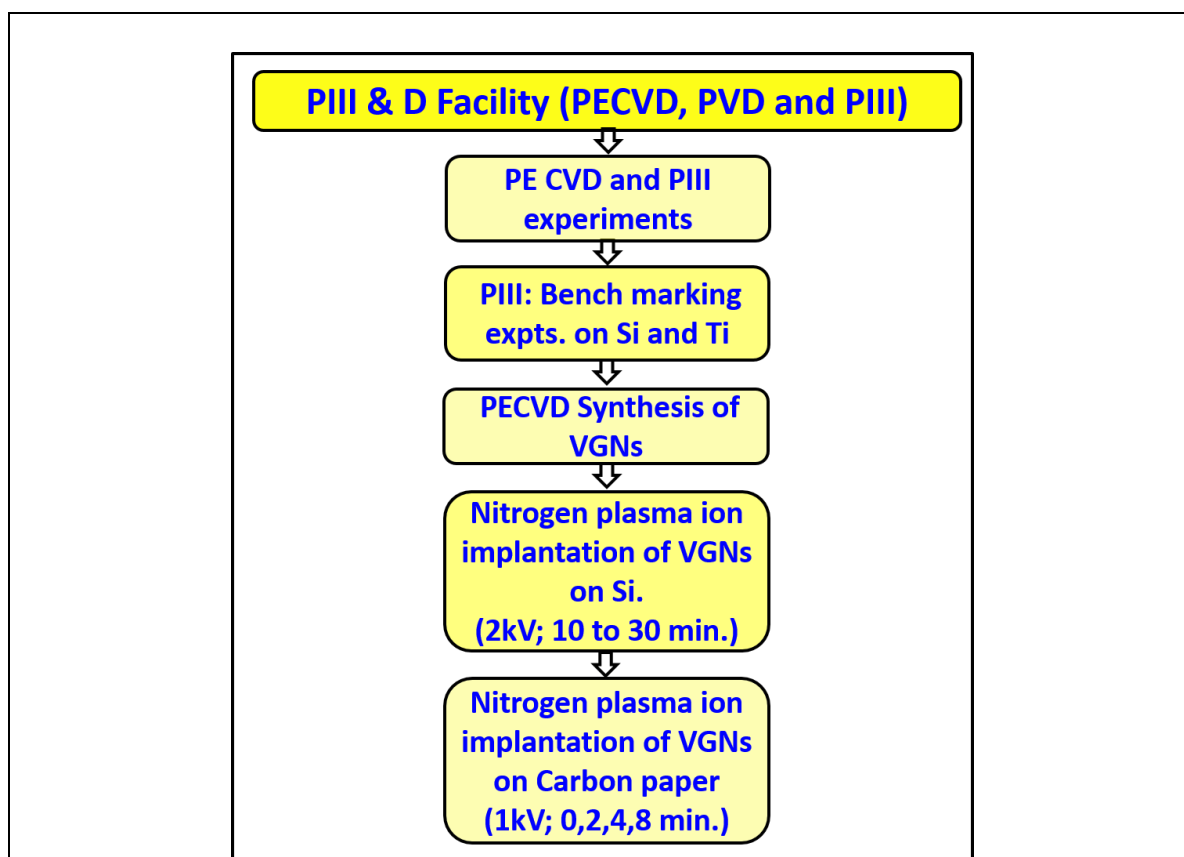


Fig. 2.2 Flow chart of the experiments.

This work is about synthesis and modification of GNWs using PIII&D facility. However, without providing the analysis of modified GNWs for a possible application, the

study will be largely incomplete. The possible applications of GNWs are based on electrochemistry and hence two powerful techniques; cyclic voltammetry and charge discharge studies of GNWs before and after nitrogen modification have been presented. Cyclic voltammetry is a basic electrochemical characterisation technique that fundamental information on electrochemical response of the electrodes for several applications such as supercapacitors, sensors, etc. can be deduced. The possible applications of GNWs and options on PIII&D process for surface modification of GNWs are enormous. Hence, a brief flavour of such is presented in future prospects.

Synthesis and modification of graphene nanowalls using plasma immersion ion implantation and deposition system aims at synthesis of GNWs and its nitrogen incorporation by plasma ion implantation for a possible application. Towards this, a set of experiments are performed as given in the experimental flow chart (Fig. 2.2).

2.2. Equipment and materials

In this section, equipment and materials used for the study is described. Plasma Immersion Ion Implantation and Deposition (PIII&D) facility (Fig. 2.3) is the equipment used for synthesis of GNWs and its modification by nitrogen plasma ion implantation. High pure Ti (99.98%) and electronic grade silicon wafer are used for preliminary implantation studies. High pure CH₄ (99.95%), Ar (99.999%), H₂ (99.9%) and N₂ (99.95%) gases are used for the synthesis of graphene nanowalls and nitrogen implantation, respectively. GNWs deposited on silicon wafer and carbon paper are used for detailed studies.



Fig. 2.3 Photograph of the PIII&D system.

2.2.1. Plasma Immersion Ion Implantation and Deposition (PIII&D) Facility

PIII&D facility consists of Plasma Enhanced/Assisted Chemical Vapour Deposition (PE/PA CVD) system, magnetron based Physical Vapour Deposition (PVD) system and Plasma Immersion Ion Implantation (PIII) system (Fig. 2.3). Hence, the PIII&D system could be used for both synthesis and modification of nanomaterials, nanostructures and thin films. In the following section each of these features will be separately discussed. PECVD aspect is used for the synthesis of GNWs and PIII feature is used for the nitrogen modification of GNWs. The PVD technique is not used in the synthesis of GNWs. However, the synthesis of zirconium thin films for studying the effect of N^+ and N_2^+ ions implantation is done using Magnetron sputtering. Hence, a small description of the magnetron sputtering is also provided.

2.2.1.1. Plasma Enhanced Chemical Vapour Deposition (PECVD)

Chemical vapour deposition (CVD) usually represent thermal CVD and involve very high temperatures ($\sim 1000^\circ\text{C}$) depends on the reaction mechanism. However, in plasma assisted CVD (PACVD)/plasma enhanced CVD (PECVD) technique, plasma is used for the enhancement of reactivity of the constituents towards lowering the thermal load. Both terminology PACVD and PECVD are used in literature without attributing much difference. In line with reports in literature, the term 'PECVD' is used for referring the synthesis process in this thesis [48,59,190]. The advantage of PECVD over thermal CVD may be explained; for example, Si_3N_4 can be deposited at 850°C by using SiCl_4 and NH_3 precursors. If N_2 is used instead of NH_3 the reaction kinetic becomes very low. This is because, the dissociation energy of N_2 (225 kcal./mol) is much higher than NH_3 (104 kcal./mol) [191]. Similarly, if easily dissociating gases such as metal organics (tetrakis dimethylamido) silicon, $\text{Si}(\text{NMe}_2)_4$ are used, the temperature can be reduced to $200\text{-}400^\circ\text{C}$. There are several other parameters, such as precursor gases (NH_3 or N_2 for nitridation), mixing (gas ratio), process gas pressure, presence of catalyst, and region (fluidised bed) which influence the CVD process. However, temperature is the crucial parameter which set the reaction on or off. However, the reaction temperature can be reduced in a PECVD process. For example, in the above reaction of Si_3N_4 deposition using SiCl_4 and NH_3 precursors; if 13.56 MHz plasma is employed, the reaction temperature can be reduced from 850°C to $400\text{-}600^\circ\text{C}$ range [192]. In PECVD process, unlike using heat energy to form energetic/active species, electromagnetic excitation at a relatively low pressure is used. Additionally, the PECVD process are more attractive for the larger,

uniform deposition as compared to CVD where uniform substrate temperature is very crucial.

Over the years, the plasma processing technology has branched into a number of variants; from simple dc discharge plasma to complex RF and electron cyclotron resonance microwave plasmas intended towards metal surface modification, etching, wafer processing and thin film and nanostructure deposition [193]. The major early development of PECVD was due to requirement of the low temperature deposition of silicon nitride films for the passivation and encapsulation of completely fabricated microelectronic devices. Because, at the final stage of fabrication, IC chip cannot be heated much above 300°C to keep the contacts, interfaces and doping at the required level of integrity. As discussed before, this temperature is much lower than traditional thermal CVD processes for silicon nitride deposition. Most of the films deposited in electronic industry are dielectrics and so, RF plasmas are preferred over DC discharges. The plasma discharges ranges anything from 100 KHz to 2.45 GHz; even higher are employed/used that the current restriction of usage is only on legal acknowledgement for the frequencies for industrial applications. Technically, to sustain a low temperature plasma, the process pressure should be low enough in the range of $\sim 1 \times 10^{-3}$ mbar to ~ 6 mbar. Reducing the pressure still lower will deter the available number of plasma species to sustain the ionization process. Increasing the pressure obviously require more energy supply to compensate the recombination or loss of plasma constituents leading to increase the temperature; a case seen in the plasma torch. In RF plasma, electrons with energies ranging from 1 to 10 eV are produced and are sufficient to decompose the gas molecules into ions, radicals, and atoms and molecules in excited states to generate plasma densities of 1×10^9 to $1 \times 10^{13}/\text{cm}^3$. The net effect is much localised high temperature reactions can be made to occur with a large quenching background even on temperature sensitive substrates. This indicate that thermodynamic limitation of a chemical reaction can be bypassed by using plasmas. For example, the TiC formation temperature can be brought down from 1000°C to $\sim 500^\circ\text{C}$ by using plasma [194].

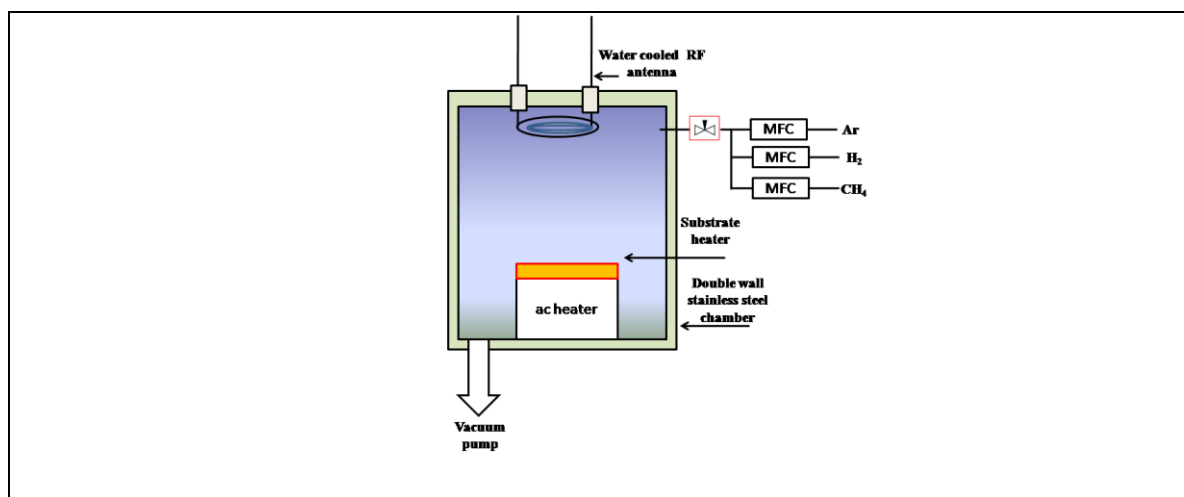


Fig. 2.4 PECVD system used for the synthesis of graphene nanowalls.

The schematic of the PE-CVD system used in sample preparation is shown in Fig. 2.4. The stainless steel (AISI SS-304) vacuum chamber (0.035 m³) can be pumped down to an ultimate vacuum of $\sim 2 \times 10^{-5}$ mbar using diffusion pumping system. A radio frequency (13.56 MHz) generator (Huttinger, PFG 600 RF) was connected to a stainless steel spiral antenna (2.5turns, 300 mm dia.) coated with aluminum oxide through an impedance matching unit for the generation of plasma. A resistive heater (RT to 850°C max.) with substrate holder capable of adjusting the height was used for heating the substrate prior to deposition. For the PECVD of GNWs ultra high pure (99.95%) CH₄, (99.999%) Ar and 99.95% H₂ gas was used. GNWs were deposited on preoxidised Si (oxide thickness > 300 nm).

2.2.1.2. Physical Vapour Deposition

Physical vapour deposition process represent coating deposition using substrate evaporation, sputtering and ion plating. Additionally, thermal spray and sol-gel techniques are also considered as PVD process. The current trend is to combine both PECVD and PVD for deposition purpose. In the present study, the PIII&D system is equipped with PVD feature using magnetron sputtering. There are reports in literature that GNWs can be synthesised using magnetron sputtering [42]. However, we have not attempted magnetron sputtering for GNWs synthesis in this study. The magnetron sputtering feature is used for synthesis of Zr thin films for implantation studies.

The objective of sputtering process is to vaporize the solid material and transport to the surface to be coated in a controlled manner. In sputtering process energetic ions are used as the projectile to sputter remove the target material. Towards the synthesis of energetic ions (plasma) vacuum is a pre requirement. Plasma is produced by RF and/or dc

excitation and the target is biased. The sputtered particles are usually considered as neutral and acquire momentum during sputtering process. The Kinetic energy of the sputtered particle largely falls within the energy window of displacing surface atoms. The basic advantage of the process is that any material can be vapourised and the film can be deposited over large area with little surface damage.

In magnetron sputtering process, a magnetic arrangement is placed at the back of the cathode target with pole pieces at the centre and at the perimeter. The magnetic field B confines the energetic electrons near the cathode. With the influence of the magnetic field the electrons follow a longer path in the magnetic field and make large number of collisions to the gas molecule to increase the intensity of plasma in front of the magnetron gun. The magnetrons can be powered by RF (13.56 MHz, suitable for non-conducting targets), dc, and pulsed dc supplies. The present system consists of two numbers of Gencoa make magnetron guns and two numbers 13.56 MHz, 600W power supplies with suitable match boxes and one 1500V dc power supply. In the present study, magnetron sputtering guns mounted on the PIII&D chamber is used for the synthesis of Zr thin films for the study of implantation profile for N^+ and N_2^+ ions.

2.2.1.3. Plasma Immersion Ion Implantation

Plasma immersion ion implantation is the process in which the positive ions of the plasma is implanted into the materials by the application of a high voltage bias. Towards improving the dose, implantation dynamics, energy of ions, controlling sheath expansion, etc., several modification of the technique have been introduced over the years [195,196]. Initially, plasma Immersion ion implantation (PIII) was put into use in the mid-1980s [197,198] as an alternate technique to beam line implantation for the generation of shallow junctions in microelectronics. Later PIII, was combined with deposition techniques to improve the mechanical properties of materials against corrosion, improve bio-compatibility and wear resistance of materials [199]. However, PIII suffers from reduced thickness of modified layer for heavy engineering applications. Nevertheless, for bulk modification of thin films and nanostructures, PIII can be effectively used.

A schematic of PIII system is shown in Fig. 2.5. The plasma generation for both PECVD and PIII are done using the same RF (Huttlinger-600W) generator. Depending on the requirements the PIII&D system is modified to accommodate the height adjustable heater for PECVD of GNWs. For implantation purpose, the PECVD stage is replaced with

a new setup capable of executing rotation along with bias. The technical details of the PIII&D system is given in Table 2.1

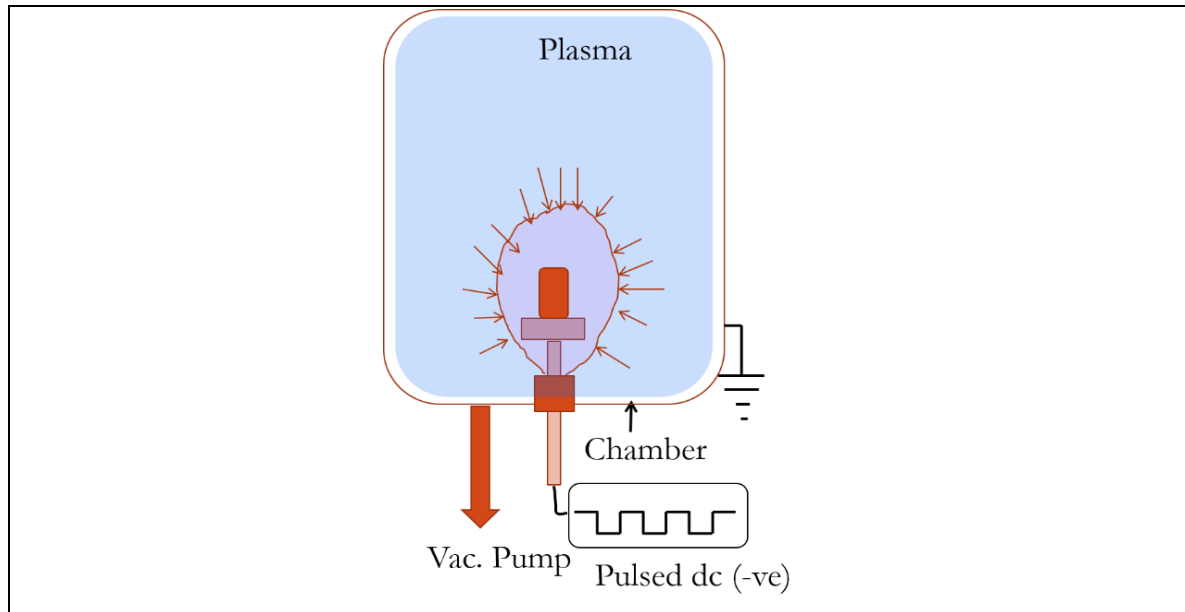


Fig. 2.5 Schematic of PIII process. The specimen placed at the centre experience ion implantation upon (-) ve pulse bias.

Table 2.1 Technical details of PIII&D System.

Components	Details
Chamber	SS, water cooled
Plasma	600W-RF (13.56 MHz)
HV bias	-40kV, 0.1-5 kHz, 5-70 μ s
Magnetron	2 nos. 600W (rf), 1no. 1500V dc
MFC	4 numbers
Substrate Heater	RT-850 $^{\circ}$ C

By the application of a negative pulse to the target material, the electrons are driven away in the time scale inverse of electron plasma frequency (ω_{pe}^{-1}) leaving an ion matrix. Subsequently, on the time scale inverse of plasma ion frequency (ω_{pi}^{-1}), the ions within the sheath are accelerated into the target. In the initial transitional phase, the energy distribution of ions depends on their initial position in the ion matrix sheath. Plasma ions arriving at the sheath edge (that is, the boundary between the sheath and plasma) are accelerated by sheath's field and therefore extracted from the plasma. As a result, the sheath edge moves away from the biased surface, i.e., sheath thickness increases. This process drive the sheath-

plasma edge further away exposing new regions and ions. On a larger time scale, the system (sheath and current density) evolves into a steady state *Child law* sheath [200]. The applied negative pulse width is usually much longer than plasma ion frequency (ω_{pe}^{-1}) and the steady state sheath thickness can be obtained from Child-Langmuir law [196]. Considering a typical plasma ($n_e=10^{10}/\text{cm}^3$, $kT_e= 1 \text{ eV}$), the sheath thickness exceeds 40 cm when the applied voltage approaches 100 kV. This is one of the major design consideration of PIII chamber and sample to be treated. Since, high voltage is applied in a conventional PIII process, the sheath expansion is fast and sheath size is large enough to exceed the plasma volume, that a steady state “Child” sheath is not formed. However, for the purpose of modeling the plasma behaviour, usually, *Child law* sheath is assumed. Several parameters are involved in the evaluation of implantation dose and energy distribution. For example, the shape of initial matrix sheath is related to the shape of the targets. Usually, theoretical models assume perfect rectangular pulse and one-dimensional planar geometry for generating models which usually represent the actual situation far from reality. Hence, experimental analysis of the actual situation is very crucial for PIII process. However, towards understanding the theoretical basis, an ideal one dimensional plasma is modelled based on Child law [8].

The controlling equations for plasma ion implantation are

$$j_c = \frac{4}{9} \epsilon_0 \left(\frac{2e}{M} \right)^{\frac{1}{2}} \frac{V_0^{3/2}}{S^2} \quad \text{Eq. 2-1}$$

$$S = S_0 \left(1 + \frac{2}{3} \omega_{pi} \right)^{1/3} \quad \text{Eq. 2-2}$$

$$S_0 = \left(\frac{2 \epsilon_0 V_0}{en_0} \right)^{1/2} \quad \text{Eq. 2-3}$$

$$\omega_{pi} = \sqrt{\frac{e^2 n_0}{\epsilon_0 M}} \quad \text{Eq. 2-4}$$

Where j_c –Current density, ϵ_0 - free space permittivity, e-Electronic charge, M-Ionic mass, V_0 -Voltage across sheath, S-Sheath thickness (time dependent), ω_{pi} - Ion plasma frequency, S_0 -Ion matrix sheath thickness, n_0 -Plasma density. The current density is the charge per unit time crossing the sheath boundary of thickness S. The basic parameter required for the estimation of dose is plasma density, plasma potential and applied bias. Ideal specimen geometry (e.g. square surface with smooth edges) is assumed for the calculation of implantation dose. However, in actual practice, the specimen geometry is far from ideal cases. Hence, experimental evidences are preferred over theoretical estimation of dose. Additionally, the experimental set up is a custom made PIII&D system and

conventional standard plasma diagnostics has not been done. Hence, the characteristics of the process need to be analysed and understood from the analysis of standard samples.

2.2.2. FESEM

Field emission scanning electron microscope (FESEM) uses a high intensity field emission electron gun to generate and focus beam of high-energy electrons in a raster scan pattern to generate a variety of signals from the specimen. For imaging purpose, three modes viz. Secondary Electron (SE) imaging and Back Scattered Electron (BSE) imaging and Scanning Tunneling Electron Microscopy (STEM) are used. To understand the morphology and characteristic surface features of GNWs and implanted GNWs, SE mode is used. The in-lens detector in SE mode provide high resolution and clarity to the surface and cross sectional images. Scanning electron microscope (FEG-SEM-Supra 55 (3 nm resolution) from Carl-Zeiss, GmbH) is used for studying the morphology of the pristine and implanted samples and using the inbuilt tool, the thickness of the samples are measured.

2.2.3. TEM

High resolution transmission electron microscopy ((HRTEM, Carl Zeiss, model-LIBRA 200 FE-(0.24 nm resolution))) is a unique materials characterisation technique that enables examination of microstructure at high resolution as well as determination of crystallographic information of a selected region.

The Selected Area Diffraction (SAD) patterns are very useful in identifying the crystal structure of a given phase. It is also useful for determining the crystal orientation or orientation relationship between co-existing planes. The angles through which the electrons are scattered are given by Bragg's law (Eq.2.5)

$$n\lambda = 2d \sin\theta \quad \text{Eq. 2-5}$$

where 'n' is an integer, 'λ' is the wavelength of the electrons, 'd' is the inter-planar spacing for the family of diffracting planes and 'θ' is the diffracting angle. Diffraction of electrons by crystal is identical to the diffraction of X-rays by a crystal. The difference lies primarily in the wavelength of the diffracting radiation. While X-rays have wavelength of the order of few angstroms (Å⁰), 100 keV electrons have wavelength of the order of ~ 0.037 Å⁰. Consequently diffracting angles for electrons are typically small. For such small angles, sin θ = θ and considering only first-order reflections (n=1), Bragg's law for electron diffraction reduces to (2.6). In the equations, L=camera length, r=radius of the diffraction ring.

$$\lambda = 2 d \theta \quad \text{Eq. 2-6}$$

$$2\theta = \frac{r}{L} \quad \text{Eq. 2-7}$$

$$r d = \lambda L \quad \text{Eq. 2-8}$$

The camera constant can be determined, for a specific microscope at a specific operating voltage, from the diffraction pattern obtained from a known standard.

The d-spacing of a specific crystallographic plane (d_{hkl}) is calculated by using equation (2.5). The 'd' value were compared with standard XRD data to find out the corresponding planes.

Nanocrystalline materials give rise to spotty ring diffraction patterns, since as many randomly oriented fine grains are included in the selected area. With reducing crystal size the spotty ring patterns transforms into diffused ring pattern.

2.2.4. EELS

In the transmission electron microscope, electrons are accelerated to an energy level (100-300 keV) which is high enough to ensure that they are transmitted through a thin specimen. During the transmission process, the electron-electron interaction takes place and are inelastically scattered. The loss of electron energy provide information about the local environment of the atomic electrons which in turn relates to the physical and chemical properties of the specimen. The energy distribution of the transmitted beam has two regions viz. the low energy loss region and high energy loss region [201]. The low loss region consists of high intensity zero loss (ZL) peak and plasmonic peaks. The width of ZL peak is 0.2-2eV and mainly reflects the energy distribution of the electron source. Along with zero loss peak, at loss of energies below ~50 eV there are a few peaks generated due to plasmonic excitation. The high loss region is formed by the excitation of orbital electrons to next higher level (ionization edges) due to interaction with incoming electrons. The high loss region consists of several peaks corresponding to the inter band electronic transitions of each element in the material. It is a powerful analytical technique which is capable of providing information about electronic structure, bond length, oxidation state, and chemical composition, with a spatial resolution down to atomic level in favourable cases.

The low loss region provide similar information as that of optical spectroscopy that information on band structure and di-electric properties can be deduced. There is no electron-electron interaction in between the zero loss peak and plasmonic peak. This indicates the onset of plasmonic edge and it can be used for calculating the band gap by eliminating the tail of the ZL peak and using parabolic function or suitable (power law) function for fitting to the plasmonic peak for direct and indirect band gap materials,

respectively [202,203]. In the high energy loss region, the intensity of electrons gradually falls with sharp edges corresponding to the absorption of energy by an inner shell electron to get excited in to a state above the Fermi level [201]. This is similar to the absorption edges of X-ray absorption spectroscopy (XAS). The ionization edge can be effectively used for the analysis of lighter elements, qualitatively. For thin samples, the intensity of the edges are proportional to the concentration of the corresponding elements.

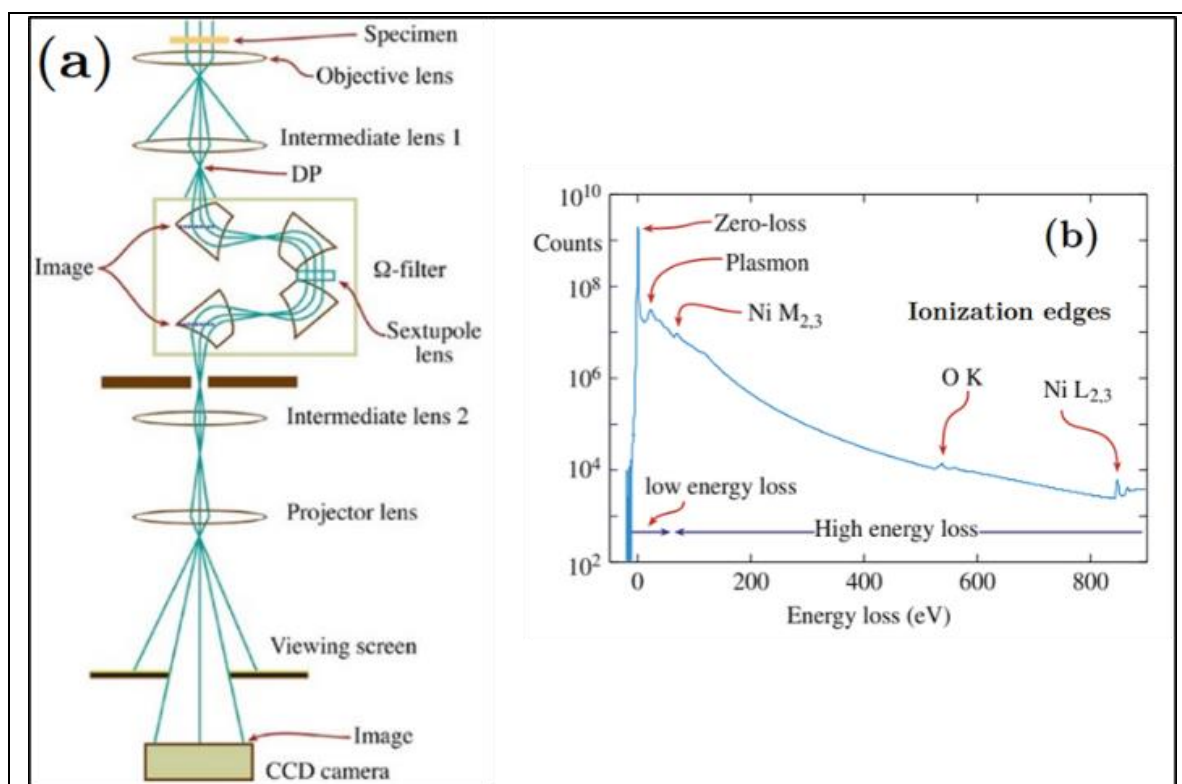


Fig. 2.6 (a) Schematic of TEM line diagram with the Ω -energy filter after the specimen stage. (b) Typical EELS spectrum showing Zero-loss peak, Plasmon peak and ionization edges for different elements [204].

The samples used for EELS measurements are GNWs of a few (~ 10) layers. The thicker regions are avoided by taking the ratio of plasmonic peak height to ZL peak as 0.1 or less. Additionally, the comparison of different spectra in the low loss region are done using ZL peak normalised intensity. The normalization against the ZL peak helps to overcome any variation in the electron intensity in between samples due to electron column, samples thickness or collection issues. In the high loss region, the peak intensity corresponding to the $\pi^* + \sigma^*$ interband transition is normalised before comparison. Hence, by doing normalization the effect of variation in thickness in the samples are reduced.

In the present study the EELS ($\pi - \pi^*$ and C K- edge) data are recorded using the LIBRA 200FE TEM having omega energy filter, under similar (Voltage -200kV,

convergence and collection angles, collection time) experimental conditions. A schematic of the TEM with specimen and Ω -energy filter is shown in Fig. 2.6(a) and the typical EELS spectrum is shown in Fig. 2.6(b). Several techniques are used for peak fitting to determine the sp^2 fraction from C K- edge energy absorption data have been proposed in the literature [205–209]. All the above techniques involve fitting of π^* and $\pi^* + \sigma^*$ peaks for certain fixed energy window and taking area ratio as against fully graphitised carbon. However, the acceptability of each is not unquestionable because of the variation in region of interest, energy window and type of functions used to fit the curves. Hence, we have used one of the most robust approach proposed by Berger *et.al* as given in equation-2.9 [210], where $I_{(g\pi^*)}$ and $I_{(u\pi^*)}$ are the integrated intensity of π - π^* C K-edge of pure graphite and sample respectively, $I_u(\Delta E)$ and $I_g(\Delta E)$ are integrated intensity of the entire C K-edge of sample and highly oriented pyrolytic graphite (HOPG) in the energy window ΔE . The C K- edge of EEL spectrum obtained from HOPG sample was assumed to have 100% sp^2 bonding for quantification. The area corresponding to π - π^* transition in the high loss region was calculated from curve fit at around 286 eV and an energy window (ΔE) of 282 eV to 315eV was considered for calculating the area under $\pi^* + \sigma^*$ transition.

$$f = \frac{I_{g\pi^*} I_u(\Delta E)}{I_{u\pi^*} I_g(\Delta E)} \quad \text{Eq. 2-9}$$

2.2.5. Raman spectroscopy

When a monochromatic radiation is scattered by molecules, a small fraction of the scattered radiation is observed to have a different frequency from that of the incident Radiation, this is known as Raman Effect. Raman spectroscopy involves two processes. The excitation of electrons in the molecule to a higher energy level due to the inelastic interaction with the electric field of the electromagnetic radiation, followed by return of the excited electrons to a lower level. The excited electron before going back to lower energy levels interact with the phonons and loss some of its energy. During the process there will be net gain or loss of energy. A material is said to be Raman active, if the molecules undergo polarization upon the influence of the electric field of the incoming radiation. It is a valuable non-destructive tool for the characterisation of materials due to its high sensitivity to the phonons in the molecular species of interest. When a radiation of frequency ν_0 (energy = $h\nu_0$) is scattered by the sample, the phonons undergo two types of interaction with the sample, (a) elastic collisions, in which the energy of the scattered photon is unchanged, is the most probable scattering and is known as Rayleigh scattering. (b) inelastic collision

(much less probable, 1×10^{-5} of the incident light intensity) of a photon with a molecule and the energy is exchanged between the photon and the molecule such that the scattered photon is of higher (anti-stokes) or lower (stokes) energy than the incident photon. The energy of the scattered photon is $h(\nu_0 \pm \nu_n)$. As the energy levels (vibrational or rotational) of the molecules are discrete and well defined, energy can be lost or gained by the molecule only in quantised or discrete amounts resulting in two types of inelastic scattering events. An energy level diagram showing the origin of the Stokes and anti-Stokes bands is given in Fig. 2.7. The scattering process is in the time scale of 10^{-12} to 10^{-13} s. At room temperature, the intensity of the anti-stokes radiation is significantly low compared to stokes radiation as it can occur only with molecules that are in excited vibrational or rotational state to start with. So Raman spectroscopy generally uses Stokes radiation [211].

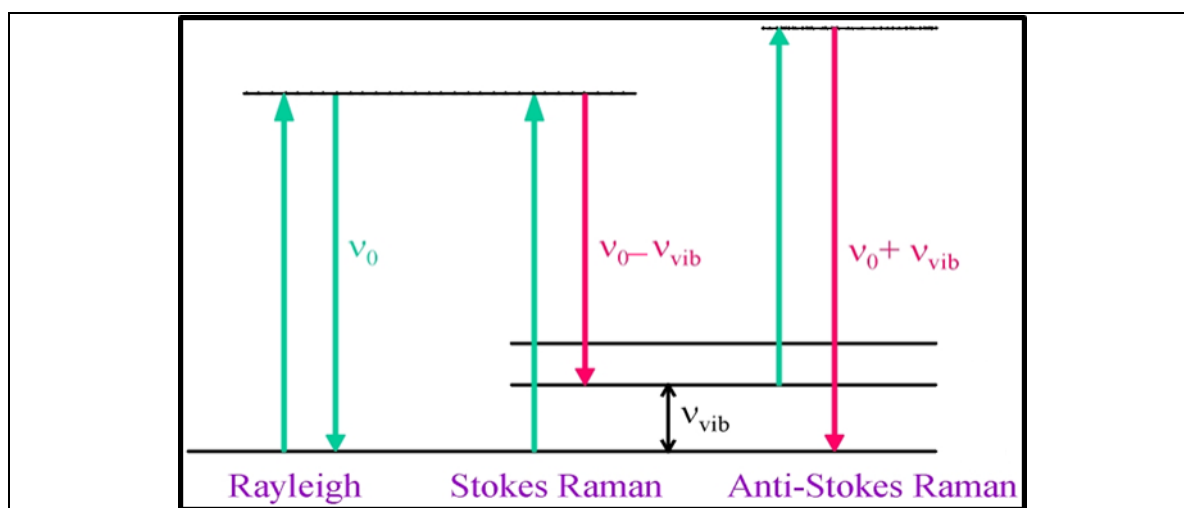


Fig. 2.7 Schematic of energy level diagram of Raman scattering.

Raman line intensities are proportional to:

$$\nu^4 \times \sigma(\nu) \times I \times \exp(-E_i/kT) \times C \quad \text{Eq. 2-10}$$

where ν is the frequency of the incident radiation, $\sigma(\nu)$ is the Raman cross section (typically 10^{-29} cm²), I is the radiation intensity, $\exp(-E_i/kT)$ is the Boltzmann factor for state i , and C is the analyte concentration.

Raman spectroscopy offers several advantages like, little or no sample preparation, easy and fast acquisition of data, relatively simpler and straight forward interpretation, and complementary type of information from different light sources. Raman spectroscopy provide information on the back bone of the molecule whereas IR spectroscopy is sensitive to the functional groups. Raman spectroscopy provide vital and specific information on

carbon materials and it has almost become an indispensable preliminary characterisation tool for carbon materials. Lasers are used almost exclusively as the excitation source in all the Raman systems. The most commonly used lasers are specific frequency semiconductor laser in both UV and visible ranges. Typical laser powers used range from milliwatts to a few watts and are generally focused using suitable optical systems to increase the power density. However, for absorbing samples, this can result in significant local heating of the sample, leading to acquiring wrong data. Hence, carbon systems usually use low power and multiple acquisitions at different locations.

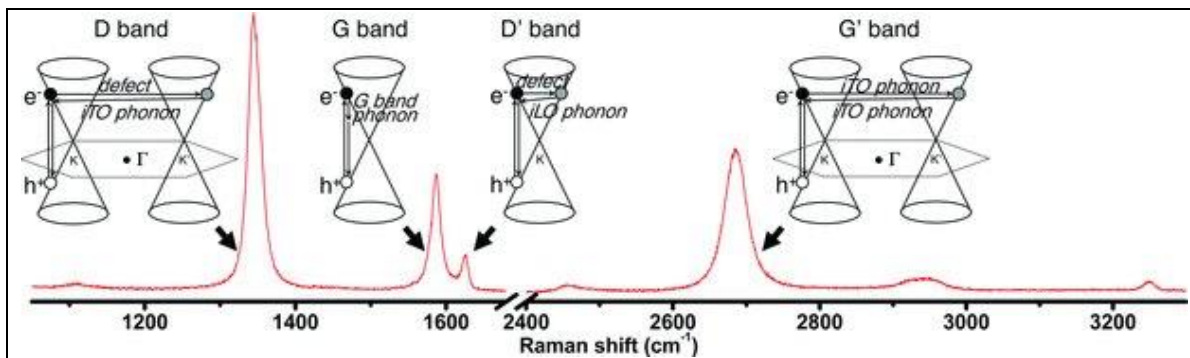


Fig. 2.8 Raman bands corresponding to defective graphene or graphene nanowalls. Respective phonon modes acting on the excited electron at the high symmetry points of Brillouin zone is shown.

The scattered light is collected with an objective onto the entrance slit of a monochromator equipped with holographically ruled gratings (200 – 2400 grooves/mm). The dispersed light from exit slit of monochromator is usually detected by the Charge-Coupled-Device (CCD) detectors which reduce the spectrum acquisition time and also improves the signal to noise ratio. Raman spectra are obtained by plotting the scattered intensity versus the frequency shift, with respect to the excitation source such that the band position will lie at frequencies that correspond to the energy levels of different phonons.

In the present study, Raman spectra were collected at room temperature using Renishaw model Invia with Leica microscope. The semiconductor laser (514.5/ 532 nm) is used as the excitation source. The Raman spectrum of Graphene provide D, G, D' and G' bands among other addition or overtones. Usually, the intensity is plotted against Raman shift after background correction. Typical Raman spectra of GNWs are shown in Fig. 2.8. Though the applicability of Breit Winger Fano (BWF) function for G-band fitting of SWNTs and graphene are generally accepted, its usage to bundled systems like MWNT and GNWs/GNWs are questionable. Because, the asymmetric line shape of BWF function (arising in graphene and SWNTs) are due to the excitation of multiple electron-hole pair in

the vicinity of the Dirac cone by coulombic interaction of phonons with metallic character of the surroundings [212]. Hence, in the present study the G-peak was deconvoluted by using the mixed (Lorentzian + Gaussian) type functions embedded in WIRE 4.2 software to assign the respective phonon modes and peak ratio calculations. Lorentzian function was used for fitting other peaks.

In the current study of Raman spectra of GNWs, G-peak normalised intensity was used for the comparison of the graphs. Since, G peak is typical of all sp^2 bonded carbon, the comparison of the samples become easier in this technique. Additionally, quality evaluation of graphene nanowalls is done using the FWHM of the peaks because there exist some confusion among various researchers on the use of integrated intensity or peak height in the calculation of ratios (I_D/I_G , $I_{G'}/I_G$, etc.). However, both the above methods are used during the discussion of results in respective chapters.

2.2.6. Infrared spectroscopy

Infrared spectroscopy is the analysis of infrared (IR) light interaction with a molecule. In infrared spectroscopy, some of the radiation is absorbed and some are transmitted. Since each material have unique combination of atoms, no two compounds produce exactly same IR spectrum, that the resulting spectrum represent a molecular finger print of the sample. The peak intensity can be correlated to the amount of material present. Historically, IR spectroscopy utilised dispersive type analysis using prism or grating to separate individual frequencies. The results of the analysis gives a plot of intensity vs frequency.

Fourier transform infrared (FTIR) spectroscopy is developed to overcome the limitations and improve the ease of collecting data. The major improvements are in the speed of acquisition and simultaneous data collection of all frequencies. An interferometer is employed in FTIR spectrometer to produce a unique signal which has the combination of all the infrared frequencies encoded into it. This is achieved by the combination of one beam splitter and two mirrors. The incident IR radiation is split into two, to fall on two flat mirrors such that the incident beam is reflected back to the beam splitter. One of the mirrors can move a few millimeters and the other is fixed. The moving mirror introduce a path difference to the reflected beam with respect to the other such that they interfere at the beam splitter as a function of the distance travelled by the mirror. Since the source is polychromatic, the resulting beam contains all the wavelength that undergo similar interference such that each wavelength of the beam is periodically blocked, transmitted,

blocked and transmitted. Different wavelengths are modulated at different rates so that at each moment the beam coming out of the interferometer has a different spectrum. The interferogram obtained is a plot of the intensity of signal versus the optical path difference. That is, all frequencies are measured simultaneously. However, the resulting signal need to be decoded to understand the response of the sample to individual frequencies. This is done by a computer using the mathematical method called Fourier transform in which frequency vs intensity plot is obtained. An extra visible (He-Ne) laser beam is usually mixed along with the IR radiation for wavelength calibration, mirror position control and data acquisition timing. A schematic of the FTIR system is shown in Fig. 2.9.

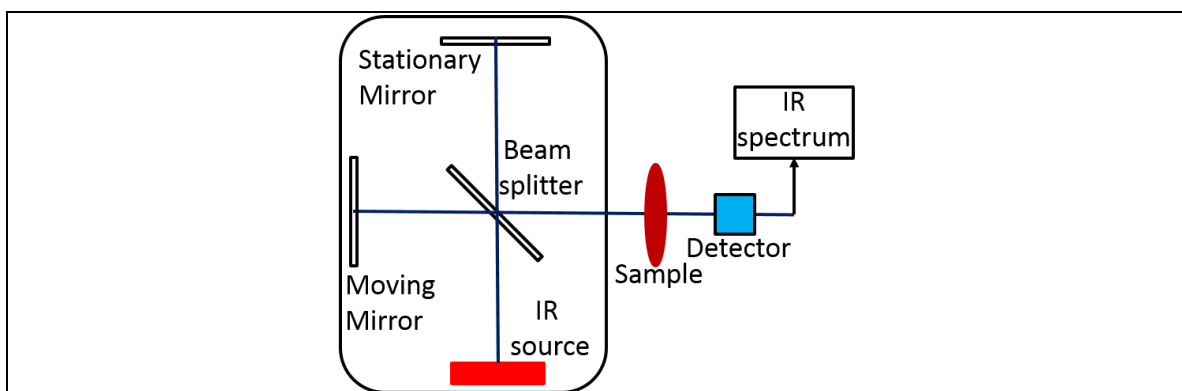


Fig. 2.9 Schematic of FTIR system.

Since there are absorption losses in the system a background spectrum is usually measured without the sample to determine the percentage transmittance. This spectrum can be used to remove the instrumental characteristics.

A molecule is said to be infrared active only when it undergo a change in its dipole moment upon interaction with the radiation. A molecule with three or more atoms can experience different types of vibrations. Infrared spectrum provides a rich array of absorption bands typical of interaction of infrared radiation with the polar nature of the molecule. The energy absorption takes place with respect to the nature (stretch, bending, torsion, etc.,) of molecular vibrations with symmetric and asymmetric modes contributes to closely spaced absorption bands in all the three physical states of matter.

In the present study, Infrared transmission measurements were carried out in the mid IR ($400\text{-}4000\text{ cm}^{-1}$) range using Bruker vertex 80V FTIR spectrometer equipped with global source and KBr beam splitter. Data were collected with 4 cm^{-1} resolution at ambient temperature and 5×10^{-2} mbar pressure. Same silicon substrate which do not have peaks in the region of interest is used as the reference. Absorption coefficient ($\alpha=2.303*A/t$, where

A = absorbance and t = thickness of GNWs in cm) is calculated to compare the background intensity of samples.

2.2.7. Secondary Ion Mass Spectroscopy (SIMS)

Secondary Ion Mass Spectrometry (SIMS) is a surface analytical technique capable of providing elemental information with high sensitivity (parts per million (ppm) to parts per billion (ppb)). It can also provide depth profile with high depth resolution (a few nm down to around one nm). SIMS employs ion beam sputtering of the specimen surface and detects the ions ejected from the specimen. Primary ions are usually produced by plasma discharge (O_2^+) in a duo-plasmatron or by thermionic surface emission from the Cs^+ source. These ions are then accelerated to 2 to 20 kV, focused to a narrow beam and allowed to impact on the surface of the specimen. The impact of the primary ions on the specimen results in a collision cascade, involving the reshuffling of some 50-500 near surface atoms, some of which are ejected from the surface as secondary particles (monoatomic, molecular or clusters). A fraction of the particles emerges positively or negatively charged. These secondary ions are extracted from the specimen and injected into the mass spectrometer through a system of ion optics.

The ions used for sputtering (primary ions) such as Cs^+ , O_2^+ , O^- , Ar^+ , and Ga^+ having an energy of the order of a few keV. The sputtered secondary species from the sample surface consists of neutral or charged atoms and clusters having energies up to a few hundred eV. The secondary ions are extracted by applying an electric potential and analysed using a mass analyser to obtain the composition of the material. A Cameca im4f and a Cameca im7f SIMS instruments were used in this study. These instruments have Cs^+ , O_2^+ , O^- , Ar^+ primary ion beams to choose from. These instruments employ double focusing analyser for the secondary ions, the energy focusing done by an electrostatic analyser (ESA), and the mass focusing done by a magnetic mass analyser. The ions are then detected using a detector such as a Faraday cup, an electron multiplier, or an image detector such as multichannel plate or resistive anode encoder.

The sensitivity of SIMS to a particular secondary ion species (M) depends on the sputter yield and ionization probability. The secondary ion current of the species M (I_{MS}) is given by the following relation,

$$I_{MS} = I_P S_M R_M C_M \eta \quad \text{Eq.2-11}$$

where I_P is the primary ion flux, S_M , R_M are the sputter yield and ionization probability, C_M is the concentration of species M , and η is the transmission and detection

efficiency of the analyser system. C_M is to be determined, R_M in the above equation is highly uncertain. It not only depends on the characteristics of M but also on those of the environment (matrix) from which M is ejected. This property made SIMS data poorly quantitative. To quantify SIMS data, matrix matched standards are used. However, making matrix matched standards is laborious. In general, a system being analysed may comprise numerous matrices varying within itself. Hence, the number of standards to be made will also be very high. In the first place, the composition of the system may not be known *a priori*. In applications as in semiconductor industry, the number of matrices is comparatively limited; the composition varies in the trace level with the dopant concentration. In such cases, it is comparatively easier to use matrix matched standards to quantify SIMS data. However, in a general application where the number of matrices involved is high, making matrix matched standards is generally impractical. Hence, feasible alternative methods are preferable to quantify SIMS data. One important such alternative technique discovered is to sputter the specimen (whether one is interested in electronegative or electropositive species) with Cs^+ primary beam and detecting CsX secondary ion complexes where X stands for an atom from the specimen [213]. Cs_2X was found to be formed more intense than CsX if X is electronegative [214]. The mechanism by which the secondary CsMX^+ species provide more quantitative data is explained below.

The value of R_M in the above equation 2-11 can range from roughly 0.05 down to many orders of magnitude lower. This means that the fraction of ions can vary by roughly 5% and the neutrals vary by 95% upto 100%. This shows that the matrix effect with the secondary neutrals is much lower compared to that with secondary ions. The CsX complexes are understood to be formed by the combination of a resputtered Cs^+ ion with a sputtered neutral species. Since the formation of CsX complexes involves the sputtered neutrals, measurement of CsX complexes are understood to be much more quantitative compared to the measurement of secondary ions.

However, in fact, sputtered composition can normally contain not only atomic neutrals but also clusters of atoms too. Hence, it would be necessary to include the sputtered polyatomic neutrals too to get more accurate composition and this has been found to yield still better quantitative data [215]. In the SIMS studies of this work, this approach has been employed to get quantitative information.

The CAMECA IMS-4f (for Ti sample)/7f (for Si sample) make SIMS were used for the current work. The spot size of the primary ion could be varied between 0.5 to 10 μm

and rastered on the sample over an area of maximum $500 \mu\text{m}^2$. A sector type magnetic analyser was used for mass analysis of the secondary ions. The mass resolution ($m/\Delta m$) can be adjusted from 200-10000 for a mass range of 1 – 300 amu. A Faraday cup and an electron multiplier are provided for the detection of mass analysed secondary particles. The instrument has an elemental sensitivity in the ppb (parts per billion) range and a depth resolution of the order of a few nanometers.

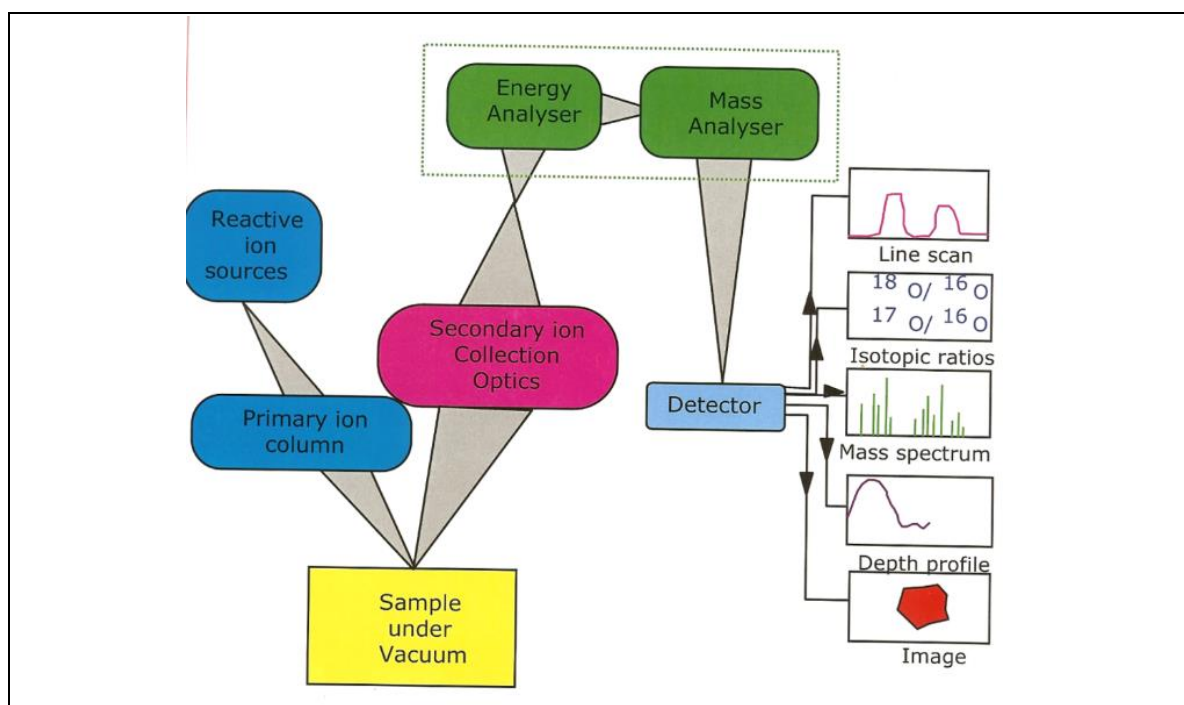


Fig. 2.10 Schematic of Secondary Ion Mass Spectrometer.

In the SIMS measurements of nitrogen implanted Si, IMS 7f instrument is used. Primary Cs^+ ions of 5nA current was accelerated by 5.5 keV bias to sputter the sample surface. The primary ion beam was rastered over a square area of width $200\mu\text{m}$ and secondary ions were collected from a circular area of $\sim 60\mu\text{m}$ diameter centred at the middle of the sputtered area. The secondary ions selected by the double focusing mass analyser were detected using the electron multiplier. The intensity vs. sputtering time profile was converted into depth profile by measuring the depth of the crater created by sputtering. The crater depth was measured using a DEKTAK 6M stylus profilometer.

2.2.8. X-ray Photo-electron Spectroscopy (XPS)

In X-ray photo-electron spectroscopy, a molecule or an atom in a solid is bombard with X-rays (200-2000 eV) under ultra-high vacuum which cause the emission of inner level–electrons. The kinetic energy (E_k) of the photo electrons are measured by an energy analyser. The binding energy (E_b) of the core-electrons are calculated using the equation E_b

$= h\nu - E_k - \phi$, where $h\nu$ is the energy of the photon and ϕ is the spectrometer work function (a constant for a given equipment). If $h\nu$ is less than $B.E + \phi$, no photoemission process will be initiated. As the B.E decreases the KE energy of the photoelectron increases. The intensity of the photoelectron emission is proportional to the intensity of photons. By analyzing the kinetic energies of the photoelectrons, the binding energy of the photoelectrons can be calculated. Since the energies of various orbitals are characteristic of an element, one can identify the elements present in the material, based on the binding energies of the emitted photo electrons. Binding energy reflects the strength of interaction between the electrons and the nuclear charge and it contains information on the initial and final state of the atoms.

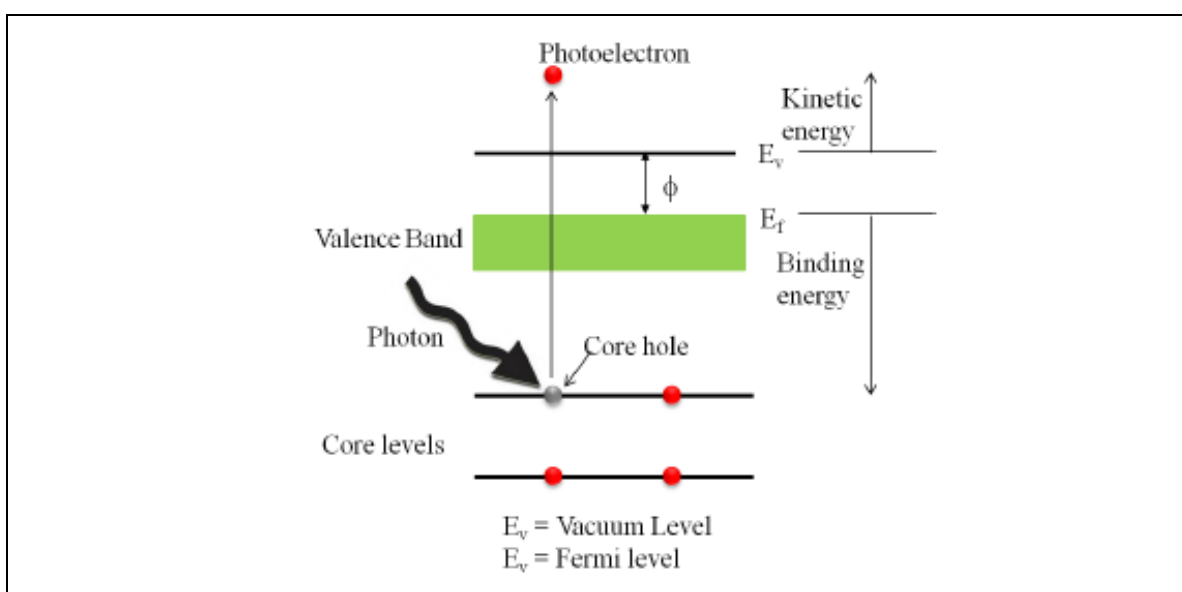


Fig. 2.11 The schematic of photoelectron emission process.

The initial state accounts for the core level binding energy shifts and is used for obtaining chemical state information. The chemical environment surrounding of an atom decides the effective charge on the core electron. With the change in the chemical surrounding, this effective charge is altered. Thus a change in binding energy is caused. This manifests as a chemical shift or surface core level shift and is indicative of the oxidation state of the atom. More the binding energy, the electron bound to the nucleus more tightly and therefore in the case of high Z elements, the binding energy will be high. The schematic of the X-ray photo electron emission process is depicted in Fig. 2.11. Ideally, to determine the binding energy; the work function of the material and the equipment should be known. The work function of the material is the energy difference between the Fermi level and vacuum level. If the sample is electrically in good contact with the chamber, the work function of the

material need not be taken separately in the calculation of binding energy. Because, the Fermi levels of the sample and the chamber materials become the same. The work function can be compensated artificially to eliminate its effect in modern equipment to give $E_b = h\nu - E_k$. A schematic of the work function compensation is given in Fig. 2.12.

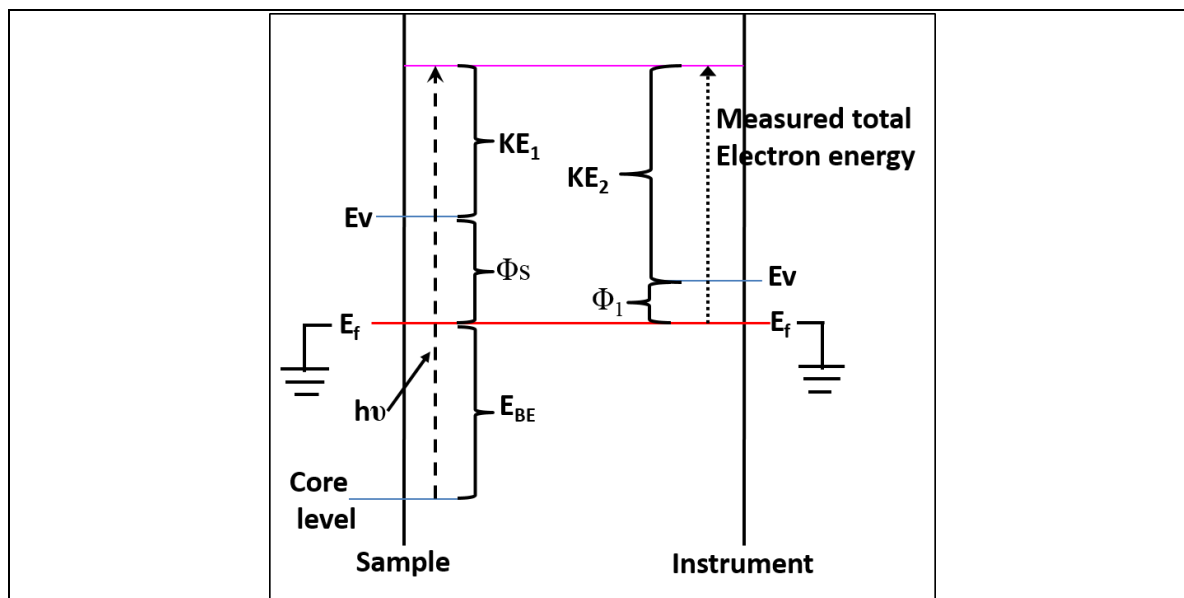


Fig. 2.12 Schematic of XPS work function compensation. For conducting samples, the Fermi level (E_f) of both sample and instrument become equal upon earthing. Φ_s and Φ_1 are work function of the sample and instrument. The total electron energy (TEE) measured is the sum of KE_2 and Φ_1 . The difference between the X-ray energy ($h\nu$) and TEE will give the binding energy.

For an electron in an orbital which possess orbital angular momentum, coupling between magnetic fields of spin (s) and angular momentum (l) occurs. The level of degeneracy of the spin - orbit splitting will be $2j+1$, where j is the total momentum. According to this, no splitting will be observed for the s orbital, whereas the p orbital electron emission will show a doublet keeping the intensity ratio at 1:2 for $p_{1/2}$ and $p_{3/2}$ [216,217].

The relative change in binding energy due to a chemical change is the most desirable way for chemical analysis. When the base material is bonded with a high electron affinity atom, the E_b of the core electrons of the base atom increases. After the ejection of photoelectrons the atom relaxes with the emission of X-ray photon known as X-ray fluorescence. The other possibility is the ejection of auger electron through secondary process. Though X-ray penetrate several nanometer into the sample, only the electrons from

the surface (2-3nm) escape self-capturing and hence, it provide very surface specific information. The detection limits for a monolayer ranges from 1% (light elements) to 0.1 % to heavy elements.

The B.E of the electrons not only depends upon the level from which it is ejected, but also on the formal oxidation state and local chemical coordination environment of the atom. Therefore, one can identify the oxidation states as well as the chemical environments from the observed BE values. An approximate composition of the material can be determined by dividing the individual peak areas corresponding to the elements of interest, after appropriate background subtraction, by their respective atomic sensitivity factor (ASF). This was done after appropriate (Shirley) background subtraction. The sensitivity factor of the element can be defined by the equation

$$ASF = f \times \sigma \times \theta_i \times y \times \lambda_{mf} \times A \times T_d \quad \text{Eq. 2-12}$$

where f is the X-ray flux (photons/cm²-sec), σ the photoelectron cross section of the atomic orbital of interest (cm²), θ_i is the instrumental angular efficiency factor between photo path and detected electron, y is the efficiency in the photoelectric process for formation of photoelectrons of the normal photoelectron energy and λ_{mf} is the mean free path of the photoelectrons in the sample. A refers to the area of the sample from which emitted photoelectrons are detected and T_d is the detection efficiency for electrons emitted from the specimen of interest. From the peak height or peak areas and atomic sensitivity factor values corresponding to the elements of interest, the stoichiometry of the material can be calculated using the equation,

$$\frac{n_A}{n_B} = \frac{I_A/S_A}{I_B/S_B} \quad \text{Eq. 2-13}$$

n_A and n_B in this equation refers to the atomic fractions of the elements A and B present in the material. I_A and I_B are the corresponding intensities whereas S_A and S_B are ASF values respectively.

In the present study, the Al $k\alpha$ (1486.6 eV) X-ray source (equipment model: VG ESCALAB MKII and MECA2000, SPECS, GmbH) was used for XPS analysis of high dose ion implanted titanium and GNWs samples. The systems operate at ultra-high vacuum conditions (1×10^{-9} mbar) and analyser resolution of 0.67 eV for 656 kcps and at a pass energy of 12 eV. The low dose GNWs samples were analysed using BL 14 beam line of

synchrotron facility at RRCAT, Indore. The XPS spectra were analysed using Casa XPS software.

2.2.9. Atomic Force Acoustic Microscopy (AFAM)

Atomic force microscopy is a type of scanning probe microscopy in which the probe mechanically feel or touch the sample and the information on the topography is gathered. The deflection of the probe is collected by using a laser light focused on it.

Several types of scanning probe microscopy for the determination of material properties are in use. SPM can map the surface magnetic, electric, di-electric, electrochemical and elastic properties of the surface. Elastic properties can be mapped and measured using atomic force acoustic microscopy (AFAM). A schematic of the AFM and AFAM set up is shown in Fig. 2.13. SPMs operates in different modes; contact, non-contacts and semi-contact modes depending on the requirements. However, AFAM measurements are in contact mode only.

Determination of contact resonance spectra is fundamental to AFAM based measurements. The local material properties of samples, such as elasticity, viscosity and stiffness influence the contact resonance spectra [218]. The contact resonance frequency helps to reasonably guess the excitation frequencies of AFAM. The excitation frequency or the frequency difference of the probe and the sample is usually kept within the resonance peak. And finally, accurate AFAM analysis of the local elastic modulus needs the operation in the linear spectral region. Monitoring the spectra can benefit appropriate selections of the excitation amplitude, normal force, etc.

In contact mode, the cantilever of an atomic force microscope is excited into flexural vibrations. Among other parameters, the frequency of the eigen modes of the cantilever depends on the contact stiffness of the tip-sample and also on the contact radius. So these eigen modes changes with the Young's modulus of the sample and the tip. Hence this technique allows one to determine the Young's modulus from the contact stiffness with a resolution of a few tens of nanometers. In this setup, the sample is placed on a piezoelectric transducer. It emits longitudinal acoustic waves into the sample, which cause out-of-plane vibrations of the sample surface. The surface vibrations are transmitted into the cantilever via the sensor tip. The cantilever vibrations are measured by a 4-sectioned photo-diode and evaluated by a lock-in amplifier. The contact-mode topography image is acquired concurrently with the AFAM image. The frequency range used covers the flexural modes of the cantilever from 10 kHz up to 5 MHz.

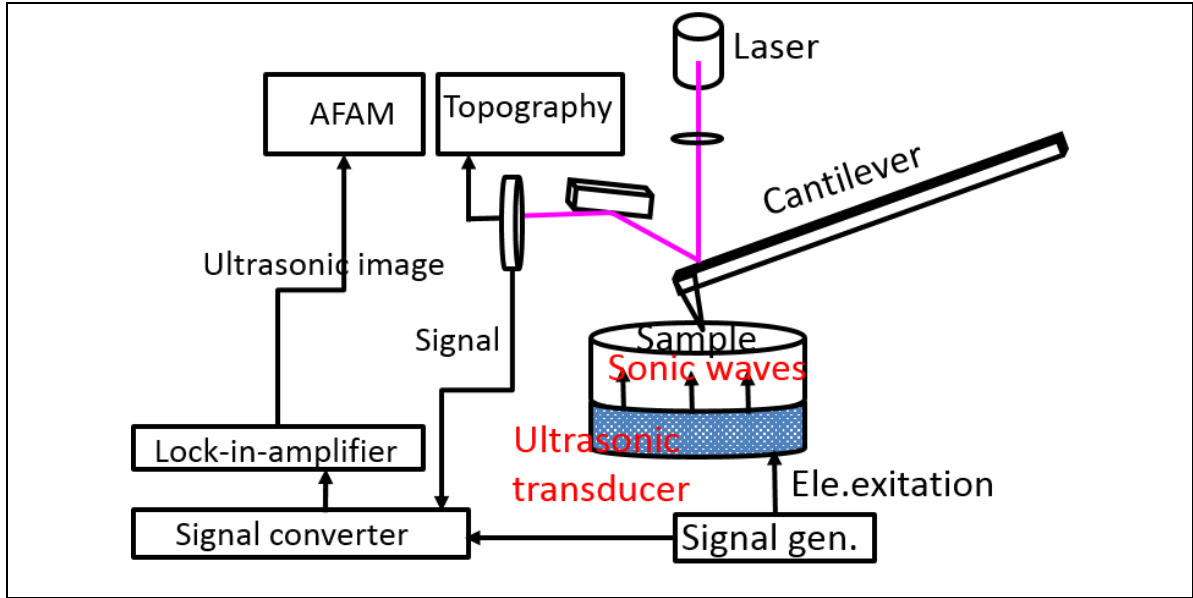


Fig. 2.13 Schematic of AFM and AFAM technique.

High resolution scanning probe microscope (SPM model: NTEGRA prima Multimode, NT-MDT) is used for the AFM and AFAM study. The contact resonance frequency was measured by sweeping the transducer frequency of the cantilever in free on air (f_0), in contact with standard $\text{Si}_{\langle 111 \rangle}$ wafer (f_{ref}), un-implanted GNWs (f_{ref}), and the implanted GNWs (f_s), using the basic formula $f_0 = \sqrt{\frac{k_c}{m}}$. The contact stiffness k_s^* of unknown sample is obtained from the equation $k_s^* = k_{ref}^* \frac{f_s^2 - f_0^2}{f_{ref}^2 - f_0^2}$, Where k_c , m and k_{ref}^* are cantilever stiffness constant, equivalent mass in the point-mass model and effective contact stiffness constant, respectively. In this analysis, the equivalent mass ' m ' before and after contact is assumed constant while deriving in contact resonance frequency.

2.2.10. Water contact angle measurement

When a liquid drop is in contact with a surface, at the interface three phases coexist (gas, liquid and solid). The wettability of a solid surface by a liquid can be quantified by measuring the contact angle (CA). The contact angle is the angle subtended by the liquid – vapour interface with the solid-liquid interface. The contact angle (wetting angle) is a measure of the wettability of a solid by a liquid. For a system of solid, liquid and vapour at a given temperature and pressure, the contact angle has a unique value. However, in practice contact angle changes with time. The equilibrium contact angle reflects the relative strength of liquid, solid and vapour molecular interaction.

The equilibrium contact angle ' θ_c ' is obtained from the equation 2-14, where γ -interfacial energy, s-solid, L-liquid and G-gas. If the water contact angle is less than 10° , the surface is said to be super hydrophilic whereas, ' $\theta_c \geq 145^\circ$ ' is called super hydrophobic.

$$\gamma_{SG} = \gamma_{SL} + \gamma_{LG} \cos \theta_c \quad \text{Eq. 2-14}$$

While recording the water contact angle the following points shall be considered. The image size should be optimum, clear and have good resolution of the edges. From the image of the droplet, the contact is measured using the following steps. 1. Define the base line. 2. Trace the droplet edge. 3. Determine the gradient. 4. Measure the contact angle. In the present study the water contact angle (WCA) measurements were carried out on samples using double deionised water $\sim 1 \mu\text{l}$ using the system APEX, Acam D1N01, India. The image J software was used to estimate the WCA from the liquid drop image.

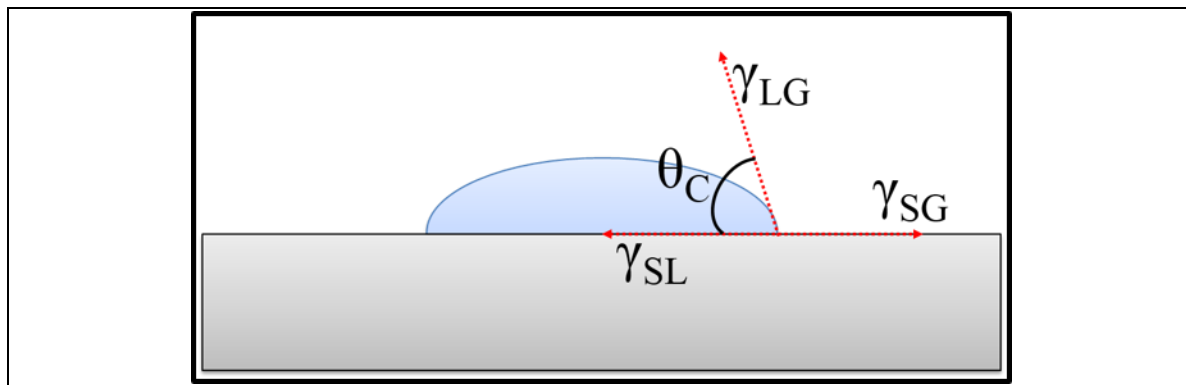


Fig. 2.14 Schematic of the liquid contact angle.

The surface wetting is explained in terms of Wenzel model and Cassie Baxter models. The fundamental assumption in the Wenzel theory is that the liquid penetrates into the grooves of the rough surface. He suggested a linear relationship between the observed CA and the surface roughness.

$$\cos \theta_r = r \cos \theta_s \quad \text{Eq. 2-15}$$

Where θ_r and θ_s are the observed (apparent) and actual CA (on a smooth surface) and r is the surface roughness or-else the ratio between the actual surface area and the geometrical surface area. If the CA on a smooth surface is smaller than 90° , then the apparent CA on the corresponding rough surface will be smaller than 90° , and vice versa. But the theory shows violation, by showing hydrophobicity, when large fraction of air is present in the pores of the material. In the Cassie Baxter model, the apparent CA is be given as follows,

$$\cos\theta_r = f_s \cos\theta_s + f_g \cos\theta_g \quad \text{Eq. 2-16}$$

Where f_s and f_g are the area fractions of the solid and gas (vapour) on the surface, respectively. Since $f_s + f_g = 1$ and $\theta_g = 180^\circ$, the equation can be written as

$$\cos\theta_r = -1 + f_s (\cos\theta_s + 1) \quad \text{Eq. 2-17}$$

Fig. 2.15 shows the schematic representation of the surface liquid interaction in Wenzel and Cassie Baxter models. Wettability on the surface is regulated by the fraction of air trapped on the rough surface. When f_g tend towards '1' the surface becomes superhydrophobic. The wettability of the surface is influenced and can be tuned by adjusting the surface roughness. However, the change in both the surface morphology and chemistry need to be considered for nitrogen plasma ion implanted GNWs.

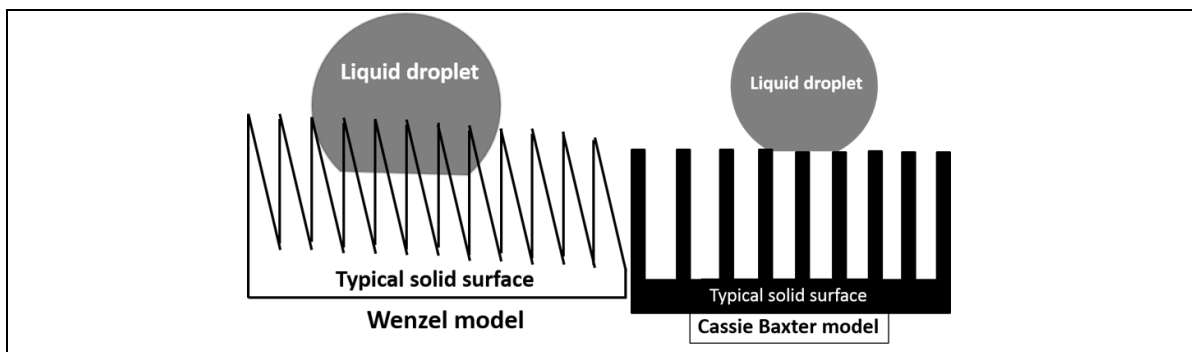


Fig. 2.15 Schematic representation of Wenzel and Cassie Baxter model of surface wetting due to variation in surface morphology.

2.2.11. Electrochemical studies

In electrochemistry, the loss of electrons (oxidation) or gain of electrons (reduction) that a material undergoes during the electrical stimulation is studied. The reduction and oxidation (redox) reactions at the electrodes can provide information on the concentration, kinetics, reaction mechanisms, chemical status and other behaviour of species specific to the nature of the electrodes in solution.

In an electrochemical experiment, four parameters are measured – potential (E), current (i), charge (Q) and time (t). Each of the above parameter can be selected to study the response of a system towards studying a targeted response. For example, for a planar and highly corrugated GNWs like electrode the frequency response will be different due to the inability of the ions to diffuse fast according to the change in the applied electric field. Hence, the frequency response can provide information on the morphology of the electrode along with other aspects. In most electrochemical techniques, three electrode configuration is used, viz. the working electrode, the reference electrode and the counter electrode.

Working electrode is the electrode where the test electrode is connected. The potential of the working electrode is measured with respect to the reference electrode. A reference electrode is a familiar saturated calomel electrode such as Ag/AgCl electrode. The idea of reference electrode is to measure the potential at the working electrode without the influence of chemical reactions taking place in the counter electrode, though counter electrodes are inert metals like Pt. In electrochemical system the current flows in the solution between the working and counter electrode. The three electrodes are connected to a potentiostat, an instrument which controls the potential of the working electrode and measures the resulting current. In one typical electrochemical experiment, a potential is applied to the working electrode and the resulting current measured then plotted versus time. In another, the potential is varied and the resulting current is plotted versus the applied potential. Different combinations of parameters and working electrode types make for a long list of techniques, including cyclic voltammetry, charge-discharge, etc.

Cyclic Voltammetry

Cyclic voltammetry (CV) is one of the most commonly used electro analytical techniques used to study electrochemical response of the electrode –electrolyte system to voltage/current/frequency, etc. In a typical CV experiment, the potentiostat applies a potential ramp to the working electrode to gradually change potential and then reverses the scan, returning to the initial potential, corresponding current is measured by the same potentiostat. These values are then used to plot the CV graph of current versus the applied potential. Usually, multiple CV experiments are performed to stabilize the system before making actual measurements and in the measurements also average of several cycles for a set of parameters are taken.

Fig. 2.16 shows the typical CV plot for both as US and IUPAC conventions. In IUPAC convention, left of zero is negative and right is positive in X-axis (voltage) and similarly, above zero is positive and below zero is negative for Y-axis (Current). Fig. 2.17 shows the voltammogram in American (US) convention. From the CV four important pieces of information is obtained – the cathodic peak height (ipc), the anodic peak height (ipa), the cathodic peak potential (E_{pc}) and the anodic peak potential (E_{pa}) (Fig. 2.17). Practically, the voltage sweeps start from zero to a positive value (0.7V) and after reaching the maximum value, the sweep immediately reverses for discharge. It probe a species in forward scan and test its response in the reverse scan in the specified scan rate. In perfect reversible reaction $ipc = ipa$. With increasing the scan rate ipc will not be equal to ipa , a non –reversible case.

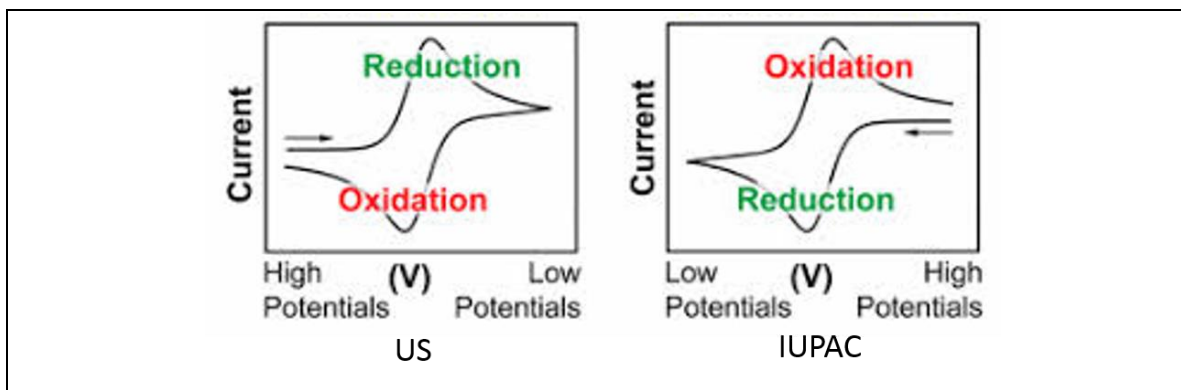


Fig. 2.16 Theoretical cyclic voltammogram of a reversible electrochemical reaction. The US convention is shown at the left and IUPAC convention is at the right [219]. In India, IUPAC convention is followed.

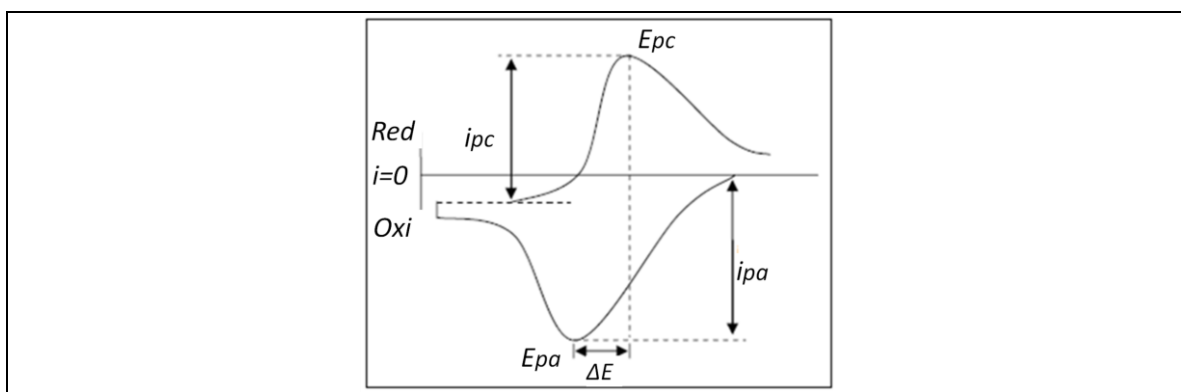


Fig. 2.17 Theoretical voltammogram showing the respective current and voltage values.

The same is true of other variables also. If the experiment induce a change of concentration during experiment or use of another electrolyte also affect the results of the experiment. Hence, the experiment is specific to particular set of gadget and conditions. The cyclic voltammogram can be used for the determination of several important electrochemical parameters such as diffusion coefficient, number of electrons, potentials, rate constants and reaction mechanism. However, such a detailed study is not in the scope of this thesis

The electrochemical performance of electrochemical capacitors can be evaluated using the applied voltage and current response. The super capacitive properties of the as-prepared GNWs and the N-doped GNWs were investigated using an electrochemical workstation (Metrohm-Autolab: PGSTAT302N). The studies were conducted in a three-electrode mode to monitor both current and potential of the given system. Three electrode system is used to keep an independent reference electrode to measure variation of voltage in the working electrode. Though several acidic (HCl, H₂SO₄, etc.) or basic (NaOH,

Na₂CO₃, etc.) electrolytes can be used, KOH is selected as the electrolyte for the present study. The concentration is selected as 1 M to have optimum density of ions. In this work, the GNWs grown over the carbon paper were used as the working electrode. Electrical contacts were made using the crocodile clips and the circuit was connected to the electrochemical workstation. No additional current collector was used in the process. Pt foil (1 x 0.5 cm²) was used as the counter electrode and Ag/AgCl was used as the reference electrode. Though the scan rate can be in millivolts to volts range, the applied potential should not cross the dissociation potential of the electrolyte. Hence, the cyclic voltammogram (CV) was conducted in more common scan rates between 100 and 500 mV/s. Likewise, the charge-discharge cycles were conducted at different current densities in the potential window of 0.4 V. Because, beyond this range there is oxidation – reduction peaks pop up in the CV. The areal specific capacitance (C_s in F/cm²) of the electrode /electrolyte systems are deduced from the equation: $C_s = \frac{\int IdV}{s.A.\Delta V}$ where ‘ $\int IdV$ ’ is the area enclosed by the CV loop, ‘s’ is the scan rate, ‘A’ is the electrode area exposed to the electrolyte and ‘ ΔV ’ is the potential window.

Charge –discharge studies

The same electro-chemical system used for CV study is used for charge-discharge studies also. Galvanostatic charge/discharge (GCD) is a traditional method to evaluate a series of SC performance parameters, such as capacitance, energy density, power density, ESR, and cycle stability. The GCD process follows the responsive potential relative to time and calculates information associated with the occurrence of electrochemical phenomenon’s occurrence in the SC electrode material. The overall GCD measurement process involves two steps: first, the SC charges via a constant current, and second, it is discharged in a specific time or voltage range. The following equations are used to obtain the charge storage properties of the electrodes.

$$C = \frac{i\Delta V}{\Delta t} \quad \text{Eq. 2-18}$$

$$E = \frac{C\Delta V}{2} \quad \text{Eq. 2-19}$$

$$P = \frac{E}{\Delta t} \quad \text{Eq. 2-20}$$

Where C denotes the specific capacitance and Δt and ΔV are the discharging time and applied voltage, respectively. E-energy density and P-power density also can be

deduced. Moreover, volumetric specific capacitance and areal capacitance are also used to evaluate the performance of the supercapacitor. The areal capacitance (F/cm^2) can be calculated by dividing capacitance of the electrode with area of the working electrode [220]. The energy efficiency (η) of the electrode -electrolyte system is calculated using the equation $\eta = \frac{t_D}{t_C} \times 100$, where t_D and t_C are discharging and charging time to elucidate GNWs application as supercapacitor electrodes. Depending on the material – electrolyte combination the charging and discharging time varies. The non-linear charging profile and asymmetric voltage-time response indicate the formation of strong electric double layer (EDL) in between the electrolyte and electrode. Additionally, the cyclic stability study gives an idea about the stability of electrode –electrolyte system.

2.3. Summary

In this chapter, the experimental methods for synthesis and characterisation is explained. The samples are synthesised using PECVD and PIII techniques. Electron microscopy based techniques are explained giving more emphasis on EELS. Raman spectroscopy, FTIR spectroscopy, secondary ion mass spectroscopy, X-ray photo electron spectroscopy, atomic force acoustic microscopy and water contact angle measurements are explained. Where ever required, necessary software used also mentioned. For the electrochemical studies, basic characterisation techniques such as cyclic-voltammetry and charge –discharge method are briefly described. Other electrochemical studies required for supercapacitor studies are omitted due to impropriety to the main topic discussed.

Chapter 3

Facility benchmarking

3.1. Introduction

Historically, the Plasma Immersion Ion Implantation and Deposition (PIII&D) system was developed towards surface modification of materials for metallurgical or mechanical applications. Surface of materials is modified by implantation of suitable ions ($N_2/C/O_2$) or deposition (PECVD/PVD) of thin films. However, the implanted layer or PVD/PECVD deposited films are usually very thin, unless the process is carried out with special provisions such as temperature above $0.3 T_m$ to facilitate diffusion, or prolonged deposition. Hence, the technical advantage of using PIII&D over other plasma modification techniques (e.g. plasma nitriding) for materials processing that demand several micrometers thick modified layer is not very attractive. However, there are several applications which benefit from the combined advantage of surface coverage of plasma and shallow modification by implantation with ion of choice. There are such applications in the domain of nanomaterials and nanostructures.

PIII&D is a custom made facility. Hence, it is essential to evaluate the performance of PECVD, PVD and PIII aspects to understand the working parameters and processes. Each of the above techniques are used in the present study after several trial experiments. However, only a few experiments used for benchmarking the performance of PIII&D system for GNWs deposition and nitrogen implantation are discussed. Though general methods and synthesis aspects of GNWs by PECVD have been discussed in the literature, data on ion implantation are scarce. Hence, there is a need to study the specific operational aspects. In the present study, the PIII&D system is utilised for the synthesis (using PECVD) and nitrogen implantation (using PIII) of GNWs. Implantation involves RF plasma generation and acceleration of ions by pulsed dc bias; in which, plasma generation is common to both PIII & PECVD. In addition, the physical vapour deposition feature (Magnetron sputtering) is used for depositing the Zr thin films at ambient temperature. The Zr thin films are N^+ and N_2^+ ion implanted using particle accelerator to study the variation in profile due to atomicity of ions.

PIII&D processes are used for metallurgical and electronic applications. A bias voltage of several 10s of kV is used for surface modification in metallurgical applications; whereas, low voltages (<10 kV) is sufficient to make shallow junctions for electronic

applications. It is conventionally considered that a bias voltage of 10 kV forms the boundary between the two [221]. Hence, the implantation experiments were conducted at 10 kV. Additionally, 10 kV bias provides a reasonable range for the ions to be probed by analytical tools like SIMS without the interference of surface oxide layer in actual range estimation.

There are reports in literature that the nitrogen ion energy calculated based on the depth profile of nitrogen implanted in Si using plasma based ion implantation is relatively low compared to the nitrogen energy calculated based on the voltage applied during processing [222]. Though RF power is used in this experiment, no mention has been made about the power used. Hence, it is difficult to understand the cause for such a behaviour. It is assumed that when the applied RF power is low, most of the ions in the plasma is N_2^+ . Hence, the energy evaluation of the ions (assuming N^+) based on the applied voltage will be erroneous. Hence, it becomes necessary to conduct experiments at low plasma power and at high plasma power to obtain better understanding of the atomicity of ions implanted in the process.

One of the basic advantage of PIII process is the large through put as compared to accelerator based implantation. Hence, the benchmarking experiments envisage long duration and short duration experiments also to know the effects of high and low dose. In this chapter, the studies on nitrogen ion implanted samples using SRIM simulation, SIMS and XPS are only presented.

3.2. Nitrogen plasma ion implantation of Titanium

Metallographically polished (250 nm) ultra-high (99.9%) pure Ti samples are mounted on the sample holder inside the chamber and biased using a pulsed dc at (-) 10.5 kV (Pulse width - 45 μ s, Frequency-100 Hz) and nitrogen ion implantation was carried out for 45 and 90 minutes using the PIII system. These specimens are named as S1 (45 minutes) and S2 (90 minutes). Fig. 3.1 shows the typical pulse generated in the bias system for 45 μ s. The schematic of the PIII process is given in Fig. 2.5. Prior to the above experiment, several surface cleaning procedures were carried out on test samples. At $\sim 8 \times 10^{-3}$ mbar pressure, high pure nitrogen (99.96%) plasma is struck at a forward RF power of 75W (a reflected power of 45 W was observed). The high value of reflected power further emphasises the need for preliminary studies. The voltage and current output from the pulsed dc source are monitored using a digital oscilloscope (Agilent DSO 5012A) to keep control over the ionic current (Fig. 3.1). From the ionic pulse current and duration, the

dose for 45 and 90-minutes implantation was estimated as $\sim 0.6 \times 10^{17}/\text{cm}^2$ (for S1) and $\sim 1.2 \times 10^{17}/\text{cm}^2$ (for S2), respectively. The basic idea of high dose implantation is to ensure TiN formation. The golden colour of TiN provides a direct visual evidence for Ti to TiN conversion immediately.

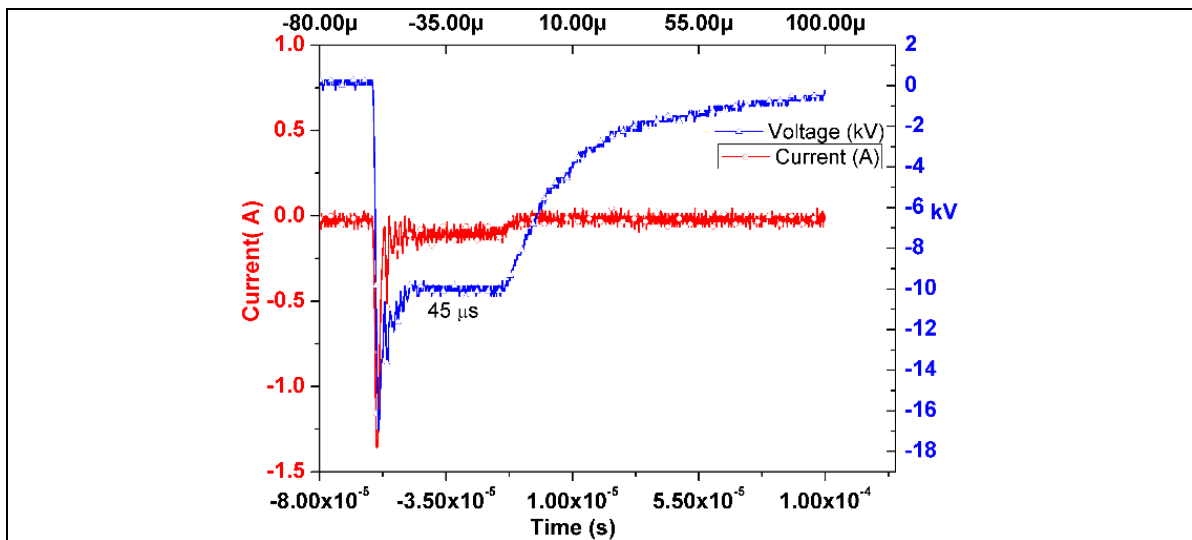


Fig. 3.1 The oscilloscope out put of a single pulse of the high voltage pulsed dc modulator at 10 kV, 0.1 KHz, 45 μs pulse width. The pulse is stabilised within a few microseconds.

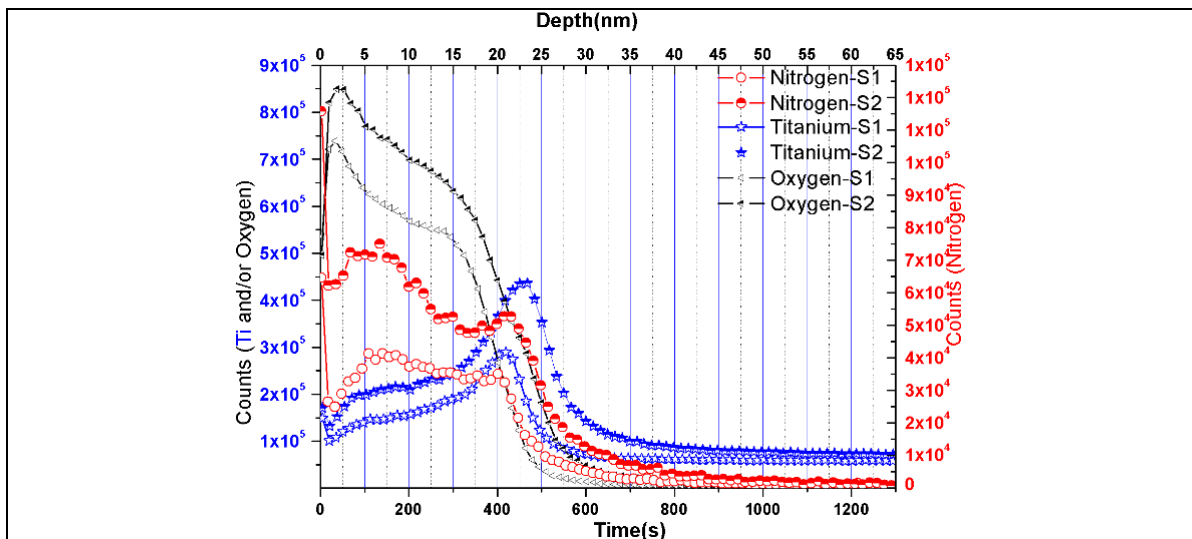


Fig. 3.2 SIMS profile of nitrogen plasma ion implanted titanium. The figure shows bimodal distribution of nitrogen and the intensity is high at low depth due to large fraction of N_2^+ ions in the plasma.

The specimens S1 and S2 were analysed using Cameca ims4f-Secondary Ion Mass Spectrometer (SIMS) to get depth profile of composition. First, mass spectra of these specimens were acquired in the mass range of 1 amu to 500 amu. By analyzing the mass spectra, the most intense Cs complex species ejected from the specimens were identified to

be, NCs, OCs, TiCs, TiNCs, TiOCs, TiO₂Cs, NCs₂, OCs₂, TiCs₂, TiNCs₂, TiOCs₂ and TiO₂Cs₂ [215,223]. However, the intensities of elemental clusters, which are contributed by all the isotopes, are required for quantitative analysis. The intensity of an elemental cluster is achieved by dividing the intensity of the acquired isotopic cluster by the natural isotopic abundance of that cluster. This correction was applied to the intensities of all the acquired cesium complex species. The number of atoms in each of Ti, N and O cesium complex species were added together to get the individual depth profile. The sputtering time was calibrated to sputtered depth by using a Dektak surface profilometer, model 6M. The methodology used for the quantification of SIMS data is further detailed in section 2.6.

The SIMS profile of the samples are shown in Fig. 3.2. Barring the surface peaks, bimodal distribution of nitrogen across the thickness is observed. This shows implantation of N⁺ ions and N₂⁺ ions. N₂⁺ ions with given energy upon entering the target split into two atoms with shared energies and have a lower range than those of N⁺ ions implanted with the same energy. The implantation behaviour of N⁺ and N₂⁺ ions is simulated using SRIM (Fig. 3.3) and compared with the SIMS data. SRIM simulations show that N⁺ and N₂⁺ ion implantations with 10.5 keV energy cause nitrogen peaks at ~25 nm depth and at 12 nm depth respectively. High intensity nitrogen peak is observed at a low depth. This indicates that the deposition of larger number of N₂⁺ ions/species compared to N⁺ ions. The peak range of N⁺ ions (SIMS data) falls almost in line with SRIM simulated value. The dose calculated from the SIMS profile for 90 min. implanted sample is approximately 1.8 times higher than that of 45 min. (Fig. 3.2). This value is in good agreement with the expected outcome because surface sputter removal of materials can reduce the amount of nitrogen. It should be noted that in the present experiment the actual power used for the production of RF plasma is ~30 W only.

In plasma ion implantation process the pulse *rise and fall* time (varying bias) of the biasing supply is important to obtain mono energetic ions. It has been followed that the pulse rise and fall time should be below 500 ns to impart similar electrostatic force on each ions [224,225]. This is an important criterion for semi-conductor application where the layer thickness is very important. However, when the biasing voltage reduces the influence of pulse rise /fall time on the thickness of the modified layer decreases. A larger pulse rise/fall time causes a broader peak. However, the effect is not seen very significant at this energy range and the bimodal peak behaviour is representative to largely mono energetic (N⁺ and N₂⁺) ion implantation. This indicate that the conditions (bias, vacuum and duration) for the plasma ion implantation are nearly ideal and suitable for ion implantations.

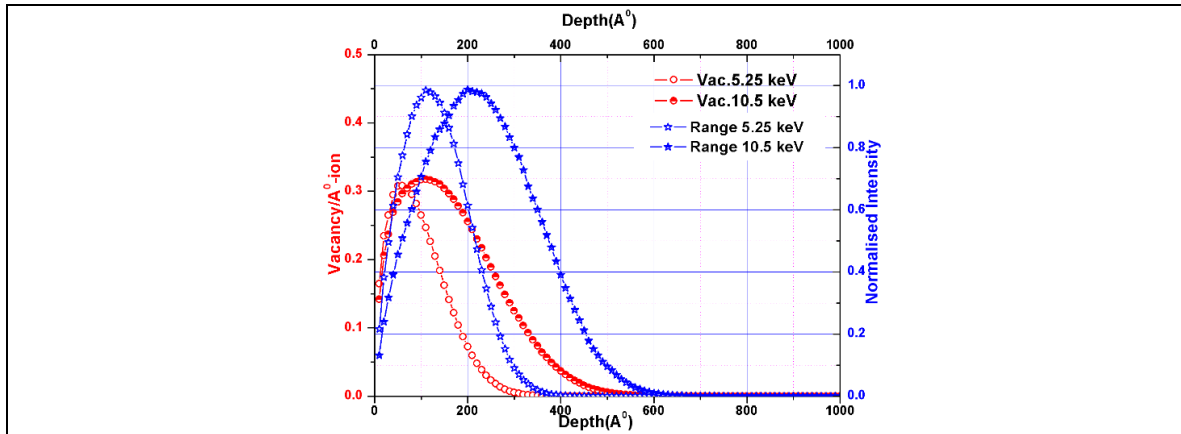


Fig. 3.3 SRIM simulation of nitrogen ions in titanium. The energy 10.5 k eV represent N^+ ions; whereas, 5.25 k eV represent N_2^+ ions. The vacancy peak of N^+ ions falls in the range peak of N_2^+ ions.

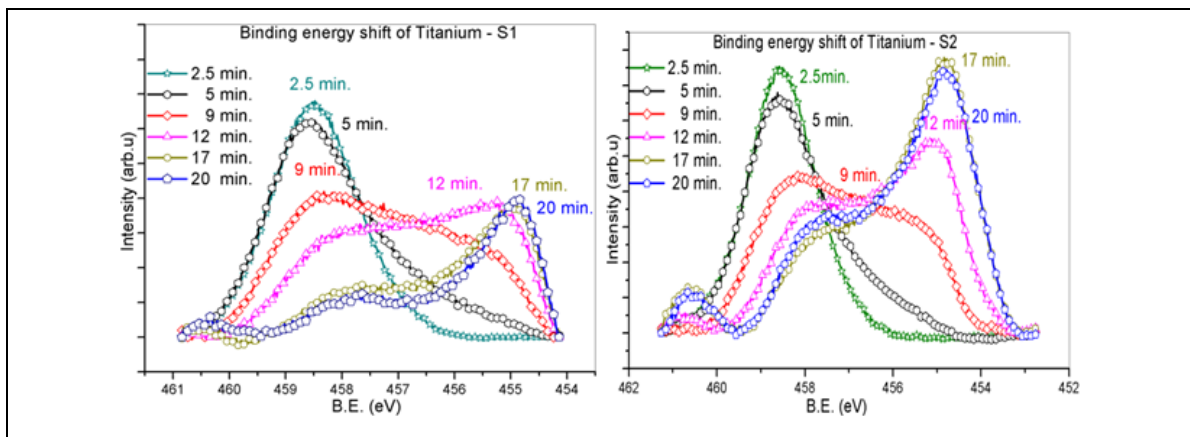


Fig. 3.4 Depth resolved XPS data of ion implanted titanium. The binding energy shift in $2P^{3/2}$ bonding state of titanium from higher energy (TiO_2) to lower energy (TiN) with corresponding time in minute is shown. (a) for sample S1 (45 minutes) and (b) for sample S2 (90 minutes).

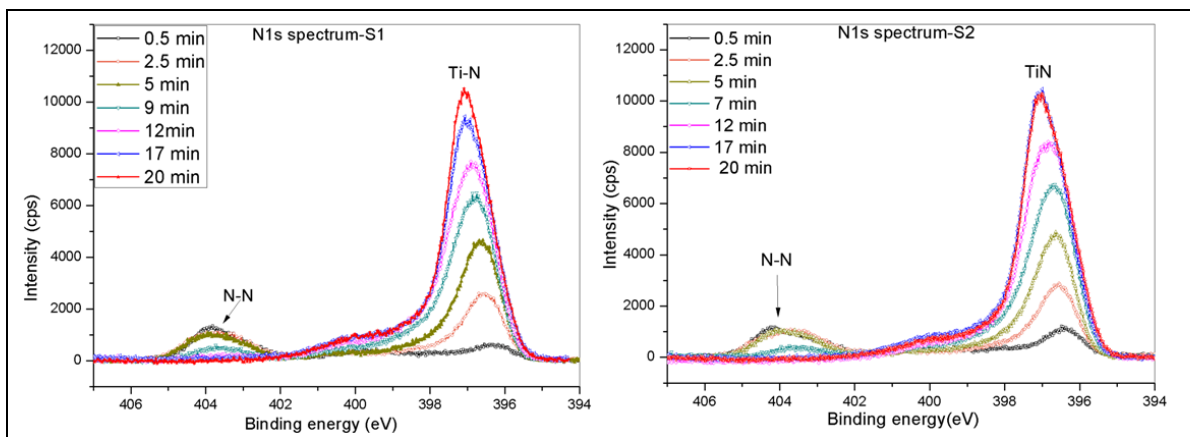


Fig. 3.5 XPS data of S1 and S2 after 0.5 minute to 20 minute of surface sputtering. The binding energy corresponding to N1s bonding state of nitrogen at 403.7 eV shows N-N bonding and 397.2 eV shows Ti-N bonding.

Nitrogen is likely to form different compounds at different depths. Because, N^+ ions are chemically more reactive than N_2^+ ions. Using depth resolved XPS studies the chemical state of nitrogen in Ti is revealed. Depth resolved XPS analysis is carried out by sputtering the specimens (S1 and S2) to various depths. The survey spectrum is obtained through Ti 2p, N 1s, and O 1s at different sputter depths. However, detailed analysis is done only on Ti 2p_{3/2} and N 1s, energy states. Fig. 3.4 shows the formation of different chemical species containing titanium, nitrogen and oxygen. At the depths of initial 1 minute sputtering (data not shown) and 2.5 minute sputtering, the Ti 2p_{3/2} peak at 458.5 eV, corresponding to Ti in TiO₂, is predominant. Further, the energy range, 453 eV to 460 eV, covers 2p_{3/2} energy states of Ti in different phases with oxygen and nitrogen. Hence, at depths corresponding to 2.5, 5, 9, 12, 17, and 20-minutes of sputtering, the state of Ti is found to be transforming from TiO₂ through Ti₂O₃ and TiO_xN_y to TiN. The peak intensity corresponding to TiN increases with sputter duration. This is due to increasing intensity of nitrogen inside Ti due to implantation. It shows that N^+ ions are inducing the Ti to TiN conversion more effectively. The reaction kinetics of N^+ and N_2^+ ions differ, N^+ reacts more vigorously to form respective nitrogen compounds whereas the reaction of N_2^+ ions occur with neutralization without the N-N bond breakage [226]. Depth resolved variation in N 1s profile of both S1 and S2 is shown in Fig. 3.5. The peaks at around 403.7 eV, 400 eV and 397.2 eV indicate nitrogen in the bonding state as N-N, N-O-Ti and N-Ti respectively [227]. The 403.7eV peak is prominent up to 9 minutes of sputter removal. This indicates that nitrogen is attached at the surface in molecular form up to ~9 nm (1nm/min.) depth. As discussed before, SIMS data also indicate relatively larger amount of nitrogen at lower depths (Fig. 3.2). SRIM simulation shows that the vacancy peak of N^+ ions falls in the range peak of N_2^+ ions (Fig. 3.3). This indicates the possibility of some molecular nitrogen getting trapped in the vacancies at lower energies.

It is concluded that in PIII experiments using nitrogen plasma at low power, both N^+ and N_2^+ ions are implanted and some amount of nitrogen remains in Ti in its molecular form whereas a certain fraction of nitrogen ions induces Ti to TiN conversion. The TiN formation is largely attributed to N^+ ions, whereas the molecular form is mainly attributed to N_2^+ ions.

3.3. Nitrogen plasma ion implantation of Silicon

In the previous study of nitrogen plasma ion implantation on Ti, the plasma is generated at a low (25 W) power. It is found that the major ions in the plasma are N_2^+ ions.

Additionally, the samples were implanted for long duration to induce the chemical changes. For long duration implantation, the metallographic surface finish of the sample is sufficient because a considerable thickness of the surface will be sputter removed during the process. However, if the duration of implantation is low (to reduce the sputter removal and damage) the surface finish should be good enough to evaluate the surface properties to a few nm. Hence, for low dose implantation studies the sample surface finish should be high (a few nm). Hence, mirror polished samples such as electronic grade silicon wafer is required. Additionally, silicon is a well-studied material and hence it will be easy for further analysis. Hence, silicon wafer is selected for low dose implantation studies. In the present study, the silicon wafer is subjected to nitrogen plasma implantation at 10 kV (45 μ s and 0.1 kHz) bias for 2, 5, 10, 20 and 30 minutes. An RF power of 100 W was employed for the generation of plasma. In addition to the above, one more sample is prepared after plasma exposure (no bias) for just 2 minutes. This is to understand the effect of plasma stabilization time on the implantation. Fig. 3.6 shows the SIMS profile of nitrogen ion implanted Si. SIMS measurements were carried out using M/s CAMECA make IMS 7f instrument. First, a mass spectrum in the mass range of 1 amu to 500 amu was acquired from around the depth range containing the nitrogen implantation peak. The following twenty five species were identified as the most abundant ones constituting the mass spectrum: NCs, AlCs, SiCs, SiHCs, SiNCs, SiOCs, SiOHCs, CrCs, FeCs, Si₂Cs, NCs₂, OCs₂, OHCs₂, FCs₂, CNCs₂, SiCs₂, SiHCs₂, NOCs₂, ClCs₂, SiNCs₂, SiOCs₂, Si₂Cs₂, Si₂HCs₂, Si₂PCs₂, Si₂O₂Cs₂ [215].

The depth profiles of the mono isotopic species of these clusters were acquired from a pristine silicon sample. The silicon specimens implanted using PIII technique for different doses were sputtered using Cs⁺ as the primary ions at 5.5keV with a beam current of 5nA. The primary ion beam was rastered over a square area of width 200 μ m and secondary ions were collected from a circular area of 62 μ m diameter centered at the middle of the sputtered area. The secondary ions selected by the double focusing mass analyser were detected using the electron multiplier. The depth profiles of the individual elements were computed [215]. The intensity vs. sputtering time profile was converted into depth profile by measuring the depth of the crater created by sputtering. The crater depth was measured using a DEKTAK 6M stylus profilometer. (The SIMS quantification procedure is discussed in chapter 2). Similar to Ti implantation, two peaks corresponding to nitrogen species are observed in the Si samples implanted for more than 2 min. High intensity peak was observed at large depth for long duration implanted samples. This indicates that the implantation condition favour the deposition of N⁺ species. It has been found that, at 2 minutes of implantation, the

nitrogen concentration on the surface of Si is higher than that in the interior (indicated by an arrow mark in Fig. 3.6). The native oxide on Si is removed only after some 5 minutes and there after a steady increase in intensity of nitrogen is observed. This information along with the process parameters were taken as directive for the low dose (<5 at %) implantation studies of GNWs. The study shows that with increasing implantation duration, the peak shape matches with SRIM profile for mono energetic ion implantation. However, a peak for N_2^+ ions can be fitted at lower energies (not shown). This indicates that under high power plasma generating conditions, the ions implanted are largely N^+ ions and the surface concentration of N ions is higher than the interior at some low implantation durations such as 2 minute. In the two previous experiments, it is seen that both N^+ and N_2^+ ions are implanted. Hence, there is a requirements to know how the N^+ and N_2^+ ions behaviour under identical energy conditions. Towards further analyzing the effect of N^+ and N_2^+ ions, separate implantation experiments were carried out using particle accelerator and are discussed in the next section.

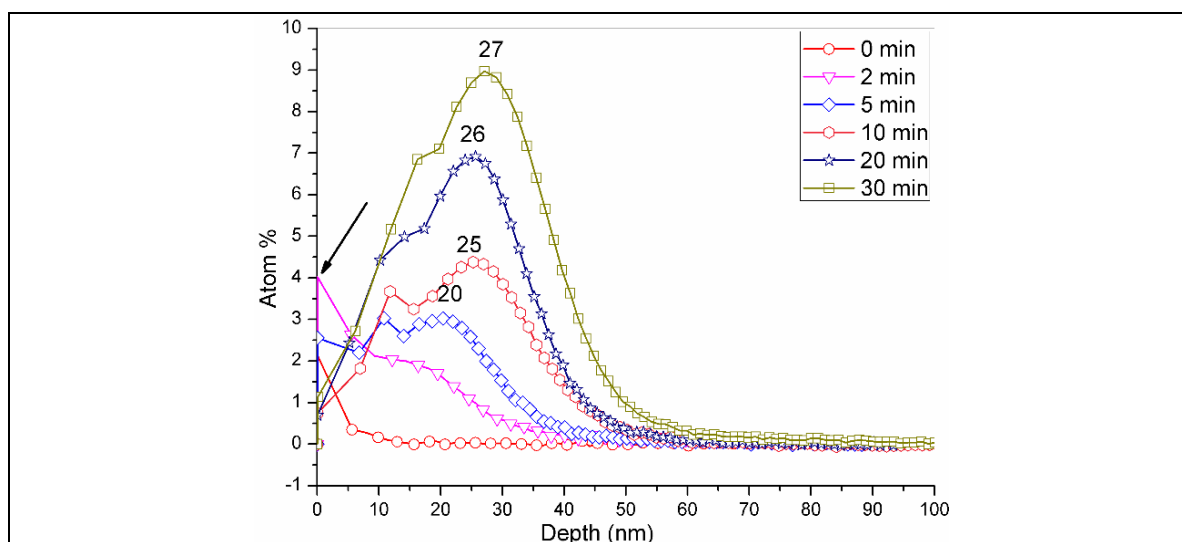


Fig. 3.6 SIMS profile of silicon wafer implanted at 10kV using nitrogen plasma upto 30 minutes. Highest surface nitrogen is observed at 2 min. implanted sample.

3.4. Nitrogen ion implantation of Zirconium thin films

The N^+ and N_2^+ ions are involved in the plasma ion implantation process and its profile, range and interactions need not be similar. Hence, N^+ and N_2^+ ion implantation was carried out using particle accelerator on magnetron sputter deposited Zr thin films (> 500 nm). The Zr thin films are deposited on Si wafer under ambient temperature and is expected to have large amount of point defects. Hence, the profile developed in the thin films will provide

better understanding on the conditions to be used for the modification of defective materials such as GNWs. The defective nature of the thin film cause lower density and hence, it will give higher range for ions in comparison to SRIM simulation. The N^+ and N_2^+ ion implantation were carried out with 10 keV and 20 keV energies, respectively. If identical energy is selected for both the ions, the N_2^+ ions will have half the energy per atom. Consequently, the range also will be half. At half the range the local environment may be different and hence comparing the ion distribution of N^+ and N_2^+ will be erroneous. Hence, the energy per atom is made equal for both N^+ and N_2^+ ions.

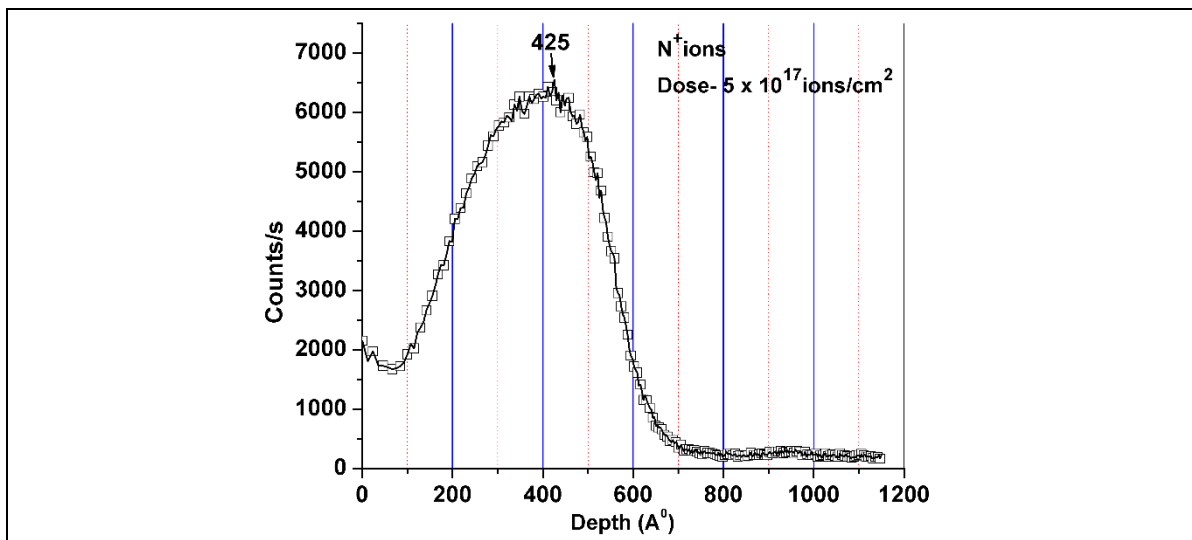


Fig. 3.7 SIMS data of Zr thin film samples. N^+ ions are implanted using particle accelerator. The peak shape is similar to SRIM simulated data as shown in Fig. 3.3. The range is almost double that of SRIM simulation.

The ion dose on Zr thin film is 5.0×10^{17} ions/cm² for N^+ , 3.5×10^{17} ions/cm² and 7.0×10^{17} ions/cm² for N_2^+ ions. The energy and dose values for implantation are chosen to such high values to induce notable changes in the behaviour of N^+ and N_2^+ ions upon implantation. The effect of ions (N_2^+ or N^+) in the profile can be understood from the above experiment and the same shall be applied while choosing the plasma power for selecting the major ion species as molecular and atomic ions. Additionally, 10 kV provides a reasonably good depth for SIMS analysis. Fig. 3.7 and Fig. 3.8 show the SIMS data of N^+ and N_2^+ ions implanted samples. The N^+ ions shows only one peak, which is similar to the general understanding of ion implantation as well as SRIM simulation. However, for the N_2^+ ions two peaks have been observed. The first peak from the surface is due to N_2^+ ions whereas the second one should be due to N^+ ions. With increase in implantation dose both peak intensity is identical. Since both peaks have shifted towards depth with increasing dose, considerable surface sputtering would have taken place during implantation.

Considering the larger fraction of N_2^+ ions in the plasma and the range of N_2^+ ions almost coinciding with the peak defect region of N^+ ions, the possibility of nitrogen getting trapped in these defects and /or bubbles is higher. Hence, it is clear that if low energy is used more N_2^+ can be put in with less chemical change in the matrix and this can be used to generate intercalating nitrogen species in graphene nanomaterials. This aspect is studied in chapter 5. However, if the requirement is chemical reaction, the interaction should be with N^+ ions. Increasing plasma power can induce more ionisation with consequent increase in N^+ ion density [228]. Thus, the implantation conditions suitable for studying the effect of N^+ and N_2^+ ion implantation are deduced.

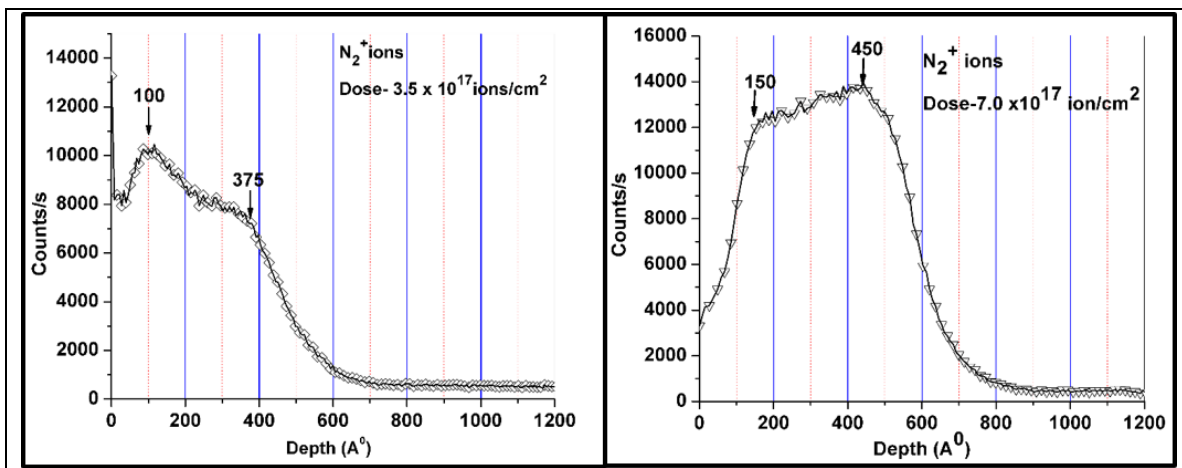


Fig. 3.8 SIMS data of Zr thin film samples. N_2^+ ion implanted using particle accelerator showing bi-modal distribution of ions. High dose implantation of N_2^+ ions gives a broad peak. The peak range is higher than SRIM simulated value as shown in Fig. 3.3.

3.5. Parameters derived for plasma ion implantation

In the present study considerable experience is gained in the operation of vacuum system, biasing unit, plasma generation and data logging of PIII&D system. With respect to the PIII&D system the following operating parameters have been arrived for ion implantation using nitrogen plasma.

- The ultimate vacuum : 8×10^{-6} mbar (DP vacuum)
- Plasma striking pressure (Ar): 1×10^{-1} to 5×10^{-2} mbar.
- Process gas pressure: 4.5×10^{-3} mbar
- RF plasma power: 25 W (N_2^+ ions-major), 100 W (N^+ ions-major)
- Bias: 10kV, 45 μ s, 0.1 kHz

3.6. Summary

The study aims at understanding the operation and working of the custom built PIII&D system. Operational experience on vacuum generation, plasma striking, and plasma ion implantation by applying bias have been gained. Further, ion implantation using nitrogen plasma is carried out on Ti and Si substrates at different conditions and the samples are studied using SIMS. Ti is implanted with nitrogen plasma and the samples are studied using SIMS and XPS. SIMS study shows the formation of two humps for N-PIII treated samples. Towards understanding the double peaked SIMS data, N^+ and N_2^+ ions are implanted on fresh samples using a particle accelerator separately. SIMS study has shown a single peak for N^+ ions and double peak for N_2^+ ions. Hence, it is confirmed that low plasma generating power and long process duration have caused larger N_2^+ ion implantation than N^+ ions. Depth resolved XPS is carried out on the plasma implanted Ti samples and it is found that the chemical change observed at larger depth is largely due to N^+ ions in the plasma. High plasma power, low duration plasma ion implantation at 10 kV have been carried out on Si samples. Higher plasma power has produced a SIMS peak more similar to N^+ ion implantations. It is found the 2 min implantation shows more surface nitrogen than the interior. The benchmarking experiments helped to understand the system towards selecting the operating parameters for shallow plasma ion implantation on GNWs for high dose and low dose.

Chapter 4

Effect of gas composition on PECVD synthesis of graphene nanowalls

This chapter describes the effect of H₂, Ar and CH₄ gases and its ratio on the formation of graphene nanowalls (VGNs or GNWs) in plasma enhanced chemical vapour deposition (PECVD) process. The aim is to arrive at the gas ratio that gives the highest deposition rate in the PECVD system and understand the influence of the gases and its ratio on the evolution of morphology and electronic structure.

4.1. Introduction

The PECVD feature of PIII&D facility is utilised for synthesis of vertical graphene nanowalls. PECVD offers uniform, conformal deposition over large area with the convenience of varying morphologies and structure by changing the process parameters. There are reports in literature works on the synthesis of GNWs using Ar-CH₄-H₂ gas mixture [25,229]. However, the process parameters vary with system to system. Additionally, the PECVD feature is a custom modification of the PIII&D system. Hence, experiments are required to standardize the deposition procedure of GNWs.

4.2. Synthesis of GNWs

The details of the PECVD system used for the synthesis of GNWs have already been discussed. The Ar:CH₄:H₂ (1:2:2) gas mixture (4.1×10^{-3} mbar) plasma is created at 100W RF power. GNWs are deposited on Si wafer placed on a substrate heater (850°C) immersed in the above plasma. Fig. 4.1 shows the surface and cross-sectional SEM images of GNWs. The corrugated nature and leaf like structure are typical morphological features of GNWs generating large surface area. The thickness of GNWs is ~70 nm for 30 minutes deposition.

Raman spectrum of the samples shows D, G, D', G', T+D, D+G peaks typical of GNWs and are deconvoluted (Fig. 4.2.). The peak position, FWHM and general quality parameters are given in the Fig. 4.2. The I_D/I_G ratio is a measure of defect and a value of 2.5 indicate that GNWs is highly defective (point, edge, etc.). The I_D/I_{D'} indicate type of defect and the value 13.7 indicate high density of sp³C type defects [230,231]. The I_{G'}/I_G indicate the graphene-like nature of GNWs, that monolayer graphene will have I_{G'}/I_G ratio

2 or more. It should be noted that intensity ratio analysis is based on the values reported in literature for monolayer graphene and the values shall be taken only as directive indicators.

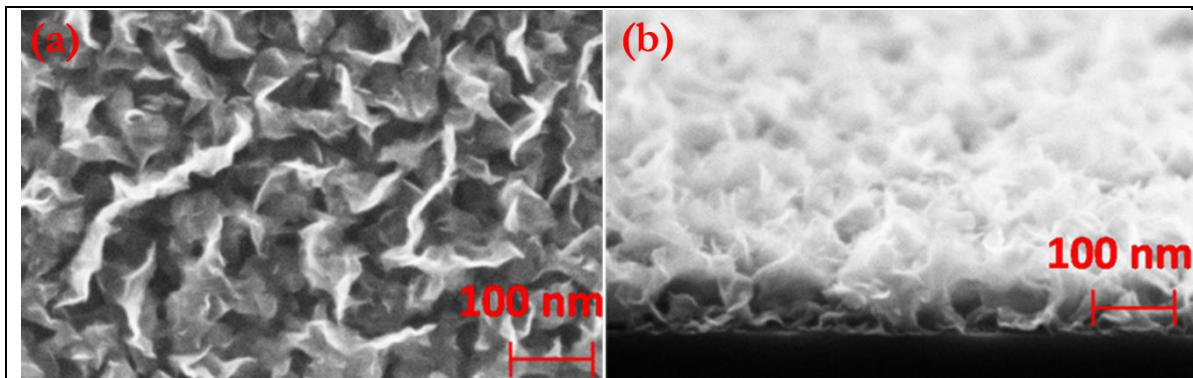


Fig. 4.1 SEM images of GNWs. (a) surface image, showing corrugated surface morphology. (b) Cross-sectional image, showing the vertical nature of growth.

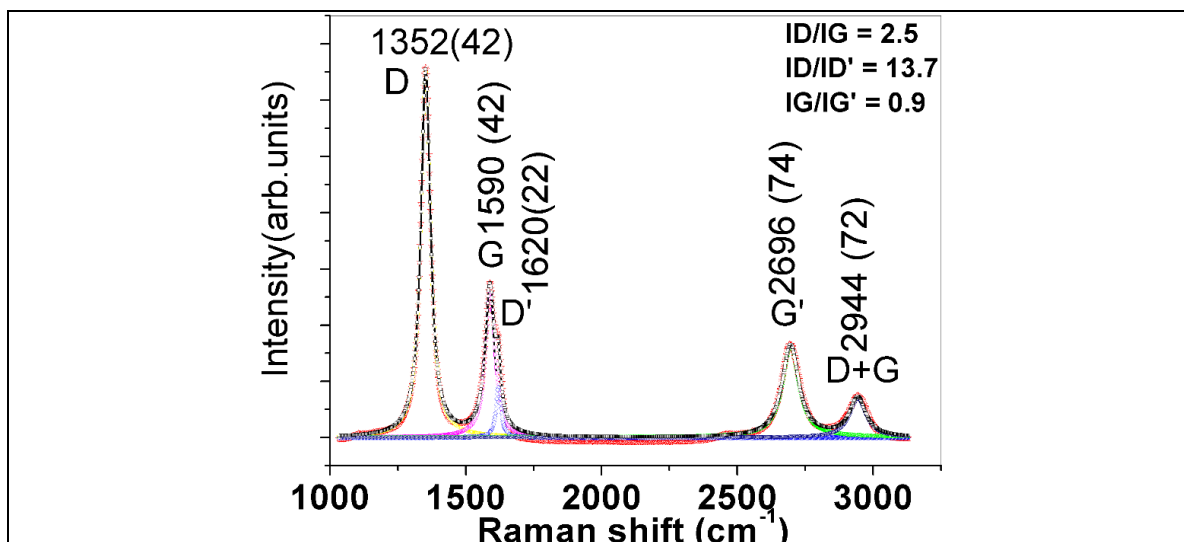


Fig. 4.2 Raman spectra of GNWs. General quality parameters are given at the right corner.

In the above gas mixture, three gases are used. The ionization of methane generates hydrogen as a by-product; which is also a constituent in the mixture. Hence, it becomes necessary to know the functionality of hydrogen in the above gas mixture. Both methane and hydrogen are explosive gases and minimizing the number of gases is good for both safety and synthesis optimization. This chapter is organised as; the results of influence of H_2 on synthesis of GNWs is discussed in the first part of this chapter, followed by the influence of Ar dilution of methane in the synthesis of GNWs by varying the Ar:CH₄ ratio.

A detailed description of deposition rate, morphological development and electronic nature are discussed in the second part.

4.2.1. PECVD of GNWs using Hydrogen–Methane gas mixture

The SEM image of GNWs deposited at different H₂:CH₄ process gas ratio is given in Fig. 4.3. The process conditions are given in Table 4.1.

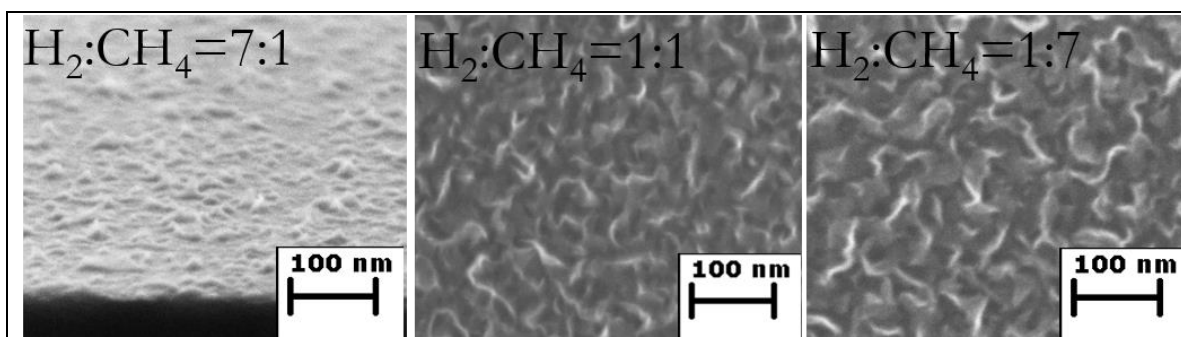


Fig. 4.3 SEM images of GNWs synthesised at different H₂:CH₄ ratios. At 7:1 ratio, a semi-cross sectional image is given to show the etch removal effect of hydrogen at higher concentrations. At 1:1 and 1:7 ratios, the morphology is identical. At 1:1 ratio, more dense GNWs are formed.

Table 4.1 Process parameters used GNWs synthesis using H₂-CH₄ mixture.

Gas composition (H ₂ :CH ₄)/ID	Forward Power (W)	Reflected Power (W)	Temperature (°C)	Process gas Pressure (mbar)	Duration
7:1(A1)	100	75	850	3.3×10 ⁻³	30 min.
1:1(A2)	100	75	850	3.3×10 ⁻³	30 min.
1:7(A3)	100	75	850	3.3×10 ⁻³	30 min.

Fig. 4.3 shows that for 1:7 and 1:1, H₂:CH₄ ratio; dense, uniform GNWs are deposited on the surface of Si wafers; whereas, with increase in hydrogen concentration (7:1) graphene walls are etched removed. This indicates that hydrogen need not be necessarily present in the gas mixture for the synthesis graphene nanowalls. However, use of pure methane as precursor gas caused large scale deposition of amorphous carbon on the walls of the chamber. The carbon deposited on cold surfaces are not conductive and such walls induce undesirable, unpredictable effects in the plasma behaviour. Hence, pure CH₄ as process gas is ruled out.

The Raman spectra of the (H₂-CH₄) samples are given in Fig. 4.4 to Fig. 4.7. For the samples 1:1 and 1:7, the Raman spectra shows similar features whereas for 7:1 sample,

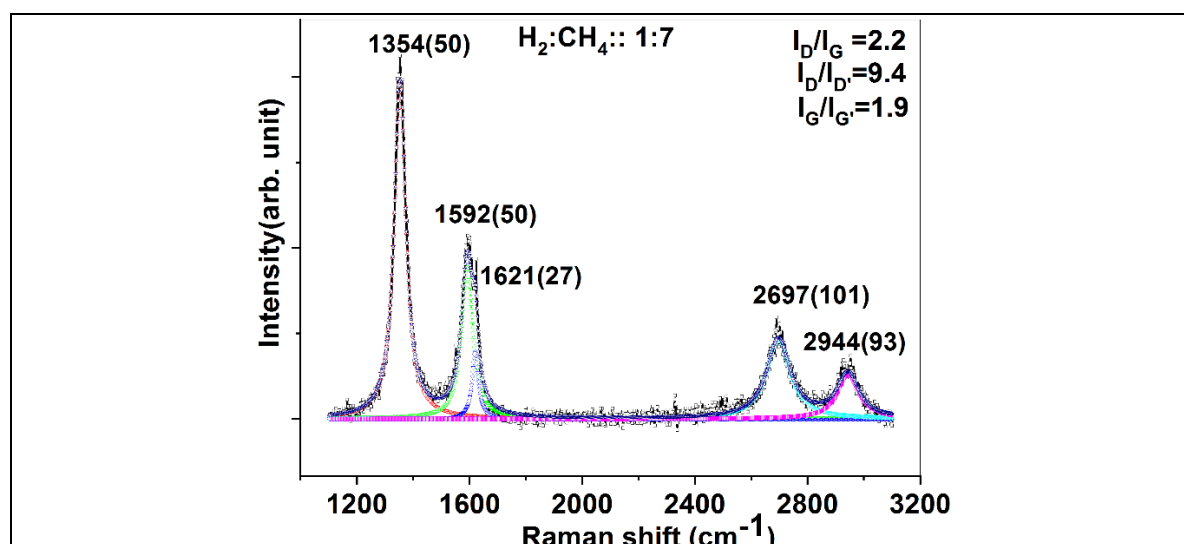


Fig. 4.4 Deconvoluted Raman spectrum of GNWs deposited at hydrogen to methane ratio 1:7. Peak positions and FWHM (in bracket) are given. General quality parameters are given at the right corner.

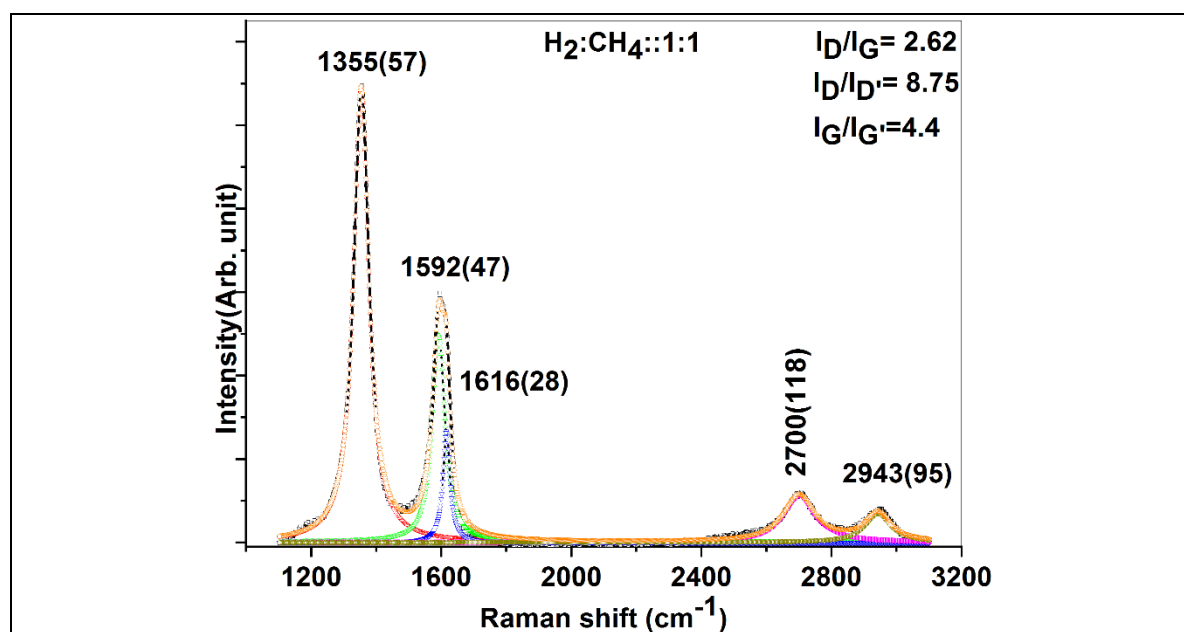


Fig. 4.5 Deconvoluted Raman spectrum of GNWs deposited at hydrogen to methane ratio 1:1. Peak positions and FWHM (in bracket) are given. General quality parameters are given at the right corner.

there is no D' shoulder band to the G band. It should be noted that the D' peak is missing and the FWHM of G' peak has increased for the $H_2:CH_4$ gas ratio, 7:1. The I_D/I_G , $I_D/I_{D'}$ and $I_G/I_{G'}$ ratios are given in the right corner of each gas ratio (figure). At 7:1 gas ratio, the

Raman spectra shows typical features of a few layer defective graphite and not a few layer graphene.

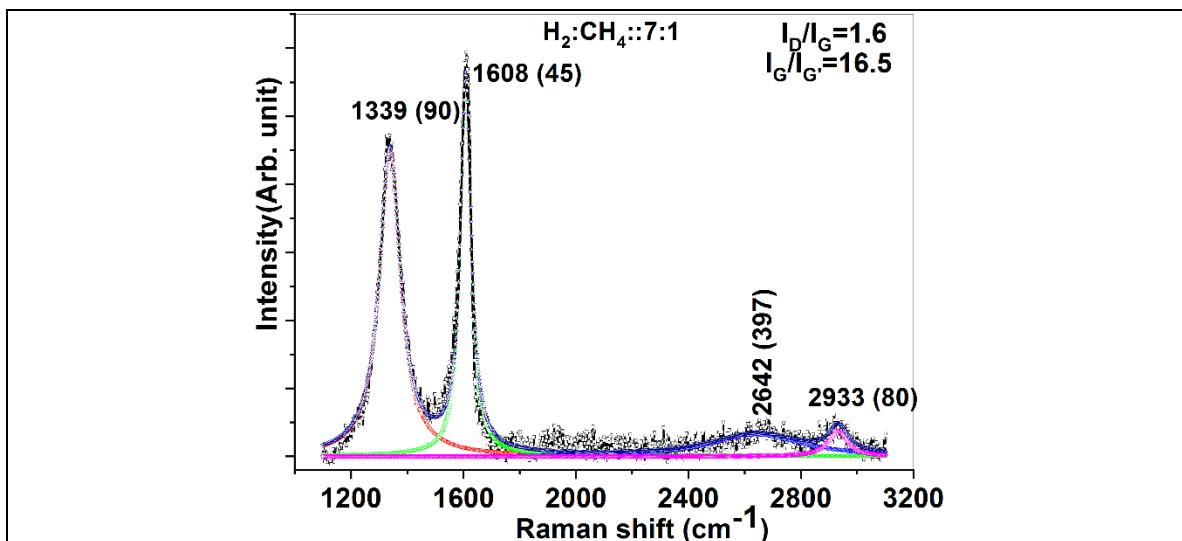


Fig. 4.6 Deconvoluted Raman spectrum of GNWs deposited at hydrogen to methane ratio 7:1. Peak positions and FWHM (in bracket) are given. General quality parameters are given at right corner.

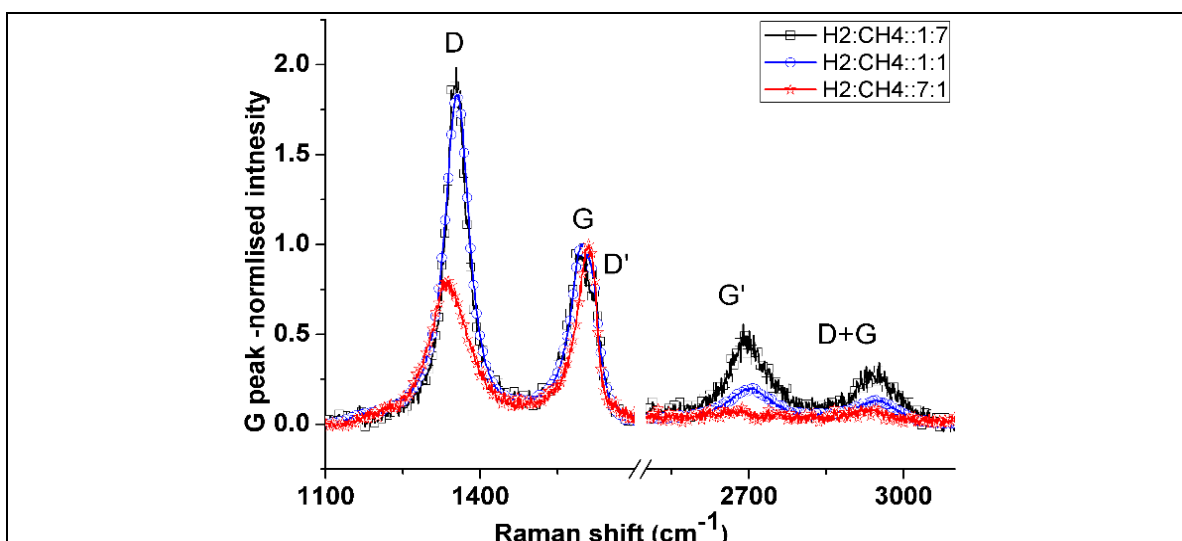


Fig. 4.7 The Raman spectrum is plotted after normalizing the G-peak intensity of all samples. With increase in hydrogen volume fraction, the graphite like nature is increasing and intensity of G' peak reduces.

This shows that increase in H_2 volume fraction promotes graphite like structure by etch removing the wall growth. Only stable graphite like structure stays in the sample. This aspect will be discussed further while discussing secondary growth in $\text{Ar}:\text{CH}_4$ mixture in the next section. The spectra after normalizing the G band are shown in Fig. 4.7, which

clearly shows that 7:1-H₂:CH₄ ratio-causes, lower intensity D band and G' band as compared to 1:1 and 1:7 ratios.

4.2.2. PECVD of GNWs using Argon–Methane gas mixture

A resistive heater with substrate holder was placed at approximately 60 mm away from the antenna. Graphene nanowalls (GNWs) were grown on pre-oxidised (≥ 300 nm thickness) Si<100> wafers at 800 °C. In general, argon rich composition promote higher growth rate and is being used for several applications. The GNWs growth with Ar:CH₄ ratios of 1:1, 3:1, 5:1 and 7:1 have been reported in literature [73]. However, studies involving higher CH₄ concentrations are not well reported in literature.

Additionally, the basic interest is to look into the driving factors behind particular morphology and electronic nature of GNWs. Hence, a detailed study using systematic variation of methane concentrations is carried out to delineate the effect of gas composition on morphology and structure. The GNWs are deposited by systematically varying the Ar-CH₄ ratio. The gas ratio are 7:1(S1), 5:1(S2), 3:1(S3), 1:1(S4), 1:3(S5), 1:5(S6), 1:7(S7) at 250W RF forward power is used for the deposition. The names of the specimens are given within parenthesis. After stopping the gas supply and plasma generation, the samples are annealed at same temperature for 1 hr. The samples were allowed to cool to ~ 100 °C in the same high vacuum (better than 1×10^{-5} mbar) conditions. The samples are taken out for examination at ambient conditions.

The SEM images show that all the Ar: CH₄ gas ratios induce the formation of GNWs of varying morphology (Fig. 4.8 and Fig. 4.9). The height of the GNWs deposited on Si wafer is measured from the cross sectional images using the inbuilt tool in the SEM. The cross sectional image analysis of GNWs indicate that the deposition rate is maximum at 3:1 Ar: CH₄ ratio (Fig. 4.10). Though determination deposition rate is an important aspect of the study; morphology and electronic nature are more fundamental properties required to be known for an application. The analysis of SEM images shows that with increasing CH₄ volume fraction, the secondary growth increases in GNWs, whereas increase in Argon fraction induce the reduction of secondary growth to have open channel morphology. This is an interesting observation since secondary growth provide more surface area and more number of active sites. Possible applications of the above aspects depend on the understanding of factors leading to secondary growth and the evolution of electronic nature in the respective GNWs. Looking at fundamental aspects, the change in

between the samples lies only on the gas composition. Since the change in morphology with gas composition is gradual and nearly uniform,

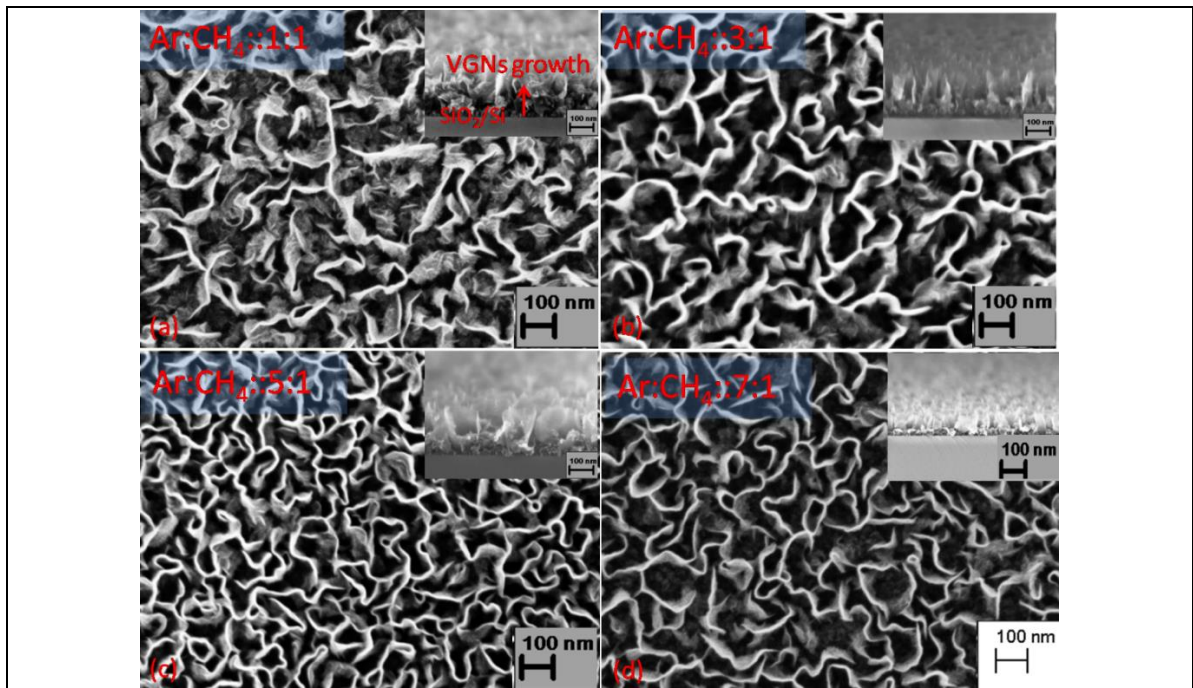


Fig. 4.8 SEM images of GNWs deposited at various Ar:CH₄ ratios. With increasing Ar volume fraction, secondary growth reduces.

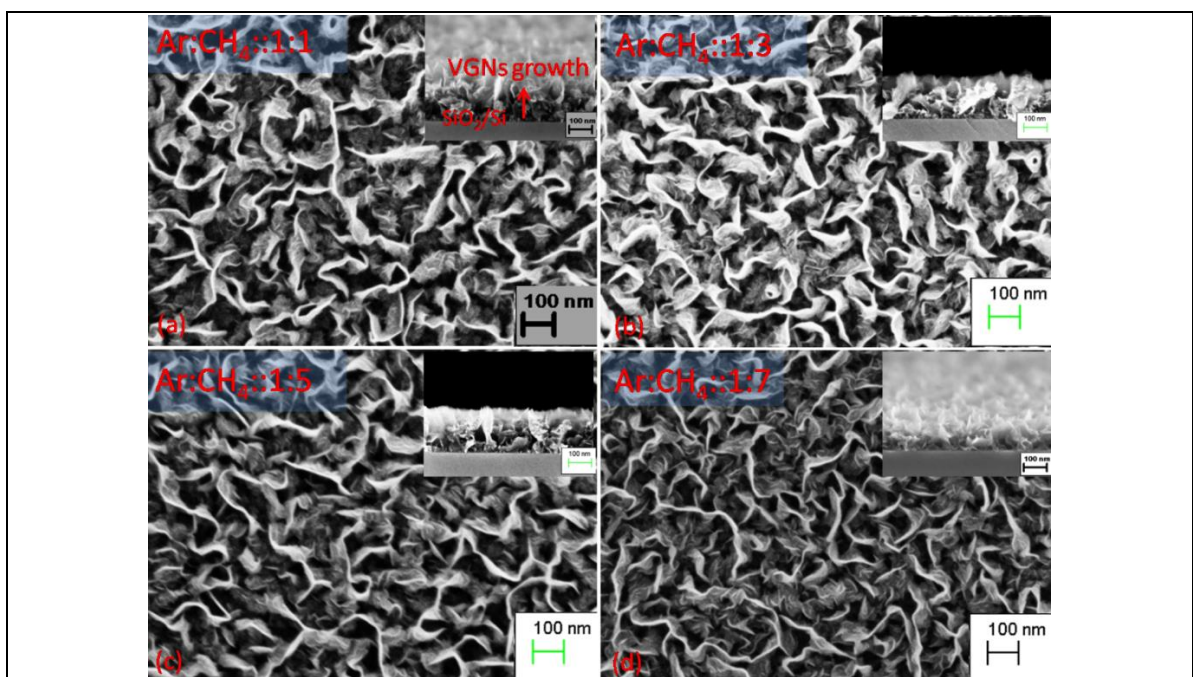


Fig. 4.9 SEM images of GNWs showing variation of morphology with change in Ar:CH₄ ratios. With decreasing Ar volume fraction, secondary growth increases.

further study is focused on three samples; two extreme (7:1-S1 and 1:7-S7) and one intermediate (1:1-S4) Ar: CH₄ ratios. The process plasma parameters, SEM images, Raman spectra, FTIR spectra, TEM images, diffraction patterns and electron energy loss spectra are analysed.

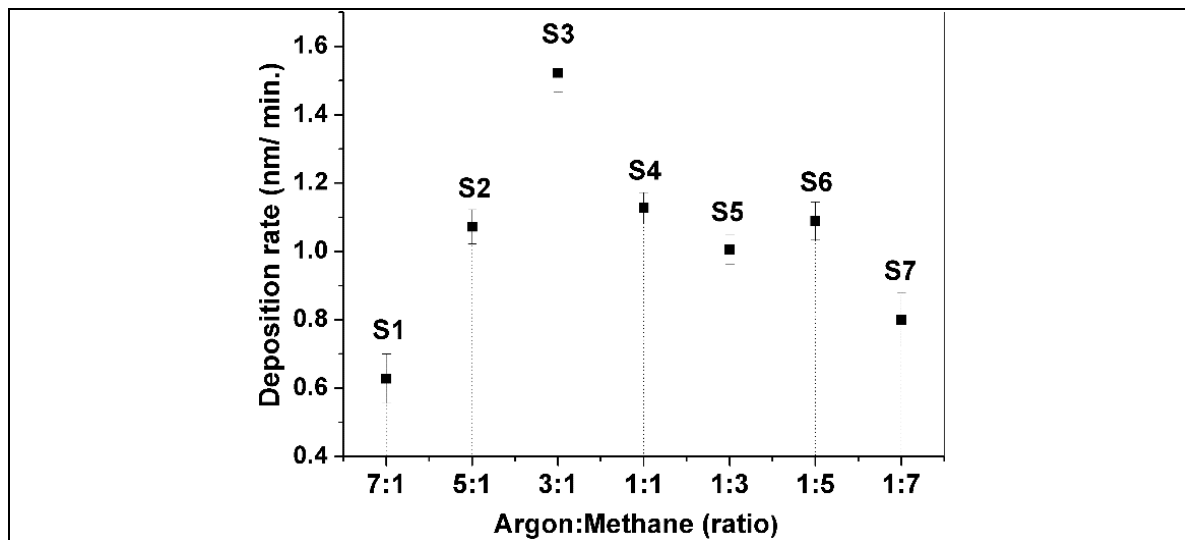


Fig. 4.10 Optimization of gas ratio for deposition. Highest deposition rate at 3:1 (Ar:CH₄) gas ratio.

4.2.2.1. Results and discussion

Process and Morphology: The SEM images of the GNWs deposited at Ar to CH₄ ratio-7:1, 1:1 and 1:7 are given in Fig. 4.11. Process parameters and results of image analysis are given in Table 4.2. GNWs grew normal to the substrate surface with clear edges to have open channel morphology in S1. With increase in methane concentration, secondary growth was observed in S4 followed by highly distorted and corrugated morphology with high density of secondary growth in S7. In the following section, the influence of gas ratio on the growth and evolution of morphology will be discussed.

The reflected RF power of the plasma system increases with the increase in argon volume fraction Table 4.2. Considering the plasma system in analogy with the secondary of a transformer, high reflected power indicates poor coupling and low power transfer at the secondary. The efficiency of energy transfer ' ξ_i ' (in RF plasma) is given by

$$\xi_i \cong (M/L_p)^2(R_p/R_a) \quad (4.1)$$

where M -mutual inductance of plasma, L_p -sum of geometrical inductance and electron-inertia inductance of plasma, R_p and R_a are resistances of plasma and antenna, respectively [232]. For increased power transfer, both (M/L_p) and (R_p/R_a) should be

neener to unity and all the terms except R_a are a function of degree of ionization. This can be correlated with the energy of ionization of the gases. The first ionization energy of argon

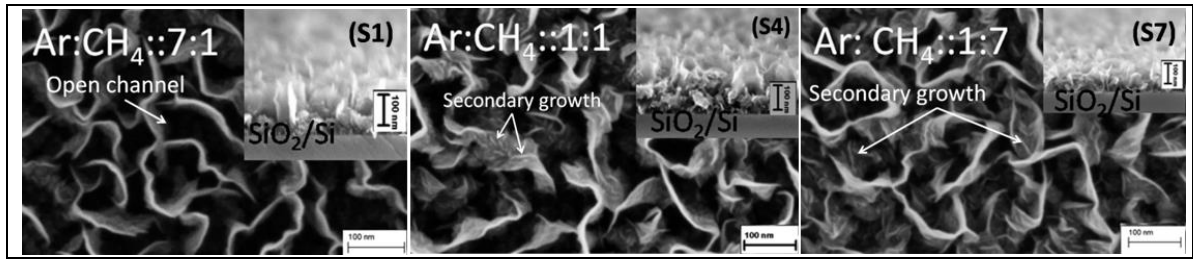


Fig. 4.11 SEM images of GNWs deposited with three different ratios. At 7:1(S1), Ar:CH₄ ratio; open channel morphology is developed. With decreasing Ar fraction, secondary growth with high corrugation is observed in S4 and S7.

Table 4.2 Deposition parameters used for Ar-CH₄ mixture.

Gas composition (Ar:CH ₄)/ID	Forward Power (W)	Reflected Power (W)	Temperature (°C)	Process gas Pressure (mbar)	Number of walls / μm
7:1(S1)	250	120.0	800	3.4×10^{-3}	12 ± 2
1:1(S4)	250	105.5	800	3.4×10^{-3}	8 ± 2
1:7(S7)	250	100.0	800	3.4×10^{-3}	8 ± 1

(Ar⁺) is 14.7 eV and that of methane (CH₄⁺) is 12.7eV [233,234]. Further ionization of argon (Ar⁺⁺) requires 28.63 eV and that of methane (CH₄⁺⁺) requires 39.97eV [234,235]. These transitions are not favoured energetically; rather it will form CH₃⁺/CH₄ (13.63eV), CH₂⁺/CH₄ (15.1eV), CH⁺/CH₄ (19.8eV), C⁺/CH₄ (20.5 eV) and so on [234]. It can be seen that the energy requirement for successive ionization of methane down to C⁺ is a few eV only. As a result, plasma chemistry becomes complex with various species of argon, hydrogen and carbon in different combinations, neutral or ionic forms orders of magnitude variation in lifetimes of participants and influence on the growth characteristics. In the following discussion, we will attempt to understand the how the gas ratio influence the deposition of GNWs.

The constituents in the plasma are highly active and readily interact with the substrate. However, only a few species have sufficiently long residence time to get attached with similar suitable species and grow further. Among the plasma species, the main species involved in the formation of GNWs are C₂, and C_nH_x ($n \geq 1$, $x = 1,2,3$) radicals generated from a carbon-source gas such as CH₄ [20,46]. Inherently, C₂ species has high desorption

barrier as compared to C_nH_x . As a result, high nucleation and growth takes place at conditions leading to high concentration of C_2 [236]. Further, the dangling bonds on the surface play an important role in generating active sites for nucleation and growth. Active argon (Ar^*) readily interacts with the substrate and being unstable, it will get detached from the surface generating dangling bonds [237]. These unsaturated bonds act as active sites for the incoming high energy (ion temp ~ 2000 K) CH_x and/or C_2 (or higher carbon) species to attach [17,47]. The initial nucleation is followed by growth. Hydrogen is generated in the plasma as a by-product of methane ionization. The hydrogen concentration increases in the vacuum chamber due to continuous removal of carbon as GNWs and due to low differential pumping efficiency of vacuum pump. An excess concentration of hydrogen results in etching as shown in Fig. 4.3 [73,238], which further reduce the growth rate. However, optimum concentration of hydrogen has a catalytic activity in enhancing armchair like edges to facilitate increased growth rate. In addition, excess hydrogen reduces the C_2 species supply to the edges further reducing the growth rate [47].

At 7:1 ($Ar:CH_4$) concentration, because of the presence of large number of active Ar^* species, which bombard with easily ionizable methane, high concentration of active hydrogen is generated (for every carbon atom 4 hydrogen is released). Methane fraction being low, reduced number density of carbonaceous species in the plasma deposit less number of carbon species. Carbon attached to thermodynamically favourable position stays and all others are etched away to have an open channel morphology and low growth rate as seen in the case of S1 (Fig. 4.11). For 1:1 and 1:7 ($Ar:CH_4$) concentrations, the number density of carbonaceous species in the plasma is high. However, the extent of consecutive ionization of CH_4 decreases because of the lower concentration of active Ar species. This results in lower concentration of active hydrogen per C_2 or other carbonaceous species leading to reduced etching at the edges. In addition, possibility of formation of hydrogen containing carbon species (like C_2H) having high sticking coefficient is high [47]. The above factors give rise to secondary growth in the samples as shown in Fig. 4.11.

Thus, the growth mechanism of GNWs can be described as, initial nucleation of C_2 or higher carbon species and/or CH/C_2H at a defect site followed by growth with further addition of species, based on the adsorption–desorption barrier of the respective species [238]. Argon rich environment enhances H^* formation which etches the edges leading to reduced secondary growth and an open channel morphology. Methane rich environment gives rise to higher concentration of carbonaceous species and lower concentration of active hydrogen per carbon leading to secondary growth formation.

During the growth process, the growing defective tip is constantly modified with the addition of more and more carbonaceous species [70]. Depending on the process gas ratio, the edges of GNWs are populated with hydrogen or hydrocarbon species. However, literature lacks further information on the effect of the edge/surface species on the crystalline and electronic nature of GNWs. In the following section we will try to understand the above aspects using Raman spectroscopy, FTIR, TEM and EELS studies.

Raman spectroscopy: Raman spectroscopy has been widely used for characterising carbon materials. The deconvoluted Raman spectrum of GNWs are given in Fig. 4.12 to Fig. 4.14. The results of conventional data analysis are given in Table 4.3. However, the new method of analysis, G-peak normalised intensity method is adopted for more realistic graphical comparison of data. The ‘G’ peak, formed due to the stretching of any pair of sp^2 bonded ($-C=C-$) carbon in chain or ring (E_{2g} phonon at the zone centre), is considered as signature peak of all sp^2 bonded carbon. Hence, we have taken ‘G’-normalised intensity in the Y-axis for gross graphical comparison of entire raw data. The profiles corresponding to different samples were largely identical in shape and intensity (Fig. 4.15).

No change in G peak position and shape are observed for the samples (Table 4.3). Hence, the bonding (the density, sp^2 content, elastic modulus and chemical composition) is not influenced *and/or* it is grossly beyond the threshold limit to distinguish the change. In comparison to HOPG, the slight blue shift of G band (at 1580 cm^{-1}) may be attributed to structural defects and/or hydrocarbon termination.

The ratio of D band and G band intensities (I_D/I_G) are generally used for comparing the defect densities in graphene samples (Table 4.3). Though D band is influenced by several defects such as vacancies, edges, grain boundaries and stacking faults, several other defects such as zigzag edges, charged impurities, intercalates and strain do not manifest in D band of graphene [72,239–241]. Similarly, the G band is influenced by several other factors which will be discussed with respect to A and T peaks [212], later. Hence, we are considering both the I_D/I_G ratio and FWHM for defect estimation in GNWs. The FWHM of D band will be a better choice to compare the defects in GNWs.

It is observed that I_D/I_G ratio increases with decrease in argon volume fraction (Table 4.3). Sample S4 shows lowest FWHM for D band indicating low defect density compared to S1 and S7. In the case of sample (S1), high Ar volume fraction is expected to give zigzag edges with hydrogen termination, as there are more active hydrogen species

which preferably attach and desorb free carbon at the arm chair edges [242]. In addition, the plasma energy (sum of dc self-bias (0-1 V) and plasma potential (~ 10 V)) is sufficient to produce defects at the growing edges leading to evolution of zigzag edges [243]. Therefore, it can be assumed that increased argon volume fraction favour zigzag edges with hydrogen termination.

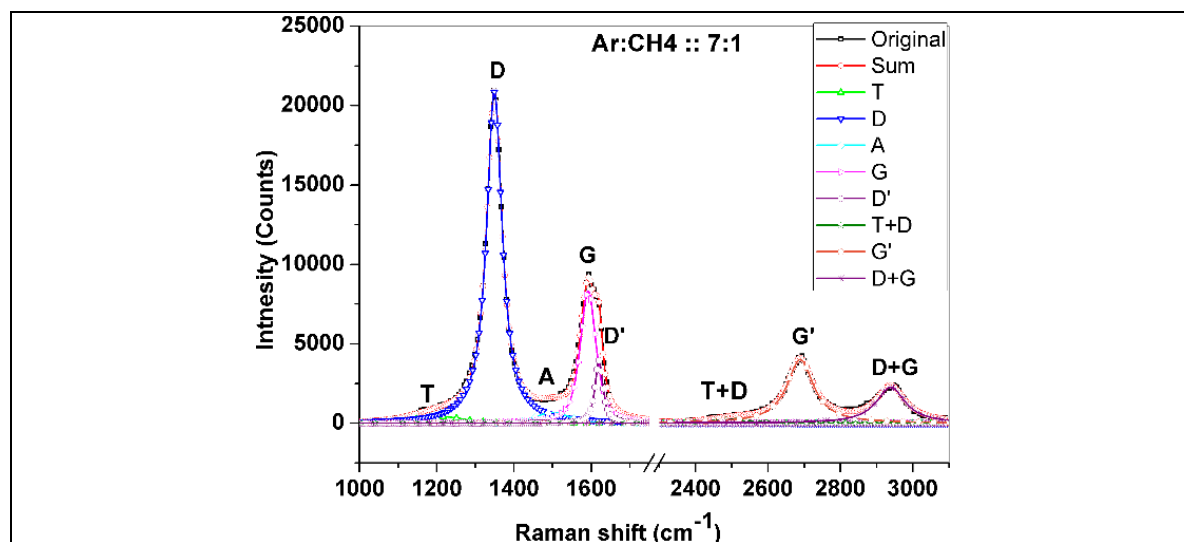


Fig. 4.12 Deconvoluted Raman spectrum of GNWs deposited at 7:1 (S1) Ar:CH₄ gas ratio. Results of analysis are given in Table 4.3.

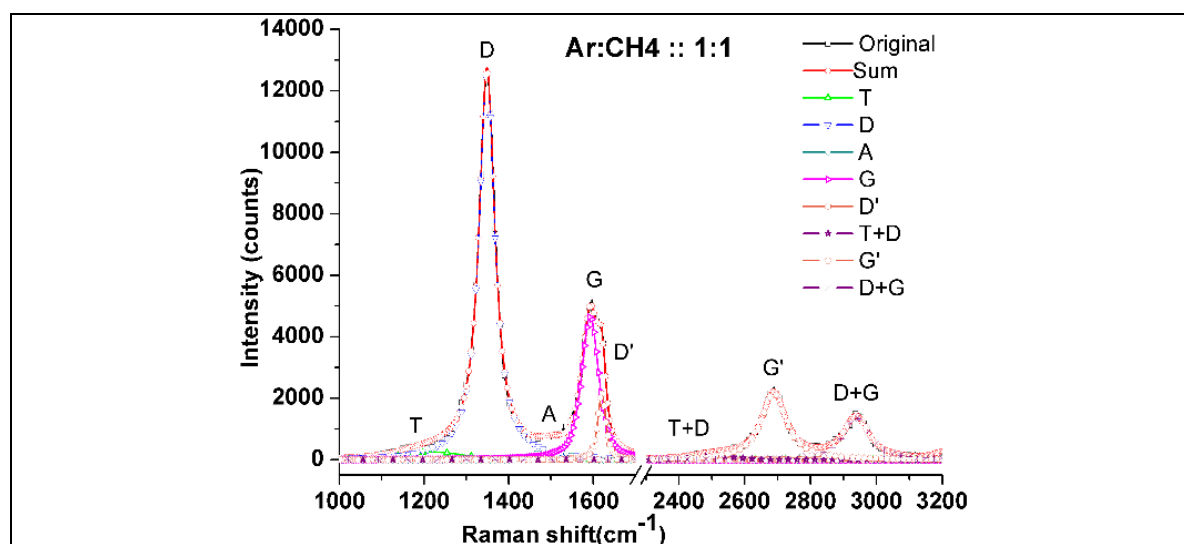


Fig. 4.13 Deconvoluted Raman spectrum of GNWs deposited at 1:1 (S4), Ar:CH₄ gas ratio. Results of analysis are given in Table 4.3.

Since, low Ar volume fraction reduces the electron temperature, the defect density is expected to be lower in the case of S7 as compared to S1 [17]. This is reflected in the FWHM of D band (Table 4.3). Though the morphology is different in between the samples,

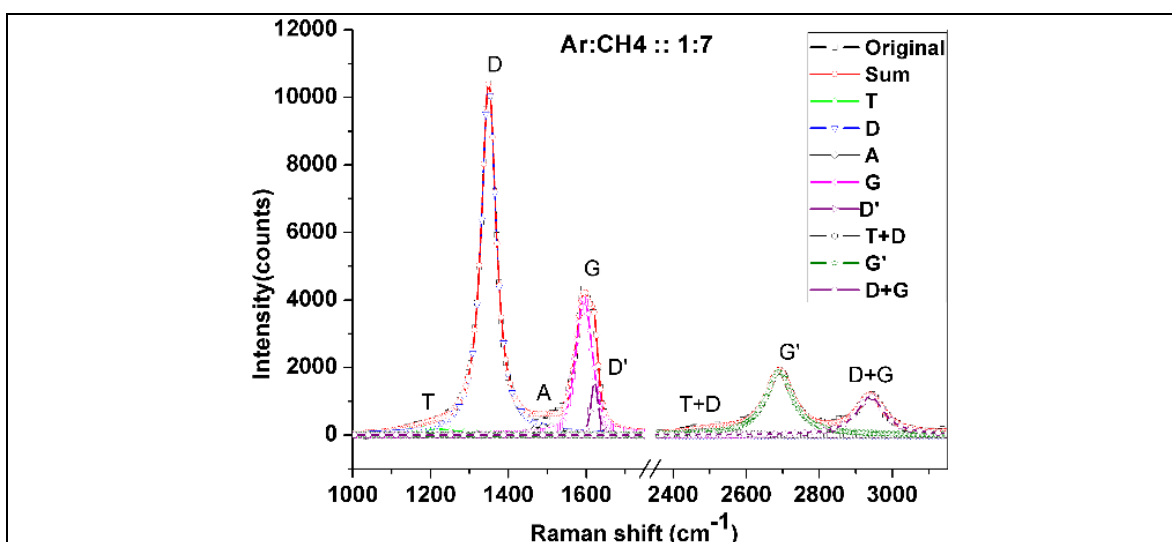


Fig. 4.14 Deconvoluted Raman spectrum of GNWs deposited at 1:7(S7), Ar:CH₄ gas ratio. Results of analysis are given in Table 4.3.

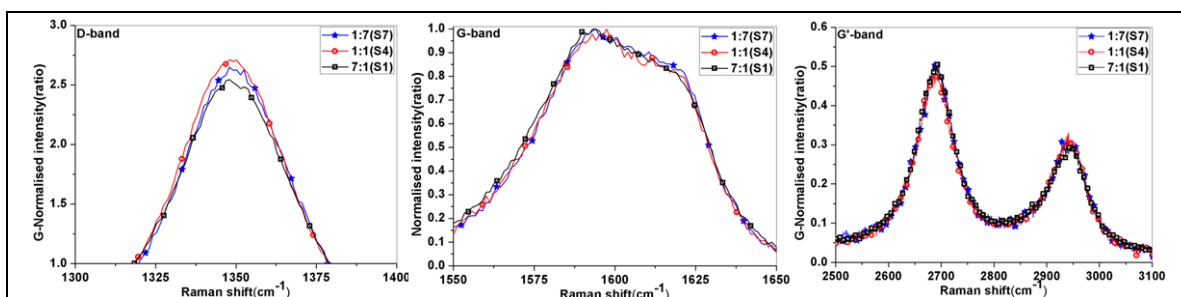


Fig. 4.15 The Raman spectrum of the three samples are plotted with G peak normalised intensity in Y-axis. The major difference is seen only in D band intensity.

Table 4.3 Comparison of Raman spectra.

Sample ID	D-peak (cm ⁻¹)	G-peak (cm ⁻¹)	D'-peak (cm ⁻¹)	G'-peak (cm ⁻¹)	La (nm)	I _D /I _G	I _D /I _{D'}	I _G /I _{G'}	T-peak	A-peak
S1	1369 (49)	1591 (43)	1619 (29)	2689 (91)	16±1	2.88	12.3	0.97	1220 (157)	1533 (119)
S4	1349 (45)	1592 (43)	1620 (26)	2688 (90)	17±2	3.05	13.7	0.95	1223 (181)	1542 (113)
S7	1349 (46)	1593 (40)	1620 (26)	2690 (89)	17±3	3.77	12.9	1.2	1229 (162)	1565 (120)

no noticeable variation in intensity and shape of D' band (1620 cm⁻¹) is observed (Fig. 4.15). However, the deconvolution results show slightly high I_D/I_{D'} ratio for S4, indicating relatively low I_{D'} value and improved long range order (Table 4.3).

The G' (2D) band is a finger print signature that distinguishes graphene from bulk graphite. The peak position and FWHM do not show any appreciable effects with change in gas ratio (Fig. 4.15). The FWHM of G' band vary from 89 to 91 (cm^{-1}) indicating that the GNWs are composed of more than five layers [244]. Lowest $I_G/I_{G'}$ ratio of S4 indicates improved 2D crystalline quality (Table 4.3). Hence, Raman spectroscopy indicates identical few layer graphene nature for the samples and improved long range order for S4.

In addition to the above, two wide peaks named as T and A are observed at $\sim 1220 \text{ cm}^{-1}$ and $\sim 1550 \text{ cm}^{-1}$, respectively [212]. Subrata et al., indicated these wide peaks at $\sim 1140 \text{ cm}^{-1}$ and 1500 cm^{-1} for ECR -CVD deposited GNWs [245]. However, wide variation in peak positions can be observed in literature. The T peak at 1220 cm^{-1} may be due to high density of edges [55], disordered hydrogenated sp^3 carbon [246] and olefinic structure similar to trans polyacetylene (zigzag C-chain structure with branching on opposite side of double bond) with linear hydrogen less C=C vibration [247]. The A peak ($1446\text{-}1450 \text{ cm}^{-1}$) is due to C5 $A_{g(2)}$ pentagonal pinch mode [247]. The seven membered ring can have one A_{1g} mode at 1303 cm^{-1} and pentagon have A_1 mode at 1444 cm^{-1} [28]. Tarrant et al., conclude that the peaks at $\sim 1280 \text{ cm}^{-1}$ is due to heptagonal rings whereas higher wave number (1450 cm^{-1}) derives from pentagonal rings [247]. The 'A' peak (1550 cm^{-1}) shows the presence of out-of-plane defects [248] pentagon, heptagon rings [247] and other defects such as trans-polyethelene [249] and fullerene like structure [250] in the system. Hence, it is concluded that the T and A peak additionally represents defects in the system as mentioned above.

FTIR studies: Though the effect of Ar:CH₄ ratio on defect characteristics could be inferred from the Raman spectra, defect types particularly the edge species could not be inferred. For this purpose FTIR spectroscopy was carried out. Fig. 4.16(a) shows the FTIR absorption spectrum of GNWs plotted against the frequency in the mid IR range. Several peaks appear in the finger print region and some of the major peaks are identified at 1370 cm^{-1} and 1460 cm^{-1} (C-H bend) [169], 1582 cm^{-1} (C=C stretch) [162,169] and 1731 cm^{-1} (C=O stretch) [168]. The peaks at $2800\text{-}3000 \text{ cm}^{-1}$ are due to sp^3 C-H stretch vibrations. No peaks beyond 3000 cm^{-1} shows the absence of sp^2 C-H or sp^1 C-H vibrations.

The peaks at $2800\text{-}3000 \text{ cm}^{-1}$ are categorised as vibrations of sp^3 carbon and hydrogen in methine group ($\equiv\text{CH}$ - sp^3 carbon attached to three carbon atoms and one hydrogen), methylene group ($=\text{CH}_2$ - sp^3 carbon attached to two carbon atoms and two hydrogen atoms) and methyl group ($-\text{CH}_3$ - sp^3 carbon attached to one carbon atoms and three hydrogen atoms). Fig. 4.16-b, c & d show that all the samples contain methine,

methylene and methyl species. The peak at 2893 cm^{-1} is assigned to stretching vibration of methine group [169]. The peaks at $\sim 2852\text{ cm}^{-1}$ and $\sim 2925\text{ cm}^{-1}$ are due to methylene group symmetric stretch and asymmetric stretch vibrations; whereas, the peaks at $\sim 2868\text{ cm}^{-1}$ and $\sim 2950\text{ cm}^{-1}$ are due to methyl group symmetric and asymmetric vibrations, respectively (Fig. 4.16(b)) [169].

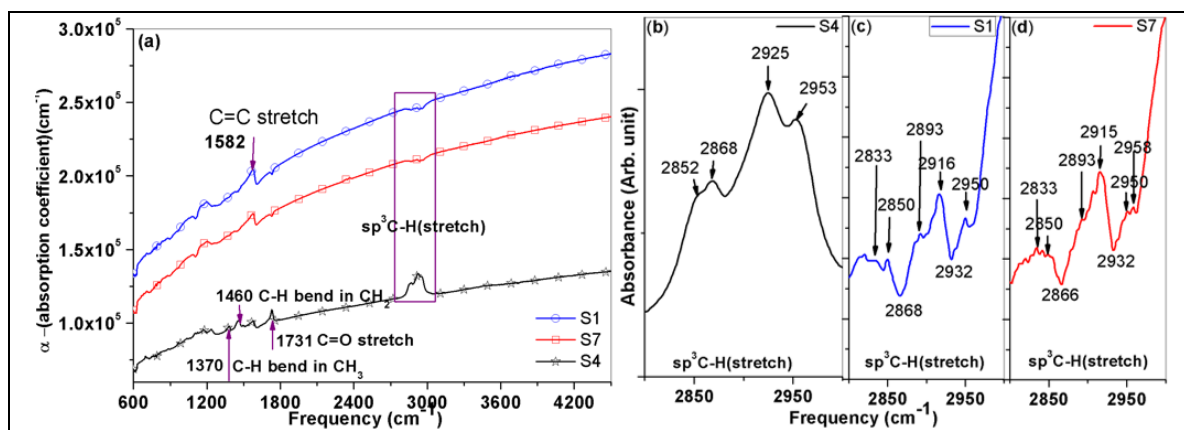


Fig. 4.16 FTIR spectrum of GNWs, (a) Absorption coefficient is used in the Y-axis to show the lower background of S4 due to better long range order. Relevant peaks in the finger print regions are marked. The sp^3C-H region in Fig. 4.16 (a) is blown up and plotted in Fig.4.16 (b), (c) and (d) to compare the methine, methylene and methyl group of sp^3 carbon – hydrogen stretching vibrations. Peak positions and its relative intensity is summarised in Table 4.4.

Though, Fig. 4.16 shows the presence of methine, methylene and methyl species in all the samples, it can be noticed that in each sample certain vibrations mentioned above are absent and some others appear weak. The absence of symmetric vibrations may be attributed to *steric hindrance* effects of crystal packing [251]. Since the methyl group is projecting away from the GNWs, the *steric hindrance* effects may have higher influence on symmetric vibrations than closely *anchored* methylene group and methine group. Again, in the case of methyl group, it can be attached to any edge carbon atom in the GNWs without breaking the sp^2 nature. Whereas, the methylene group can be attached in two ways, viz. methylene attached to sp^3 carbon in the ring and as bridging methylene group connecting two sp^2 bonded carbon in two separate layers. Methine group can be formed only on the surface of GNWs by converting the sp^2C in the ring into sp^3C co-ordination. It should be noted that the spectra observed are dependent on the relative abundance and energy of the species in the plasma and that the species attached can be converted into the other depending on the addition or removal of atoms. For example, loss of one hydrogen atom of an attached methyl group makes it methylene momentarily.

Table 4.4 FTIR spectroscopic study of GNWs.

Sample ID/ Vibration	Methine sp^3C-H cm^{-1}	sp^3C-2H (Methylene) cm^{-1}		sp^3C-3H (Methyl) cm^{-1}		Bridging $>CH_2$ 2833 cm^{-1}	C=O stretch	C=C stretch	C-H bend in $>C$ H_2	C-H bend in $-$ CH_3
		Sym.	Asym.	Sym.	Asym.					
S1	2893	2850 (medium)	2916 (medium)	Absent	2950 (medium)	Weak	Absent	Strong	Weak	Weak
S4	Not visible	2852 (strong)	2925 (strong)	2868 (strong)	2953 (strong)	Absent	Strong	Strong	Strong	Strong
S7	2893	2850 (weak)	2916 (medium)	Absent	2950 (weak)	Medium	Absent	Strong	Weak	Weak

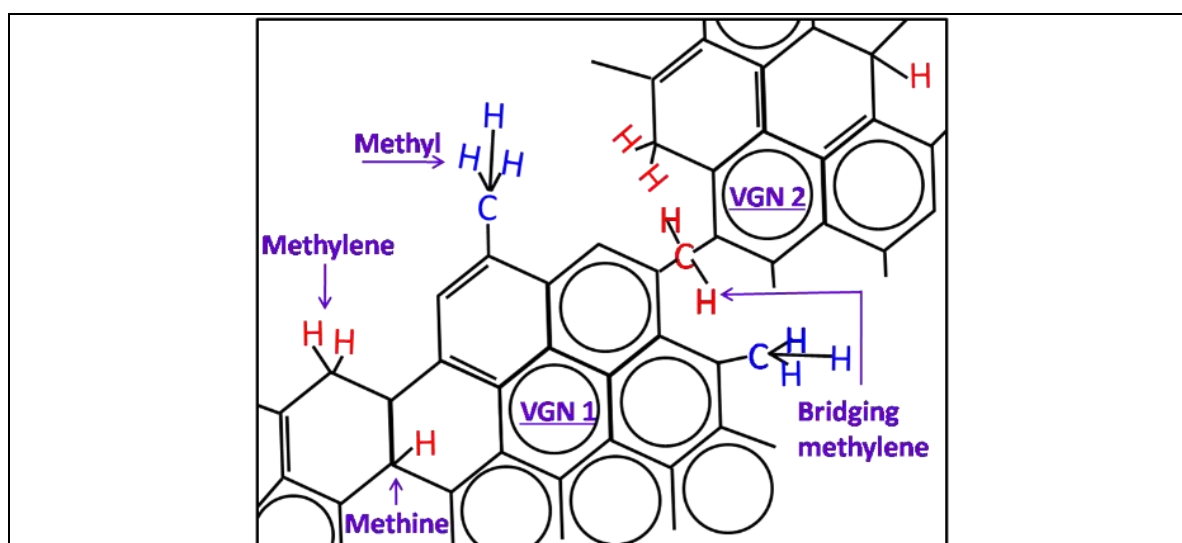


Fig. 4.17 Schematic of proposed geometrical arrangement of methine, methylene and methyl groups in GNWs. Methine group is formed by attaching hydrogen to a tertiary carbon on the surface. Methylene group is attached to the sp^3 carbon in the graphene ring or connected to sp^2 carbon in the ring as bridging methylene. Methyl group is attached to sp^2 carbon and protrude out of the graphene system.

This is true for all the constituents in the plasma contributing to growth including methine, methylene and methyl. Hence, the observed FTIR spectrum is unique and represents the remnant effect of the above processes and it will not change with time of deposition and is characteristic to the process conditions. A schematic of possible geometric arrangements of the groups is given in Fig. 4.17. The methine peak (2893 cm^{-1}) can be observed in S1 and S7 whereas; it is not very prominent in S4. This indicates hydrogen

attached to the surface of GNWs is relatively less in S4. In the case of S1 and S7, symmetric (2850 cm^{-1}) and asymmetric (2916 cm^{-1}) stretch vibrations of methylene are observed. However, peak at 2833 cm^{-1} corresponding to bridging methylene is seen only in S7 [169]. This shows that at 1:7 ratio, bridging methylene is favored and as a result, secondary growth is enhanced. The sample S4 has prominent methyl symmetric and asymmetric stretch at 2868 cm^{-1} and 2950 cm^{-1} , respectively. Methyl symmetric vibrations are absent and asymmetric vibrations are present S1 and S7 samples. This indicates *high steric hindrance* for the methyl group in S1 and S7. However, the asymmetric stretch peak of S7 has split into two at 2950 cm^{-1} and 2958 cm^{-1} and is attributed to two out-of-phase vibrations corresponding to three H-C-H combinations of methyl group [252]. Hence the methyl group in S7 experience higher *steric hindrance* than both S1 and S4. This is attributed to lack of long range order in S1 and S7 as seen in electron diffraction studies later. Sample S4 generate strong symmetric and asymmetric stretch vibrations of methyl and methylene groups, indicating long range ordered nature with stable edge (carbon dangling bond) termination (Fig. 4.16, Table 4.4). Though the effect of gas ratio on variation in defect density could be inferred from Raman spectroscopy and nature of edge species from FTIR spectroscopy, the structural and electronic nature of the samples could not be discerned. Hence TEM and EELS were carried out. Fig. 4.18 shows the HRTEM pictures of GNWs imaged perpendicular to (001) planes.

TEM and EELS studies: Results of image analysis are given in Table 4.5. For the samples synthesised at 1:7 and 7:1 Ar:CH₄ ratios, an increase in number of layers per GNWs is observed. The *d*-spacing of the layers were calculated both from the electron diffraction pattern and directly from the high resolution images. Typical regions used for interplanar spacing measurement are highlighted. The *d*-spacing ($>0.335\text{ nm}$) was corroborated with (002) lattice spacing of graphite given in ICDD data base no.00-056-0159. In general, the *d*-spacing of the GNWs were higher than that of HOPG. The increase in *d*-spacing may be attributed to the presence of methine group on surfaces as observed in FTIR studies. Both S1 and S7 show large deviation from HOPG due to high stacking fault disorder because of methine, methylene and methyl groups and is seen as diffused ring diffraction pattern [72]. However, the diffraction pattern of GNWs grown at 1:1 - Ar:CH₄ ratio (S4) shows spotty ring pattern indicating nanocrystalline nature.

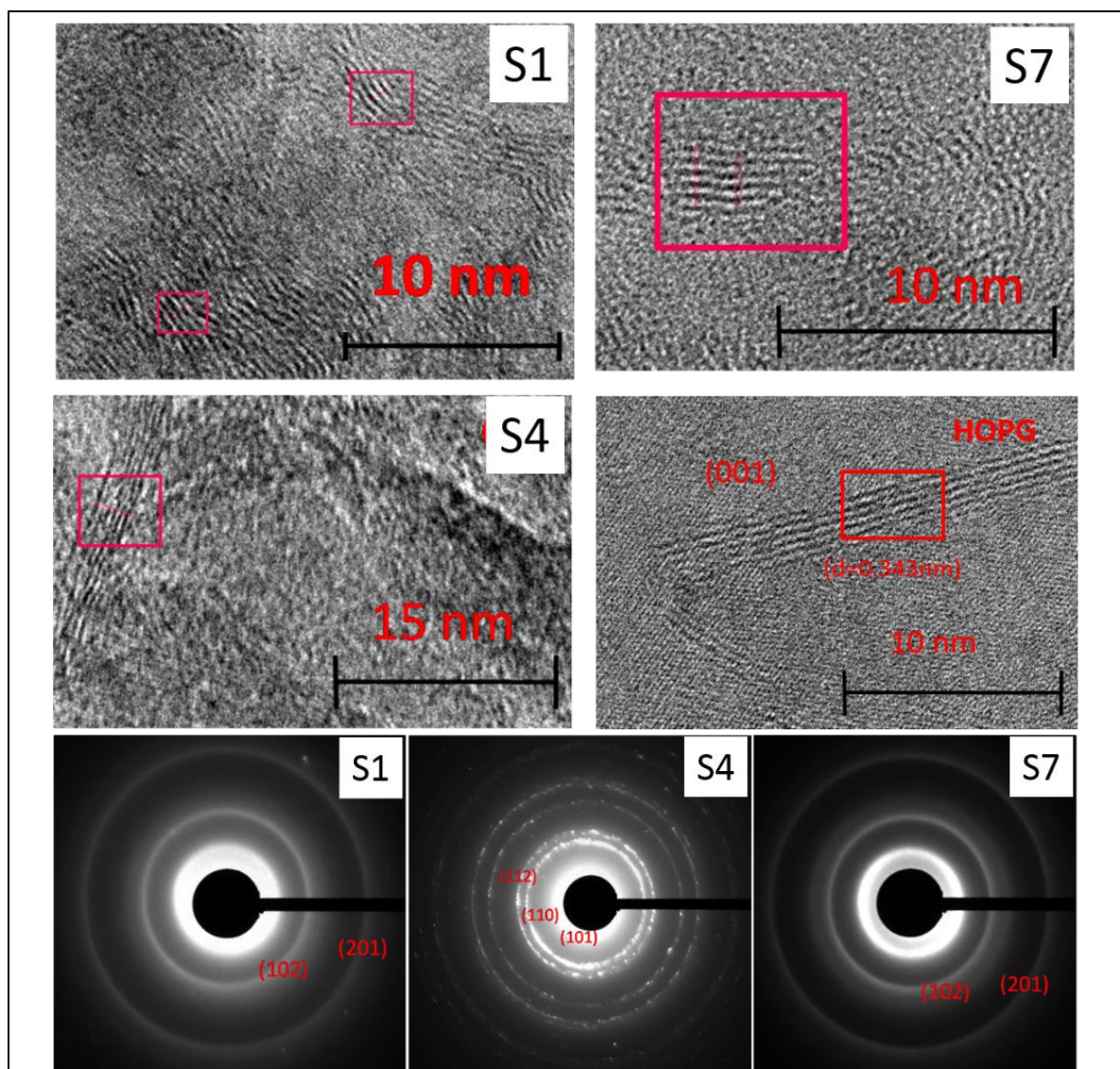


Fig. 4.18 TEM images of S1, S4, S7 and HOPG. Typical regions where interplanar spacing measured using image J software is highlighted. Images are taken in the direction perpendicular to (001) plane. The electron diffraction pattern of S1, S4 and S7 are shown below. Diffused ring pattern indicate lack of long range order (of S1 and S7) and spotty ring pattern (of S4) indicate nanocrystalline nature.

Fig. 4.19 shows the zero loss (ZL) peak normalised carbon electron energy loss spectra (EELS) of GNWs, HOPG and diamond. The normalization helps us to improve the ease of comparison of both the intensity and shape of EELS. The EEL spectra have two regions viz. low loss (elastic interaction) region and high loss (inelastic interaction) region.

In the low loss region of EELS, electron-plasmon interaction takes place and the valence electrons undergo intra band transitions. The bulk plasmon energy is given by

$$E_p = \hbar (\sqrt{n_c e^2 / m^* \epsilon_0}) \quad (4.3)$$

where ϵ_0 is the dielectric function, m^* and e are the electron rest mass and charge, and n_c the carrier density. The plasmon energy E_p is directly proportional to $n_c^{1/2}$, which is a function of both valence state and mass density. Crystallinity, bonding and doping influence the valence state and mass density. Low mass density as compared to HOPG was deduced from the increase in d -spacing of GNWs. Similarly, the FTIR spectrum indicates variation in bonding states of GNWs. Hence, a semi-quantitative assessment of the properties of GNWs has been made in comparison to HOPG and diamond.

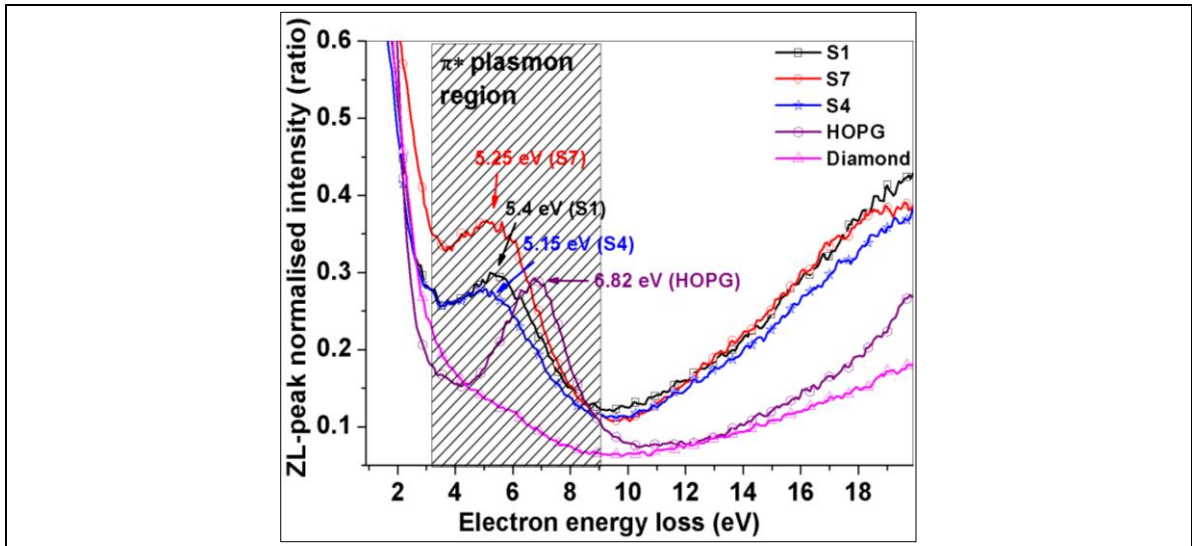


Fig. 4.19 ZL peak normalised low loss region of electron energy loss spectroscopy (EELS) data of S1, S4, S7 and HOPG showing typical π - π^* transition region of sp^2 type bonding. By convention the shaded portion is considered as zero loss region. Actual zero loss peak is at 0 eV. Because of no π bonding in diamond, π - π^* peak is absent. Individual curve fit is given in Fig. 4.20.

In the zero loss region, electron energy loss takes place due to elastic interaction with the ' π ' valence electrons (Fig. 4.19). In fact only zero loss peak is truly elastic. The plasmonic peak loss is very low compared to several hundreds of keV of incoming electron energy and hence, the interaction is some time referred to as elastic. The π - π^* plasmon excitation (edge) occur at 3.57 eV for S4 followed by S1 and S7 at 3.63 and 3.77 eV, respectively. Corresponding excitation edge in HOPG is at 4.31 eV. The π - π^* plasmonic peak falls at 5.15 eV (S4), 5.25 eV (S7), 5.4 eV (S1) and 6.82 eV (HOPG) (Fig. 4.19 and Fig. 4.20). It can be observed that the π - π^* peak in GNWs falls in the range of 4.7 eV (for free standing graphene having linear dispersion of π -plasmon) to 7.0 eV (of graphite having quadratic dispersion of π -plasmon) (Fig. 4.19). The up-shift of plasmon peak as compared to

graphene is due to increase of screening and interlayer coupling of graphene layers in GNWs [253–255]. The π - π^* plasmonic peak values show that S4 has the transition closer to monolayer graphene as compared to S1 and S7. Practically, a high plasmon peak value indicates the existence of high energy intraband transition states of π -electrons. The high value π - π^* plasmonic peak (of S1 and S7) may be attributed to shifting of the Fermi level upward away from the Dirac point due to supply of electrons into the π^* band by edge species [256]. The edge species in GNWs have been identified as methine, methylene and methyl groups from the FTIR studies. Methyl group is more electro positive than methylene and methine. Since, S1 shows a higher plasmonic peak (5.4eV) than S7 (5.25eV) and S4 (5.15eV), the edges of S1 may have more methyl group than S7 and S4. S4 shows a lower peak value than both S1 and S7, which may be due to lower number of edge species as a result of better 2D crystalline nature and lower number of layers per GNWs. It should be noted that the area under the curve of HOPG (crystalline material) is lower than GNWs (low crystallinity).and among the GNWs, S4 has lowest area under the curve. The observation is in line with the view obtained from electron diffraction studies earlier.

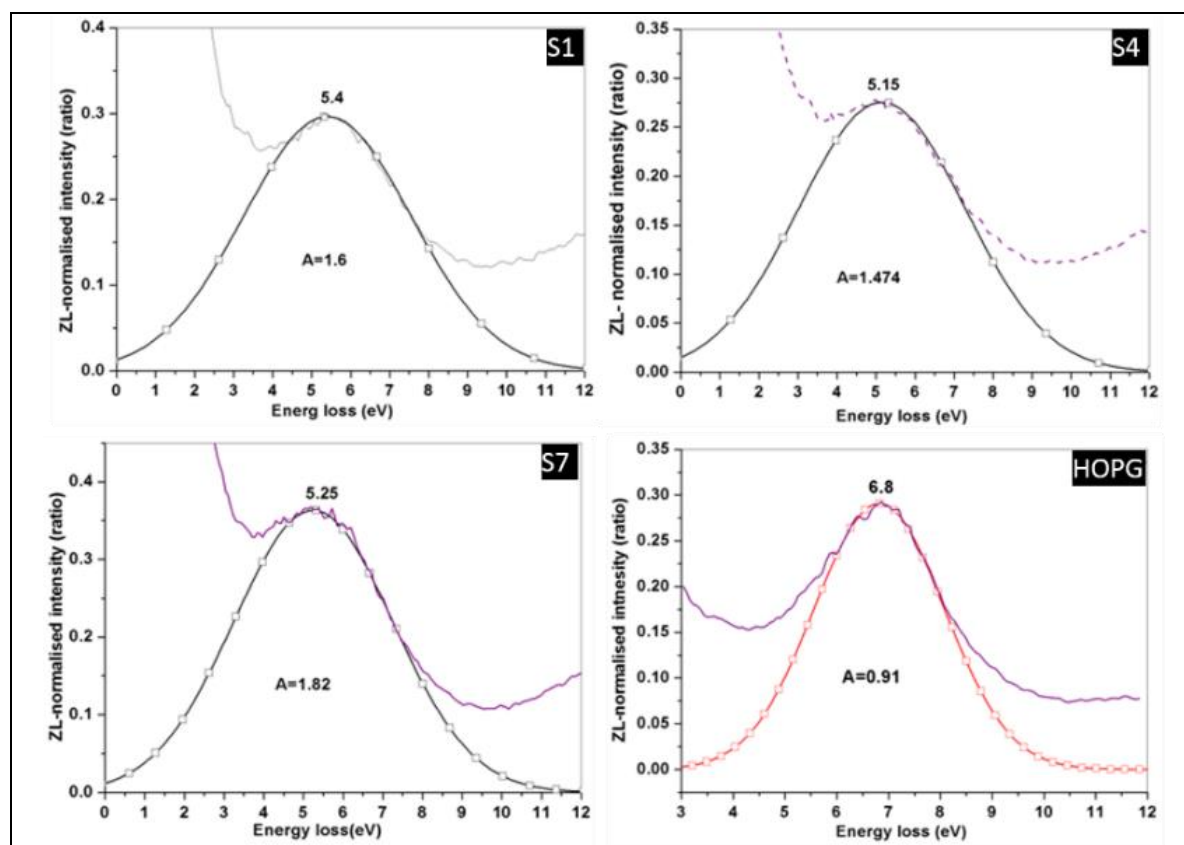


Fig. 4.20 Gaussian fitting of π - π^* plasmonic peak of S1, S4, S7 and HOPG. ZL-peak normalised intensity was used to compare the area under the curve.

Fig. 4.21 shows high loss region of EELS manifesting the C –K edge of samples S1, S4, S7 and HOPG. Both N- K edge and O – K edge were absent in the present work. C–K edge region originates at around 283.5 eV due to the inter band excitation of K electrons of carbon, generating π^* region in the EEL spectrum. All other inter band excitations contribute to $\pi^*+\sigma^*$ region. The C–K edge of HOPG is at around 285 eV. The low C–K edge value of GNWs indicate reduced binding energy of K-electrons as compared to HOPG. However, the π^* and $\pi^*+\sigma^*$ peak positions of both GNWs and HOPG are the same (Table 4.5). Fig. 4.21 shows that the π^* and $\pi^*+\sigma^*$ region of EEL spectrum overlap and extend several 10s of eVs. The overlapping of the peaks is described to have two origins viz. a) physical: the *c*-axis mixing of graphitic layers to the incoming beam of electrons and b) chemical: the bonding of carbon [257,258].

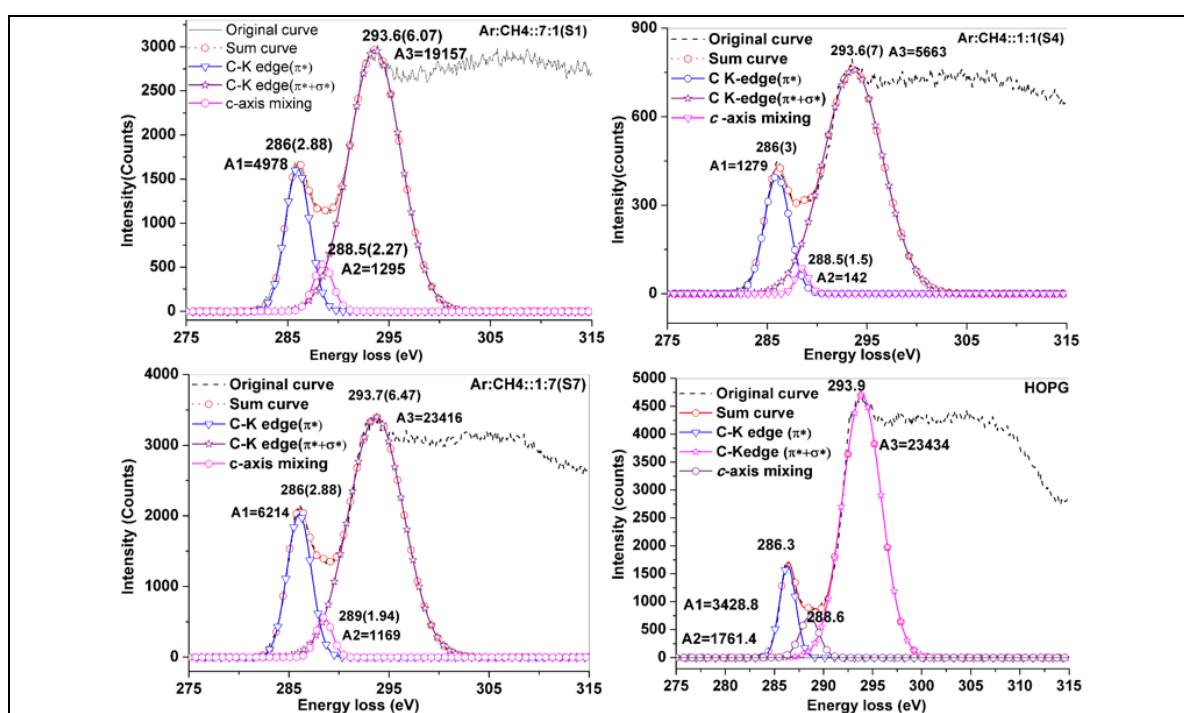


Fig. 4.21 The deconvoluted high loss region of electron energy loss spectroscopy (EELS) of GNWs and HOPG. The area under the curve (A1) was used for estimating the sp^2 fraction of respective samples along with the EELS spectrum of HOPG. The ratio A2/A1 was used for analyzing the *c*-axis mixing in GNWs. The curve A3 was generated to determine $\pi^*+\sigma^*$ peak and to fit A1 and A2.

Due to the corrugated and/or turbo static character, the orientation mixing of different layers with the direction of incoming high energy electrons is a quite plausible phenomenon. Additionally, due to methine, methylene or methyl species, the chemical aspects are also equally viable. Irrespective of the reason, the peak overlap is due to the

formation several discrete states in the π^* and $\pi^*+\sigma^*$ region due to coulombic interaction. Papworth *et. al.*, described it as due to molecular transition within the sample [257]. However, we use the term ‘*c*-axis mixing’ in a generic sense to represent the quality of GNWs for further discussions. Therefore, we have fitted the C –K edge region with three Gaussians A1, A2 and A3 corresponding to π to π^* -transition, *c*-axis mixing and $\pi^*+\sigma^*$ -transition, respectively as shown in Fig. 4.21 [257,259].

Table 4.5 Results of TEM images, diffraction pattern and EELS analysis.

Sample	D-spacing (nm)	Layers per sheet (Numbers)	(π^*) plasmon			K- π^* edge ($\pm 0.03\text{eV}$)			sp^2 fraction ($\pm 5\%$)
			Edge ($\pm 0.03\text{eV}$)	Peak ($\pm 0.03\text{eV}$)	Area (arbUnit)	Edge ($\pm 0.03\text{eV}$)	Peak ($\pm 0.03\text{eV}$)	A2/A1	
S1	0.418 ± 0.028	5-7	3.63	5.4	1.6	283.5	286	0.26	51
S4	0.3587 ± 0.029	3-5	3.57	5.15	1.5	283.3	286	0.11	51
S7	0.3949 ± 0.046	7-9	3.77	5.25	1.8	283.6	286	0.19	45
HOPG	0.343 ± 0.002	many	4.31	6.82	0.91	284.9	286.3	0.51	100

The area corresponding to π - π^* inter band transition (A1) of each sample was used for the calculating the sp^2 bonding fraction using eq.2.9 and the results are given in Table 4.5. The low (50 %) sp^2 fraction of GNWs is attributed to methine on the surface and the methylene at the rings, in both cases the $sp^2\text{C}$ is converted into $sp^3\text{C}$, locally. Further for the π - π^* curve deconvolution, the peak (with area A2) at around 288.5 eV is chosen [257,259]. We have conservatively not used A3 for any calculation except for the purpose fitting the A1 (π - π^* transition) and A2 (peak mixing), respectively [257]. It is experimentally observed that A2/A1 of HOPG is nearly equal to 0.5 whereas S1, S7 and S4 are 0.26, 0.19 and 0.11 respectively. It should be noted that the A2/A1 ratio and π - π^* plasmonic peak in the zero loss region follows the same order indicating the similarity in electronic structure and plasmonic properties of S1 with HOPG and S4 with monolayer graphene (Table 4.5). Hence, we propose the A2/A1 ratio shall be used for evaluating the quality of GNWs.

The study may be summarised as follows. With increase in argon concentration in Argon-methane mixture, the surface is populated with methine and the edges, largely with

methyl group. Surface methine increases the d spacing and the edge methyl group restricts further growth. The highest π - π^* plasmonic peak of S1 is attributed to presence of relatively large number of electro positive methyl group. With increase in methane volume fraction, methylene at the edges in bridging form dominates and enhances the secondary and/or corrugated growth. Intermediate value π - π^* plasmonic peak of S7 indicates relatively lower supply of electrons to the π^* band by the edge species than S1. In the case of S4, graphene like structure with minimum but ordered methine, methylene and methyl edge groups are developed. Using EELS studies, the c -axis mixing parameter is derived from C-K edge interband transition and shown to represent the quality of GNWs.

Morphology of GNWs is the primary physical factor contributing to high surface area to volume ratio for an application. By correlating structural, plasmonic and electronic properties of GNWs with process gas ratio and consequent attachment of edge hydrocarbon species, the science of process parameter selection for making tailor made GNWs by doping, intercalation and stripping is better eased out. Hence, the results of the study will be useful for both pristine and modified GNWs based applications.

4.3. Summary

In order to study the main factors influencing the deposition rate, evolution of morphology, structure and electronic nature of GNWs, the process gas (Ar, CH₄ and H₂) ratio is varied systematically while keeping all other parameters same. Though GNWs is deposited for various ratios of H₂ and CH₄, increase in hydrogen fraction has an etching effect on the GNWs. Presence of hydrogen promotes graphitic structures. Since, the presence of hydrogen and etching effect can be attributed to the ionization of CH₄, experiments are directed towards optimizing Ar:CH₄ ratio. The presence of Ar in the process gas can improve the electron temperature and extent of ionization. The change in process gas ratio induces difference in morphology, deposition rate, microstructure and electronic nature of GNWs and are important factors towards its choice for any application. Hence, three samples are deposited at argon to methane ratio 7:1(S1), 1:1(S4) and 1:7(S7) while keeping all other plasma process parameters unchanged. The GNWs were studied using SEM, Raman spectroscopy, FTIR, TEM and EELS.

Though extreme gas ratios (1:7 and 7:1) manifested low deposition rate and different morphologies, Raman spectra of the samples are found to be identical except for D band. At extreme ratios, the reduction in long range order is reflected as high background intensity and absence of symmetric stretch vibrations of methylene and methyl groups.

Surface methine increases the d spacing and the edge methyl group restricts secondary growth. With increase in methane volume fraction, methylene at the edges in bridging form dominates and enhances the secondary and/or corrugated growth. The highest π - π^* plasmonic peak of S1 is attributed to presence of relatively large number of electro positive methyl group. Whereas, the intermediate range π - π^* plasmonic peak value of S7 indicates relatively lower supply of electrons to the π^* band by the edge species (methylene) than S1. In the case of S4, graphene like structure with minimum but ordered methine, methylene and methyl groups are developed with plasmonic peak closer to monolayer graphene. All the GNWs register identical sp^2 bonding fraction. The peak mixing parameter derived from C K -edge data of HOPG was proposed to correlate the c -axis mixing of GNWs and thus, its quality.

In the PECVD synthesis of GNWs, the edge species influences the evolution of morphology, crystalline nature and plasmonic properties. However, the core level electron transition (C K -edge) is not affected. In comparison to HOPG, GNWs register a red shift in C K -edge. It has been found that intermediate volume fractions of Ar and CH₄ give rise to GNWs with characteristics close to graphene. Since GNWs are poised for several applications, the understanding on the nature of edge species and their influence on the plasmonic properties will provide ample input in designing the synthesis methodology and doping choices with morphological control. In addition, the methodology described for Raman and EELS are novel and shall be used for characterisation of GNWs. In FTIR characterisation studies, the absence of symmetric stretch vibration is termed as lack of long range order and hence low crystalline nature of GNWs.

Chapter 5

High dose nitrogen plasma ion implantation of graphene nanowalls

This chapter describes the first of its kind attempts to study the effect of shallow ion implantation of GNWs using nitrogen plasma. The morphological, structural and chemical changes taken place in the GNWs on nitrogen ion implantation are described. Since mechanical property evaluation of GNWs have not been described in any published literature so far, an attempt is made to evaluate the stiffness of GNWs before and after ion implantation using AFAM technique. To improve the understanding of influence of nitrogen in electronic and chemical properties of GNWs, a new approach based on the location of nitrogen in GNWs is proposed; further, the same is utilised to describe the stiffness variation.

5.1. Process, Materials and Methods

The PECVD system, synthesis of GNWs and the details of plasma immersion implantation system are described in chapter 2. GNWs were deposited on Si_{<100>} wafers (4 numbers) at 850°C using argon-hydrogen-methane plasma (in 1:2:2 ratio) at $\sim 4.2 \times 10^{-3}$ mbar pressure for a plasma forward power of 100W. Plasma immersion ion implantation is carried out in the PIII chamber using high (99.89%) pure nitrogen plasma such that positive nitrogen ions in the evolving plasma sheath bombard the specimen surface at normal incidence when the sample is biased to a negative pulsed DC voltage of 2 kV (100 Hz with a pulse width of 45 μ s). Both RF plasma power and chamber pressure (3.4×10^{-3} mbar) are kept constant during the above process. One pristine sample (*S0*) and three ion implanted samples for 10 minutes (*S1*), 20 minutes (*S2*) and 30 minutes (*S3*) are taken for experimental study. No post implantation annealing is carried out on these samples. The voltage and current output from the pulsed transformer are monitored using a digital oscilloscope (Agilent DSO 5012A) to control the process and dose. The Stopping and Range of Ions in Matter (SRIM) software is used for estimating the range of ions in the GNWs.

The surface and cross section of the samples are examined using Carl Zeiss supra-55 FESEM for morphological changes and implantation induced visible structural changes. Using the built-in measuring tool, the thickness of the film, implantation induced sputtering and other structural features are measured. Raman spectra are taken at room temperature

using Renishaw Model Invia with Leica microscope and an XYZ motorised positional stage microscope with 50 mW laser (514.5 nm) excitation for an acquisition time of 150 sec. The G-peak normalised intensity after background correction is plotted against Raman shift. The D-peak and other peaks are deconvoluted with Lorentzian and G peak is deconvoluted by voigt (Gaussian + Lorentzian) profile fitting to assign the respective phonon modes of GNWs. Al $\kappa\alpha$ (1486.6 eV) X-ray source is used for XPS analysis. The intensity of photoelectrons escaped from the surface (~3-nm depth) against binding energy is plotted. The spectra is analysed using CASA XPS software by considering *Shirley* type background deduction to decompose and assign the peak energy corresponding to different chemical states of carbon, nitrogen and oxygen. The atomic force microscopy (AFM) and atomic force acoustic microscopy (AFAM) studies are carried out on the samples.

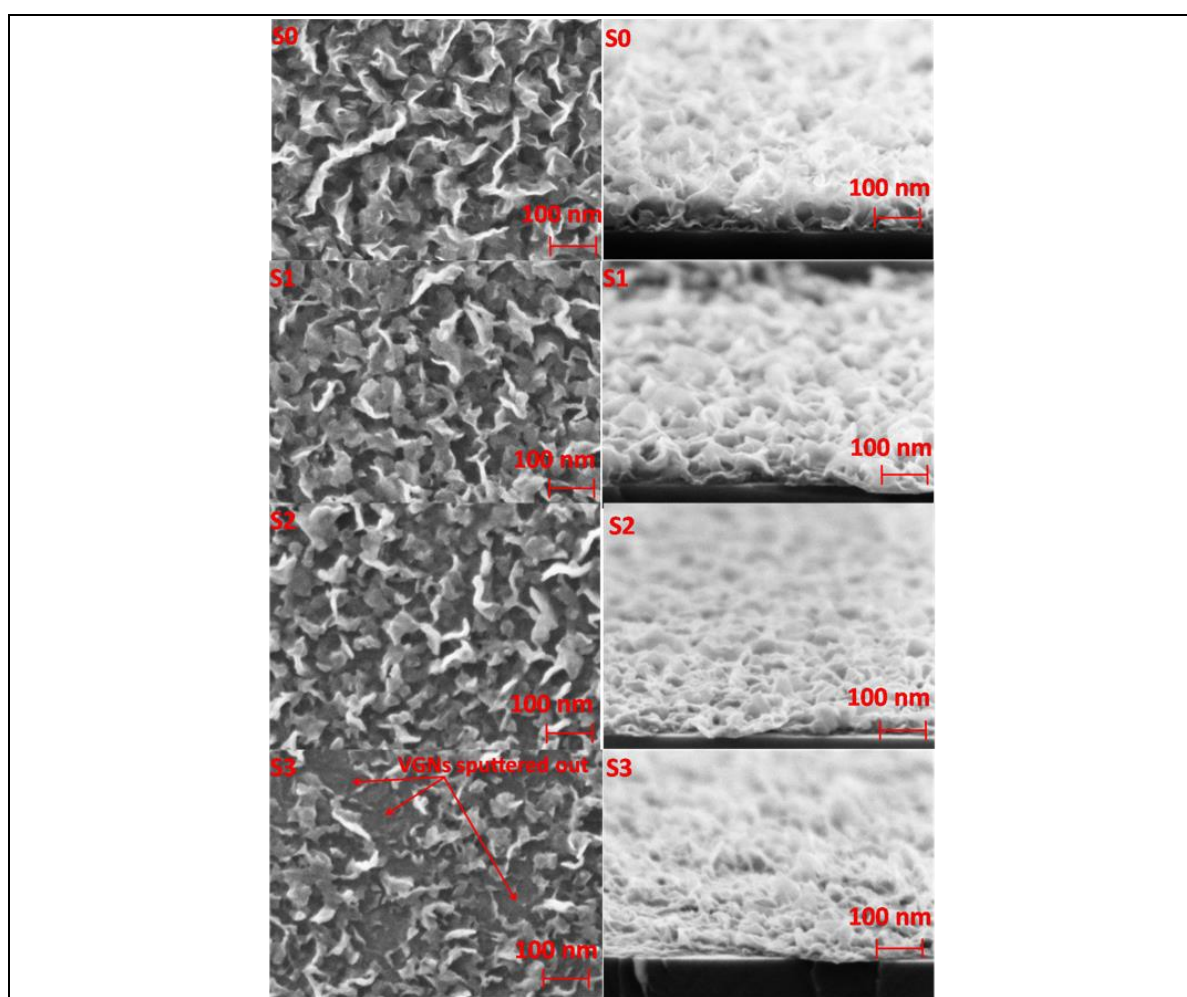


Fig. 5.1 FESEM image showing the surface and cross-section of GNWs, pristine (S0), nitrogen plasma implanted for 10 min.(S1), 20 min.(S2) and 30 min.(S3). The sputter removal of material due to implantation is seen in S3.

5.2. Results

Fig. 5.1 shows the SEM images of surface and cross section of pristine and implanted GNWs. The GNWs film consist of randomly oriented corrugated vertical walls of length ~ 250 nm (max) and thickness 60 ± 5 nm uniformly spread over an area of 10 mm \times 10 mm (sample size). These samples are taken plasma ion implantation studies. Since the ratio of sample size to substrate size (dia:80 mm) is very less, the unbiased plasma density on the sample surface is uniform [260]. However, GNWs exhibit sharp edges which makes the electric field intensity nonuniform upon electrical bias. The high intensity electric field around these edges drive the positive ions and directed neutrals into it upon negative pulse bias [261]. Hence, the implantation is mainly restricted to the surface. Since each vertical nanowalls consists of a few layers of graphene oriented perpendicular to the surface [70], during implantation, depending on the acquired energy, nitrogen species get implanted on the edges as well as few nanometers into the layers. At a bias voltage of 2kV, SRIM simulation shows that the ions trace through a few (~ 5 nm) nanometers into the sample. (Fig. 5.2). Considering the non-planar morphology, the ions pass through several layers and in that process, sputtering also takes place. Fig. 5.1 shows that no remarkable change in morphology for samples implanted for 10 and 20 minutes. However after 30 min, because of the extensive sputtering, substrate surface is seen along with the GNWs. The change in sample thickness with implantation duration is given in Fig.5.3.

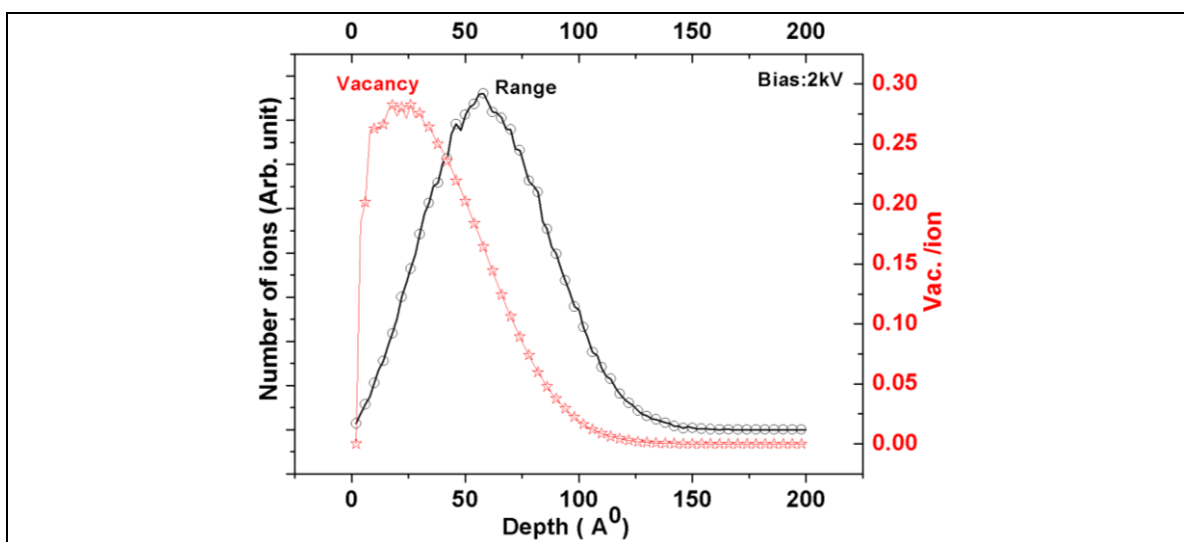


Fig. 5.2 SRIM simulation of N^+ ion implanted at 2 kV bias. Peak range is at 5.7 nm and peak vacancy generation is at 2.5 nm deep from surface. At half the energy ion implantation (N_2^+ ions), the above values can be reduced by half and hence, the collision cascade intercepts the surface and cause excessive sputtering of material.

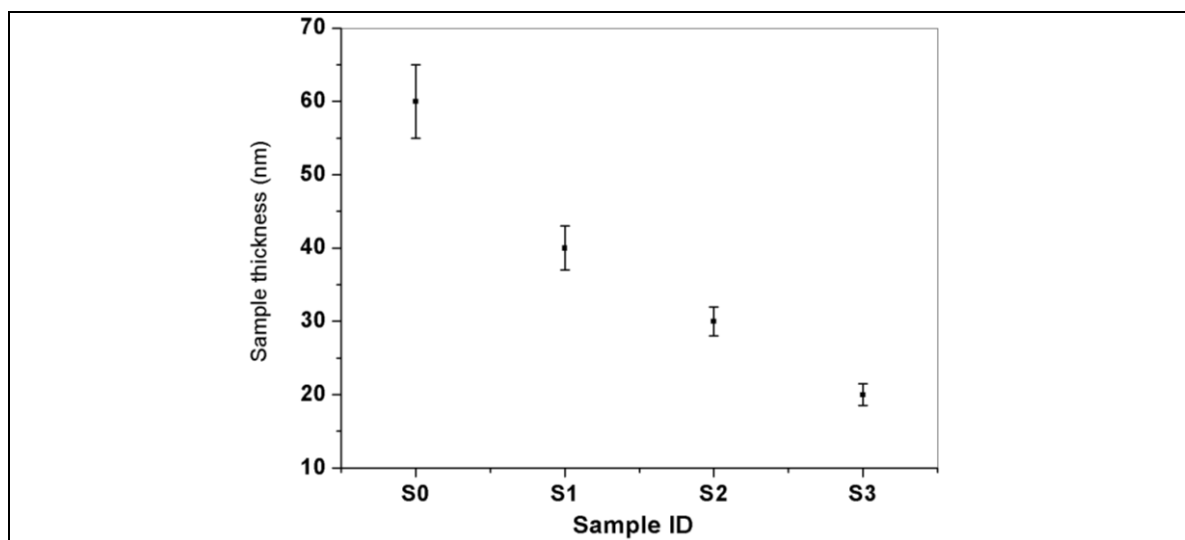


Fig. 5.3 Variation in sample thickness of pristine (S0) and implanted for 10, 20 and 30 min. (S1, S2 and S3, respectively), showing reduction in thickness due to sputter removal of material.

5.2.1. Raman spectroscopic studies

Raman data of pristine and implanted samples are deconvoluted and typical Raman spectrum of S0, S1, S2 and S3 are shown in Fig. 5.4, Fig. 5.5 and Fig. 5.6 respectively. The curves are deconvoluted and integrated intensity ratio is tabulated. The integrated intensity ratio (I_D/I_G) become more meaningful when the Raman spectra is fitted with T and A peaks, as in the present case for implanted samples. Using this method, Raman spectrum of samples of pristine and implanted samples are compared.

Ado Jorio et al evaluated intensity, FWHM and int. area for D and G peaks in graphene as a function of distance between defects. Lower the distance or larger the L_D (defect density), intensity ratio vary strongly. For lower values of L_D both I_D/I_G and A_D/A_G similar behaviour. [262]. GNWs are inherently highly defective and both D peak and G are influenced by several factors (such as defects, foreign atom, bonding, etc.) and deconvoluting the spectrum corresponding to each factor is not viable. In such cases, the intensity ratio is recommended because it is direct. Since, GNWs are inherently defective and is implanted with other foreign atoms, the intensity ratio is also chosen for comparison of the samples. For improved understanding of the spectrum, graphical way of representing the intensity ratio is chosen by using G-normalised intensity for all samples. In Raman spectroscopy, G-peak is manifested by all sp^2 bonded carbon in ring or chain and hence, fundamental to all graphitic materials. Hence, the G-peak intensity normalised graphical representation of Raman spectra gives a full spectrum comparison of data (Fig. 5.7). While

analyzing the spectrum both the above methods have been utilised in chapter 5 and chapter 6.

Raman spectra of S0 showed peaks at $\sim 1589 \text{ cm}^{-1}$ (G-band), $\sim 1353 \text{ cm}^{-1}$ (D band) and $\sim 2695 \text{ cm}^{-1}$ (G' band) due to bond stretching of sp^2 carbon atoms, defects in rings and double resonance scattering of the rings, respectively. The peak at 1620 cm^{-1} (D'-shown in Fig. 5.4) is due to intravalley transitions and the peak at 2455 cm^{-1} (D+D'') and 2945 cm^{-1} (D+G) are due to resonance of multiple phonon modes [230]. It appears that T and A peaks are not required for obtaining a reasonably good fit for the pristine sample (Fig. 5.4). Raman spectrum confirms the few graphene layer nature of samples. The I_D/I_G ratio-2.5 and $I_D/I_{D'}$ ratio-7.3 of sample S0 can be associated with the presence of graphitic structure having large number of edges and vacancy type defects [231]. The results obtained from the Raman spectra of various samples are given in Table 5.1.

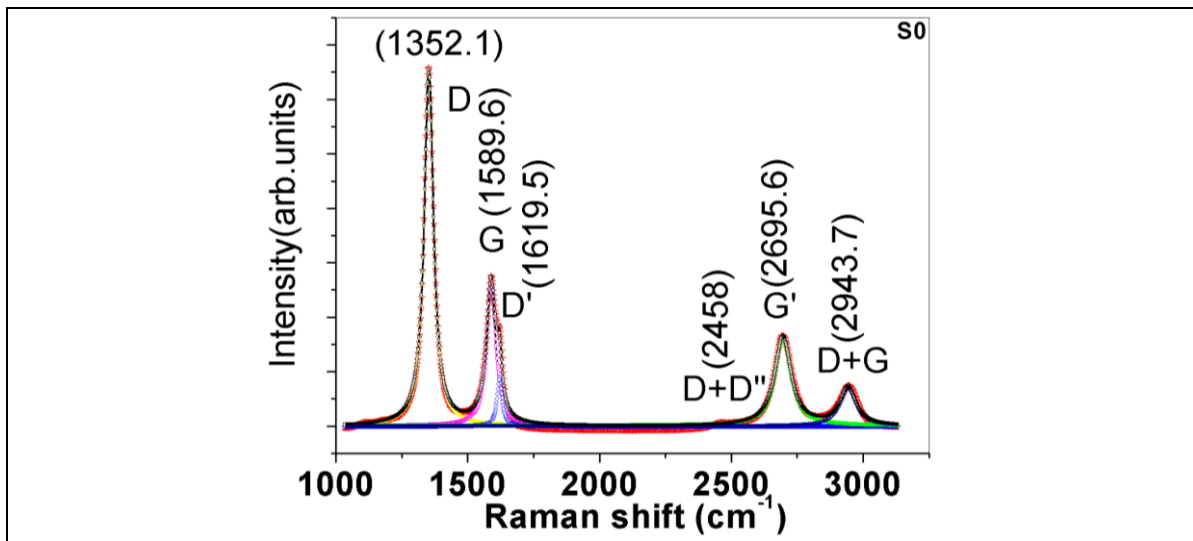


Fig. 5.4 Raman spectrum of pristine sample showing the typical peaks corresponding to graphene nanowalls.

Raman spectra of nitrogen ion implanted GNWs show increase in background intensity, broadening of FWHM and reduction in I_D/I_G and $I_{G'}/I_G$ with respect to pristine GNWs; owing to generation of structural disorder [155]. From the I_D/I_G values (Table 5.1), based on the results of study of Ferrai *et al.*, [263] it can be inferred that during the initial 10 minutes of implantation, the pristine sample has entered the second regime of the amorphization trajectory. And, further implantation has caused only some marginal change in the spectrum. The shift of G-peak position is influenced by several parameters such as defects, doping, strain, etc. which has opposite effect in peak shift. For example, compressive strain shift the peak position to a high value whereas, tensile has the opposite

effect. The high background intensity in between D and G peak and merger of D' peak with G peak make the accurate positioning of G peak very difficult. Since the G peak is manifested by all sp^2C bonded atoms, G-band position in pristine and in implanted samples appeared as more or less unaltered in this study. However, a clearer picture is expected when the dose level is low as discussed in chapter 6.

Table 5.1 Raman spectroscopic analysis of GNWs (S1, S2 and S3).

Sample ID	Peak position (cm^{-1})					I_D/I_G	$I_{G'}/I_G$
	D	G	$C\equiv N$	G'	D+G		
S0	1353 (42)	1589 (42)	----	2695 (74)	2945 (72)	2.5	1.1
S1	1359 (97)	1587 (98)	2218	2723	2936	1.3	0.2
S2	1361 (107)	1588 (108)	2218	2712	2941	1.3	0.3
S3	1361 (104)	1592 (103)	2218	2704	2939	1.3	0.3

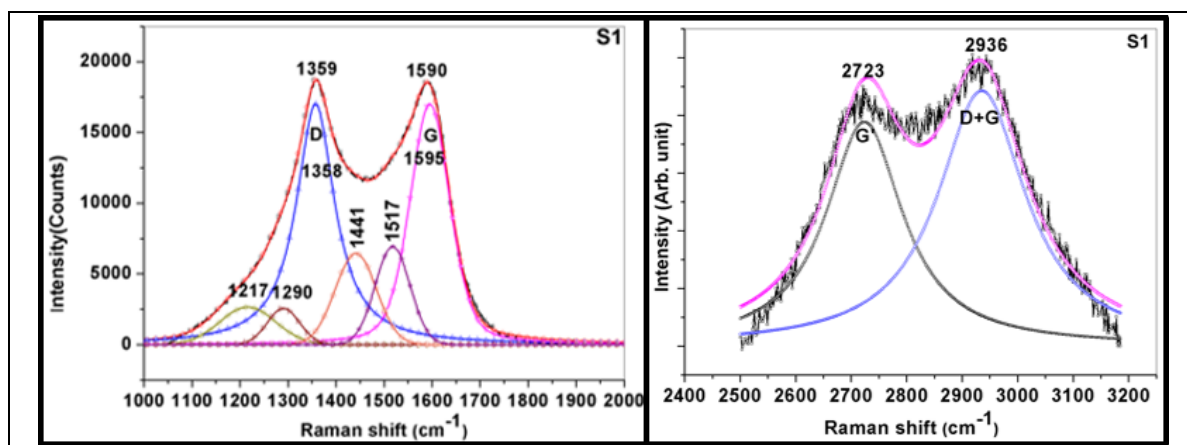


Fig. 5.5 Deconvolution of Raman spectrum of S1. The G-peak shown is formed by the merger of G and D' peaks of pristine. The peaks at $\sim 1441\text{ cm}^{-1}$ and $\sim 1517\text{ cm}^{-1}$ (A- peaks) are due to fullerene and other structural defects. The peaks at ~ 1217 and ~ 1290 (T-peaks) are due to high density of edges, disordered hydrogenated sp^3 carbon and olefinic structure similar to trans polyacetylene. The G' and D+G peaks are also shown.

It is observed that the D and G-peak intensities are reduced upon implantation (Fig. 5.7). Lucchese *et al.*, explained it as due to the reduction in Raman relaxation length due to defects [155]. The D and G' peaks are shifted to high energy and it may be attributed to hardening of $A1g$ phonon mode due to the presence of more electronegative graphitic

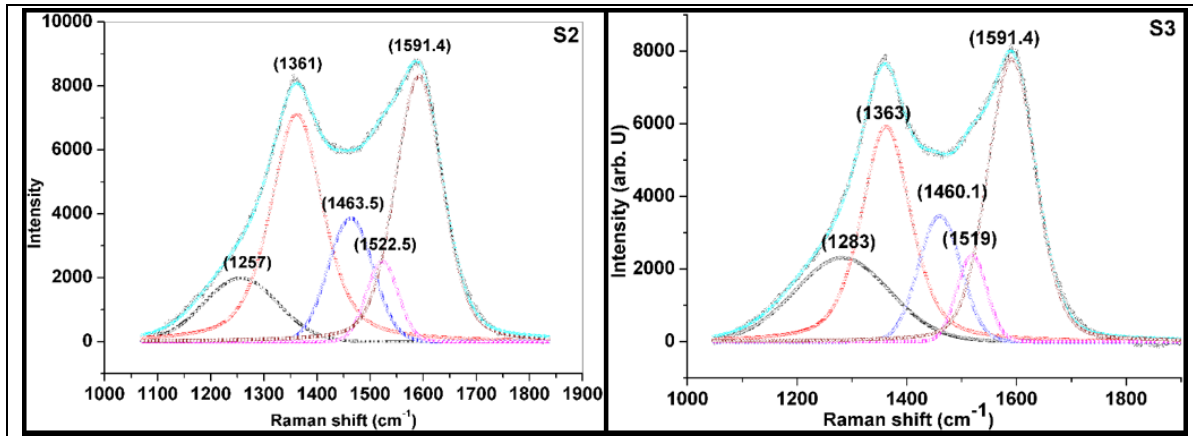


Fig. 5.6 Deconvolution of Raman spectrum of S2 and S3. The peak positions are shown. The G-peak is formed by the merger of G and D' peaks. The peaks at $\sim 1460\text{ cm}^{-1}$ and $\sim 1520\text{ cm}^{-1}$ (A-peaks) are due to fullerene and other structural defects. The peaks at ~ 1257 and ~ 1283 (T-peaks) are due to high density of edges, disordered hydrogenated sp^3 carbon and olefinic structure similar to trans polyacetylene.

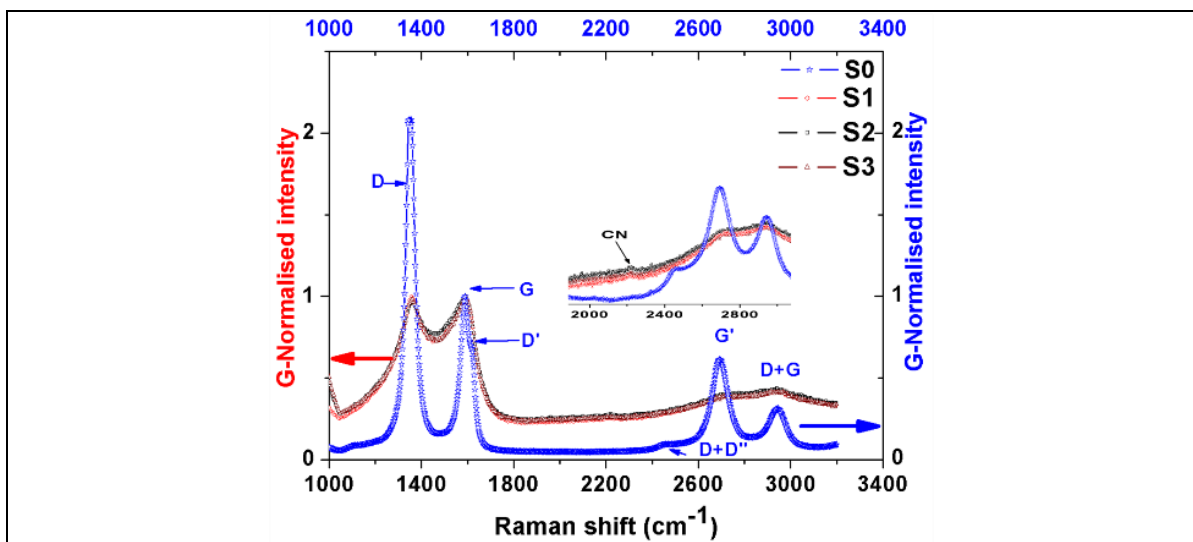


Fig. 5.7 Raman spectrograph of pristine and nitrogen plasma ion implanted samples. The variation in intensity is shown against G-peak. The respective GNWs peaks and $\text{-C}\equiv\text{N}$ are identified. The $\text{C}\equiv\text{N}$ peak is highlighted in the inset.

nitrogen. The pristine sample (S0) shows a well-defined D'-peak as shown in Fig. 5.4. However D' is absent in S1, S2 and S3 (Fig. 5.5 and Fig. 5.6). The small peak at 2218 cm^{-1} shows the generation of $sp^1\text{C}\equiv\text{N}$ type bonding (Fig. 5.7) [263]. Lucchese *et al.*, shown the generation of D'-band at a low dose ion implantation (1×10^{11} ions/ cm^2) and its merger with G-band at a high dose (1×10^{14} ions/ $\text{cm}^2 \sim 10$ atom%) in monolayer graphene [155]. In the current study, all the implanted GNWs contain nearly similar amount of nitrogen (as

discussed in XPS studies later) and the D' band is merged with G-band. This clearly shows that implantation has increased the point defect density.

In addition to the common graphene related peaks a few peaks at lower energy than the D peak and in between D and G peaks are also fitted for the implanted GNWs. These peaks corresponds to T and A peaks [212] and are attributed to defects. Since high dose have generated large amount of defects, it is difficult to assign exact peak position for T and A peaks for the samples S1, S2 and S3. However, a more reasonable treatment of these peaks are given in chapter 6, when the dose and defects are relatively low.

5.2.2. XPS studies

The change in chemical state of carbon due to nitrogen implantation is the subject of interest and is monitored by acquiring the C_{1s} , N_{1s} and O_{1s} spectra. In this chapter, the 1s energy level is used as subscript to atoms to avoid confusion to N1, N2 and N3 type nitrogen as discussed later. The survey spectrum of pristine sample (S0) shows peaks corresponding to carbon and oxygen only (Fig. 5.8.). The Fig. 5.9 shows the de-convoluted C_{1s} spectrum of S0. The peaks at 283.3 eV (1.5 eV), 284.6 eV (1.4 eV) and 285.7 eV (1.5 eV) correspond to hydrogen terminated vacancy (14 at%), sp^2C (56 at%) and sp^3C (17 at%), respectively [140,264]. The origin of hydrogen terminated vacancy peak may be explained. The sp^2C appear at 284.5 eV, in the case of PECVD GNWs the sp^2C peak appear very broad (FWHM >2 eV) and is not considered as typical C_{1s} peak. Barinov et al., indicated four components (284.25, 284, 283.7 and 283.4 eV) for to the vacancy defect for C_{1s} spectrum of HOPG [265].

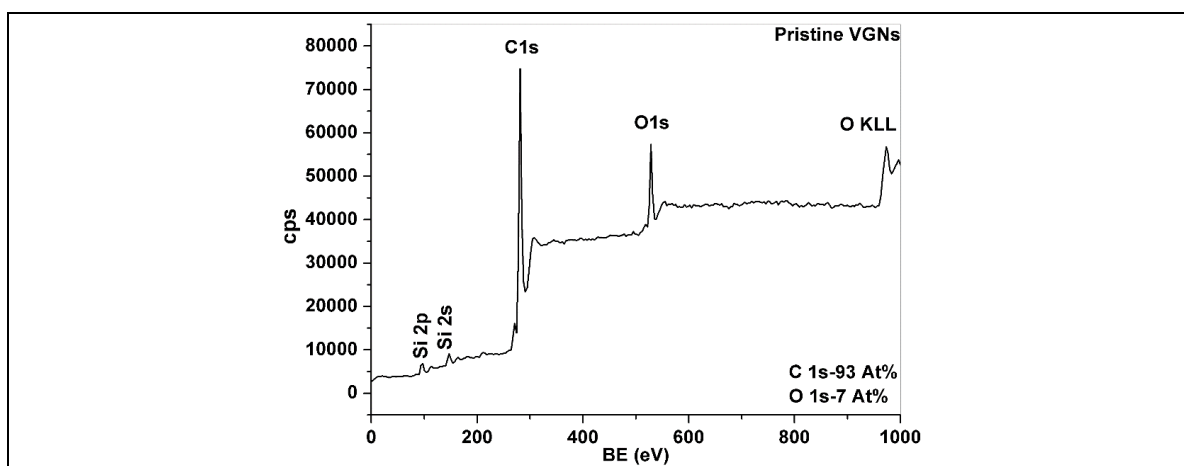


Fig. 5.8 The survey spectrum of photo-electron spectra of pristine GNWs. The peaks are labelled. No peak corresponding to N 1s is seen.

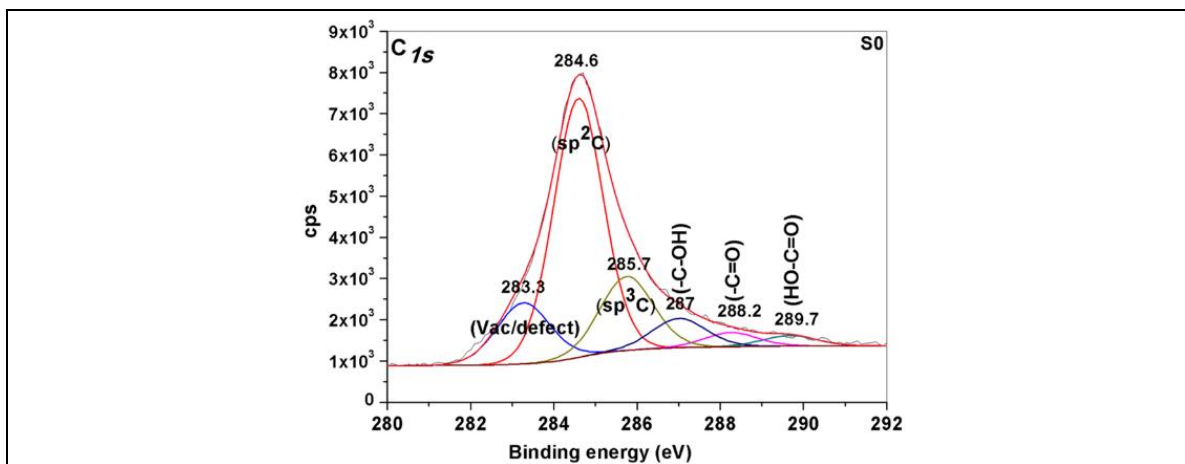


Fig. 5.9 Carbon 1s photo-electron spectra of pristine GNWs. The peaks are labelled.

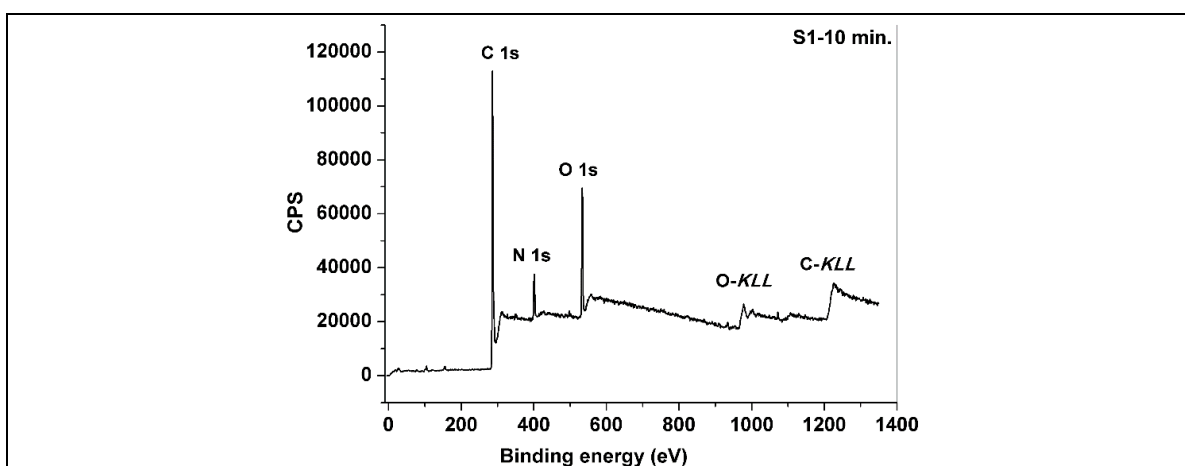


Fig. 5.10 The survey spectrum of S1-Peaks corresponding to carbon, nitrogen and oxygen is given.

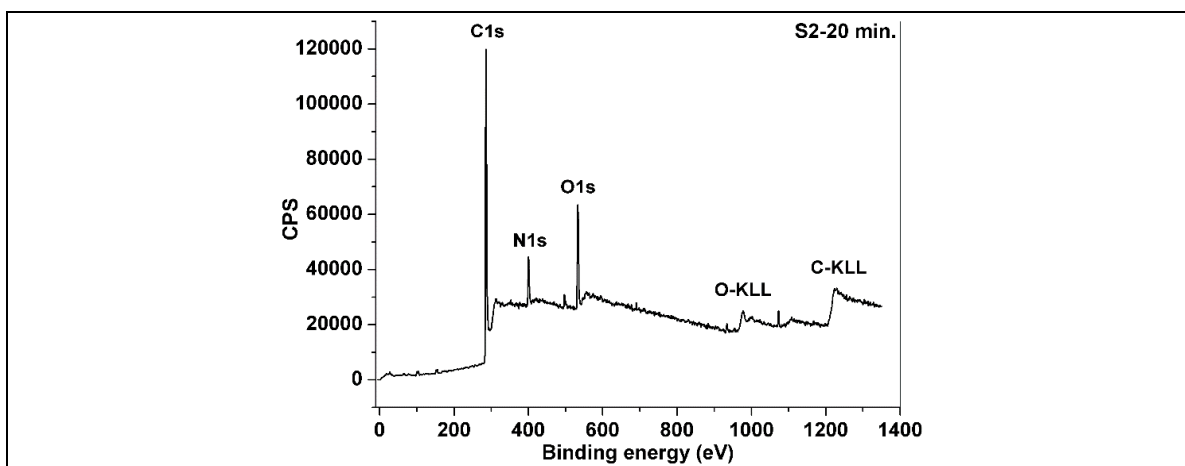


Fig. 5.11 The survey spectrum of S2-Peaks corresponding to carbon, nitrogen and oxygen is given.

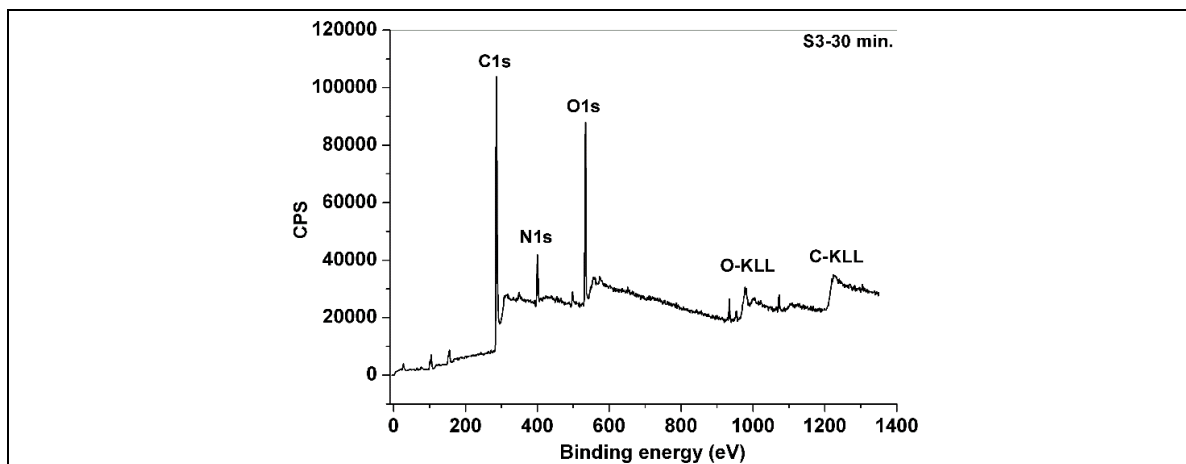


Fig. 5.12 The survey spectrum of S3-Peaks corresponding to carbon, nitrogen and oxygen is given.

Since GNWs are synthesised at high temperature and in presence of hydrogen radical, it is assumed that the vacancies are occupied by hydrogen. Hence, we assign one peak at ~ 283.3 eV as defect (d) peak [140,265,266]. Three peaks at 287 eV (1.5 eV), 288.2 eV (1.5 eV) and 289.7 eV (1.5eV) can be attributed to the functional groups generated on high temperature synthesised carbon due to adsorbed oxygen and /or moisture (13 at%) [140,264,265,267].

The chemical state of implanted samples were studied using XPS. The survey spectrum of S1, S2, and S3 shows peaks corresponding to carbon, nitrogen and oxygen (Fig. 5.10, Fig. 5.11 and Fig. 5.12). From the survey spectrum, the total nitrogen atom percentage in the implanted samples is estimated as 7.6 ± 0.5 , 7.9 ± 0.5 and 8.8 ± 0.5 (at %) for S1, S2 and S3, respectively. Fig. 5.13 shows the deconvoluted C_{1s} XP spectrum (of S1, S2 and S3). The deconvolution results of S1, S2 and S3 are summarised in Table 5.2. The peak assignment of C_{1s} is often ambiguous because of the broadening and overlap of energy levels due to various defects and doping. The peak at 285.2 eV can be assigned to sp^2 type bonding of carbon [146,264,267]. The high intensity peak at 285.8 eV corresponds to sp^3 C [146,264,267] and it shows the sp^2 to sp^3 conversion upon implantation. The peak at ~ 287.4 eV is assigned to sp^3 C bonded with nitrogen and /or oxygen and the other two peaks (at 291.1 and 289.9 eV) are due to sp^3 C bonded with adsorbed oxygen/moisture (Fig. 5.13) [18,121,146,264,268,269]. Fig. 5.14 and Fig. 5.15 shows the N_{1s} XP spectrum of S1, S2 and S3. The N_{1s} spectrum of S1, S2 and S3 are deconvoluted and the results are tabulated in Table 5.3. The N_{1s} peak intensity as deduced from the survey spectrum has only increased marginally with increasing process duration indicating that the implantation rate is not linearly proportional to the process duration. The broad peak centered at

~ 400.7 eV demonstrates multiple chemical states of nitrogen. The nitrogen spectrum was decomposed into three mixed Gaussian-Lorentzian type curves [18,146,264]. Since, nitrogen implantation is carried out for doping graphitic structures, the analysis of nitrogen

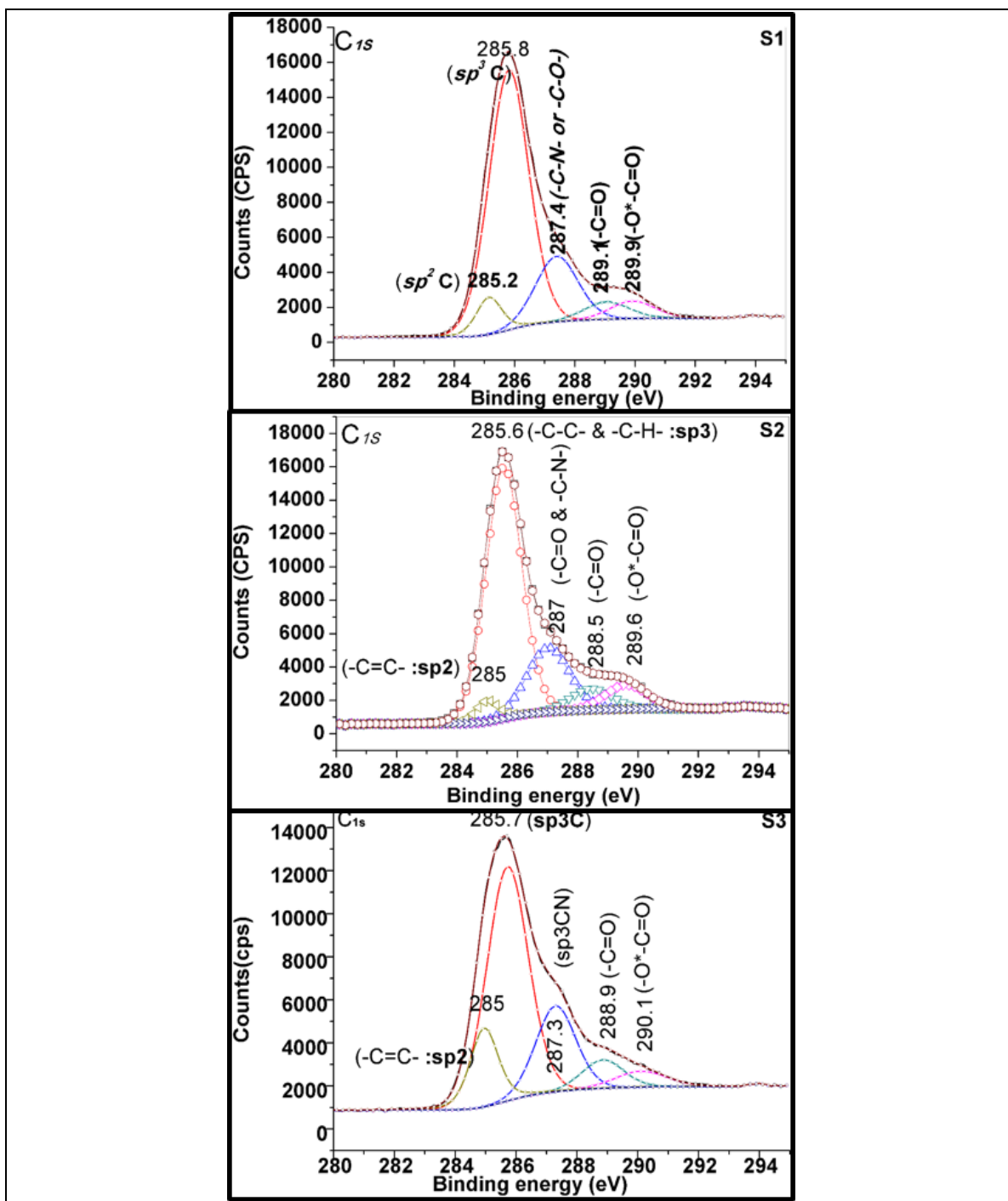


Fig. 5.13 C_{1s}-XP spectrum of S1, S2 and S3. Significant increase in sp³ C was due to structural disorder and destruction of crystalline nature of the sp² C structure at the surface.

Table 5.2 Carbon 1s photoelectron analysis of S1, S2 and S3.

Sample ID	C-(SP2)		C-(SP3)		-CN		-C=O		-O-C=O	
	Position (eV)	At %	Position (eV)	At %	Position (eV)	At %	Position (eV)	At %	Position (eV)	At %
S1	285.2 (1)	6.8	285.8 (1.55)	65.6	287.4 (1.65)	17.6	289.1 (1.75)	5	289.9 (1.75)	5
S2	285 (1)	10.5	285.6 (1.55)	62.1	287 (1.75)	17.8	288.5 (1.85)	4.7	289.6 (1.95)	4.9
S3	285 (1.1)	14.3	285.7 (1.6)	55	287.3 (1.55)	19.5	288.9 (1.6)	6.7	290.1 (1.1)	4.5

bonding state is crucial. There is a lot of ambiguity with respect to assigning of N_{1s} binding energies against the geometrical configuration and naming the nitrogen species as pyridinic, pyrrolic, nitrile like, graphitic, oxidised and quaternary nitrogen [18,29,146]. Hence, a simple method for categorization of nitrogen species based on the status of the lone pair of electrons in nitrogen is adopted. Please note that in this chapter where ever the above names (Pyridinic, pyrrolic, etc.) are referred, it is taken from the respective literature cited. The band structure calculation of non-graphitic (pyridinic-N and pyrrolic-N) N-graphene shown to have p -type character whereas graphitic N-graphene is n -type [270]. Consequently, the N_{1s} binding energy and chemical state are different. However, most of the literature is not keen on specifying the state of nitrogen as graphitic or non-graphitic. A cross over from p -type to n -type has been observed by Lu *et al.*, in the case of CVD grown N-doped graphene [271]. This is attributed to the decrease in pyridinic-N (398.3 eV) and increase in pyrrolic N (399.4 eV) fraction in N-graphene with increased nitrogen doping [271]. Schiros *et al.*, attributed the p -type to n -type transition to hydrogenation of nitrogen [272]. On the other hand, the geometrical cross over from pyrrolic N (399.7 eV) to pyridinic N (398.6 eV) is reported in ion implanted graphene [29]. Both the above changes may be explained. Fundamentally, if nitrogen substitutes a carbon atom and form 3 σ bonds in the hexagonal carbon ring, it cannot be a part of the low energy resonance structure by keeping the lone pair localised. Hence, nitrogen become a part of the resonance structure by sharing 0.5 electrons per nitrogen [272]. As a result, nitrogen becomes electron deficient and the N_{1s} binding energy increases. However, the N-GNWs free electron density increases and it becomes n -type. On the other hand, if nitrogen forms at least 1(or2) σ bond and 2 (or 1) π - bonds, the octet rule are satisfied with its lone pair localised and are fully *available* for the nitrogen. As a result, the system has p -type character. In both cases, the electron density of states changes and is reflected in the band structure as p or n type character. In addition, point defects also influence the bonding state of nitrogen. The pyrrolic (399.7 eV) to

pyridinic (398.6 eV) conversion is correlated with reduction of di vacancy to mono vacancy ratio due to thermal spike (defect generation) during plasma treatment [29]. This indicates that evolution of geometric factors also can change the electronic nature of N-graphene. Further, due to bonding variation with (1 or 2) hydrogen, even identical geometric configurations of pyrrolic or pyridinic nitrogen in graphene is shown to have different chemical nature such as catalytic activity [273].

Hence, it becomes clear that irrespective of the position of nitrogen in the carbon ring, their bonding state with surrounding atoms determines the electronic and chemical nature. Hence, representing the nitrogen configuration in graphene by conventional (pyridinic, pyrrolic, graphitic, nitrile, etc.) naming do not easily convey the electronic and chemical nature, completely. Additionally, nitrogen atom in GNWs can occupy interlayer (quaternary/trapped) position also. This makes the analysis more complex. Consequently, large overlap of N_{1s} binding energies corresponding to pyridinic, pyrrolic, nitrile, graphitic and quaternary nitrogen in graphene have been reported in literature [146]. Hence, there is a need to categorize nitrogen in graphene representing the chemical nature to make it more meaningful. Nitrogen has five valence electrons and usually its valence is three, that the two electrons form a lone pair, not participates in bonding. However, the stable configuration is found to vary from lone pair localised and delocalised due to its location in the ring, proximity to defects or bondings [29,107,270–275]. Hence, in the present study, the N_{1s} spectra was deconvoluted as; nitrogen in the matrix with localised lone pair of electron, termed as N1 (~399.6 eV), nitrogen with lone pair of electrons delocalised, termed as N2 (~400.9 eV) and nitrogen in quaternary configuration, N3 (~402 eV) [269,275–280]. Using first principle calculations, Titantah *et al.*, obtained similar results for amorphous carbon nitride from the XPS spectra by considering the contribution of lone pair on the screening effect on N_{1s} electrons [281]. The schematic representation of each type of nitrogen is shown in Fig. 5.14.

N1- represent the pyridinic N and pyrrolic N attached at the edge and/or at a vacancy in the carbon ring, and nitrile like N attached by a triple bond to the carbon [27,132]. In all the three states, the lone pair electron in nitrogen is localised [18,272]. The localised lone pair of electrons and availability of three paired valence electrons, register lowest N_{1s} binding energy (~399.6 eV). This type of configuration can make N-graphene *p*-type [271,272]. N2- represents graphitic N, with the lone pair delocalised. As mentioned before, delocalization of the lone pair results in supply of 0.5 electron per nitrogen to the graphitic system and the binding energy of N_{1s} photoelectron increases to ~401 eV [272].

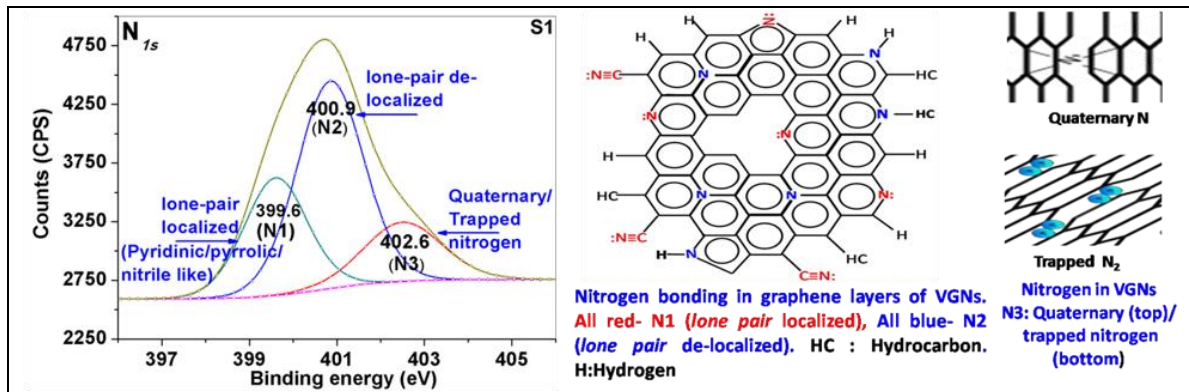


Fig. 5.14 N_{1s} -XP spectrum of nitrogen implanted GNWs (S1) sample. Based on the binding energy of N_{1s} electron, the nitrogen is categorised as lone pair localised (N1), lone pair delocalised (N2) and quaternary and trapped nitrogen (N3). Respective location of nitrogen in implanted GNWs is shown at the right.

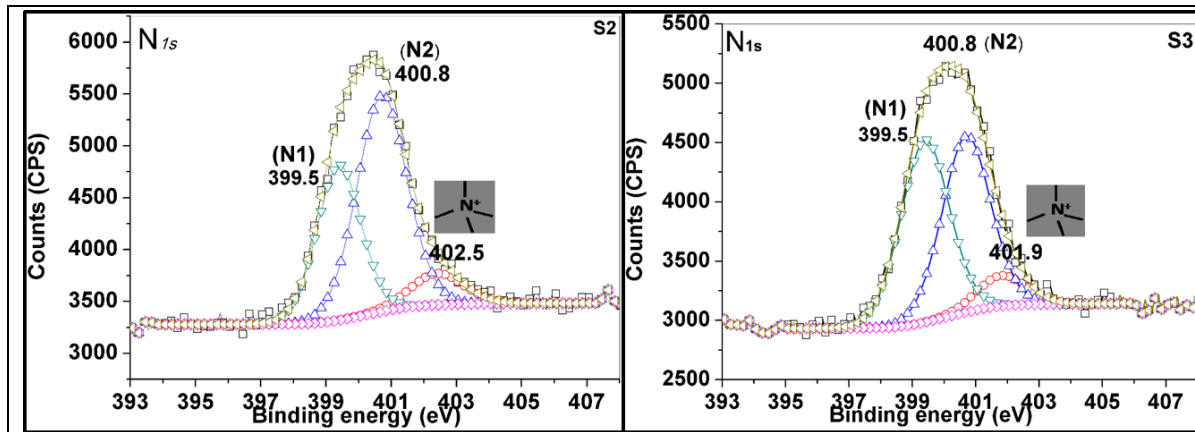


Fig. 5.15 N_{1s} -XP spectrum of nitrogen implanted GNWs (S2 and S3) sample. Based on the binding energy of N_{1s} electron, the nitrogen is categorised as lone pair localised (N1), lone pair delocalised (N2) and quaternary and trapped nitrogen (N3).

Table 5.3 Nitrogen 1s photoelectron analysis of S1, S2 and S3.

Sample ID	Lone pair localised (N1)		Lone pair delocalised (N2)		Trapped N_2 or N bonded to 4 neighbours (Quaternary N) (N3)	
	Position (eV)	At %	Position (eV)	At %	Position (eV)	At %
S1	399.6(1.7)	25.8	400.85(1.8)	53.8	402.5(1.7)	20.4
S2	399.4(1.6)	35.6	400.71(1.8)	55.9	402.41(1.9)	8.5
S3	399.4(1.8)	46.8	400.7(1.8)	45.4	401.8(1.8)	7.8

Thus, graphitic configuration of nitrogen in the ring make it n -type [271,272]. Studies indicated that binding energy in the range of 402-403 eV corresponds to quaternary nitrogen

(N3) and not due to oxidised nitrogen [18,281]. The quaternary nitrogen occupies the interlayer position and is bonded to 4 carbon atoms. Nitrogen with 4 σ - bonds will have an *extra* electron in nitrogen and is not permitted. Hence, the *extra* electron is transferred to the graphitic system leaving one unit positive charge on nitrogen. This leads to enhanced

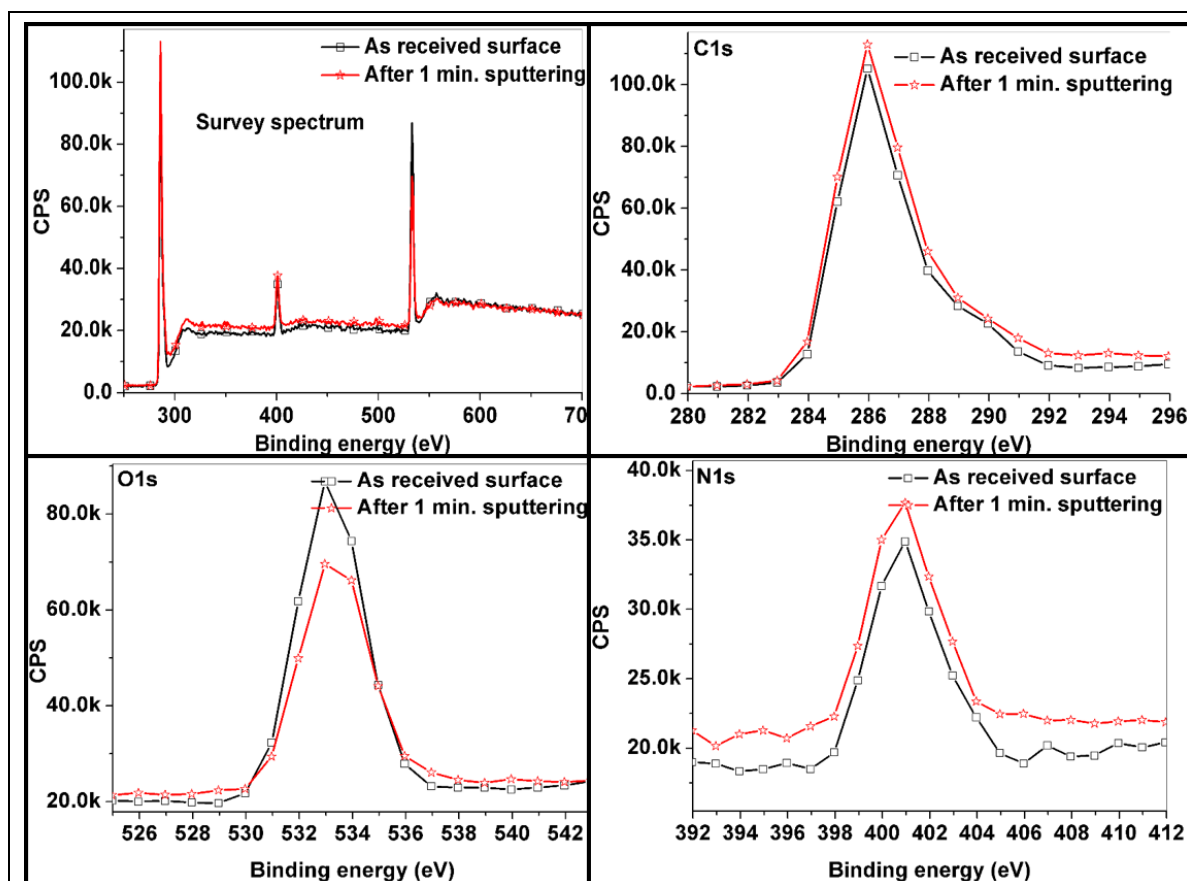


Fig.5.16 Survey spectrum of SI: As-received and after 1 min. Ar- ion sputtering. The O1s peak shows a reduction in photoelectron intensity by 20-30 % after sputtering.

binding energy of core electrons. Hence, in the present study, the N_{1s} binding energy of 402.6 eV is assigned to nitrogen occupying the interlayer position with bonding to 4 carbon atoms (i.e., nitrogen in the quaternary position (N3)). There are reports in literature that binding energy in the range of 402-403 eV can also be due to trapped nitrogen [223,227,282,283]. However, we will follow N3 configuration as chemically bonded nitrogen in between two layers. GNWs have a layered graphitic structure. DFT simulation on graphitic layers showed the structural damage as (a) C_{2v} vacancy (b) spiro-interstitial (C_2 symmetry) and (c) Diens (defect with C_{2v} symmetry) [284]. Nitrogen attached to the ring adjacent to a C_{2v} vacancy energetically prefers to have lone pair localised nitrogen (N1) configuration (C_{2v} vacancy implies *mono* (odd) vacancy, di vacancy

give C_{2h} symmetry). Sumet *et al.*, experimentally proved that high energy projectile produce larger number of mono vacancy and nitrogen

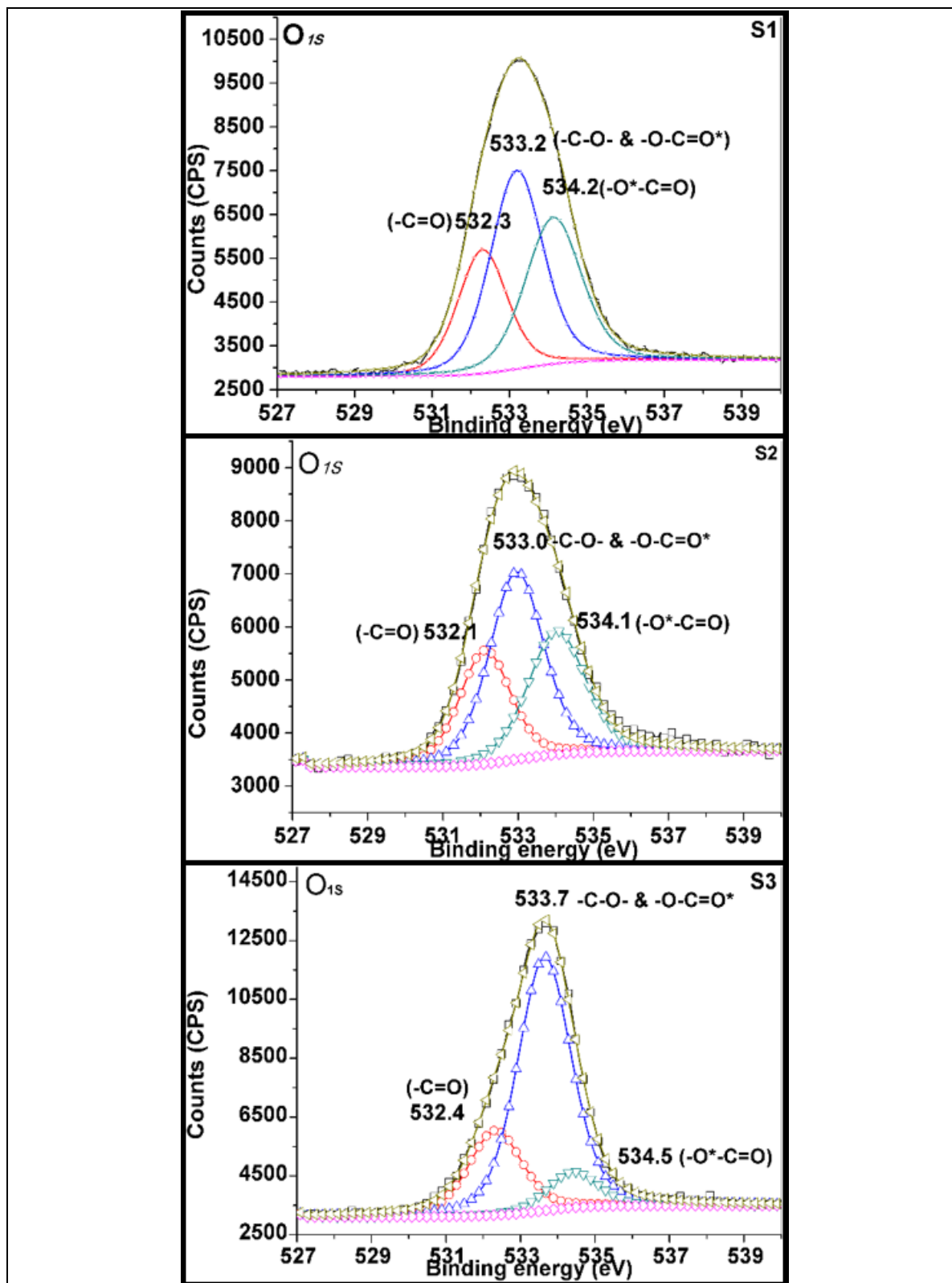


Fig. 5.17 O_{1s} -XPS spectra of nitrogen implanted GNWs (S1, S2 and S3) sample. Oxygen is attached or deposited to the GNWs inadvertently due to exposure of the sample to atmosphere (O_2 and H_2O).

Table 5.4 Oxygen 1s photoelectron analysis of S1, S2 and S3.

Sample ID	-C=O		-C-O-		-O*-C=O	
	Position(eV)	At %	Position(eV)	At %	Position(eV)	At %
S1	532.3(1.5)	24.7	533.19(1.6)	42.2	534.13(1.7)	33.1
S2	531.12(1.6)	25.1	532.96(1.7)	44.1	534.03(1.8)	30.8
S3	532.33(1.7)	22.7	533.64(1.8)	68.2	534.4(1.6)	9.1

prefers to have pyridinic (here, N1) configuration [29]. Nitrogen and carbon in spiro-interstitial (C_2 symmetry) is similar to quaternary (N3) nitrogen and sp^3 bonded carbon, respectively [284]. The Diens, defect constitutes both pentagonal and heptagonal rings and have similar structural configuration of Stone-Walace defect. In Diens, having C_{2v} symmetry, nitrogen can have N1 and/or N2 configurations [135,284]. Nitrogen plasma exposure or post treatment ion implantation is reported to induce relatively more pyrrolic configuration in a di vacancy or Stone-Walace defect [29] (it can be N1 or N2 type depending on the status of lone pair of electrons). Hence, the theoretical assessment of defect formation in graphitic systems can be correlated with experimental results in literature to validate the geometrical basis for categorization of nitrogen status in 3D graphene structures.

Fig.5.16 shows the survey spectrum of pristine and 1 minute surface sputtered GNWs by Ar^+ ions inside the XPS chamber. The O_{1s} peak shows a reduction in photoelectron intensity by 20-30 % after sputtering. This indicates that the oxygen present in the implanted samples are surface adsorbed. Fig. 5.17 shows the O_{1s} XP spectrum of *S1*, *S2* and *S3*. The O_{1s} spectrum of *S1*, *S2* and *S3* were deconvoluted and the results are tabulated in Table 5.4. The broad oxygen peak at around 533 eV is fitted with three curves as shown in Fig. 5.17. The relative peak positions, in the samples, remain nearly the same with a small difference in intensity. The major peak at 533.2 eV (O1) is assigned to oxygen bonded with two carbon, 534.2 eV (O2) peak is two oxygen attached to one carbon and the peak at 532.3 eV (O3) is assigned to oxygen double bonded with carbon [146]. Oxygen showed 20-30 % reduction in photo-electron intensity after 1 minute of argon ion sputtering inside the XPS chamber. Hence, it is clear that oxygen remain in surface adsorbed state.

5.2.3. Atomic Force Acoustic Microscopic studies

Fig. 5.18 shows the concurrent atomic force microscopic (AFM) and atomic force acoustic microscopic (AFAM) images collected from *S0* and *S1* samples. Similar images are taken for *S2* and *S3*. AFM images shows marginal increase in surface roughness with implantation (Ra of *S0* is $\leq 6 \pm 0.5$ nm and that of *S1* is 7.5 ± 0.5 nm). Since the vertical walls

bend upon AFM tip contact, the images did not show well defined vertical walls. AFAM image shows the spatial distribution of elastic modulus. Since the sample vibrates perpendicular to the sample surface, it measures the stiffness of buckled region; that the measurements has a considerable flexural component around the GNWs [285]. Hence, we have attempted a semi-quantitative analysis by comparing the relative stiffness of $S0$ and those under different implantation conditions. Implanted samples showed contact resonance frequency (CRF) higher than $S0$ indicating an increase in stiffness constant. The peak feedback current of $S1$ (Fig. 5.18 b and d) shows that relative stiffness is increased more than 2-3 times the value of $S0$. Further, image analysis of AFAM showed that pristine sample (Fig. 5.18) has 10% of region harder than the rest. Whereas, nitrogen ion implanted GNWs (Fig. 5.18) have more than 50% of the region harder than the rest. Similar measurements were carried out on $S2$ and $S3$ samples also. Fig. 5.19 shows the comparison of the stiffness of the $S0$, $S1$, $S2$ and $S3$.

5.3. Discussion

Up on biasing the substrate, both N^+ and N_2^+ ions in the nitrogen plasma impinge on the substrate surface and get neutralised via a resonant or Auger neutralization mechanism [286]. Further, an incoming ion can transfer its energy and/or charge to another atom that a neutral atom /molecule with high energy can also get implanted [261]. Since the plasma is biased to a target having vertically layered structure with corrugated morphology, implantation takes place at different acquired energies and at various angles. The incoming projectile produce point defects such as vacancies, interstitials and ad-atoms by momentum transfer in primary, secondary and high energy knock-on N-C collisions [284]. The minimum displacement energy of carbon for normal *head-on-collision* is ~ 25 eV [287].

In the course of point defect formation, interstitials are formed in excess [287]. Additionally, a considerable portion of the projectile and knocked out carbon atoms occupies vacant lattice positions, as well as finds a space in between the layers. Hence, several possible combinations of interaction between carbon and nitrogen are possible. Accordingly, the results are discussed to understand the structural and chemical changes in GNWs on plasma nitrogen ion implantation.

For N^+ ions, at 2kV bias, the peaks of ion and defect depth profiles are at ~ 6 nm and 2.5 nm, respectively (Fig.5.2). Since N_2^+ ions have almost double the mass, half of the above values shall be assigned. Upon entering the sample, the molecular nitrogen ions (N_2^+) were

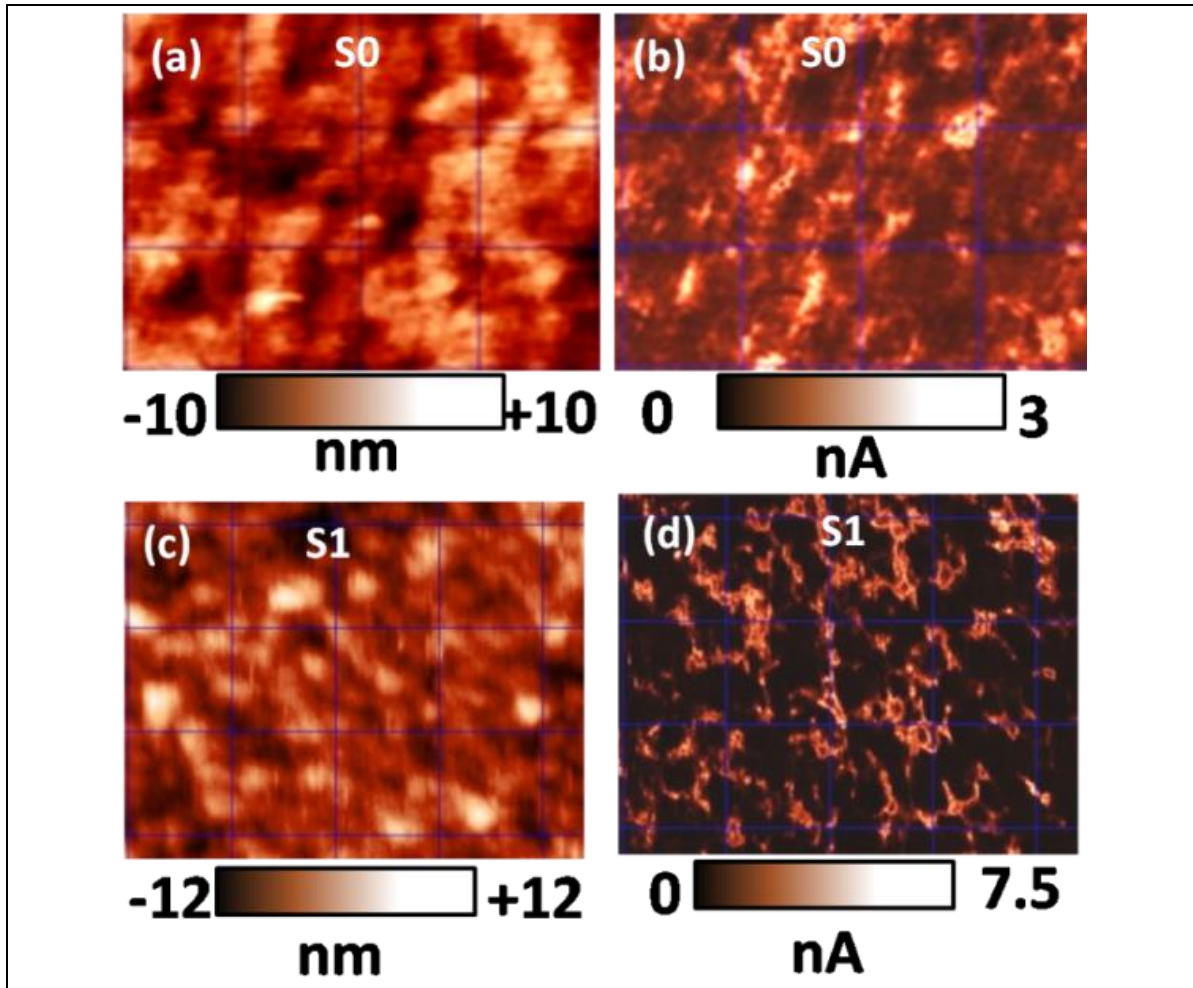


Fig. 5.18 AFM (figures (a) and (c)) and AFAM (figures (b) and (d)) images of S0 and S1, respectively. The scan area is $2.5 \mu\text{m}^2$ in all the images. The scale bar for topography (AFM) and AFAM feedback signal in nano ampere are given just below the respective images. The acoustic force feedback signal in S1 is more than 2 times the value of S0. The stiffness constant derived from the AFAM of S1 (as seen from fig. (d)) is ~ 2 times higher than stiffness constant of S0 (fig. (b)).

dissociated into two nitrogen atoms with shared kinetic energies and conserved momentum. Being N_2^+ ions constitute 75-80% of the ions in *rf*-nitrogen plasma [288,289] and have approximately half the penetration depth of N^+ ions, the defect produced by N_2^+ ions dominate the region near the surface whereas deep regions are influenced by N^+ ions. Hence, the region of interaction of N_2^+ ions is nearer to the surface compared to that of N^+ ions.

However, the scenario is slightly complex due to the morphological factors of GNWs. GNWs have a thin edge and a fat bottom and because of the overlapping sheath, implantation is mostly confined to the top regions and is continuously sputter removed. This prevents the accumulation of low energy ions more than high energy ones. Hence, the

nitrogen fraction is not doubled or tripled with corresponding increase in process time. Since the penetration of N^+ ions is considered to be almost double that of N_2^+ ions, the tail of N^+ ions profile reach deeper than that of N_2^+ ions and is retained more in samples implanted for longer duration. Additionally, the GNWs don't have a close packing (ABAB type) for the vertical walls similar to HOPG. Hence, the space in between two layers can offer free path ways for *channeling* of *small* N^+ ions than *big* N_2^+ ions. XPS being a surface technique, collect information from the top 3nm thickness and carry vital data to distinguish the effect of N^+ and N_2^+ ions. At half the energy ion implantation (N_2^+ ions), the above values can be reduced by half and hence, the collision cascade intercepts the surface and cause excessive sputtering of material. Since the range of N_2^+ ions is ~ 3 nm and defect peak is at ~ 1.3 nm, the N_2^+ ions induced changes are relatively more reflected in XPS measurements than that of N^+ ions, which has range and defect peaks at ~ 6 nm and at ~ 3 nm, respectively. For N^+ ions the range is more than what is estimated and larger part of the range and tail of defect profile will be relatively less sputtered than N_2^+ ions. Hence, we assign that the peak characteristics observed in S1, S2 and S3 have identical contribution from N_2^+ ions and relatively more cumulative contribution of N^+ ions.

Raman and XPS studies show that pristine graphene is largely sp^2C bonded and plasma implantation causes large scale sp^2C to sp^3C conversion due to defect generation. A defect free assembly of graphitic layers does not have any chemical bonding between the layers. However, GNWs inherit a large number of defects and these defective sheets can form bonds with adjacent atoms of neighboring sheets [108]. An interlayer carbon or nitrogen can form four bonds and hence induce sp^2 to sp^3 coordination. Hence, the reason for the large scale sp^2C to sp^3C conversion as observed in neutron irradiated polycrystalline graphite [290]. In the present study, after the initial buildup of sp^3 coordination on implantation, there was a reduction in sp^3C content (66% to 55%) and an increase in sp^2C content from S1 to S3 (7% to 14%) as shown in table 5.2. This can be attributed to the exposure of unimplanted regions which were screened by the sheath. Further, the growth model shows that GNWs grow as layers supported from the bottom and the top will have lesser number of layers than the bottom [70]. As a result, with process duration sputter removal of GNWs exposed more vertical layers, that the effective change per layer induced by the impinging ions is reduced.

The graphene layers in pristine GNWs are highly defective (point defect, SW defects, etc.) [291]. It is indicated that high energy nitrogen ion (4keV) implantation prefer to stabilize pyridinic N (here N1) in a mono vacancy, whereas low energy nitrogen ions

implantation ($\sim 100\text{eV}$), stabilizes pyrrolic N (here N2) in a di-vacancy [29]. The defective graphene layers, even on just exposure to low energy plasma can undergo exothermic pyrrolic nitrogen (399.7eV , here N2 type) incorporation at defects [29,292]. Hence, the sample S1 exposed to 10 minutes of implantation shows relatively high fraction of N2 type nitrogen (Table 5.3). Sample S2 and S3 show an increase in N1 fraction with increasing plasma exposure (Table 5.3). That is, as the duration of implantation increases, the effect of high energy (N^+) tail is more prominent in graphitic layers and large number of edge atoms with dangling bonds are formed, so that the incoming nitrogen atoms preferably occupy the edges causing an increase in N1 type nitrogen.

Sumet *et al.*, showed that the probability of mono vacancy production is high for high energy and longer plasma ion implantation process which stabilize pyridinic (N1 here) (398.6eV) nitrogen [29]. Hence, with increase in implantation duration, N1 fraction increases. The reduction in *quaternary* nitrogen in S2 and S3 can be attributed to the decrease in interlayer area due to successive sputtering and concomitant increases in edges which prefer to have N1 type configuration [293]. Hence, with increase in process duration, N1 type nitrogen was increased whereas, N2 type and N3 types are decreased.

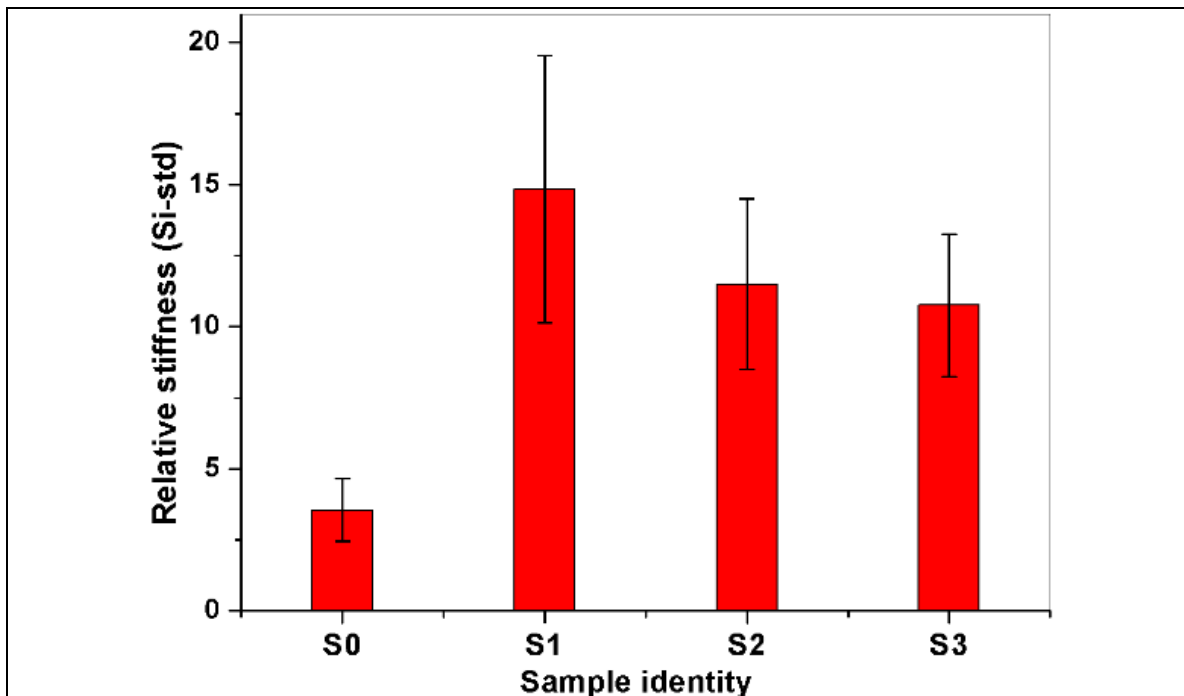


Fig. 5.19 Relative stiffness calculated against standard Silicon. Highest change in stiffness was observed in S1.

Significant increase in elastic properties was observed by AFAM measurements for implanted GNWs compared to pristine GNWs. Theoretical studies on nitrogen incorporated graphene layers have indicated curvature formation and cross linking leading to the formation of fullerene like CN_x (FL CN_x) [291]. The sample *S1* was having 53.8 % N2 type and 20.4 % N3 type nitrogen, and can generate FL CN_x with inter linked layers [278]. A carbon atom in between two graphitic layers induces local bonding which in turn introduce changes in the stacking sequence leading to bulge, curvature, cross linking of the layers and compressive strain [278,284]. GNWs experiencing compressive strain are further stiffened under low dose irradiation [294]. Hence, the increased stiffness constant is attributed to disorder/curvature induced stiffening, cross linking and CN_x formation. Additionally, the increased stiffness of implanted GNWs is attributed to the conversion of flexible sp^2C bonding (in *S0*) into the tight binding induced by sp^3C (in *S1*) type bonding. However, increasing the duration to 30 minutes reduces sp^3 fraction and the N2 and N3 type nitrogen (Table.2 and Table.3). As a result, the relative stiffness is reduced even though C-N fraction has increased marginally (Table 2) and Fig. 5.19.

A largely sp^2 C bonded GNWs is converted into sp^3 C bonded, due to structural and chemical changes produced by implantation. Raman spectroscopy has distinguished the above changes as shift of D and G' peaks to high values and increased FWHM. Knocked out carbon and implanted nitrogen occupy defects, graphitic carbon ring and interlayer positions. At 10 minutes of implantation, the interlayer deposited carbon and nitrogen form four bonds with nearby carbon atoms in the nitrogenated graphitic layers to facilitate cross linking of layers resulting an increase in stiffness constant.

Summary

Structural integrity and evolution of the chemical structure decide the aptness of surface modification process in nanostructured materials. PECVD synthesised pristine GNWs (*S0*) are nitrogen plasma ion implanted at 2kV for 10 (*S1*), 20 (*S2*) and 30 (*S3*) - minutes to study the effect of implantation on structure and chemistry using SEM, RS, XPS and AFM techniques. No obvious morphological changes due to sputtering are observed in *S1*. Whereas, the substrate surface become visible along with GNWs in *S3*. Defect formation is observed as reduction in I_D/I_G and $I_{G'}/I_G$ ratio and increase in FWHM and background intensity. However, the *G-peak* normalised Raman spectrum has indicated that the extent of defect generation is similar in the implanted samples. The shift of *D* and

G' peaks to higher energies indicate hardening of A_{1g} phonon mode due to more electronegative nitrogen in the hexagonal ring. No obvious shift in G -peak observed.

XPS study showed that the sample $S0$ is largely graphitic, whereas implanted samples were largely sp^3 C hybridised. Based on the N_{1s} binding energy, the bonding configurations of nitrogen in GNWs were categorised as N1, N2 and N3 type with lone pair localised, lone pair de-localised and quaternary nitrogen, respectively. In the beginning, N2 type and N3 type configuration are dominated and its effect is reflected as increased stiffness constant in $S1$ from AFAM studies. With increase in process duration, there is enhanced formation of edges which leads to increased N1 type configuration and reduction in interlayer linking. As a result, $S3$ exhibited a lower stiffness constant than $S1$. The new method of categorization of N implanted GNWs represent the actual chemical state of N-GNWs and is more useful for tuning the process parameters towards the desired doping.

Chapter 6

Low dose nitrogen plasma ion implantation of graphene nanowalls

Low dose and low energy nitrogen plasma implantation studies of GNWs is described in this chapter. GNWs are deposited both on Si wafer and carbon paper. The effects of implantation are studied with the help of SEM, water contact angle, Raman, FTIR spectroscopy and XPS. The GNWs deposited on carbon paper is further characterised using cyclic-voltammetry and charge-discharge studies towards exploring possible supercapacitor applications. The possible reasons for the enormous increase in areal capacitance of 2 min. implanted sample are briefly discussed.

6.1. Introduction

The basic requirement in the study is to introduce nitrogen into GNWs by plasma ion implantation with minimum damage to the hexagonal network and evaluate the properties. Structural damage occurring to materials are directly related to energy and dose of implantation. Hence, projectiles of low energy and high reactivity can be implanted for a low duration (dose). It has been reported in literature that N^+ ions is more reactive than N_2^+ ions [226]. Additionally, the XPS studies on nitrogen plasma implanted Ti (Chapter 3) has indicated that Ti to TiN conversion is more prominent at the interior indicating the high reactivity of N^+ ions over N_2^+ ions. Hence, conditions conducive for N^+ ions need to be selected. The implantation study on silicon (Chapter 3) has shown that high power (100W) nitrogen plasma constitutes more of N^+ or N^* species and the surface is populated with more nitrogen than the interior, at a low implantation duration (2 min.). Hence, similar plasma conditions (100 W) is selected for plasma generation for implantation. Details of the experimental process, materials and methods are given in the next section.

6.2. Process, Materials and Methods

The schematic of the PECVD system and plasma ion implantation setup used for sample preparation are given in Chapter 4 (Fig.4.1) and Chapter 5 (Fig.5.1) respectively. Prior to GNWs deposition, all the silicon wafer substrates were surface cleaned using argon plasma at 60W for 10 minutes. The optimised process gas ratio, $Ar:CH_4 :: 3:1$ and conditions described in chapter 4 are used for the synthesis of 4 numbers of GNWs on Si and carbon paper substrates. All the GNWs samples are vacuum annealed at the same deposition temperature (800 °C) for 90 minutes and vacuum cooled to room temperature in

60 minutes. High pure (99.97%) nitrogen was fed into the chamber and plasma was created at 100W (150W forward) RF power. Both RF plasma power (100W) and chamber process pressure (4.2×10^{-3} mbar) were kept constant during the process. All the samples (3 numbers of GNWs on Si_{<100>} and 3 numbers of GNWs on carbon paper) are loaded into the PIII chamber together. A low bias voltage (-1 kV) is selected to minimise the energy of the projectile and thus the structural damage. The same biasing conditions (0.1 kHz, 45µs) used in previous studies are selected and monitored for the voltage and current output from the pulsed dc supply through a digital oscilloscope (Agilent DSO 5012A) to control the process and dose. Two samples (1 Si and 1 carbon paper) are removed each after 2, 4 and 8 minutes of implantation. A maximum nitrogen concentration ~6 at% is obtained in the implanted GNWs (as discussed later in XPS studies). The samples are studied for the chemical and structural changes.

No post implantation annealing was carried out on these samples. The samples were examined using FESEM, wetting contact angle measurement setup, Raman spectroscope, FTIR spectroscope, XPS and electrochemical work station.

6.3. Results

Fig. 6.1 shows the FESEM images of pristine and implanted GNWs on Si substrate. The GNWs have grown to a height of ~350 nm over SiO₂/Si substrate in 3 hrs. After 8 minute of implantation, 20 nm (max.) of material is sputter removed which is equal to ~5 % of the GNWs thickness. However, it is difficult to correlate the change in surface morphology with the extent of sputtering from the SEM images. In general, the morphology appear similar for the samples.

Fig. 6.2 shows the SEM image of carbon paper (CP) showing its fibrous structure. Carbon paper has been used in electrochemical studies as electrode (e.g. fuel cell) owing to its conducting nature along with large surface area. In the present study also, both the above properties are utilised. Fig. 6.3 shows the SEM image of GNWs deposited on carbon paper at different magnifications. It can be seen that GNWs are deposited uniformly on the entire surface of carbon fibres. Fig. 6.4 shows the SEM image of pristine GNWs and those implanted for 2, 4 and 8 minutes. The SEM images show some variation in the morphology of GNWs on CP with implantation duration. For the GNWs deposited on carbon paper there can be substrate influence in the data for certain sensitive examinations due to the fact that both substrate and sample are carbon based. In order to avoid the interfering effects, some sensitive characterisations (Raman, FTIR and XPS) are conducted in GNWs deposited on

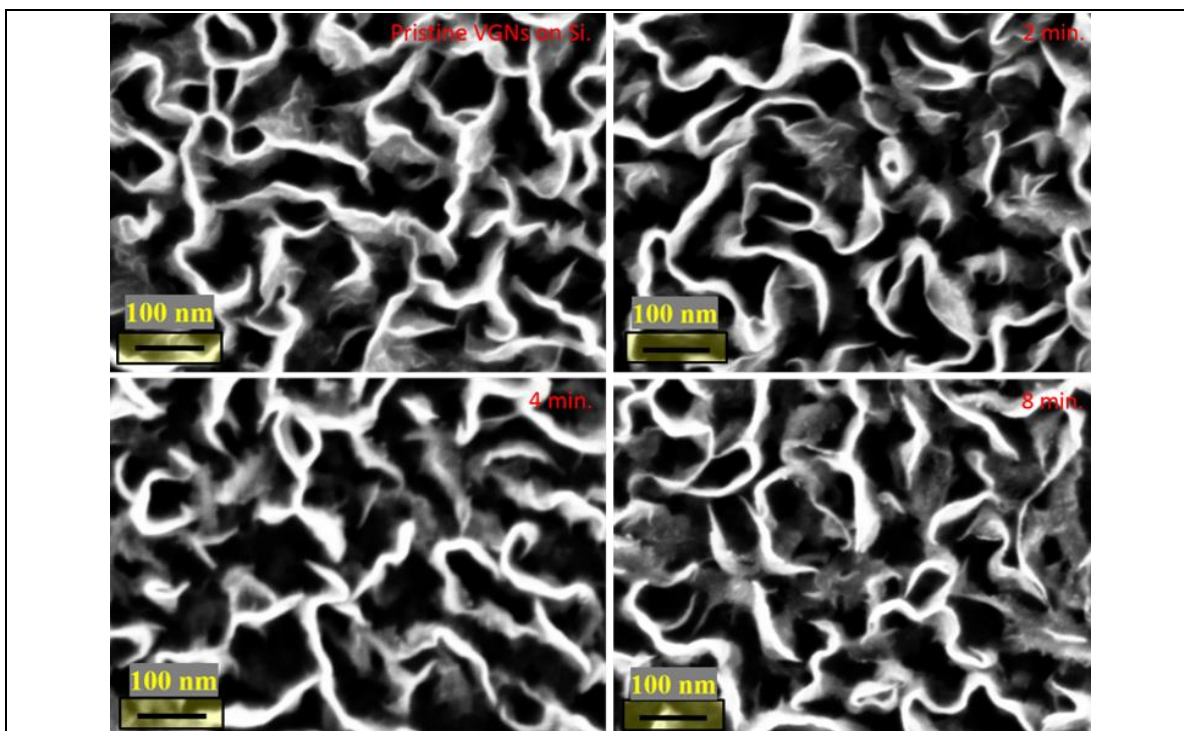


Fig. 6.1 SEM images showing the surface morphology of GNWs on SiO₂/Si substrate. No visible change in morphology could be seen with implantation duration (as shown in the right corner of the images).

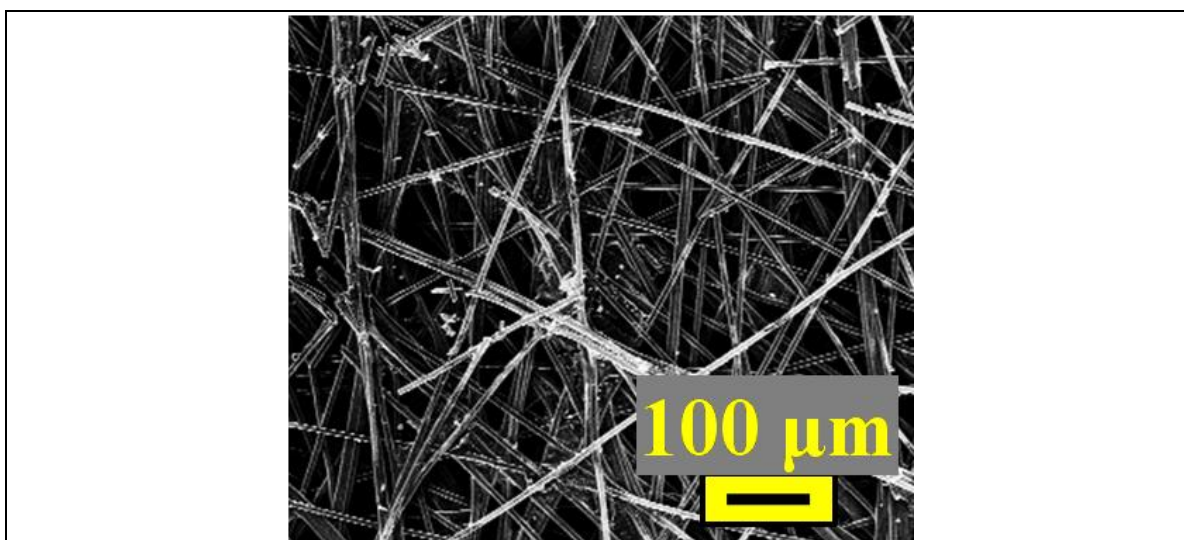


Fig. 6.2 SEM image of carbon paper reveals the fibrous nature and thus large surface area.

Si, subjected to all synthesis processes carried out side by side with the carbon paper. However, the water contact angle (CA) and electrochemical studies are conducted on the GNWs deposited on carbon paper. In the following the section, the analytical characterisation of N-GNWs is discussed followed by the electrochemical characterisation of N-GNWs on carbon paper.

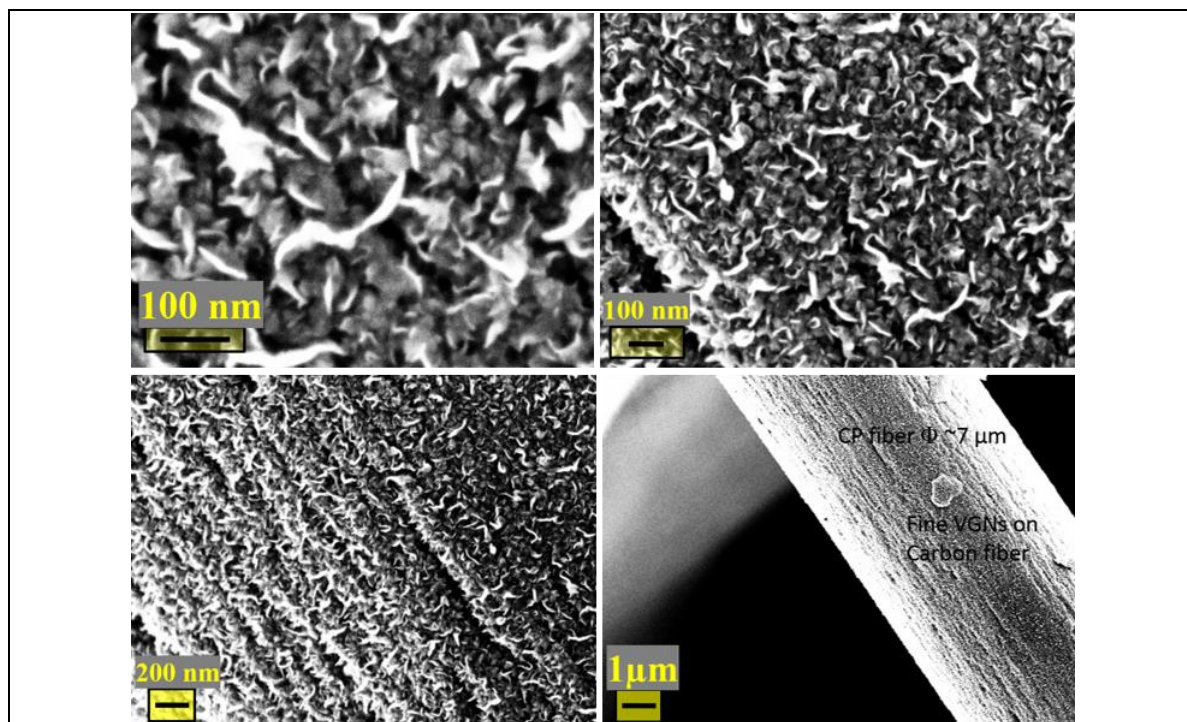


Fig. 6.3 SEM image shows the full coverage of surface area of carbon fibre by GNWs at different magnifications.

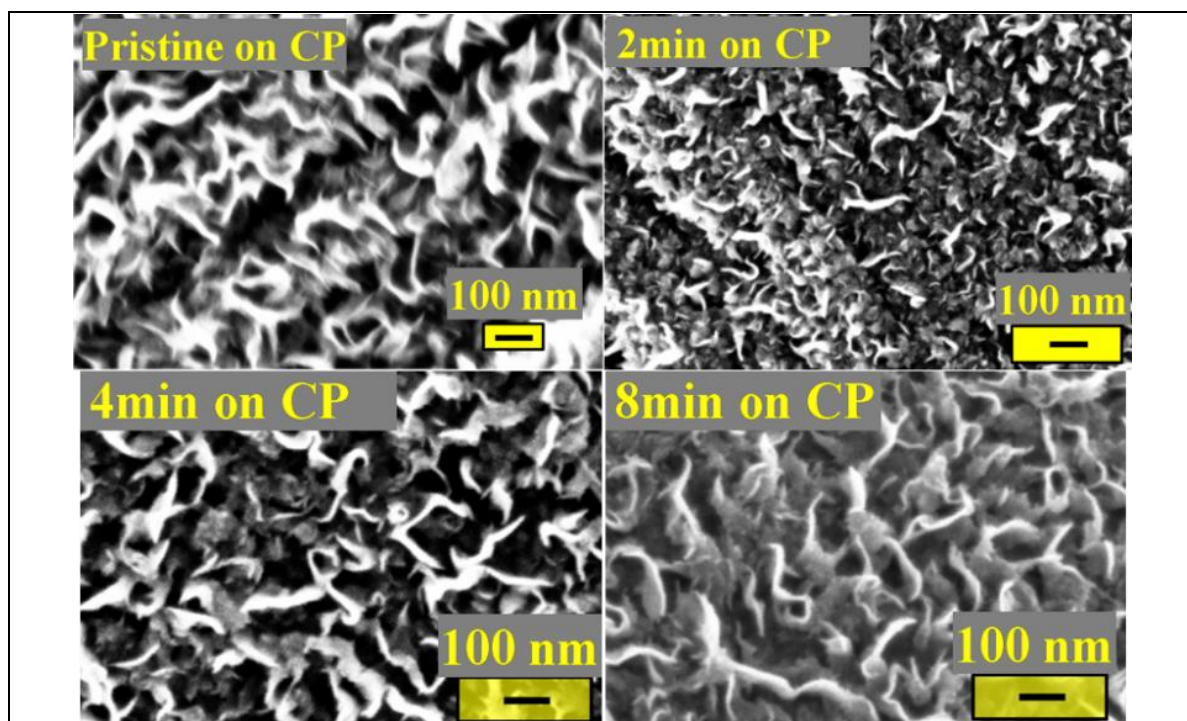


Fig. 6.4 GNWs on carbon paper pristine and nitrogen plasma implanted for 2, 4 and 8 minutes. With increase in implantation duration etch removal of material increases.

SRIM simulation of range of nitrogen ion in graphite at 1keV energy indicate ~ 3.4 nm peak range for the ions. However, in the case of GNWs this value cannot be taken rigorously.

Because, the materials under consideration for SRIM is graphite and it (graphite) has a higher density and different crystal packing as compared to GNWs. Since, GNWs constitute a few graphene layers oriented vertically, the N-ions will penetrate several layers many times depend on the angle and energy of the projectile. Hence, the range measured using SRIM is an approximate value. Additionally, as discussed in the previous chapter, both deposition and sputtering takes place simultaneously. However, the present study did not intent to analyse the implantation process; but, the change in surface chemistry and its influence on the electrochemical properties.

6.3.1. Raman spectroscopic studies

Fig. 6.5 shows the deconvoluted Raman spectrum of pristine and plasma nitrogen implanted GNWs for 2, 4 and 8 minutes. Regular description of peaks and its origin and the effects of implantation are omitted to avoid repetition with previous chapters.

Table 6.1 shows the results of deconvolution of the Raman spectra. All the major peaks are identified and labelled in Fig. 6.5 [230]. The D' peak is getting merged with G band in the implanted samples. All the peak positions are changed due to implantation. The G peak is shifted to higher energy and may be associated to merger with D' peak on implantation [295]. The *D* and *G'* peaks are shifted to higher energy and it may be attributed to hardening of A_{1g} phonon mode due to the presence of more electronegative graphitic nitrogen.

Table 6.1 Results of deconvolution of Raman spectra.

Sample ID	Peak position (cm ⁻¹)							I _D /I _G	I _{G'} /I _G
	T	D	A	G	D'	G'	D+G		
Pristine	1175	1349	1547	1595	1623	2688	2939	3.6	1.26
2 min.	1226	1349	1545	1601	-	2690	2941	3.12	1.4
4 min.	1232	1350	1544	1601	-	2692	2939	3.12	1.20
8 min.	1230	1356	1526	1605	-	2697	2939	2.93	0.56

In addition to the regular D, G, D', G' and D+G peaks above, two wide peaks named as T and A are also deconvoluted. In the pristine sample T peak occurs at 1175 cm⁻¹ and the A peak occurs at 1547 cm⁻¹. With implantation the T and A peaks are observed at ~1230 cm⁻¹ and ~1540cm⁻¹, respectively. The 'T' peak shifts to high energy with implantation. It has

been reported in literature that the T peak at 1220 cm^{-1} is associated to high density of edges [55], disordered hydrogenated sp^3 carbon [246], olefinic structure similar to trans polyacetylene (zigzag C-chain structure with branching on opposite side of double bond) with linear hydrogen less C=C chain [247]. It should be noted that the ‘T’ peak is shifted to high energy and the ‘A’ peak is shifted to low energy due to implantation. It has been reported that the peak at ($1446\text{-}1450\text{ cm}^{-1}$) is due to $\text{C5 A}_{g(2)}$ pentagonal pinch mode [247].

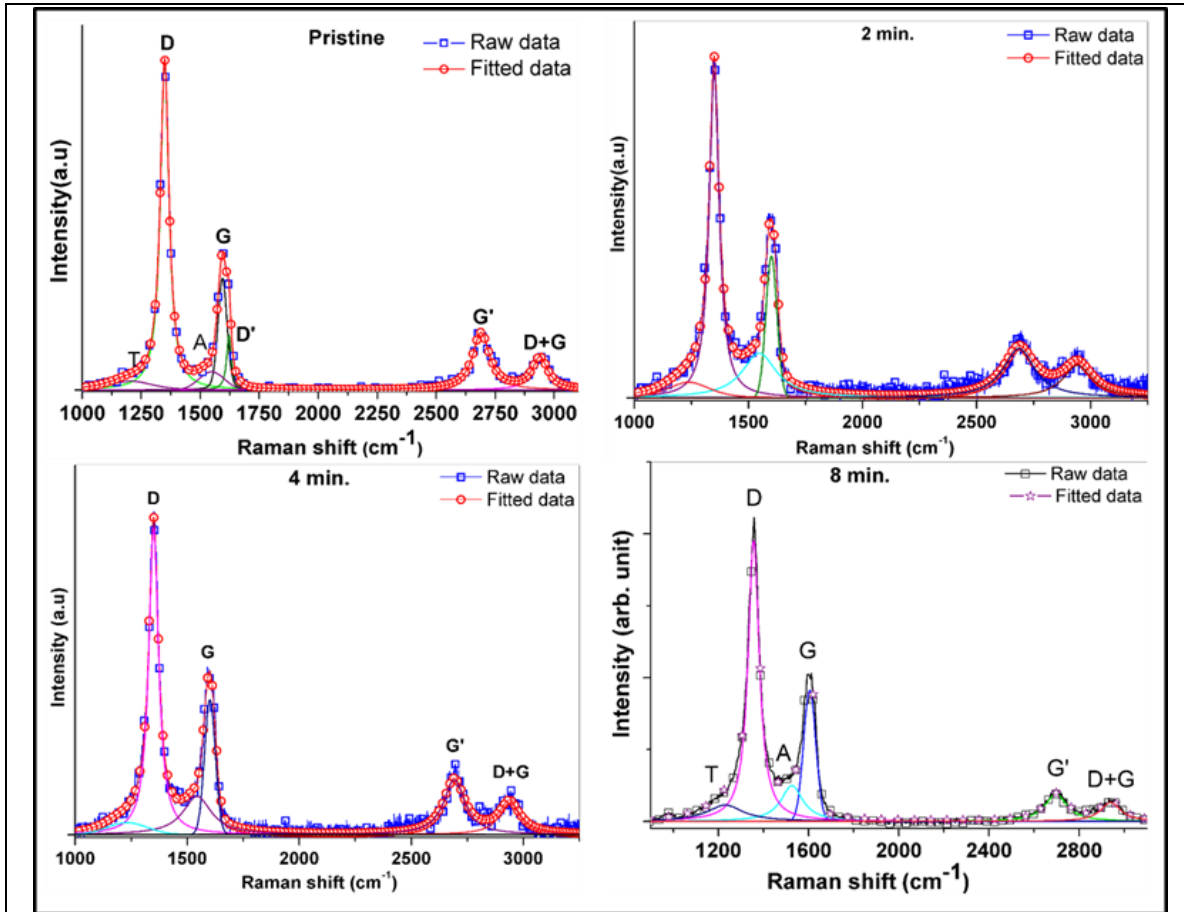


Fig. 6.5 Deconvoluted Raman spectrum of GNWs. Respective nitrogen plasma implantation duration is given in each figure.

The A peak at (1550 cm^{-1}) shows the presence of out-of-plane defects [248], pentagonal, heptagonal rings [247] and other defects such as trans-polyethelene [249] and presence of fullerene like structure [250] in the sample. Tarrant et al., conclude that the peaks at $\sim 1450\text{ cm}^{-1}$ derives from pentagonal rings [247]. In the defected region there is a possibility of formation of sp bonded carbyne upon implantation [296]. However, the Raman peaks corresponding to carbyne at 1050 cm^{-1} and 2175 cm^{-1} is not prominent in the spectra [297]. Hence, nitrogen ion implantation has induced structural defects such as (vacancies, interstitials, edges, pentagon and heptagon) in implanted GNWs.

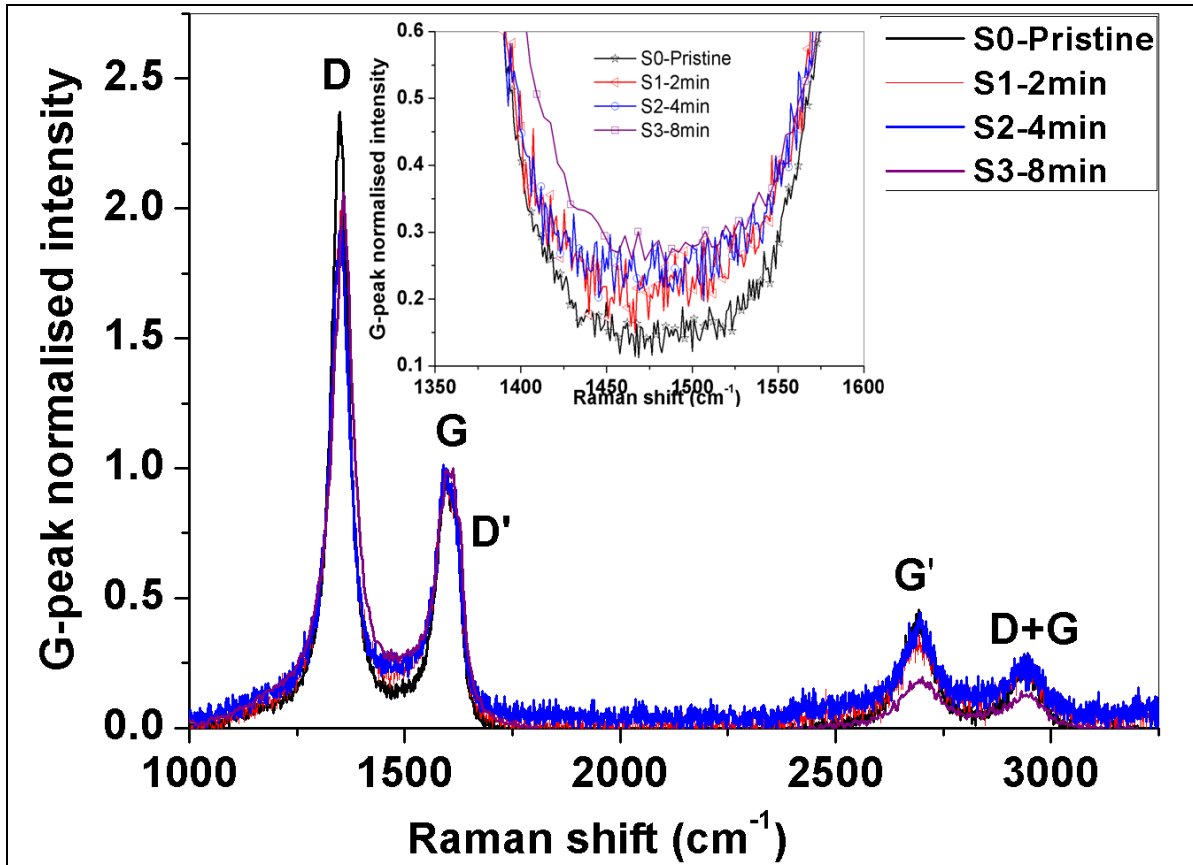


Fig. 6.6 The G-normalised full spectrum comparison of Raman spectrum of implanted GNWs. The inset shows the increase in background intensity in between D and G peaks due to implantation. The 'A' peak falls in this region.

The region in between D and G peak lifted up progressively with increase in implantation. These aspects are clearly observable in the G normalised Raman spectra (Fig. 6.6). It is reported that the seven membered ring can have one A_{1g} mode at 1303 cm⁻¹ [247] and the same will influence other peaks. The hardening of 'T' peak with implantation may be associated any one of the above effects and additionally due to increase in FWHM of D band. Tarrant et al., indicate that the peaks at ~1280 cm⁻¹ is due to heptagonal rings [247]. With several postulates on the origin and peak values, it may be concluded that the implanted region consists of several different types of defects and by fitting the A and T peaks, a better assessment of more familiar D and G peaks shall be made. Unlike monolayer graphene, merely taking the intensity of the peaks or FWHM will not reflect the actual status of the implanted sample. Hence, in addition to graphical comparison of the data using G-peak normalised intensity, integrated intensity of the deconvoluted peaks also analysed and given in Table 6.1.

Table 6.1 shows that the I_D/I_G ratio of the samples decreases with implantation. A similar phenomenon is observed in the case GNWs implanted for longer duration which has already discussed in chapter 5. The reduction in I_D/I_G shows that the GNWs falls in the 2nd regime of Ferrari amorphization trajectory [263] or the GNWs are inherently highly defective and defect density increases with implantation. It may be noted that the $I_{G'}/I_G$ ratio also decreases with implantation duration. The G' band manifest the mono layer graphene like behaviour of GNWs whereas G band represent the graphite like. With decreasing the $I_{G'}/I_G$ ratio, GNWs undergo reduction in monolayer graphene like nature or reduction in double resonance due to defects in the hexagon. Hence, it is concluded that nitrogen plasma implantation increases the defect nature of GNWs. In fact this result validate the choice of high intensity, low energy N^+ ion selection for implantation to minimise the defect generation and reduce the structural damage.

With reference to I_D/I_G and $I_{G'}/I_G$ ratio, Fig. 6.6 clearly provide a full graphical representation of the data as given in Table 6.1. A similar effect was observed in the long duration implantation in chapter 5 also. The G band position is shifted to high energy owing to the merger of D' peak with G peak. The G -peak position in GNWs is influenced by several competing parameters such as defects, doping, strain, *etc.* and cannot be used to derive specific information. Unlike long duration implantation, no peak corresponding to $sp^1C\equiv N$ at 2218 cm^{-1} is observed. In the current study, all the implanted GNWs has $\sim 4\text{-}5$ atom% nitrogen implanted into it (as discussed in XPS studies later) and the D' band is merged with G band (Fig. 6.5 and Fig. 6.6). Hence, it is concluded that the implanted GNWs constitute additional structural defects such as pentagon, heptagon and fullerene like structure.

6.3.2. FTIR spectroscopic studies

The FTIR spectrum of GNWs in the mid IR range is shown in Fig. 6.7. In order to avoid confusion about the absorption peaks of GNWs/N-GNWS and silicon, IR transparent (undoped) Si is used as substrate. In the IR spectrum, very prominent peaks in the range 1000 to 1800 cm^{-1} are identified and labelled (Fig. 6.8). The pristine and 2 min. implanted GNWs show identical FTIR pattern whereas 4min and 8 min. implanted GNWs show several new vibrational modes in the finger print region. There are prominent peaks corresponding to C-N (1270 cm^{-1}) [168] or sp^3C-N ($1430\text{-}1480\text{ cm}^{-1}$) [163] in the spectrum of 4 and 8 min. samples. However, no peak corresponding to $C\equiv N$ is observed [170]. The

C=C [162,169] become more prominent after implantation and C=O stretch [163] is present in both (pristine and implanted). Also, the carbonyl/carboxy groups ($\sim 1730\text{ cm}^{-1}$) presence is very obvious [161,168] in both pristine and implanted samples. Though there are peaks corresponding to $\text{sp}^3\text{C-H}$, peaks corresponding to O-H (stretch) and N-H (stretch) are not very much visible in the range $3000\text{-}3500\text{ cm}^{-1}$ [156]. Similarly, the $\text{sp}^3\text{C-H}$ vibrations are influenced by implantation; the peaks corresponding to symmetric vibration (e.g. 2953 cm^{-1}) getting smoothed due to implantation (Fig. 6.9). From the previous study (Chapter 5) of GNWs, a peak at 2893 cm^{-1} corresponds to methine ($\text{sp}^3\text{C-H}$) and that peak is not clearly distinguishable in these samples. The pristine and 2 min. implanted samples have only minor variation in the FTIR spectrum. This indicate that no new functional groups having high intensity (to the visible level) is generated in the present study. Laser flashing of HOPG has resulted in the formation of carbyne [296] and hence, the possibility of carbyne formation cannot be ruled out. However, the peak corresponding to $\text{-C}\equiv\text{C-}$ at 2157 cm^{-1} [297] is not visible.

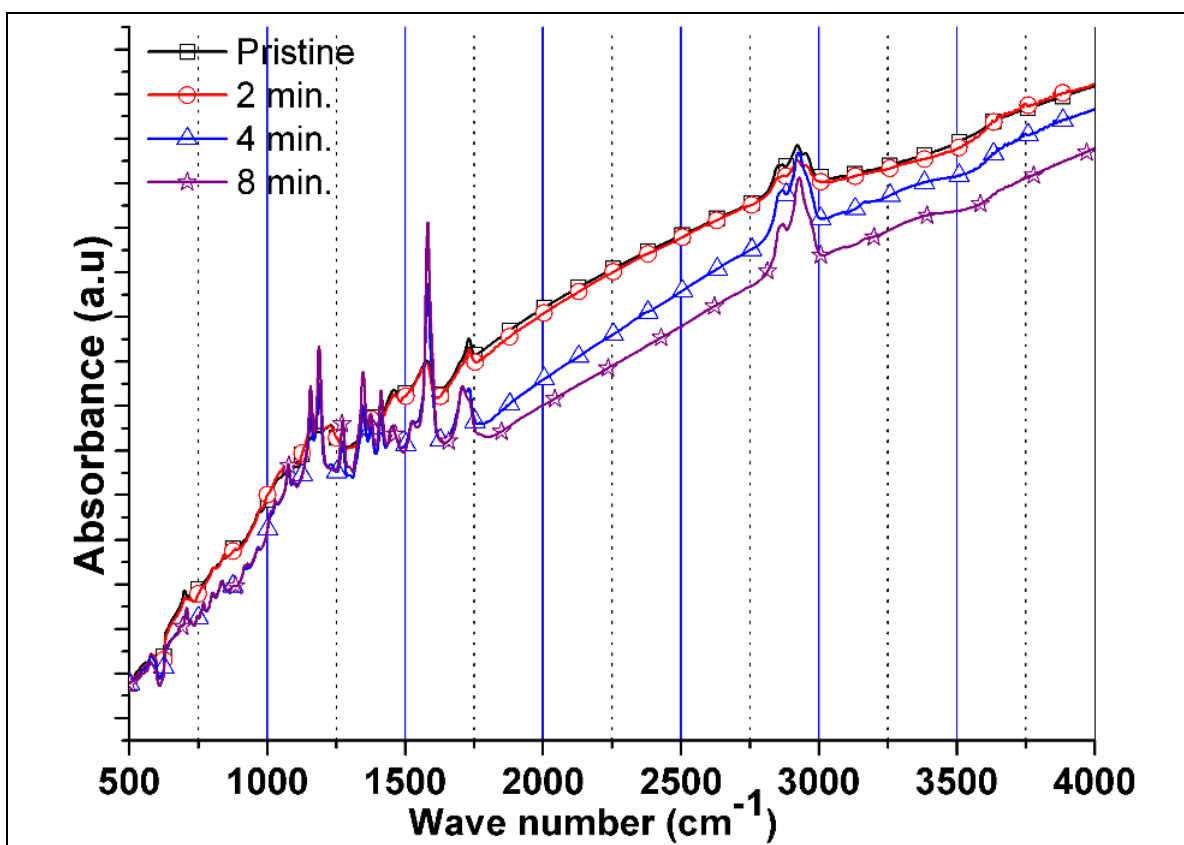


Fig. 6.7 FTIR spectrum of GNWs in the mid IR range. IR transparent Si is used as the substrate. The background intensity decreases with implantation duration.

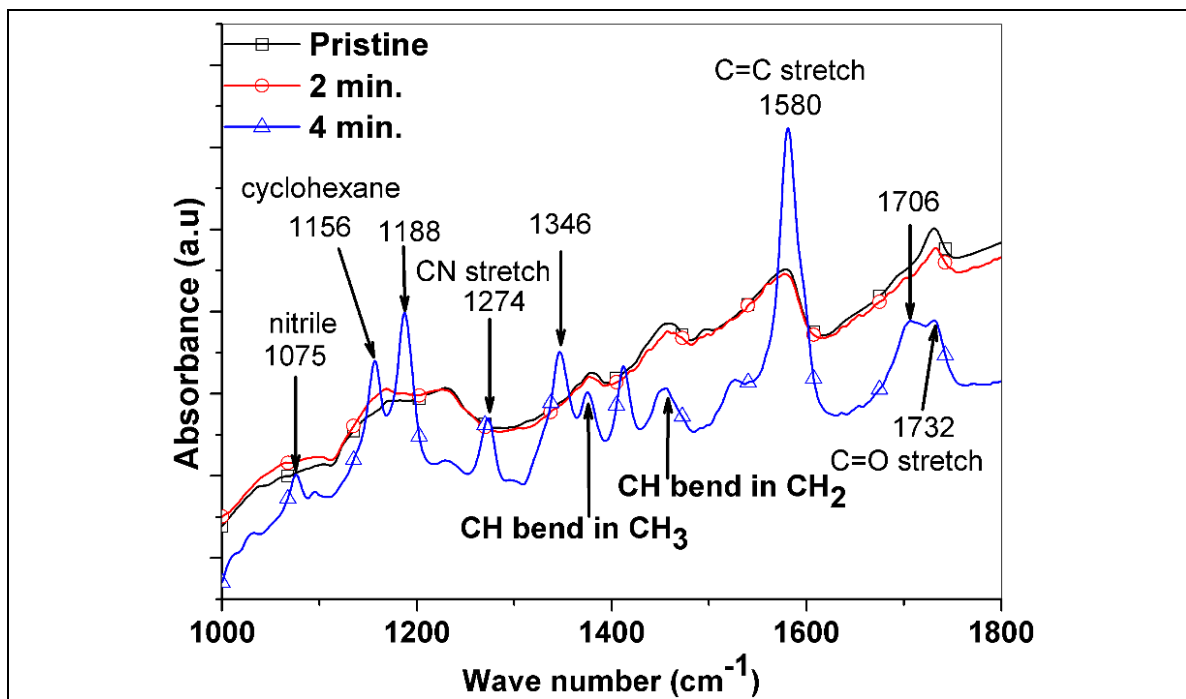


Fig. 6.8 FTIR spectrum of GNWs in 1000 -1800 (cm^{-1}) range. The respective peaks are identified. Pristine and 2 min. samples show identical graphical pattern indicating definite functional groups are not formed in 2 minutes of nitrogen plasma implantation. Functional groups are generated only after 4 min. of implantation.

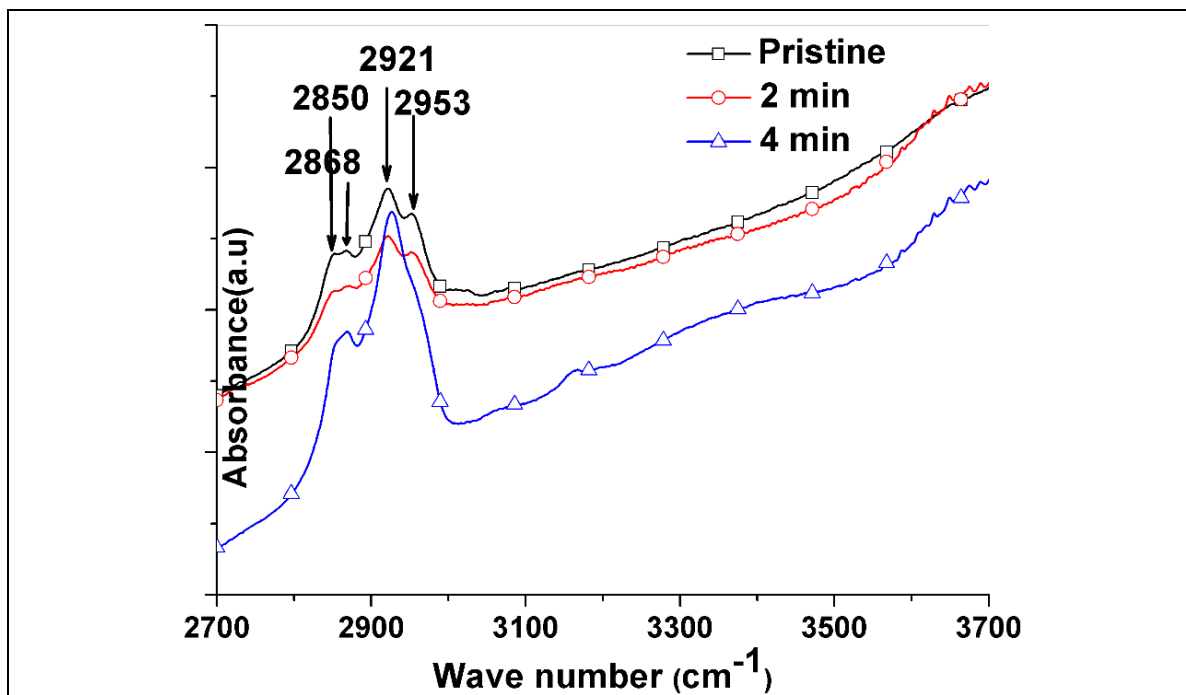


Fig. 6.9 FTIR spectrum of GNWs in 2700-3700 (cm^{-1}) range. The spectrum shows change in the sp^3C bonding pattern. The peak 2852 and 2921 (cm^{-1}) are due to methylene ($\text{sp}^3\text{C}-2\text{H}$) symmetric and asymmetric stretch vibration. The peaks 2868 and 2953 (cm^{-1}) are due to methyl group ($\text{sp}^3\text{C}-3\text{H}$) symmetric and asymmetric stretch vibrations.

However, the confirmed presence of nitrogen and oxygen (as seen from XPS studies later) containing functional groups in the 4 and 8 min. FTIR spectrum indicate the initialization several functional groups. High intensity of C=C stretch in 4 and 8 min. implanted sample indicate the breaking of the hexagon for more open ended (not double bonded with carbon) carbon. This not happening in the 2 min. implanted samples, whereas strong C=C and CNO peaks appear in 4 and 8 min. implanted samples. Effectively, more broken ring and C bonded with O and N occurs in 4 and 8 min. implanted samples. As indicated earlier, the reduction in symmetric vibrations (2953 cm^{-1}) intensity also shows reduced structural quality with implantation.

6.3.3. X-ray photoelectron spectroscopic studies

The X-ray photoelectron spectroscopy of 1s electron for carbon, oxygen and nitrogen are carried out. The survey XP spectrum of pristine GNWs and implanted GNWs are shown in Fig. 6.10. For the pristine sample, the survey spectrum shows peaks corresponding to C 1s and O 1s only. The survey spectra of implanted samples (Fig. 6.10), shows the presence of carbon, nitrogen and oxygen. This confirms the implantation of nitrogen into GNWs. The elemental quantification of all the samples has been carried out from the survey spectra.

Table 6.2 gives the details of elemental composition of pristine and implanted GNWs. The 1 s XP electron spectra of carbon, nitrogen and oxygen are separately discussed. Table 6.2 shows that nitrogen atomic fraction is ~4.2% in 2 min. implanted sample, whereas 4 and 8 min. implanted sample show slightly increased atomic fraction of nitrogen. This indicate that under the present conditions, the nitrogen incorporation is almost saturated and thereafter increase in atomic fraction is very less. It is interesting to note that for ultrahigh pure nitrogen implantation, oxygen at% has increased inadvertently. This is because of surface adsorption of oxygen due to exposure to atmosphere. This aspect has been discussed in the previous study (Chapter 5). The plasma exposure / implantation, cause the formation of dangling bonds on the surface of GNWs and oxygen/moisture form bonds on exposure to atmosphere.

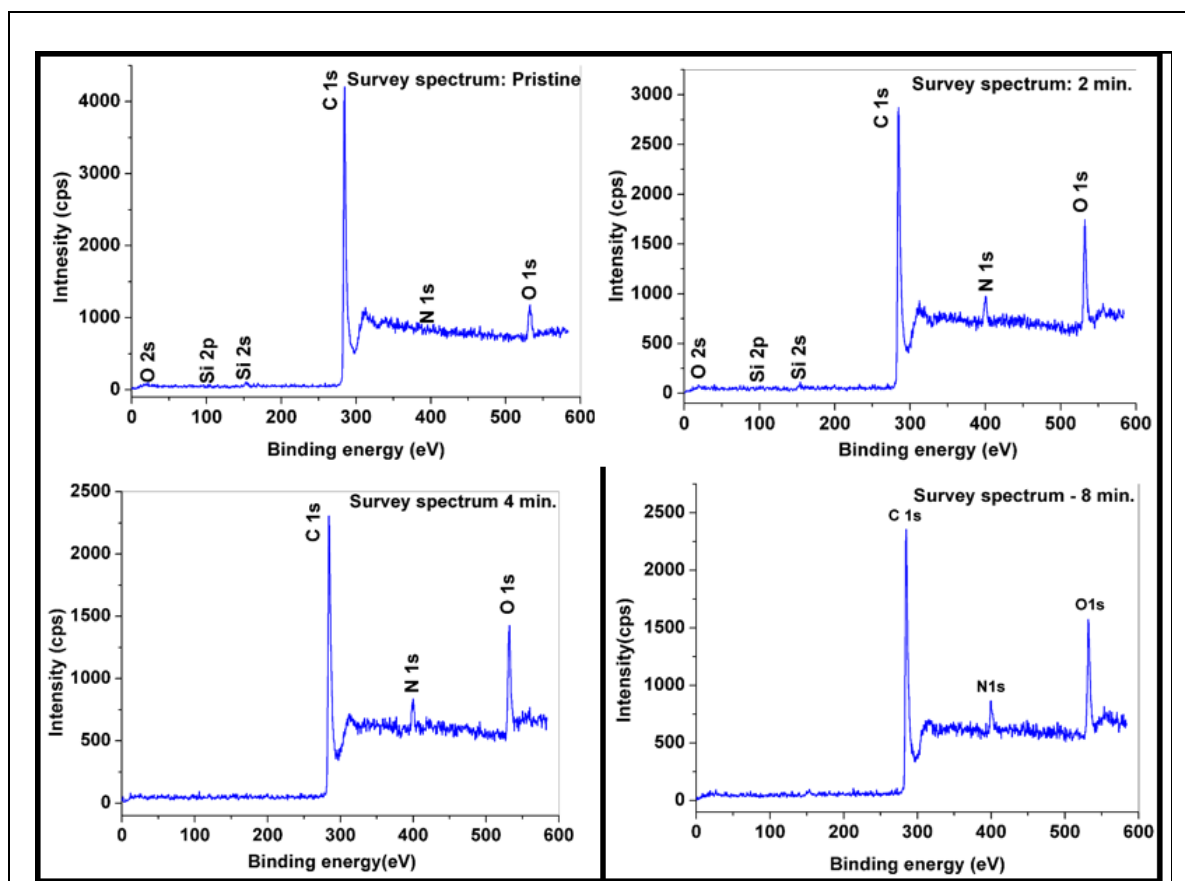


Fig. 6.10 Survey spectrum of GNWs. Peaks corresponding to C 1s and O 1s can be observed in pristine GNWs. Survey spectrum of 2 min., 4 min. and 8 min. implanted GNWs show the peaks corresponding to C 1s, N 1s and O 1s.

Table 6.2 Elemental composition of pristine and implanted GNWs.

Sample	C	N	O
Pristine	96	-	4.0
2 min	84.4	4.2	11.3
4 min	83.8	5.5	10.8
8 min	81.2	6.2	12.7

In order to analyse the effect of implantation, the 1s XPS spectra of each sample for carbon, nitrogen and oxygen are deconvoluted. Fig. 6.11 shows the deconvoluted 1s electron binding energy of carbon and oxygen of the pristine sample [146]. In the deconvolution, a new peak corresponding to defect 'd' peak is assigned to reduced binding energy for 1s electron of carbon. This binding energy corresponds to the carbon in the hexagon adjacent to a vacancy possibly bonded with a hydrogen atom [140]. Another possibility of reduced binding energy is due to the formation of sp bonded carbyne [296]. Considering both the above possibilities, this peak is named as defect peak 'd'.

The O 1s spectrum of pristine sample is deconvoluted into 3 curves as shown in Fig. 6.11. The origin of surface oxygen may be traced out from exposure of the sample to atmospheric oxygen and moisture. Large overlap of binding energy and different values of FWHM of oxygen /hydroxyl group bonded to carbon has been reported in literature [146].

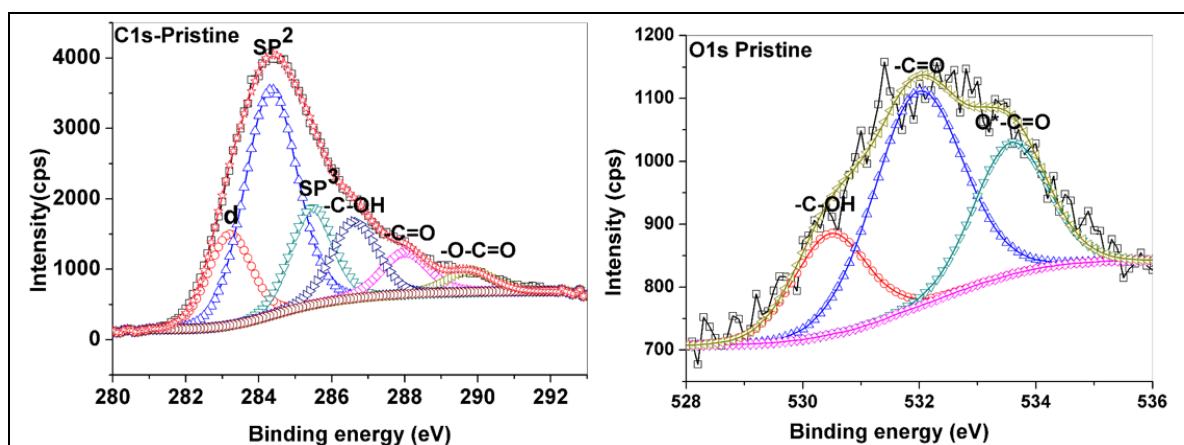


Fig. 6.11 The C 1s and O 1s X-ray photo electron spectrum of pristine GNWs. Respective peaks are identified. The D peak in C1s pristine stands for hydrogen terminated defect peak.

Carbon: In the C 1s energy state analysis, the defect peak (d) position is more or less remains same in all the samples. A sudden reduction in defect peak intensity is observed in the 2 min. sample compared to the pristine. It should be noted that FTIR studies shows the carbon skeleton is largely undisturbed in the 2 min. implanted sample (as discussed earlier). So, some of the carbon dangling bonds which has hydrogen in the pristine GNWs may have modified upon 2 minute implantation. Additionally, in the 2 min. implanted sample, the electronegative nitrogen (4.2 at%) and oxygen (11 at%) can pull the bonded electrons of carbon towards it. As the number of carbon atoms experiencing this effect increases, the C 1s peak shift to higher energy and the curve intensity corresponding to the 'd' peak fraction reduces. In addition to this, some of the carbyne present in the pristine may be modified. Hence, the immediate reduction in defect peak fraction is explained. However, later on, the defect volume fraction increases with increase in implantation duration. Beyond 2 minutes, the increase in defect peak intensity may be attributed to the shift of sp^2C peak low values due to defects.

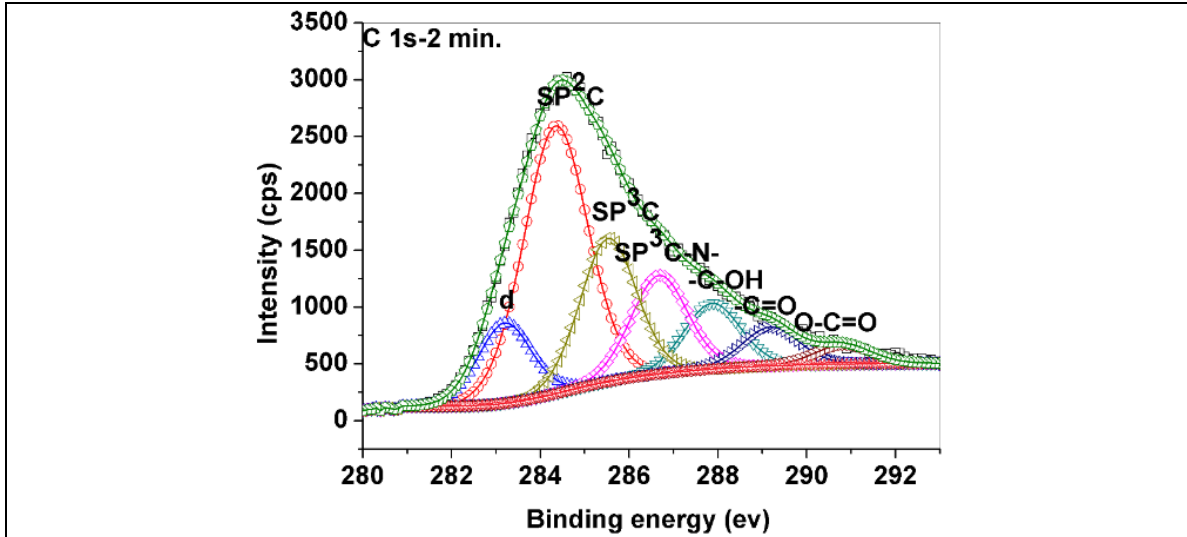


Fig. 6.12 *C 1s* spectrum of GNWs nitrogen plasma implanted for 2 min. The *C 1s* BE variation due to defect and bonding is shown.

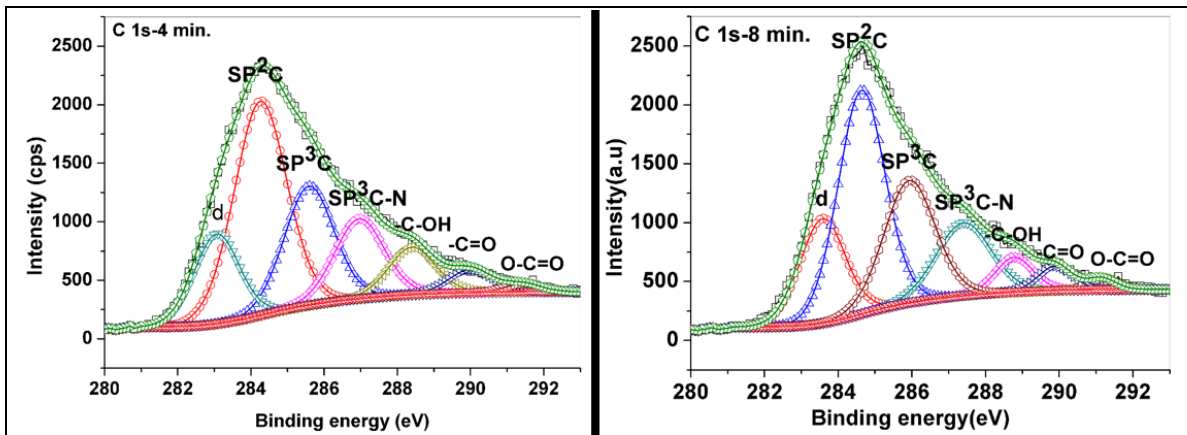


Fig. 6.13 *C 1s* spectrum of GNWs, nitrogen plasma implanted for 4 min. and 8 minutes.

Zhu et al., indicated that the sharp *C 1s* peak at 284.7 eV (1.05 eV) is shifted to lower binding energy (284.3 eV, FWHM-2.0 eV) due to Ar ion irradiation [298]. Further, it has been seen from Raman spectroscopy that implantation induces pentagons, heptagons, Fullerene and edges. Hence, rather than doubling the nitrogen doping fraction, doubling the implantation duration has increased the defects in the carbon skeleton. Hence, an increase in 'd' peak intensity is observed with implantation duration in 4 min. and 8 min. implanted samples. With reference to sp^2C bonding, the 284.3 (1.7) eV peak of pristine GNWs is shifted to 284.6 eV (1.6) eV after 8 min. implantation. Table 6.3 shows that the sp^3C fraction increases with implantation duration at the cost of sp^2C bonding fraction. The *C 1s* spectrum shows only marginal increase in C-N/C-O fraction with increase in implantation duration. This is because there is an ambiguity in assigning functionalities containing carbon [146],

especially with surface moisture, oxygen and nitrogen with a probability of different bonding combination upon implantation. However, on an engineering point of view; the defect, sp^2C , sp^3C peaks and to a lesser extent C-N/O peak are considered for understanding the implantation effect. Since both oxygen and nitrogen have comparable electronegativity, the assignment of atom percentage of carbon can vary. Hence, more specific treatment of implantation effects is discussed with N 1s energy. However, the damage to the hexagonal network is very obvious from the sp^2 and sp^3 fractions.

Table 6.3 Results of C 1s analysis of samples.

Sample ID	Defect		C-(SP2)		C-(SP3)		-C-N/-C-O-		-C-OH		-C=O		-O-C=O	
	Position (eV)	At %												
Pristine	283.2 (1.4)	14.9	284.3 (1.7)	44.9	285.5 (1.4)	15.9	-	-	286.6 (1.5)	13.4	288.0 (1.5)	7.3	289.7 (1.5)	3.7
2 min.	283.2 (1.4)	10.2	284.3 (1.7)	40.7	285.5 (1.5)	19.2	286.7 (1.5)	13.2	287.9 (1.5)	8.8	289.2	5.2	290.8 (1.5)	2.6
4 min.	283.1 (1.5)	14.1	284.3 (1.7)	39.2	285.6 (1.6)	20.6	287.1 (1.6)	13.8	288.4 (1.5)	7.7	290.1 (1.4)	3.5	291.4 (1.1)	1.0
8 min.	283.6 (1.5)	16.9	284.6 (1.6)	37.5	285.9 (1.6)	22.3	287.4 (1.5)	14.3	288.7 (1.2)	4.7	289.9 (1.1)	3.0	291.2 (0.9)	1.2

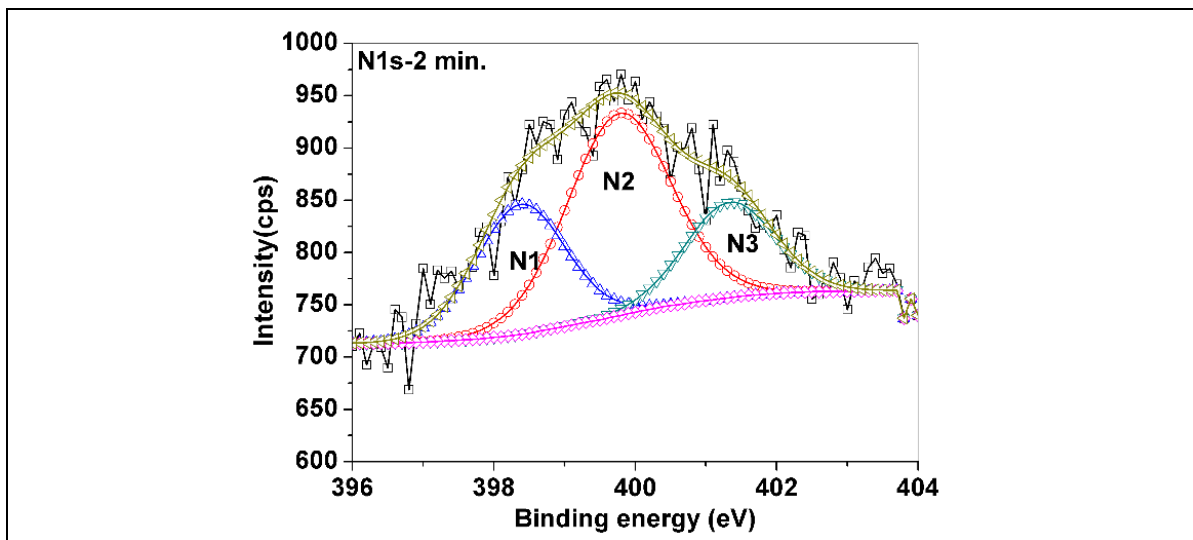


Fig. 6.14 N 1s spectrum of GNWs nitrogen plasma implanted for 2 min. The nitrogen is categorised as N1, N2 and N3 based on the binding energy of N 1s electron. More details are this categorization is discussed in chapter 5.

Nitrogen: The deconvoluted N 1s spectra of 2, 4 and 8 min. samples are shown in Fig. 6.14 and Fig. 6.15. Each spectrum is deconvoluted into three peaks to assign N1, N2 and N3

type configuration to nitrogen [295]. In the implanted sample, the N1 (lone pair unshared) fraction reduces with process duration. This may be due to opening up of the layers and exposure to atmosphere induce bonding with other atoms. Consequently, the N2 fraction (lone pair shared) nitrogen increases with implantation duration.

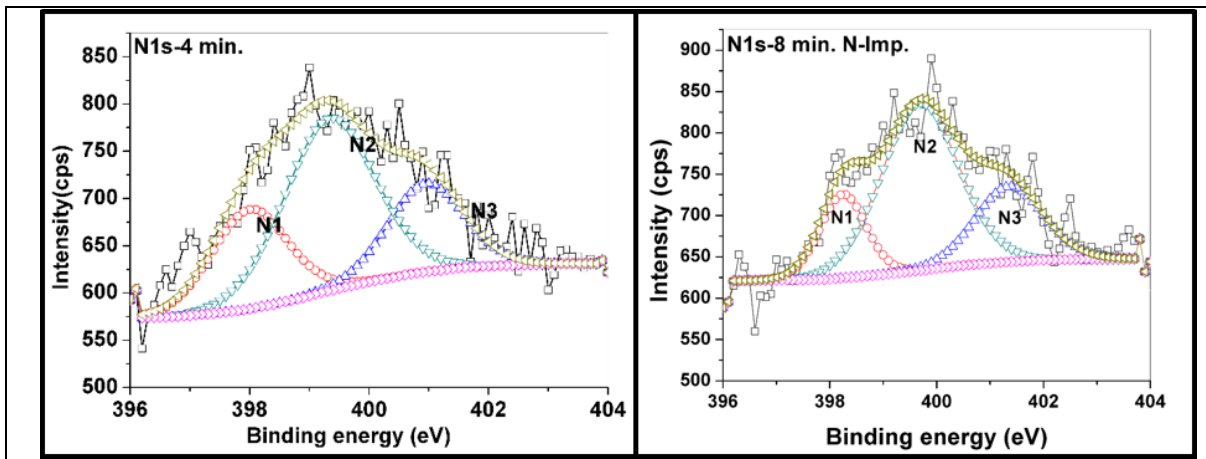


Fig. 6.15 N 1s spectrum of GNWs, nitrogen plasma ion implanted for 4 and 8 minutes. The peaks corresponding to N1, N2 and N3 are marked. The area fraction is given in table 6.4.

Table 6.4 Results of N1s analysis of samples.

Sample ID	N bonded to 2 neighbours (Lone pair unshared)		N bonded to 3 neighbours (Lone pair shared)		Trapped N ₂ or N bonded to 4 neighbours or Oxidised N (Quaternary N)	
	Position (eV)	At %	Position (eV)	At %	Position (eV)	At %
2 min.	398.4(1.5)	28.3	399.8(1.7)	51	401.3(1.5)	20.8
4 min.	398(1.5)	25.2	399.3(1.8)	52.5	401(1.5)	22.4
8 min.	398.2(1)	17.7	399.7(1.7)	58.9	401.4(1)	23.5

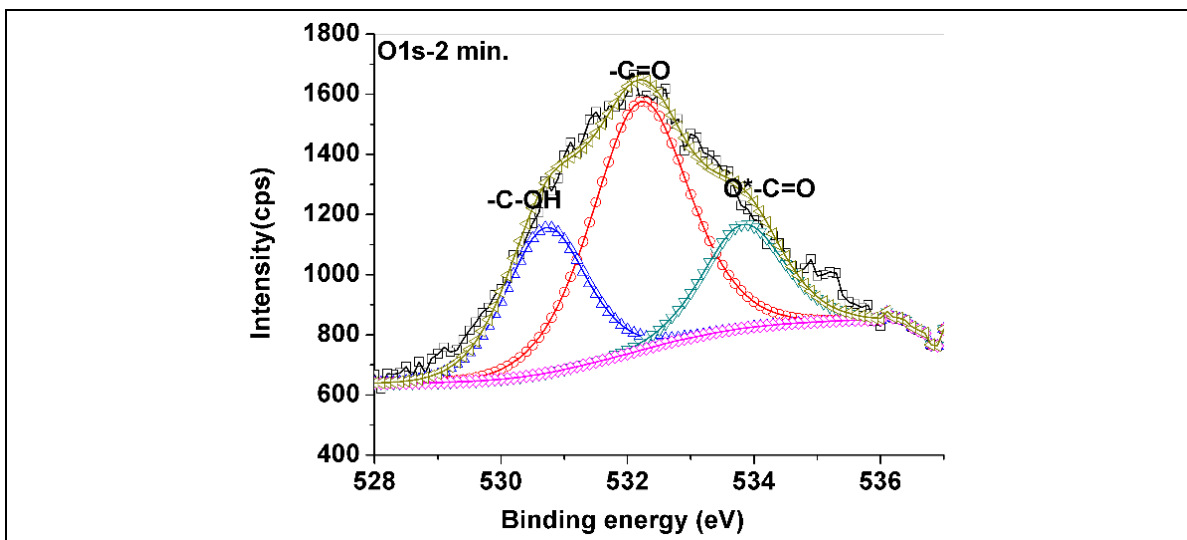


Fig. 6.16 The O 1s XPS spectrum of GNWs. The oxygen is assumed to be in surface adsorbed state.

The N3 fraction also increases and is attributed to implantation induced fragmentation of the GNWs make the nitrogen to form 4 bonds with surrounding atoms or trap a nitrogen molecule. Additionally the contribution to N3 fraction is from oxidised nitrogen also.

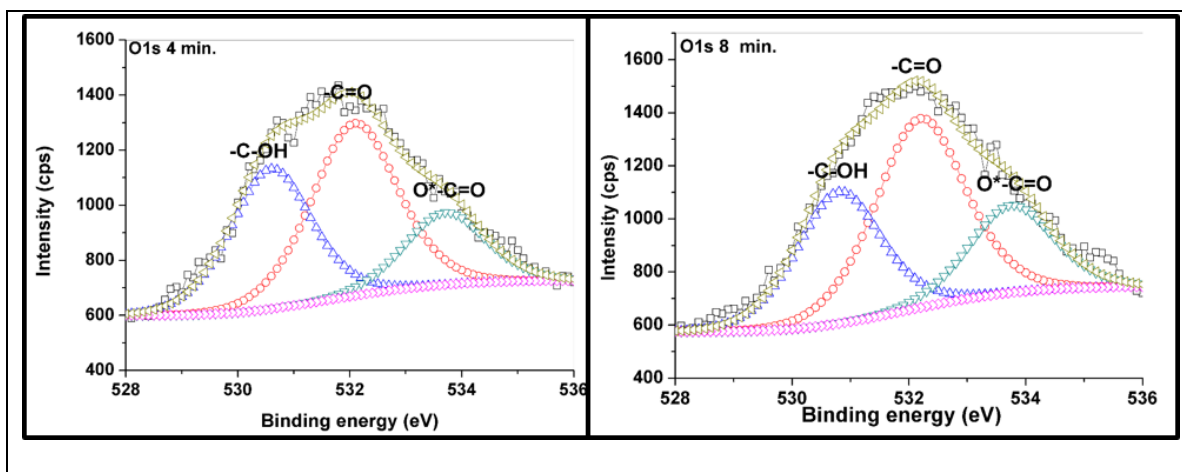


Fig. 6.17 O 1s spectrum of GNWs, nitrogen plasma ion implanted for 4 and 8 minutes. The peaks corresponding to O1, O2 and O3 are marked. The area fraction is given in table 6.5.

The oxygen is more reactive than nitrogen ions in the plasma; however oxygen is surface adsorbed due to nitrogen implantation induced defects on the carbon network [188]. The oxygen analysis shows that the $-C-OH$ fraction increases with implantation duration. However, the $-C-OH$ fraction in carbon analysis shows an opposite trend. This is because there is large overlap in BE of 1s electron of carbon when bonded nitrogen, oxygen or OH groups. The $-C=O$ fraction shows a reduction from pristine to 8 min. implanted sample. This may be due to sputter removal of surface adsorbed oxygen.

Table 6.5 Results of O1s analysis of samples.

Sample ID	-C-OH		-C=O		-O*-C=O	
	Position(eV)	At %	Position(eV)	At %	Position(eV)	At %
Pristine	530.5(1.5)	20.5	532.0(1.8)	52.6	533.6(1.5)	26.9
2 min.	530.7(1.5)	26.6	532.2(1.8)	54.5	533.8(1.5)	19
4 min.	530.6(1.7)	35.5	532.1(1.8)	46	533.7(1.7)	18.3
8 min.	530.8(1.7)	31.4	532.2(1.8)	47.7	533.7(1.7)	20.9

The $-O^*-C=O$ fraction (B E is for the stared oxygen) generally reduces with increase in process duration. This is in line with the reduction in increment of the atomic fraction of $\sim (532 \text{ eV})$ - oxygen ($-C=O$). The 8 min. implanted sample shows more $-C=O$ and $-O^*-C=O$ fraction as compared to 2 min. and 4 min. samples. This may be attributed to the implantation induced fragmentation of carbon network and consequent increase in bonding percentage with atmospheric oxygen.

6.3.4. Water contact angle measurement

Water contact angle measurements were carried out on the pristine and implanted GNWs on carbon paper using double distilled water. A photograph of the actual measurement setup is shown in Fig. 6.18.

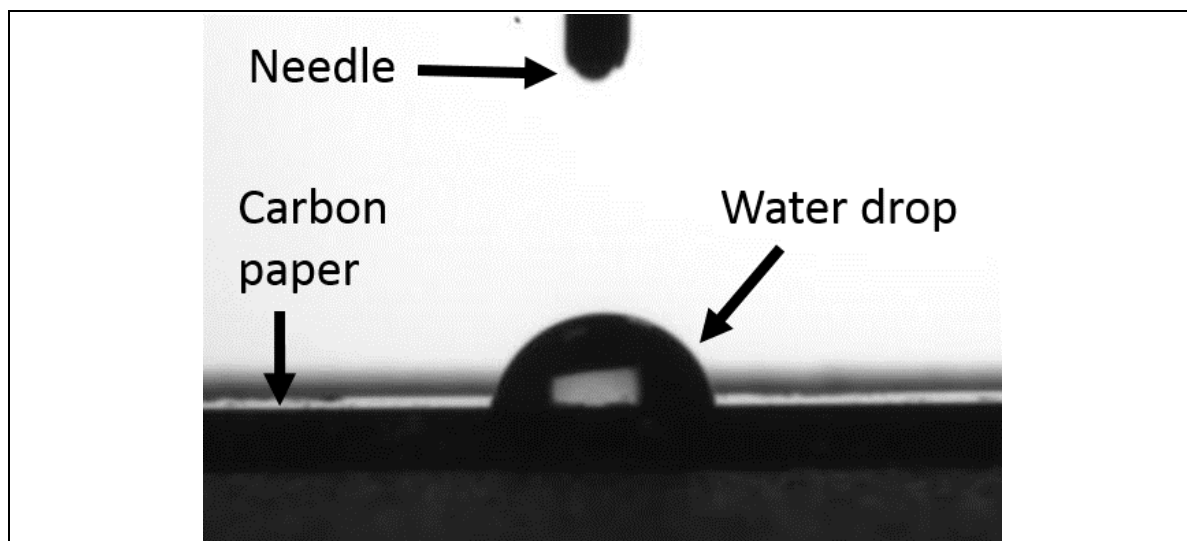


Fig. 6.18 Typical water contact angle measurement of GNWs on carbon paper

The results of measurements are given in the Table 6.6. It is observed that the pristine sample show a contact angle of 125° and after 1 minute it reduces to 120° indicating super hydrophobic nature of as prepared GNWs. Up on implantation the surface become super hydrophilic ($CA \sim 10^\circ$) after 20 minutes. All the implanted samples show similar behaviour. The reduction in contact angle have been reported in plasma treated samples [299,300]. The reduction in water contact angle may be due to both physical and chemical modification of the surface [299].

The Cassie-Baxter treatment of contact angle may be applicable to the pristine GNWs. However, when the surface is plasma exposed the contact angle reduces. Similar effects have been reported even with Ar, H₂, O₂ or F₂ plasma exposure [299,300]. Hence, the basis of hydrophilic behaviour of GNWs is dangling bond formation on the surface and possibly the reduction in the contact area due to sharpening of the tip. Additionally, the reduction in contact angle is also attributed to higher inter graphene wall distance and increase in defect density [141]. It was indicated that the contact angle for pristine graphite is $68 \pm 7^\circ$ [301] and for graphene $56 \pm 4^\circ$, [302] are slightly hydrophilic and the basic reason for hydrophobic behaviour is due to surface adsorption of hydrocarbons on exposure to atmosphere [303,304]. Considering the above views, the decrease in contact angle or increased wettability of graphene nanowalls after plasma nitrogen ion implantation may be

attributed to thinning of individual layers, sharpening of the edges, widening of the GNWs leaves, surface sputter removal of adsorbed hydrocarbons, generation of dangling bonds and changed surface chemistry. The water contact angle measurements were repeated on the pristine and n-GNWs after ~6 months of the first test. Surprisingly, these samples showed *tissue paper like water* absorption. This indicate that the high stability of nitrogen plasma implanted GNWs surface.

Table 6.6 Water contact angle measurements on GNWs.

Sample ID	H ₂ O Contact angle	
	<1 min.	After 20 min
Pristine	125	120
2 min. imp.	35	<10
4 min. imp.	22	13
8 min. imp.	24	13

6.3.5. Electrochemical studies

Electro-chemical studies are conducted on the pristine and implanted GNWs deposited on carbon paper. In this regard, the cyclic voltammetry, charge – discharge studies are discussed towards possible application of nitrogen implanted GNWs as supercapacitor electrode material.

6.3.5.1. Cyclic voltammetry

Fig. 6.19, Fig. 6.20 and Fig. 6.21 shows the voltammograms of the pristine GNWs and the N-GNWs (on CP). The cyclic voltammetry (CV) measurements were conducted at various scan rates (100, 200, 300, 400 and 500 mVs⁻¹). The area of the electrode samples,

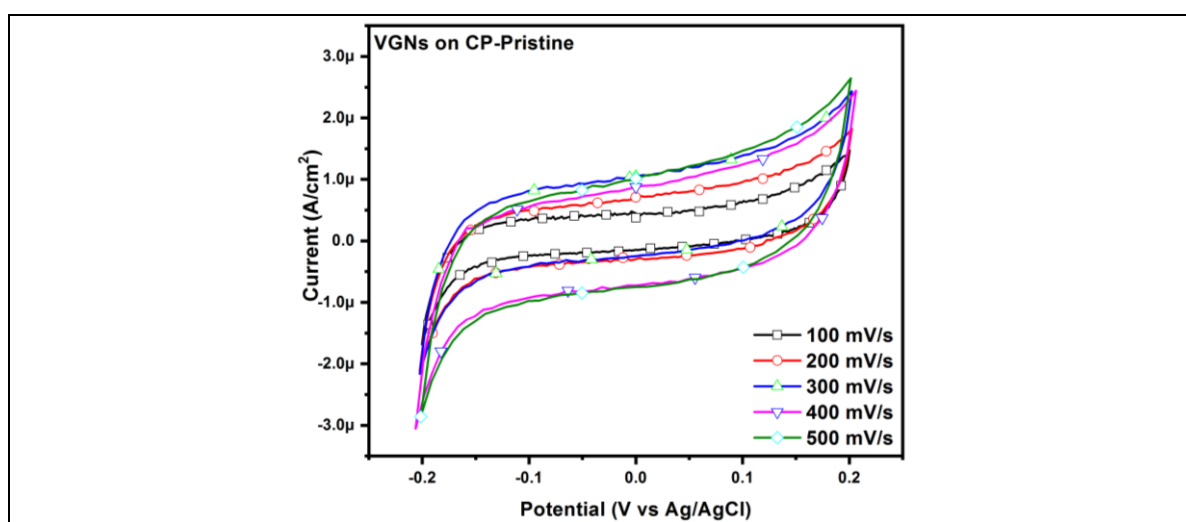


Fig. 6.19 Cyclic voltammogram of pristine GNWs at different scan rate. With increase in scan rate the area enclosed by the curve also increases.

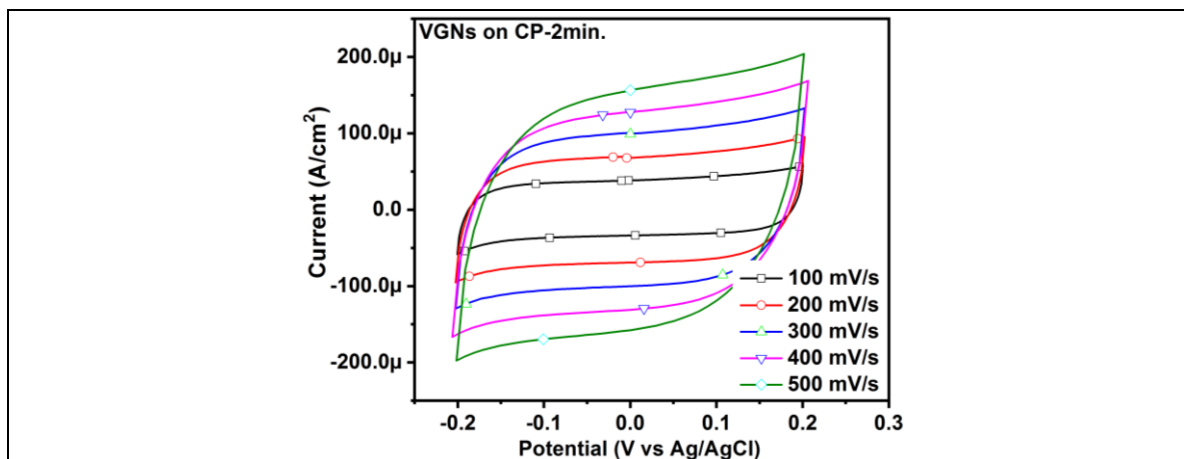


Fig. 6.20 Cyclic voltammogram of GNWs on CP nitrogen plasma implanted for 2 minutes. The area enclosed by the curve increases with scan rate. Near square like pattern indicate charge storage.

exposed to 1 M KOH electrolyte is fixed as $1 \times 0.5 \text{ cm}^2$ in a three electrode configuration. The Y-axis shows current per cm^2 and necessary correction of enclosed area is done in calculation. The potential window for the CV measurements was maintained between -0.2 and 0.2 V (0.4 V) Vs Ag/AgCl reference electrode. The areal capacitance of the electrodes based on the CV studies was estimated. The areal capacitances of all the samples under discussion are presented in Table 6.7. The voltammogram maintain quasi-rectangular shape of CV for the pristine GNWs and near oval shape CVs for the N-GNWs, clearly denoting uniform electrolyte ion access to the surfaces of the electrode material. This shape is ideal for reversible capacitive behaviour [305]. However, the cathodic as well as the anodic ends of the CV curves display

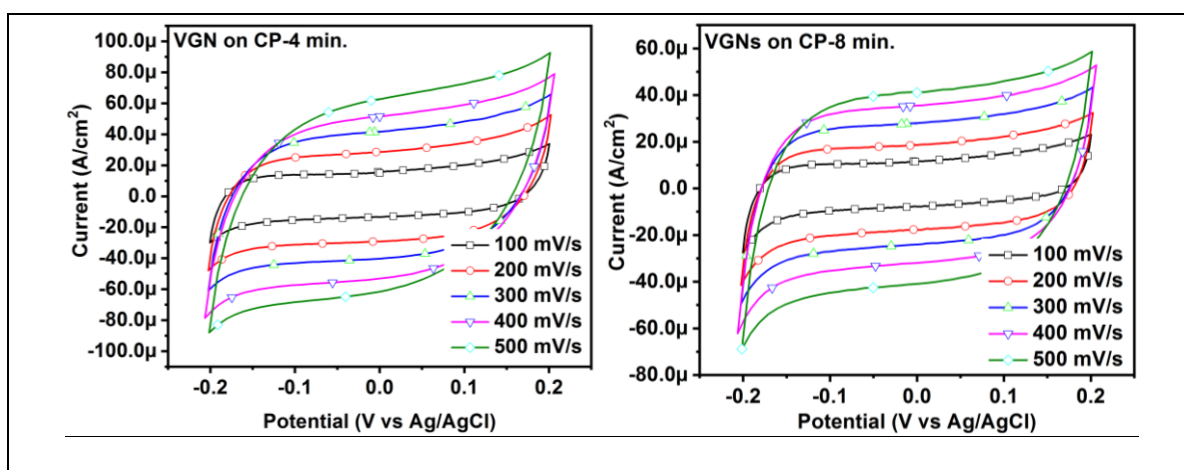


Fig. 6.21 Cyclic voltammogram of GNWs on CP, nitrogen plasma implanted for 4 minutes and 8 minutes. The area enclosed by the curve increases with scan rate in both cases. Near square like pattern indicate charge storage.

Table 6.7 Capacitance calculated from cyclic voltammetry. The 2 min. sample show highest capacitance improvement.

Scan rate (mV/s)	Capacitance ($\mu\text{F}/\text{cm}^2$)				2 min./ Pristine Ratio
	Pristine	After 2 min. implantation	After 4 min. implantation	After 8 min. implantation	
100	11.55	1387.04	559.93	384.60	120
200	9.07	1219.82	522.46	349.38	135
300	7.48	1134.25	473.58	323.80	152
400	7.20	1082.86	447.66	296.34	150
500	6.10	991.08	403.27	265.72	163

slight shifts denoting the reduction in the rate of ion diffusion with increase in scan rate (Fig. 6.19, Fig. 6.20 and Fig. 6.21). Maintaining the Quasi rectangular CV shape shows good high frequency response. Notably, the increase in the scan rates has not affected the shape of the voltammogram which clearly indicates the good conduction of electrons in the electrodes and excellent cyclic reversibility [175]. In order to provide a comparison of the variation of capacitance, the GNWs implanted for 2, 4 and 8 min. are shown along with pristine GNWs for 100 mV/s scan rate in Fig. 6.22.

It has been pointed out that mention of capacitance per cm^2 is slightly misleading because large area in the carbon paper is empty and if the carbon fibre has large amount of GNWs deposited (by employing long duration or higher power etc.), the available area can be increased several times. GNWs deposited for longer duration obviously show enhanced capacitance owing to high surface area coverage in the carbon paper. Because, in the equation $C_s = \frac{\int IdV}{s.A.\Delta V}$, the area-‘A’ is always taken as the area of the strip (say 1 cm^2), which is not the actual case. Hence, reporting the capacitance will vary with samples prepared from different systems. However, for comparison of similar samples before and after some treatment, this approximation is acceptable. Since, the aim of the present study is to evaluate change in capacitive properties in between the pristine and implanted samples, the same equation is used for calculating the capacitance and the improvement is reported in terms of ratio or multiple. It can be seen that the increase in areal capacitance is more than two order high. With increase in scan rate the performance of implanted sample improves (Table 6.7).

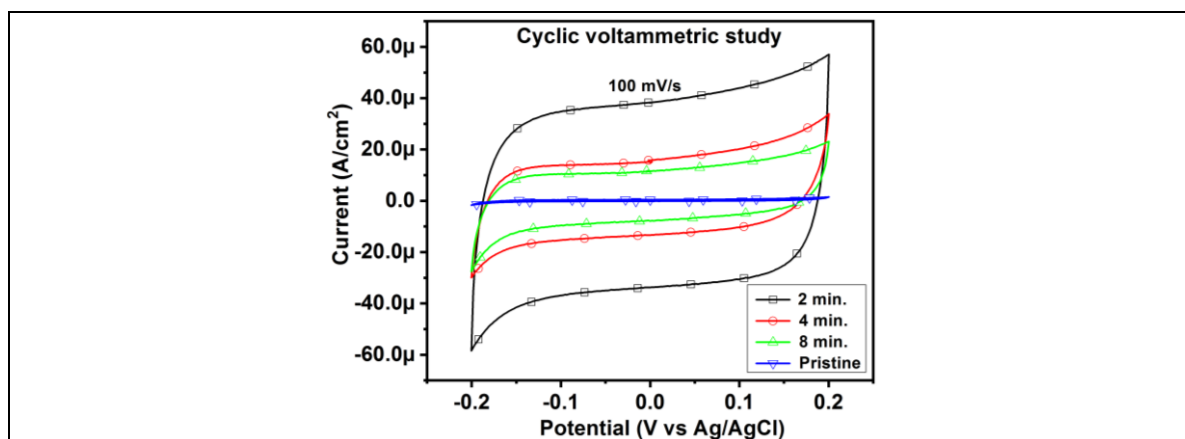


Fig. 6.22 Comparison of Cyclic voltammogram of VGNs on CP pristine and nitrogen plasma implanted samples at 100mV/s scan rate. All the implanted samples show increase in area enclosed by the curve as compared to the pristine. The 2 min. implanted sample show highest area.

A clear distinctive enhancement in the current range of the CVs is indicative of the fact that the capacitance is increased in the N-GNWs as compared to that of pristine GNWs. The comparative CV plot (Fig. 6.22) signifies that the sample implanted for 2 min. has superior ability to store charges more than longer implanted one. The capacitance 2 minute implanted sample to pristine ratio is lowest for 100 mV/s scan and it improves with increasing scan rate. Similarly, for other samples also the capacitance ratio compared to pristine increases.

The smooth region in between the edges of the CV plot indicate that possible increased capacitance occurring in the entire region of the applied voltage. This aspect is not familiar metal oxide dispersed electrodes where the CV plot slope change occurs at definite voltage and it gradually shift with increased scan rate. Hence, it appears that the mechanism operating is not the conventional *psuedocapacitance*. Hence, response of N-GNWs to CV is not similar to metal oxide dispersed electrodes.

6.3.5.2. Galvanostatic Charge-Discharge

The effectiveness of the capacitances observed in voltammograms of GNWs and the N-GNWs are further validated by galvanostatic charge-discharge (GCD) measurements at different current densities in the potential range 0.2 to -0.2 V. Fig. 6.23 indicates that the profile patterns are symmetrical and nearly linear, thereby exhibiting effective CD performance. It also confirms the absence of major faradaic processes. GCD results are in synchronisation with the CV data indicating superior properties of the 2 min. N-GNWs with comparatively longer charge and discharge time. Moreover, 2 min. N-GNWs displays a

smaller IR (voltage) drop compared to that of other N-GNWs (4 min. and 8 min. implanted samples) indicating better contact at the electrode/electrolyte interface. The result is unswerving as it matches well with the contact angle measurements (Table 6.6) of 2 min. implanted sample showing superhydrophilic properties. The columbic efficiency was calculated using the Eq. 6-1

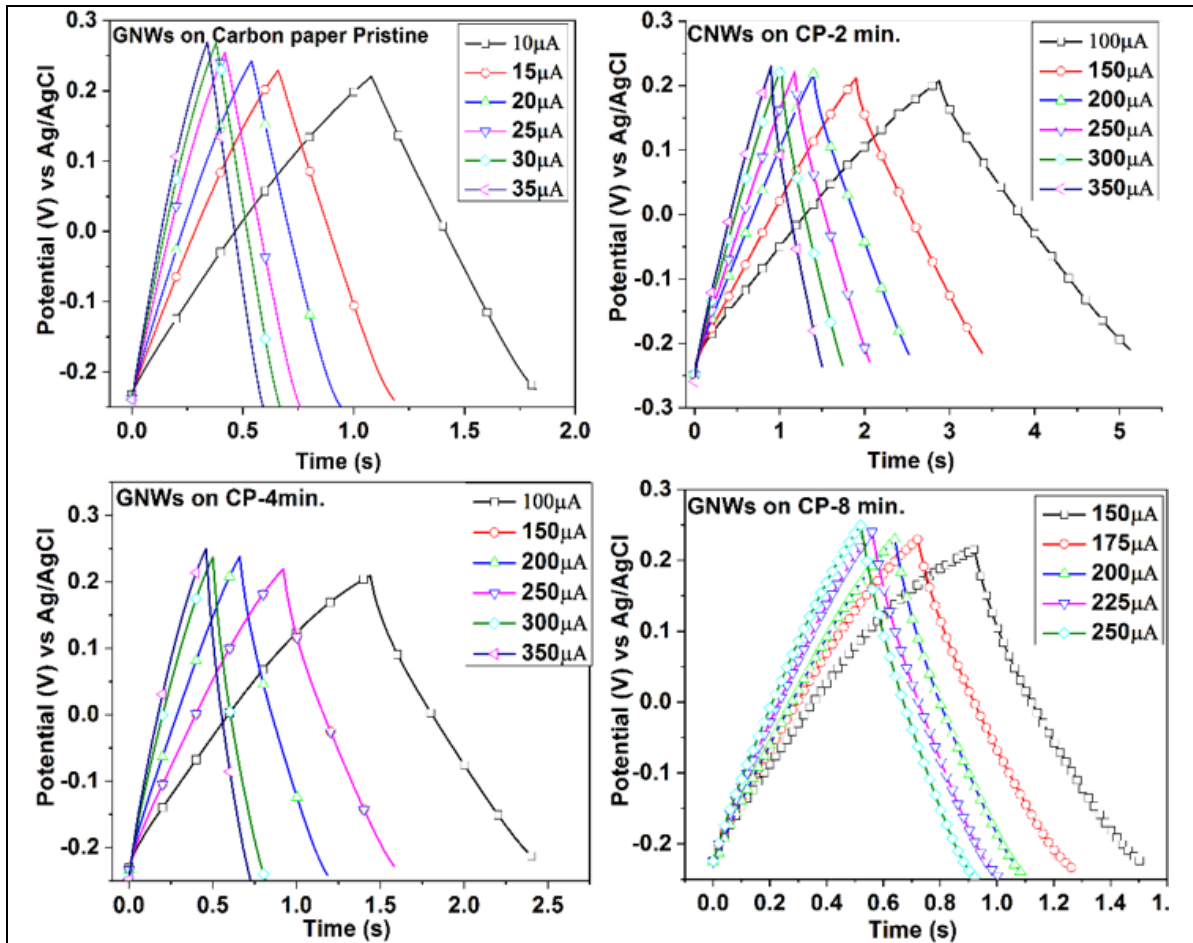


Fig. 6.23 The change-discharge curve of GNWs pristine and implanted for 2, 4 and 8 min. The 2 min. implanted GNWs show improved charge-discharge behaviour.

$$\eta = \frac{t_d}{t_c} \quad \text{Eq. 6-1}$$

Where, ‘ η ’ is the columbic efficiency, t_d and t_c are time taken for discharging and charging during every cycle. A supercapacitor need to have good the cycle stability. However, in the present case, fluctuations in the capacitance retentions were witnessed in CP and pristine GNWs throughout the 2000 cycles. Whereas, in the case of N-GNWs the oscillation in the retentions are observed initially and it eventually stabilised itself as the time prolonged. Initial irreversible capacity loss in a supercapacitor is inevitable, during the initial cycles,

which are owing to the formation of electrode-electrolyte interface layer. Thereafter, the development of steady state in retention could be possibly due to the increase in the effective interfacial surface area between N-GNWs and electrolyte (1 M KOH).

The N-GNWs displayed better retention behaviour; however, 2 min. sample show excellent retention up to 96 % along with attainment of early steady state in capacitance retention. Such improved Columbic efficiency and higher retention of capacitance may be attributed, at first place, to uniform surface modification due to anchoring of nitrogen atoms over the GNWs. The phenomenon also verifies that there is mild structural damage caused to the N-GNWs. In the following section the mechanism responsible for super capacitance on N-GNWs will be discussed.

Table 6.8 The charge / discharge characteristics of GNWs.

ID	Charging (0.2V)		Discharging		Coulombic efficiency
	Time(s)	Current	Time(s)	Current	
Pristine	1	10 μ A	0.8	10 μ A	0.8
2 min.	2.8	350 μA	2.3	350 μA	0.82
4 min.	1.4	350 μ A	1	350 μ A	0.71
8 min.	0.9	250 μ A	0.6	250 μ A	0.67

6.4. Discussion

Fig. 6.1 shows the SEM images of pristine and implanted GNWs. The GNWs film consists of randomly oriented corrugated interconnected vertical walls of 275 ± 10 nm thickness having sharp growing edges uniformly spread over an area of 10 mm x 20 mm (carbon paper or the Si substrate). During implantation, the electric field densities at the edges become higher than that of its surroundings. As a result, the implantation as well as the sputtering at the tip of the GNWs takes place simultaneously. With reference to implantation, at a bias voltage of 1kV, SRIM simulation shows that the ions impinge on graphitic surfaces trace through several layers of the sample. Due to relatively low process duration, the sputtering effect is not visible and no obvious change in morphology is observed in the SEM of implanted samples.

The contact angle measurements shows that the wettability of the GNWs has increased upon implantation. It should be noted that due to high contact angle the capacitance of pristine GNWs is found to be very low. Increased wettability is known to improve the electro active surface area [306]. It is reported that the presence of nitrogenised functionalities has a positive contribution towards increasing capacitance by modifying the electronic properties as well as wettability [307]. Hence, increased wettability is one of the contributing factors towards improving the capacitance of nitrogen implanted GNWs. Apart

from 2 min. sample, 4 min. and 8 min. implanted samples also shows increased wettability. However, in the present study, it is observed that the capacitance has decreased for 4 min. and 8 min. implanted samples as compared to 2 min. implanted sample. This aspect clearly shows that there are some other major factors which plays more pivotal role in the supercapacitance than wettability.

The GNWs are inherently defective, and plasma ion implantation deposit nitrogen and generate extra defects in it. Hence, in the present study there are two origins for increased capacitance, viz.(i). the structural defects in the carbon back bone due to nitrogen, displaced carbon and attached oxygen [295,308,309] and (ii). nitrogen doping of graphene induce an increase in the quantum capacitance due to the change in density of states [310,311]. Nitrogen, oxygen and water vapour attachment takes place preferentially to the broken edges or defects (of the carbon back bone) and which increases with implantation duration. These defects (extra edges and vacancies, pentagon, heptagon, nitrogen replaced hexagon, etc.,) influence the density of states in graphene layers as compared to the pristine GNWs. Hence, a very complex state of affairs is evolved due to nitrogen plasma implantation and is difficult to describe the effect of each on capacitance independently. Without getting deep into electronic property changes due to nitrogen incorporation in the hexagon, the data from Raman, FTIR and XPS are used to understand the electrochemical response of implanted GNWs.

Working on from the synthesis aspects, GNWs are deposited using RF-PECVD and the basic difference in between the MW-PECVD synthesised GNWs and that of RF-PECVD one, are the high defect density, due to the higher energy of plasma species associated with RF plasma. It is shown that in comparison to MW - PECVD synthesised GNWs, RF-PECVD synthesised GNWs have higher edge density and as a result approximately 2.3 times higher capacitance [288]. Hence, it is clear that one of the contributing factors for increased capacitance is high defect density. Higher defect density is observed for 4 min. and 8 min. implanted samples (as seen from Raman, XPS, and FTIR) compared to 2 min implanted ones. However, these high defect density samples are not showing a corresponding increase in capacitance. This aspect shows that there are some other component, in addition to defect density operate which enhance the capacitance of implanted samples.

The primary effect of irradiation is defect generation and the defects are known to reduce the electrical conductivity in vertical graphene [87]. However, nitrogen doping has shown to improve the conductivity in graphene [312]. Hence, there could be an optimum

nitrogen concentration to have best defect structure and conducting nature for the material. Possibly, these two competing aspects will have the best value in 2 min. implanted sample as compared to 4 min. and 8 min. implanted samples. The CV diagram confirms that lowest resistance for the 2 min. implanted sample (Fig. 6.22). In addition to this, Raman and FTIR spectroscopic data shows lowest structural damage to 2 min. implanted samples. Hence, it is confirmed that increased electrical conductivity due to nitrogen addition is one of the contributing factors for increased capacitance. Additionally, studies shows that nitrogen induces sp^2 to sp^3 conversion of carbon and/or attach itself with the carbon back bone and/or the attached nitrogen form bond with oxygen and moisture. Each of these will be discussed.

The process of sp^2 to sp^3 structural conversion in N-GNWs and its effect in GNWs has already been discussed in the previous chapter. In the current context, the (sp^2 to sp^3) conversion reduces the electrical conductivity of GNWs or there can be strained regions due to the 2D and 3D nature of sp^2 and sp^3 bonding, respectively. The strain in graphene induce local change in density of states and deformation of Dirac cones and its displacement away from the K point [313]. Additionally, enhanced surface functionalization at regions of high local curvature has been observed in strained graphene [314]. Hence the strained regions in graphene have enhanced chemical reactivity and electronic properties to contribute towards increased capacitance. Another effect of implanted nitrogen is bond formation with the graphene. From the XPS analysis of nitrogen, as summarised in the previous chapter, nitrogen bonded with carbon and/or oxygen has been grouped into three types viz. N1, N2 and N3. The N1 (~398.5eV) and N2 (~400 eV) are based on the lone pair of electron unshared and shared, respectively. The N3 (~402 eV) type nitrogen binding energy corresponds to quaternary nitrogen or oxidised nitrogen. Since literature lacks reports of quaternary nitrogen, the description is clubbed with NO functionalities in the GNWs. The supercapacitance observed in the samples will be correlated with at% of nitrogen as N1, N2 and N3. In the study of N doped graphene, Hassan et al., indicate that the pyrrolic nitrogen (BE 400.3 eV) contribute to increased supercapacitance [305]. DFT simulation of pyrrolic nitrogen with K^+ ions shows the existence of optimum binding energy [305]. This energy range of nitrogen resembles with our N2 type nitrogen in which the lone pair of electron is delocalised. In another study, the pyridinic nitrogen present in nitrogen-functionalised graphene (N-FG) is considered to be enhancing the redox reactions whereas the electronegative pyrrolic nitrogen reduces the electron transfer rate [23,315]. Similarly, Haibo et al., indicates that the basal-plane pyridinic N has dominant role in the capacitance enhancement whereas, pyrrolic N has an opposite effect [23]. Based on the N 1s

energy, the pyridinic and pyrrolic peaks correspond to N1 and N2 type nitrogen in our categorization. Table 6.4 shows that N1 type nitrogen is maximum in 2min. implanted sample and its fraction decreases thereafter. Whereas, N2 and N3 fraction steadily increases with implantation duration. In the capacitance measurements, it is observed that capacitance increases for 2 min. of implantation and steadily decreases thereafter with increases in implantation duration. Just going by the experimental evidences it appears that pyridinic N (N1) promote capacitance whereas both graphitic (N2) and quaternary or oxidised nitrogen (N3) has the opposite effect. The effect of increase in oxygen functional groups with implantation is also studied.

The oxygen analysis is summarised in Table 6.5. The $-C-OH$ group fraction initially increases for 2 min. and 4 min. implanted samples and then decreases. However, the capacitive measurements indicate a sudden increase in the case of 2 min. implanted sample followed by continuous reduction. In the case of $-C=O$ group at%, an increase in 2 min. of implantation followed by its reduction is observed. This is in line with observed trend in capacitance. Whereas, the oxygen in $-O^*-C=O$ group initially reduces for 2 min and then shows an increasing trend. From the observations, we could not discern a uniform picture regarding the role of oxygen functionalities with reference to the pristine and implanted samples. However, there a few reports in literature which indicate the increase in capacitance is favoured by both $-C-OH$ (Hydroxyl) and $-C=O$ (Carbonyl) groups whereas, $-O-C=O$ (Carboxyl) groups reduces the capacitance [300,316]. The present study also finds a similar trend in the case of hydroxyl group with reference to pristine and 2 min. implanted samples and carbonyl groups for pristine and implanted samples.

Working on C 1s BE analysis of samples (Table 6.3), with increase in the hydrogen terminated vacancy defect and sp^3 C fraction, the capacitance decreases. There are reports in literature that laser ablated HOPG produce carbyne which undergo oxidation or graphitization by cross linking upon exposure to air [296]. It appears that initial (2 min.) nitridation/oxidation is occurring at the defects (carbyne or hydrogen terminated carbon at the vacancy) with minimum structural damage on the carbon backbone of GNWs. This is beneficial in increasing the capacitance. However, increased implantation causes structural damage leading to the reduction in capacitance. Similarly, the capacitance decreases with reduction in sp^2 C fraction. The increase in CO or CN fraction (~ 287 eV) actually appears to reduce the capacitance. More intense study is required to identify the effect of reduction in defect band of XPS upon implantation. However, for $-C-OH$ group, highest at% shows highest capacitance for the implanted sample.

Though the capacitance has increased enormously, the charge –discharge time is not increased in the same order. It appears the presence of nitrogen prevent hydrocarbon anchoring and subsequent loss of super hydrophilicity. The removal of surface adsorbed hydrocarbon may have opened up the electron transport channel inducing better conductivity. Sahoo et al., have shown that oxygen plasma treated GNWs show super hydrophilic nature and with ageing, the contact angle increases because of the adsorption of oxygen and moisture from the atmosphere to the dangling bonds [317]. However, N-GNWs have maintained the same hydrophilic nature even after 6 months of the first test. Hence, N-GNWs appear better candidate than oxygen plasma treated GNWs.

The pyridinic centres (N1 type nitrogen) in N-GNWs contribute to increases super capacitive nature. Additionally, the hydroxyl and carbonyl fraction also appear to enhance the capacitance for the implanted samples. However, the overall increase in capacitance due to N-implantation may be due to several factors such as increased number density of chemically active sites, wettability, improved morphological features, charge distribution, charge density, spin density and electrical conductivity adding to quantum capacitance, electric double layer capacitance and pseudo capacitance. Examining and correlating each of this is required to fine tune the process of nitrogen plasma ion implantation for supercapacitor applications of GNWs, which is beyond the scope of this work and left for future prospects.

Chapter 7

Summary, Conclusion and Future prospects

7.1. Summary

Nitrogen doped graphene offers ample electrochemical advantage as an electrode material in a variety of applications. Hence GNWs, a self-standing vertical arrangement of a few layers of graphene, attracts the attention as a substitute to graphene in its pristine or doped form. The conducting nature with the possibility for doping along with large surface area make GNWs a potential candidate for application in fuel cells, sensors, supercapacitors, etc.. However, a systematic study on the influence of process parameters on the development of morphology and electronic nature is scarce in literature. Additionally, nitrogen incorporation and its influence on the electronic, mechanical and electrochemical properties are seldom discussed. Hence, there is a need to study the synthesis and nitrogen incorporation process and its effect on GNWs towards understanding and developing future applications of high surface area carbon nano architectures.

A custom made plasma immersion ion implantation and deposition (PIII&D) facility is used for the plasma enhanced chemical vapour deposition (PECVD) of GNWs and plasma immersion ion implantation (PIII) for nitrogen incorporation in graphene nanowalls. Being a custom made equipment, both PECVD and PIII aspects need to be evaluated. Hence, the basic experimental aspects of PIII&D facility for low power (~25W), long duration (upto 90 min.) plasma ion implantation is carried out by nitrogen PIII (at ~10kV) on titanium and is analysed using SRIM simulation, SIMS and XPS techniques. High power (100W), short duration (2, 5, 10 (min.) etc.) plasma ion implantation aspects are studied by nitrogen plasma ion implantation (at10kV) of silicon substrate using SIMS technique. It is found that higher fraction of N^+ ions are generated when the rf plasma power is large. Additionally, the N^+ ions are found to be more reactive than N_2^+ ions. These two aspects are considered for nitrogen plasma ion implantation of GNWs.

Though GNWs can be synthesised by plasma enhanced chemical vapour deposition, the morphology and structure of GNWs vary with process parameters. Hence, there is need to understand the influence of process parameters on the morphology and structure of GNWs. In a PECVD process, several parameters such as process gas ratio, pressure, plasma power, temperature and type of substrate influence the morphology and structure. Though

there are reports in literature on this topic, systematic study on influence of given parameters (e.g. gas ratio) by keeping all the other parameters constant is scarce. Hence, it is necessary to understand the influence of gas ratio on the morphology and structure. GNWs are synthesised at different gas ratios on SiO₂/Si wafer and the atomistic growth mechanism leading to a given morphology, structure and electronic nature are deduced using Raman, FTIR, TEM and EELS. The G-peak normalised intensity plot of Raman spectra shows major variation only in the D peak of GNWs with change in gas ratio. The formation of bridging methylene (>CH₂) group is found to be responsible for secondary growth. The TEM and electron diffraction pattern of GNWs show that the gas ratio influences the crystalline nature and d-spacing. For GNWs, the plasmonic peak energy falls in between monolayer graphene and that of graphite. The C K-edge of GNWs registered a lower value by ~1eV as compared graphite. Additionally, highest deposition rate is observed for Ar:CH₄ ratio, 1:3.

Nitrogen doped graphene exhibit several interesting properties and thus, find a lot of electrochemical applications. In this line, nitrogen doped GNWs can induce revolutionary changes in its applications. However, the process of nitrogen incorporation in GNWs is not well established. Mixing nitrogen with PECVD precursor gases is the most common method followed. However, nitrogen has etching effects on GNWs and it adversely influences the growth rate. One of the possible alternatives is nitrogen ion implantation. There are reports in literature on using ion guns to implant nitrogen in GNWs. However, the basic drawback of all line-of-sight ion implantation technique is low dose and inherent sputtering. Hence, to start with, low energy (2kV) long duration (upto 30 min.) plasma ion implantation is carried out on GNWs for the first time. SEM studies shows the sputter removal of material at longer implantation duration. Raman studies shows generation of defects and damage to sp²C network and approximately 8 at% of nitrogen is estimated from XPS studies. The nitrogen plasma implanted samples were analysed using XPS to understand the chemical nature of the samples. A large volume of literature describe the nature of nitrogen in GNWs by correlating it with respective nitrogenous organic compounds such as pyridine, nitrile, etc. However, this description did not convey the electronic nature of GNWs which is important for an application. In order to overcome this difficulty, the nitrogen in GNWs are categorised into three groups as N1, N2 and N3 based on the binding energy of N 1s electron and possible location in GNWs. In this method the status of lone pair of electron whether shared or not determine N2 or N1 type categorization. The oxidised or quaternary nitrogen falls in N3 category. This new approach is used to

explain the improved mechanical properties of N-GNWs as estimated from AFAM technique.

Material sputter removal is observed in the high dose implantation experiment and the electrochemical reactions are occurring on the surface of GNWs and so, it is not necessary to implant nitrogen with 2 kV and high dose. Hence, low energy (1 kV) low dose 4-6 at% plasma nitrogen ion implantation is carried out. Towards exploring the N-GNWs for electrochemical applications, the above experiment is conducted on GNWs deposited on SiO₂/Si and on carbon fibre paper. The samples are characterised using SEM, Raman, FTIR, XPS and electrochemical techniques. XPS studies have shown that at two minutes of implantation, ~4 at% nitrogen appear to be surface bonded with minimum structural defects. Increase in implantation time duration (4 min. and 8 min.) resulted slight increases in nitrogen atomic fraction (upto 6 at %). XPS study further shows that hydrogen terminated vacancy peak found to have reduced intensity compared to pristine sample. There is a gradual reduction in sp²C and increase in sp³C with increase in process duration. FTIR spectrum did not show any appreciable variation in 2 min. of plasma ion (nitrogen) implantation. However, with increase in implantation duration the FTIR spectrum shows some new peak generation or loss of intensity of some existing peaks. Electrochemical studies show that 2 min. implanted samples have highest capacitance value compared to 4 and 8 min. implanted samples. However, the most obvious thing is the super hydrophilic nature developed upon implantation. As a result, the electrode/electrolyte area of contact (wetting) has increased enormously. The 2 min. implanted sample show an increase in capacitance more than 00 times and is due to the fact that shallow ion implantation had produced several defects on the surface which act as charge storage centres. Though specific functional groups are not developed in 2 min. of implantation; nitrogen, oxygen and carbon local bonding lead to increase in capacitance. However, with increase in implantation time (4 min and 8 min.) the capacitance is reduced. This can be due to the damage occurred to the conducting sp² bonded hexagonal structure (as seen in Raman spectroscopy) and consequent increase in impedance. Hence, it appears that two competing effects are generated in the material (a) increase in contact area and pseudocapacitance resulting in the overall capacitance enhancement and (b) the excess structural damage to the hexagonal network with prolonged implantation resulting in impedance increase and capacitance reduction.

The present work indicate that GNWs of highly corrugated morphology with secondary growth can be prepared in RF PECVD process by using an Argon-Methane gas

mixture. The GNWs are nitrogen incorporated to different concentrations by varying the applied voltage or the ions of interest (N^+ or N_2^+ -major plasma) can be chosen by varying the plasma power. Nitrogen incorporation enhances the super capacitive behaviour of GNWs due to enhancement of electrode –electrolyte contact area, enhanced wetting, increase in quantum capacitance, increase in EDLC and generation of pseudocapacitance. There is bright scope for using N-GNWs for future supercapacitor applications.

Present study brought out the following results

- i. For a RF plasma power of 150W, GNWs of highest growth rate is synthesised by using Argon–Methane gas at 3:1 ratio (3.5×10^{-3} mbar pressure, 800° C, SiO_2/Si -substrate). The rate can be enhanced by increasing the RF power.
- ii. The morphology and crystallinity are influenced by the process gas ratio and resulting plasma conditions. GNWs of improved crystalline quality register higher growth rate, whereas secondary growth is caused by methylene species in the plasma.
- iii. EELS study indicate that the plasmonic peak of GNWs lie in between that of monolayer graphene and HOPG. Lower the value, better the crystallinity and monolayer graphene like nature. Defects and electropositive edge species push the plasmonic peak of GNWs up.
- iv. The K edge of carbon register a reduction for GNWs compared to HOPG. However, the π^* and $\pi^* + \sigma^*$ peak position remain same.
- v. By controlling the RF plasma power and bias, relative enhancement of N^+ or N_2^+ ions is achieved in plasma ion implantation process. The chemical reactivity of N^+ ions is higher than that of N_2^+ ions.
- vi. Nitrogen, depending on its location in the hexagonal graphene structure of GNWs, localise, delocalise and transfer electrons to induce local p-type, n-type and polar type character, respectively. N-doped GNWs exhibit improved mechanical properties.
- vii. Low energy and short duration plasma exposure of GNWs induce surface bonding with carbon and oxygen with minimum defect. This is the key for high capacitance value of N-GNWs. Additionally, GNWs become superhydrophilic after plasma treatment.

-
- viii. N-GNWs register enormous (more than 100 times) increase in charge storage when tested with 1M KOH solution and thus, shallow plasma ion implantation offer huge prospects for surface modification of GNWs towards enhancing the supercapacitive properties.
 - ix. Nitrogen with lone pair unshared configuration (N1) found to enhance the capacitance in GNWs. Additionally, the hydroxyl (OH) and carbonyl group (-C=O) may also help to increase in capacitance. Effectively the EDLC, the quantum capacitance and pseudo capacitance has increased due to plasma treatment.

7.2. Conclusion

Process parameters during synthesis influence surface morphology, surface energy states and ordered arrangement of layers in GNWs. Shallow plasma surface modification of GNWs using nitrogen influence the electronic nature and enhances the mechanical properties. N-GNWs poise for a promising electrode material in electrochemical devices such as supercapacitors.

7.3. Scope for future works

The work on synthesis and shallow nitrogen plasma ion implantation of vertical graphene nanowalls is a success and opens up several areas with huge prospects for future works on improving the relevant properties towards selected applications. This is the first work on shallow plasma ion implantation of GNWs ever reported in literature.

Experiments on synthesis of GNWs of specific morphology and structure at relatively lower temperature, on other substrates and with various dopants can be an active area of research for materials development.

The influence of gas ratio on the crystalline nature and the identification of bridging methylene as a species responsible for secondary growth in GNWs, will continue to enhance the research in this area for controlling morphology and crystalline character.

Since the plasmonic peaks of GNWs can be tuned in between graphene and graphite, GNWs can be used as mechanical back bone for a variety of heteroatoms/structures to improve their performance and extend utilization such as surface enhanced Raman scattering (SERS) and fuel cells.

The N^+ ions are more reactive than N_2^+ ions in nitrogen plasma. Shallow ion implantation of chosen ion can be used to induce reactions or intercalation of nitrogen species to make materials of new properties.

Generation of plasma with gases containing boron and nitrogen along with methane open up synthesis of GNWs of interesting properties because of the generation of p-type and n-type regions along with zero band gap graphene. This could be a very promising super electrode material for sensors, supercapacitors, etc.

In the field of sensors, smaller the sensing region better the uniformity and response. Hence, one of the most promising area for future research is related to sensors. Due to the high electro-chemical activity, electrochemical sensing for several medical application has already been reported. [122,318]. In addition to that, our own studies based on AFM/PFM shows colossal piezo –electric effect in GNWs. This open up the application in the field of physical sensors. The tips of GNWs are magnetic and magnetism based sensors are a promising application. Hence, the work on GNWs based sensors are very promising future area of research. Inherent hydrophobic nature and super hydrophilic behaviour upon plasma treatment can be used be used for making novel surfaces. Depositing metal nanoparticles such as Pt, Ag, Au, etc. or carbide forming elements such as Si can be explored in sensors and energy harvesting devices for work function smoothening or making for making ohmic contacts.

Enhanced capacitance of nitrogen implanted GNWs indicate the presence of charge storage centres. In GNWs, Schottky barriers may be formed in between regions whose electronic energy state differ. Understanding the mechanism of charge storage in implanted GNWs demand controlled conductive and/or electrochemical AFM or similar methods. The contribution of electric double layer capacitance, quantum capacitance and pseudocapacitance to overall capacitance has to be addressed separately. Hence the study on the this area can yield rich applied physics results.

More sophistication in GNWs synthesis specific to an application, electrolyte, and nitrogen incorporation will continue be an active area of research. Enhancing the energy density of GNWs or N-doped GNWs based supercapacitors will be a high priority challenge.

The PIII & D process is suitable for research related to the synthesis of MXenes. MXenes are a few layer transition metal carbides with general formulae $M_{n+1} X_n T_x$, where M –transition metal, X-C/N and n-between 1 to 3, T_x represents for surface functional groups. It has a conducting inner transition metal carbide layer for electron supply, a

transition metal oxide like surface generated during synthesis is redox active and 2D morphology and pre-intercalated water enable fast electron transport. Being the synthesis method and applications of GNWs, N-GNWs, PECVD and plasma ion implantation are relatively new, versatile and novel, several variants of process optimization can be experimented towards specific applications such as nanofiltration, isotopic separation, adsorption and composite material for nuclear waste immobilization, and radiation detection.

GNWs consists of a few to several layers, sharp edges, corrugated morphology, several junctions and large variety of defects. The theories based on monolayer graphene and a few defects or attributing graphite like behaviour for a bunch of graphitic layers did not represent the actual behaviour. Hence, in the characterisation front, data analysis based on the theoretical and experimental results of graphene or bulk graphite should be properly addressed. There is a requirement of GNWs specific modifications in simulation theory and data analysis. Hence, the studies conducted on Raman, FTIR and XPS can be extended on GNWs synthesised with specific defects density, attachment of functional groups and specific dopants. Studies on EELS can be extended to arrive benchmarking parameters for the quality of GNWs. There are reports of tiny band gap in GNWs due to morphological factors. However, very few studies have been carried out to actually probe the influence of morphology on band gap. Similarly, each of the characterisation tools specific to GNWs need special attention in data interpretation. All the possible application of GNWs and N-GNWs that have been mentioned are of preliminary in nature and these subjects are continue to be an active area of research for improvement and enhancement of performance.

References

- [1] M. D. Stoller, S. Park, Z. Yanwu, J. An, and R. S. Ruoff, *Nano Lett.* **8**, 3498 (2008).
- [2] A. A. Balandin, S. Ghosh, W. Bao, I. Calizo, D. Teweldebrhan, F. Miao, C. N. Lau, A. A. Balandin, S. Ghosh, W. Bao, I. Calizo, D. Teweldebrhan, F. Miao, and C. Ning Lau, *Nano Lett.* **8**, 902 (2008).
- [3] C. Lee, X. Wei, J. W. Kysar, and J. Hone, *Science* **321**, 385 (2008).
- [4] E. Pop, V. Varshney, and A. K. Roy, *MRS Bull.* **37**, 1273 (2012).
- [5] R. J. Young and M. Liu, *J. Mater. Sci.* **51**, 3861 (2016).
- [6] G. Mittal, V. Dhand, K. Y. Rhee, S.-J. Park, and W. R. Lee, *J. Ind. Eng. Chem.* **21**, 11 (2015).
- [7] Y. H. Wu, T. Yu, and Z. X. Shen, *J. Appl. Phys.* **108**, (2010).
- [8] T. Mahmoudi, Y. Wang, and Y. B. Hahn, *Nano Energy* **47**, 51 (2018).
- [9] K. Cui and S. Maruyama, *Prog. Energy Combust. Sci.* **70**, 1 (2019).
- [10] N. N. Rosli, M. A. Ibrahim, N. Ahmad Ludin, M. A. Mat Teridi, and K. Sopian, *Renew. Sustain. Energy Rev.* **99**, 83 (2019).
- [11] S. Zheng, Z. S. Wu, S. Wang, H. Xiao, F. Zhou, C. Sun, X. Bao, and H. M. Cheng, *Energy Storage Mater.* **6**, 70 (2017).
- [12] V. Tozzini and V. Pellegrini, *Phys. Chem. Chem. Phys.* **15**, 80 (2013).
- [13] L. Schlappbach and A. Züttel, *Nature* **414**, 353 (2001).
- [14] M. R. Al Hassan, A. Sen, T. Zaman, and M. S. Mostari, *Mater. Today Chem.* **11**, 225 (2019).
- [15] N. Lisi, R. Giorgi, M. Re, T. Dikonimos, L. Giorgi, E. Salernitano, S. Gagliardi, and F. Tatti, *Carbon N. Y.* **49**, 2134 (2011).
- [16] Z. Bo, S. Mao, Z. Jun Han, K. Cen, J. Chen, and K. Ostrikov, *Chem. Soc. Rev.* **44**, 2108 (2015).
- [17] Z. Bo, Y. Yang, J. Chen, K. Yu, J. Yan, and K. Cen, *Nanoscale* **5**, 5180 (2013).
- [18] N. Hellgren, R. T. Haasch, S. Schmidt, L. Hultman, and I. Petrov, *Carbon N. Y.* **108**, 242 (2016).
- [19] C. Zhang, R. Hao, H. Liao, and Y. Hou, *Nano Energy* **2**, 88 (2013).
- [20] A. Ariharan, B. Viswanathan, and V. Nandhakumar, *Graphene* **06**, 41 (2017).
- [21] Y. Lu, Y. Huang, M. Zhang, and Y. Chen, *J. Nanosci. Nanotechnol.* **14**, 1134 (2014).
- [22] Y. Wang, Y. Shao, D. W. Matson, J. Li, and Y. Lin, *ACS Nano* **4**, 1790 (2010).
- [23] H. Wang, T. Maiyalagan, and X. Wang, *ACS Catal.* **2**, 781 (2012).
- [24] Z. Wang, M. Shoji, and H. Ogata, *Appl. Surf. Sci.* **257**, 9082 (2011).
- [25] K. Bystrov, M. C. M. Van De Sanden, C. Arnas, L. Marot, D. Mathys, F. Liu, L. K. Xu, X. B. Li, A. V. Shalpegin, and G. De Temmerman, *Carbon N. Y.* **68**, 695 (2014).

-
- [26] G. Sato, T. Morio, T. Kato, and R. Hatakeyama, *Japanese J. Appl. Physics, Part 1 Regul. Pap. Short Notes Rev. Pap.* **45**, 5210 (2006).
- [27] Y. P. Lin, Y. Ksari, J. Prakash, L. Giovanelli, J. C. Valmalette, and J. M. Themlin, *Carbon N. Y.* **73**, 216 (2014).
- [28] K. J. Kim, S. Yang, Y. Park, M. Lee, B. Kim, and H. Lee, *J. Phys. Chem. C* **117**, 2129 (2013).
- [29] S. Sakulsermsuk, P. Singjai, and C. Chaiwong, *Diam. Relat. Mater.* **70**, 211 (2016).
- [30] L. Huang, Y. Cao, and D. Diao, *Appl. Surf. Sci.* **470**, 205 (2019).
- [31] Y. Hao, X. Li, X. Sun, and C. Wang, *Mater. Sci. Eng. B* **213**, 83 (2016).
- [32] Y. Wu, P. Qiao, T. Chong, and Z. Shen, *Adv. Mater.* **14**, 64 (2002).
- [33] H. W. Kroto, J. R. Heath, S. C. O'Brien, R. F. Curl, and R. E. Smalley, *Nature* **318**, 162 (1985).
- [34] Y. Ando, X. Zhao, and M. Ohkohchi, *Carbon N. Y.* **35**, 153 (1997).
- [35] K. S. Novoselov, A. K. Geim, S. V. Morozov, D. Jiang, Y. Zhang, S. V. Dubonos, I. V. Grigorieva, and A. A. Firsov, *Science (80-)*. **306**, 666 (2004).
- [36] T. Kuila, S. Bose, A. Kumar, and P. Khanra, *Prog. Mater. Sci.* **57**, 1061 (2012).
- [37] X. H. Chen, H. S. Yang, G. T. Wu, M. Wang, F. M. Deng, X. B. Zhang, J. C. Peng, and W. Z. Li, *J. Cryst. Growth* **218**, 57 (2000).
- [38] W. Weng and C. Wu, *Carbon N. Y.* **41**, 619 (2003).
- [39] G. Chen, W. Weng, D. Wu, C. Wu, J. Lu, P. Wang, and X. Chen, *Carbon N. Y.* **42**, 753 (2004).
- [40] M. Hirata, T. Gotou, S. Horiuchi, M. Fujiwara, and M. Ohba, *Carbon N. Y.* **42**, 2929 (2004).
- [41] D. H. Seo and A. E. Rider, *Carbon N. Y.* **60**, 221 (2013).
- [42] J. H. Deng, S. L. Wu, Y. M. Yang, R. T. Zheng, and G. A. Cheng, *Nucl. Instruments Methods Phys. Res. Sect. B Beam Interact. with Mater. Atoms* **307**, 177 (2013).
- [43] H. Wang, E. Gao, P. Liu, D. Zhou, D. Geng, X. Xue, L. Wang, K. Jiang, Z. Xu, and G. Yu, *Carbon N. Y.* **121**, 1 (2017).
- [44] T. Itoh, *Thin Solid Films* **519**, 4589 (2011).
- [45] T. Mori, M. Hiramatsu, K. Yamakawa, K. Takeda, and M. Hori, *Diam. Relat. Mater.* **17**, 1513 (2008).
- [46] S. Vizireanu, S. D. Stoica, C. Luculescu, L. C. Nistor, B. Mitu, and G. Dinescu, *Plasma Sources Sci. Technol.* **19**, (2010).
- [47] W. Jacob, *Thin Solid Films* **326**, 1 (1998).
- [48] E. Sandoz-Rosado, W. Page, D. O'Brien, J. Przepioski, D. Mo, B. Wang, T.-T. Ngo-Duc, J. Gacusan, M. W. Winter, M. Meyyappan, R. D. Cormia, S. Takahashi, and M. M. Oye, *J. Mater. Res.* **29**, 417 (2014).
- [49] N. M. Santhosh, G. Filipič, E. Tatarova, O. Baranov, H. Kondo, M. Sekine, M.
-

- Hori, K. (Ken) Ostrikov, and U. Cvelbar, *Micromachines* **9**, (2018).
- [50] O. Baranov, I. Levchenko, S. Xu, J. W. M. Lim, U. Cvelbar, and K. Bazaka, *2D Mater.* **5**, 44002 (2018).
- [51] R. Vitchev, A. Malesevic, R. H. Petrov, R. Kemps, M. Mertens, A. Vanhulsel, and C. Van Haesendonck, *Nanotechnology* **21**, (2010).
- [52] S. Chugh, R. Mehta, N. Lu, F. D. Dios, M. J. Kim, and Z. Chen, *Carbon N. Y.* **93**, 393 (2015).
- [53] S. Ghosh, K. Ganesan, S. R. Polaki, T. Mathews, S. Dhara, M. Kamruddin, and A. K. Tyagi, *Appl. Surf. Sci.* **349**, 576 (2015).
- [54] L. Nang, D.-O. Kim, T. N. Trung, V. Arepalli, and E.-T. Kim, *Appl. Microsc.* **47**, 13 (2017).
- [55] J. J. Wang, M. Y. Zhu, R. A. Outlaw, X. Zhao, D. M. Manos, B. C. Holloway, and V. P. Mammana, *Appl. Phys. Lett.* **85**, 1265 (2004).
- [56] C. Zhang, J. Hu, X. Wang, X. Zhang, H. Toyoda, M. Nagatsu, and Y. Meng, *Carbon N. Y.* **50**, 3731 (2012).
- [57] S. Kondo, S. Kawai, W. Takeuchi, K. Yamakawa, S. Den, H. Kano, M. Hiramatsu, and M. Hori, *J. Appl. Phys.* **106**, 94302 (2009).
- [58] M. Acosta Gentoiu, R. Betancourt-Riera, S. Vizireanu, I. Burducea, V. Marascu, S. D. Stoica, B. I. Bitu, G. Dinescu, and R. Riera, *J. Nanomater.* **2017**, 8 (2017).
- [59] A. Malesevic, R. Vitchev, K. Schouteden, A. Volodin, L. Zhang, G. Van Tendeloo, A. Vanhulsel, and C. Van Haesendonck, *Nanotechnology* **19**, 305604 (2008).
- [60] G. Kalita, K. Wakita, and M. Umeno, *RSC Adv.* **2**, 2815 (2012).
- [61] N. Soin, S. S. Roy, C. O’Kane, J. A. D. McLaughlin, T. H. Lim, and C. J. D. Hetherington, *CrystEngComm* **13**, 312 (2011).
- [62] N. Soin, S. S. Roy, T. H. Lim, and J. A. D. McLaughlin, *Mater. Chem. Phys.* **129**, 1051 (2011).
- [63] K. Lehmann, O. Yurchenko, and G. Urban, *RSC Adv.* **6**, 32779 (2016).
- [64] M. H. Syed, S. K. Chong, N. M. Huang, and S. Abdul Rahman, *Carbon N. Y.* **86**, 1 (2015).
- [65] C. Yang, H. Bi, D. Wan, F. Huang, X. Xie, and M. Jiang, *J. Mater. Chem. A* **1**, 770 (2013).
- [66] M. Zhu, J. Wang, B. C. Holloway, R. A. Outlaw, X. Zhao, K. Hou, V. Shutthanandan, and D. M. Manos, *Carbon N. Y.* **45**, 2229 (2007).
- [67] S. Y. Kim, W. S. Choi, J. H. Lee, and B. Hong, *Mater. Res. Bull.* **58**, 112 (2014).
- [68] S. Ghosh, S. R. Polaki, M. Kamruddin, S. M. Jeong, and K. Ostrikov, *J. Phys. D: Appl. Phys.* **51**, 145303 (2018).
- [69] K. Yu, P. Wang, G. Lu, K. H. Chen, Z. Bo, and J. Chen, *J. Phys. Chem. Lett.* **2**, 537 (2011).
- [70] J. Zhao, M. Shaygan, J. Eckert, M. Meyyappan, and M. H. Rummeli, *Nano Lett.* **14**, 3064 (2014).

- [71] H. Yoshimura, S. Yamada, A. Yoshimura, I. Hirosawa, K. Kojima, and M. Tachibana, *Chem. Phys. Lett.* **482**, 125 (2009).
- [72] M. A. Pimenta, G. Dresselhaus, M. S. Dresselhaus, L. G. Cançado, A. Jorio, and R. Saito, *Phys. Chem. Chem. Phys.* **9**, 1276 (2007).
- [73] S. Ghosh, K. Ganesan, S. R. Polaki, S. Ilango, S. Amirthapandian, S. Dhara, M. Kamruddin, and A. K. Tyagi, *RSC Adv.* **5**, 91922 (2015).
- [74] S.-M. Dubois, Z. Zanolli, X. Declerck, and J.-C. Charlier, *Eur. Phys. J. B* **72**, 1 (2009).
- [75] T. C. Nguyen, M. Otani, and S. Okada, *Phys. Rev. Lett.* **106**, 106801 (2011).
- [76] S. Okada and T. Kawai, *Jpn. J. Appl. Phys.* **51**, 02BN05 (2012).
- [77] M. S. Dresselhaus and G. Dresselhaus, *Adv. Phys.* **51**, 1 (2002).
- [78] J. Wang, M. Zhu, R. A. Outlaw, X. Zhao, D. M. Manos, and B. C. Holloway, *Carbon N. Y.* **42**, 2867 (2004).
- [79] K. Nakada, M. Fujita, G. Dresselhaus, and M. S. Dresselhaus, *Phys. Rev. B* **54**, 17954 (1996).
- [80] M. Fujita, K. Wakabayashi, K. Nakada, and K. Kusakabe, *J. Phys. Soc. Japan* **65**, 1920 (1996).
- [81] D. H. Seo, S. Kumar, and K. Ostrikov, *J. Mater. Chem.* **21**, 16339 (2011).
- [82] G. López-Polín, C. Gómez-Navarro, V. Parente, F. Guinea, M. I. Katsnelson, F. Pérez-Murano, and J. Gómez-Herrero, *Nat. Phys.* **11**, 26 (2014).
- [83] M. C. Strus, R. R. Lahiji, P. Ares, V. López, A. Raman, and R. Reifengerger, *Nanotechnology* **20**, 385709 (2009).
- [84] M. R. Begley and T. J. Mackin, *J. Mech. Phys. Solids* **52**, 2005 (2004).
- [85] G.-H. Lee, R. C. Cooper, S. J. An, S. Lee, A. van der Zande, N. Petrone, A. G. Hammerberg, C. Lee, B. Crawford, W. Oliver, J. W. Kysar, and J. Hone, *Science (80-.)*. **340**, 1073 LP (2013).
- [86] A. Zandiatashbar, G. H. Lee, S. J. An, S. Lee, N. Mathew, M. Terrones, T. Hayashi, C. R. Picu, J. Hone, and N. Koratkar, *Nat. Commun.* **5**, 1 (2014).
- [87] C. Lin, K. Davami, Y. Jiang, J. Cortes, M. Munther, M. Shaygan, H. Ghassemi, J. T. Robinson, K. T. Turner, and I. Bargatin, *Nanotechnology* **28**, 295701 (2017).
- [88] K. Davami, Y. Jiang, J. Cortes, C. Lin, M. Shaygan, K. T. Turner, and I. Bargatin, *Nanotechnology* **27**, 155701 (2016).
- [89] Y. Liu, B. Xie, Z. Zhang, Q. Zheng, and Z. Xu, *J. Vac. Sci. Technol. B Microelectron. Nanom. Struct.* **25**, 23 (2011).
- [90] B. Ouyang, Y. Wang, Z. Zhang, and R. S. Rawat, *Electrochim. Acta* **194**, 151 (2016).
- [91] X. Xiao, P. Liu, J. S. Wang, M. W. Verbrugge, and M. P. Balogh, *Electrochem. Commun.* **13**, 209 (2011).
- [92] T. Jiao, D. Wei, X. Song, T. Sun, J. Yang, L. Yu, Y. Feng, W. Sun, W. Wei, H. Shi, C. Hu, and C. Du, *RSC Adv.* **6**, 10175 (2016).

- [93] J. R. Miller, R. A. Outlaw, and B. C. Holloway, *Science* (80-.). **329**, 1637 (2010).
- [94] M. Cai, R. A. Outlaw, S. M. Butler, and J. R. Miller, *Carbon N. Y.* **50**, 5481 (2012).
- [95] S. Vizireanu, G. Dinescu, L. C. Nistor, M. Baibarac, G. Ruxanda, M. Stancu, and D. Ciuparu, *Phys. E Low-Dimensional Syst. Nanostructures* **47**, 59 (2013).
- [96] G. Sahoo, S. Ghosh, S. R. Polaki, T. Mathews, and M. Kamruddin, *Nanotechnology* **28**, 415702 (2017).
- [97] E. Luais, M. Boujtita, A. Gohier, A. Tailleur, S. Casimirius, M. A. Djouadi, A. Granier, and P. Y. Tessier, *Appl. Phys. Lett.* **95**, 014104 (2009).
- [98] A. Taheri Najafabadi and A. T. Najafabadi, *Renew. Sustain. Energy Rev.* **41**, 1515 (2015).
- [99] A. Malesevic, R. Kemps, A. Vanhulsel, M. P. Chowdhury, A. Volodin, and C. Van Haesendonck, *J. Appl. Phys.* **104**, 1 (2008).
- [100] J. L. Qi, X. Wang, W. T. Zheng, H. W. Tian, C. Q. Hu, and Y. S. Peng, *J. Phys. D. Appl. Phys.* **43**, (2010).
- [101] S. Mao, K. Yu, J. Chang, D. A. Steeber, L. E. Ocola, and J. Chen, *Sci. Rep.* **3**, 33 (2013).
- [102] O. Akhavan, E. Ghaderi, and R. Rahighi, *ACS Nano* **6**, 2904 (2012).
- [103] V. A. Krivchenko, S. A. Evlashin, K. V. Mironovich, N. I. Verbitskiy, A. Nefedov, C. Wöll, A. Y. Kozmenkova, N. V. Suetin, S. E. Svyakhovskiy, D. V. Vyalikh, A. T. Rakhimov, A. V. Egorov, and L. V. Yashina, *Sci. Rep.* **3**, 1 (2013).
- [104] J. L. Qi, W. T. Zheng, X. H. Zheng, X. Wang, and H. W. Tian, *Appl. Surf. Sci.* **257**, 6531 (2011).
- [105] A. Kawabata, T. Murakami, M. Nihei, and N. Yokoyama, *Jpn. J. Appl. Phys.* **52**, 8 (2013).
- [106] W. Takeuchi, M. Ura, M. Hiramatsu, Y. Tokuda, H. Kano, and M. Hori, *Appl. Phys. Lett.* **92**, 4 (2008).
- [107] S. Jalili and R. Vaziri, *Mol. Phys.* **109**, 687 (2011).
- [108] C. Hu and L. Dai, *Adv. Mater.* **31**, 1804672 (2019).
- [109] C. P. Ewels, D. Erbahar, P. Wagner, X. Rocquefelte, R. Arenal, P. Pochet, M. Rayson, M. Scardamaglia, C. Bittencourt, and P. Briddon, *Faraday Discuss.* **173**, 215 (2014).
- [110] M. Inagaki, M. Toyoda, Y. Soneda, and T. Morishita, *Carbon N. Y.* **132**, 104 (2018).
- [111] D. Deng, X. Pan, L. Yu, Y. Cui, Y. Jiang, J. Qi, W.-X. Li, Q. Fu, X. Ma, and Q. Xue, *Chem. Mater.* **23**, 1188 (2011).
- [112] C. H. Chuang, S. C. Ray, D. Mazumder, S. Sharma, A. Ganguly, P. Papakonstantinou, J. W. Chiou, H. M. Tsai, H. W. Shiu, C. H. Chen, H. J. Lin, J. Guo, and W. F. Pong, *Sci. Rep.* **7**, 1 (2017).
- [113] Z. Wen, X. Wang, S. Mao, Z. Bo, H. Kim, S. Cui, G. Lu, X. Feng, and J. Chen, *Adv. Mater.* **24**, 5610 (2012).

-
- [114] K. Parvez, S. Yang, Y. Hernandez, A. Winter, A. Turchanin, X. Feng, and K. Müllen, *ACS Nano* **6**, 9541 (2012).
- [115] Y. Xue, J. Liu, H. Chen, R. Wang, D. Li, J. Qu, and L. Dai, *Angew. Chemie Int. Ed.* **51**, 12124 (2012).
- [116] H. F. Yen, Y. Y. Horng, M. S. Hu, W. H. Yang, J. R. Wen, A. Ganguly, Y. Tai, K. H. Chen, and L. C. Chen, *Carbon N. Y.* **82**, 124 (2015).
- [117] Z. Luo, S. Lim, Z. Tian, J. Shang, L. Lai, B. MacDonald, C. Fu, Z. Shen, T. Yu, and J. Lin, *J. Mater. Chem.* **21**, 8038 (2011).
- [118] Y. Xue, B. Wu, L. Jiang, Y. Guo, L. Huang, J. Chen, J. Tan, D. Geng, B. Luo, W. Hu, G. Yu, and Y. Liu, *J. Am. Chem. Soc.* **134**, 11060 (2012).
- [119] D. Wei, Y. Liu, Y. Wang, H. Zhang, L. Huang, and G. Yu, *Nano Lett.* **9**, 1752 (2009).
- [120] Y. Shao, S. Zhang, M. H. Engelhard, G. Li, G. Shao, Y. Wang, J. Liu, I. A. Aksay, and Y. Lin, *J. Mater. Chem.* **20**, 7491 (2010).
- [121] A. Achour, S. Vizireanu, G. Dinescu, L. Le Brizoual, M. A. Djouadi, and M. Boujtita, *Appl. Surf. Sci.* **273**, 49 (2013).
- [122] R. Ion, S. Vizireanu, C. E. Stancu, C. Luculescu, A. Cimpean, and G. Dinescu, *Mater. Sci. Eng. C* **48**, 118 (2015).
- [123] S. Ghosh, S. R. Polaki, N. G. Krishna, and M. Kamruddin, *J. Mater. Sci.* **53**, 7316 (2018).
- [124] K. Teii, S. Shimada, M. Nakashima, and A. T. H. Chuang, *J. Appl. Phys.* **106**, 084303 (2009).
- [125] D. Aradilla, M. Delaunay, M. Buhagiar, D. Aldakov, J. Faure-Vincent, H. Okuno, J.-M. Gerard, and G. Bidan, *Curr. Smart Mater.* **3**, 32 (2017).
- [126] J. P. McClure, J. D. Thornton, R. Jiang, D. Chu, J. J. Cuomo, and P. S. Fedkiw, *J. Electrochem. Soc.* **159**, F733 (2012).
- [127] Y. W. Chi, C. C. Hu, H. H. Shen, and K. P. Huang, *Nano Lett.* **16**, 5719 (2016).
- [128] M. Scardamaglia, M. Amati, B. Llorente, P. Mudimela, J. F. Colomer, J. Ghijsen, C. Ewels, R. Snyders, L. Gregoratti, and C. Bittencourt, *Carbon N. Y.* **77**, 319 (2014).
- [129] F. Xu, M. Minniti, C. Giallombardo, A. Cupolillo, P. Barone, A. Oliva, and L. Papagno, *Surf. Sci.* **601**, 2819 (2007).
- [130] M. Guo, D. Li, M. Zhao, Y. Zhang, D. Geng, A. Lushington, and X. Sun, *Carbon N. Y.* **61**, 321 (2013).
- [131] M. Scardamaglia, B. Aleman, M. Amati, C. Ewels, P. Pochet, N. Reckinger, J. F. Colomer, T. Skaltsas, N. Tagmatarchis, R. Snyders, L. Gregoratti, and C. Bittencourt, *Carbon N. Y.* **73**, 371 (2014).
- [132] L. Zhang, Y. Ye, D. Cheng, W. Zhang, H. Pan, and J. Zhu, *Carbon N. Y.* **62**, 365 (2013).
- [133] S. Zhao and J. Xue, *Phys. Rev. B - Condens. Matter Mater. Phys.* **86**, 1 (2012).
- [134] F. Xu, M. Minniti, P. Barone, A. Sindona, A. Bonanno, and A. Oliva, *Carbon N. Y.*
-

- 46**, 1489 (2008).
- [135] T. Kondo, S. Casolo, T. Suzuki, T. Shikano, M. Sakurai, Y. Harada, M. Saito, M. Oshima, M. I. Trioni, G. F. Tantardini, and J. Nakamura, *Phys. Rev. B - Condens. Matter Mater. Phys.* **86**, 1 (2012).
- [136] J. R. Pels, F. Kapteijn, J. A. Moulijn, Q. Zhu, and K. M. Thomas, *Carbon N. Y.* **33**, 1641 (1995).
- [137] C. Y. Cheng and K. Teii, *IEEE Trans. Plasma Sci.* **40**, 1783 (2012).
- [138] S. Vizireanu, M. D. Ionita, G. Dinescu, I. Enculescu, M. Baibarac, and I. Baltog, *Plasma Process. Polym.* **9**, 363 (2012).
- [139] Y. Ma, P. O. Lehtinen, A. S. Foster, and R. M. Nieminen, *New J. Phys.* **6**, 1 (2004).
- [140] K. Ganesan, S. Ghosh, N. Gopala Krishna, S. Ilango, M. Kamruddin, and A. K. Tyagi, *Phys. Chem. Chem. Phys.* **18**, 22160 (2016).
- [141] L. X. Zhang, Z. Sun, J. L. Qi, J. M. Shi, T. D. Hao, and J. C. Feng, *Carbon N. Y.* **103**, 339 (2016).
- [142] Z. Y. Sui, X. Li, Z. Y. Sun, H. C. Tao, P. Y. Zhang, L. Zhao, and B. H. Han, *Carbon N. Y.* **126**, 111 (2018).
- [143] J. R. Pels, F. Kapteijn, J. A. Moulijn, Q. Zhu, and K. M. Thomas, *Carbon N. Y.* **33**, 1641 (1995).
- [144] R. Arrigo, M. Hävecker, R. Schlögl, and D. S. Su, *Chem. Commun.* 4891 (2008).
- [145] P. H. Matter, L. Zhang, and U. S. Ozkan, *J. Catal.* **239**, 83 (2006).
- [146] B. Imre, L. Krisztina, M. Miklós, I. Bertóti, M. Mohai, and K. László, *Carbon N. Y.* **84**, 185 (2014).
- [147] S. Kurita, A. Yoshimura, H. Kawamoto, T. Uchida, K. Kojima, M. Tachibana, P. Molina-Morales, and H. Nakai, *J. Appl. Phys.* **97**, 104320 (2005).
- [148] N. Ferralis, *J. Mater. Sci.* **45**, 5135 (2010).
- [149] A. Jorio, *ISRN Nanotechnol.* **2012**, 1 (2012).
- [150] F. Tuinstra and J. L. Koenig, *J. Chem. Phys.* **53**, 1126 (1970).
- [151] L. M. Malard, M. A. Pimenta, G. Dresselhaus, and M. S. Dresselhaus, *Phys. Rep.* **473**, 51 (2009).
- [152] L. Zhao, R. He, K. T. Rim, T. Schiros, K. S. Kim, H. Zhou, C. Gutiérrez, S. P. Chockalingam, C. J. Arguello, L. Pálová, D. Nordlund, M. S. Hybertsen, D. R. Reichman, T. F. Heinz, P. Kim, A. Pinczuk, G. W. Flynn, and A. N. Pasupathy, *Science (80-.)*. **333**, 999 (2011).
- [153] M. H. Mineo Hiramatsu, Hiroki Kondo, in *NEW Prog. GRAPHENE Res.* (INTECH, 2013), pp. 243–268.
- [154] I. Childres, L. A. Jauregui, W. Park, H. Caoa, and Y. P. Chena, in *New Dev. Phot. Mater. Res.*, edited by J. I. Jang, Illustrate (Nova Science Publishers, Incorporated, New York, 2013), pp. 1–20.
- [155] M. M. Lucchese, F. Stavale, E. H. M. Ferreira, C. Vilani, M. V. O. Moutinho, R. B. Capaz, C. A. Achete, and A. Jorio, *Carbon N. Y.* **48**, 1592 (2010).

- [156] L. G. Wade Jr, in *Org. Chem.* (Pearson education Inc. NJ, USA, 2003), pp. 490–538.
- [157] S. Li, Z. Wang, H. Jiang, L. Zhang, J. Ren, M. Zheng, L. Dong, and L. Sun, *Chem. Commun.* **52**, 10988 (2016).
- [158] Y. G. Seol, T. Q. Trung, O. J. Yoon, I. Y. Sohn, and N. E. Lee, *J. Mater. Chem.* **22**, 23759 (2012).
- [159] S. Y. Toh, K. S. Loh, S. K. Kamarudin, and W. R. W. Daud, *Chem. Eng. J.* **251**, 422 (2014).
- [160] X. Xu, T. Yuan, Y. Zhou, Y. Li, J. Lu, X. Tian, D. Wang, and J. Wang, *Int. J. Hydrogen Energy* **39**, 16043 (2014).
- [161] P. Lian, X. Zhu, S. Liang, Z. Li, W. Yang, and H. Wang, *Electrochim. Acta* **55**, 3909 (2010).
- [162] M. P. Kumar, T. Kesavan, G. Kalita, P. Ragupathy, T. N. Narayanan, and D. K. Pattanayak, *RSC Adv.* **4**, 38689 (2014).
- [163] A. K. Mageed, R. A. B. Dayang, A. Salmiaton, S. Izhar, A. Razak, H. M. Yusoff, F. M. Yasin, and S. Kamarudin, *Int. J. Appl. Chem.* **12**, 104 (2016).
- [164] K. Zhou, Y. Zhu, X. Yang, X. Jiang, and C. Li, *New J. Chem.* **35**, 353 (2011).
- [165] A. Misra, P. K. Tyagi, M. K. Singh, and D. S. Misra, *Diam. Relat. Mater.* **15**, 385 (2006).
- [166] G. Shao, Y. Lu, F. Wu, C. Yang, F. Zeng, and Q. Wu, *J. Mater. Sci.* **47**, 4400 (2012).
- [167] C. Liu, K. Wang, S. Luo, Y. Tang, and L. Chen, *Small* **7**, 1203 (2011).
- [168] H. W. Lu, X. R. Zou, J. Q. Xie, and J. Y. Feng, *J. Phys. D: Appl. Phys.* **31**, 363 (1998).
- [169] C. Russo, F. Stanzione, A. Tregrossi, and A. Ciajolo, *Carbon N. Y.* **74**, 127 (2014).
- [170] L. G. Bulusheva, A. V Okotrub, A. G. Kurennya, H. Zhang, H. Zhang, X. Chen, and H. Song, *Carbon N. Y.* **49**, 4013 (2011).
- [171] F. Zheng, Y. Yang, and Q. Chen, *Nat. Commun.* **5**, 1 (2014).
- [172] D. Passeri, A. Bettucci, and M. Rossi, *Anal. Bioanal. Chem.* **396**, 2769 (2010).
- [173] D. Passeri, M. Rossi, A. Alippi, A. Bettucci, M. L. Terranova, E. Tamburri, and F. Toschi, *Phys. E Low-Dimensional Syst. Nanostructures* **40**, 2419 (2008).
- [174] T. Wang, C. Ma, W. Hu, Y. Chen, and J. Chu, *Microsc. Res. Tech.* **80**, 66 (2017).
- [175] Y. Xu, Z. Lin, X. Huang, Y. Wang, Y. Huang, and X. Duan, *Adv. Mater.* **25**, 5779 (2013).
- [176] R. Tsu, *8 - Capacitance, Dielectric Constant, and Doping Quantum Dots*, 2nd ed. (Superlattices to Nanoelectronics, Elsevier, London, 2011).
- [177] Y. Hanlumyung and P. Sharma, *JOM* **66**, 660 (2014).
- [178] Z. S. Iro, C. Subramani, and S. S. Dash, *Int. J. Electrochem. Sci.* **11**, 10628 (2016).
- [179] K. B. M Jayalakshmi, M. Jayalakshmi, K. Balasubramanian, and K. B. M Jayalakshmi, *Int. J. Electrochem. Sci.* **3**, 1196 (2008).

-
- [180] T. V. Magdesieva, P. V. Shvets, O. M. Nikitin, E. A. Obraztsova, F. T. Tuyakova, V. G. Sergeev, A. R. Khokhlov, and A. N. Obraztsov, *Carbon N. Y.* **105**, 96 (2016).
- [181] H. J. Cho, H. Kondo, K. Ishikawa, M. Sekine, M. Hiramatsu, and M. Hori, *Jpn. J. Appl. Phys.* **53**, (2014).
- [182] L. Huang, Y. Cao, and D. Diao, *Electrochim. Acta* **262**, 173 (2018).
- [183] S. Casolo, R. Martinazzo, and G. F. Tantardini, *J. Phys. Chem. C* **115**, 3250 (2011).
- [184] Y. C. Zhou, H. L. Zhang, and W. Q. Deng, *Nanotechnology* **24**, 225705 (2013).
- [185] T. Lin, I.-W. Chen, F. Liu, C. Yang, H. Bi, F. Xu, and F. Huang, *Science (80-.)*. **350**, 1508 (2015).
- [186] D. Guo, R. Shibuya, C. Akiba, S. Saji, T. Kondo, and J. Nakamura, *Science (80-.)*. **351**, 361 (2016).
- [187] H. M. Jeong, J. W. Lee, W. H. Shin, Y. J. Choi, H. J. Shin, J. K. Kang, and J. W. Choi, *Nano Lett.* **11**, 2472 (2011).
- [188] S. A. Evlashin, Y. M. Maksimov, P. V. Dyakonov, A. A. Pilevsky, K. I. Maslakov, Y. A. Mankelevich, E. N. Voronina, S. V. Vavilov, A. A. Pavlov, E. V. Zenova, I. S. Akhatov, and N. V. Suetin, *Sci. Rep.* **9**, 1 (2019).
- [189] E. Paek, A. J. Pak, K. E. Kweon, and G. S. Hwang, *J. Phys. Chem. C* **117**, 5610 (2013).
- [190] B. L. French, J. J. Wang, M. Y. Zhu, and B. C. Holloway, *Thin Solid Films* **494**, 105 (2006).
- [191] M. Szwarc, *J. Chem. Phys.* **17**, 505 (1949).
- [192] H. O. Pierson, *Handbook of Chemical Vapor Deposition, 2nd Edition, Second Edition: Principles, Technology and Applications*, 2nd ed. (Noyes Publications, New York, 1999).
- [193] S. M. Rossnagel, J. J. Cuomo, and W. D. Westwood, *Handbook of Plasma Processing Technology: Fundamentals, Etching, Deposition, and Surface Interactions* (Noyes Publications, New Jersey, U.S.A., 1990).
- [194] N. J. Archer, *Thin Solid Films* **80**, 221 (1981).
- [195] A. Anders, *Surf. Coatings Technol.* **156**, 3 (2002).
- [196] J. Pelletier and A. Anders, *IEEE Trans. Plasma Sci.* **33**, 1944 (2005).
- [197] J. Tendys, I. J. Donnelly, M. J. Kenny, and J. T. A. Pollock, *Appl. Phys. Lett.* **53**, 2143 (1988).
- [198] J. R. Conrad, J. L. Radtke, R. A. Dodd, F. J. Worzala, and N. C. Tran, *J. Appl. Phys.* **62**, 4591 (1987).
- [199] M. Ueda, R. M. Oliveira, J. O. Rossi, C. B. Mello, R. C. C. Rangel, and M. S. Vieira, *Surf. Coatings Technol.* **229**, 97 (2013).
- [200] M. A. Lieberman, *J. Appl. Phys.* **66**, 2926 (1989).
- [201] F. Hofer, F. P. Schmidt, W. Grogger, and G. Kothleitner, *IOP Conf. Ser. Mater. Sci. Eng.* **109**, 012007 (2016).
-

- [202] R. Erni and N. D. Browning, *Ultramicroscopy* **104**, 176 (2005).
- [203] J. Geiger, *Phys. Status Solidi* **24**, 457 (1967).
- [204] D. B. Williams and C. B. Carter, *Transmission Electron Microscopy: A Textbook for Materials Science* (Plenum Press, New York, 2009).
- [205] N. Bernier, F. Bocquet, A. Allouche, W. Saikaly, C. Brosset, J. Thibault, and A. Charai, *J. Electron Spectros. Relat. Phenomena* **164**, 34 (2008).
- [206] J. Bruley, D. B. Williams, J. J. Cuomo, and D. P. Pappas, *J. Microsc.* **180**, 22 (1995).
- [207] L. Lajaunie, C. Pardanaud, C. Martin, P. Puech, C. Hu, M. J. Biggs, and R. Arenal, *Carbon N. Y.* **112**, 149 (2017).
- [208] L. Ponsonnet, C. Donnet, K. Varlot, J. M. Martin, A. Grill, and V. Patel, *Thin Solid Films* **319**, 97 (1998).
- [209] M. Diociaiuti, S. Casciardi, and R. Sisto, *Micron* **90**, 97 (2016).
- [210] S. D. Berger, D. R. McKenzie, and P. J. Martin, *Philos. Mag. Lett.* **57**, 285 (1988).
- [211] G. A. L. Pemberton J E, *Metals Handbook* (ASM, Ohio, 1986).
- [212] G. Freihofer, S. Raghavan, and D. Gosztola, *Appl. Spectrosc.* **67**, 321 (2013).
- [213] Y. Gao, *J. Appl. Phys.* **64**, 3760 (1988).
- [214] Y. Gao, Y. Marie, F. Saldi, and H. N. Migeon, in *Proc. 9th Int. Conf. Second. Ion Mass Spectrom. Yokohama, Japan* (1993), pp. 382–385.
- [215] A. K. Balamurugan, S. Dash, and A. K. Tyagi, *Int. J. Mass Spectrom.* **386**, 56 (2015).
- [216] K. D. B. Moulder, John F, William F. Stickle, Peter E Sobol, *Handbook of X-Ray Photoelectron Spectroscopy* (Perkin-Elmer Corporation, Eden Praire, USA, 1993).
- [217] D. Briggs and J. T. Grant, *Surface Analysis by Auger and X-Ray Photoelectron Spectroscopy* (SurfaceSpectra, Manchester , U.K., 2012).
- [218] C. Ma, Y. Chen, T. Wang, and J. Chu, *Scanning* **37**, 284 (2015).
- [219] N. Elgrishi, K. J. Rountree, B. D. McCarthy, E. S. Rountree, T. T. Eisenhart, and J. L. Dempsey, *J. Chem. Educ.* **95**, 197 (2018).
- [220] W. Li, L. Xin, X. Xu, Q. Liu, M. Zhang, S. Ding, M. Zhao, and X. Lou, *Sci. Rep.* **5**, 1 (2015).
- [221] A. Anders, *Handbook of Plasma Immersion Ion Implantation and Deposition* (Wiley, New York, 2000).
- [222] T. Tanaka, S. Watanabe, and T. Takagi, *Nucl. Instruments Methods Phys. Res. Sect. B Beam Interact. with Mater. Atoms* **242**, 371 (2006).
- [223] P. A. Manojkumar, V. A. Chirayath, A. K. Balamurugan, N. G. Krishna, S. Ilango, M. Kamruddin, G. Amarendra, A. K. Tyagi, and B. Raj, *Nucl. Instruments Methods Phys. Res. Sect. B Beam Interact. with Mater. Atoms* **383**, (2016).
- [224] A. Burenkov, P. Pichler, J. Lorenz, Y. Spiegel, J. Duchaine, and F. Torregrosa, in *Int. Conf. Simul. Semicond. Process. Devices* (IEEE, 2011), pp. 231–234.
- [225] S. Mukherjee, F. Prokert, E. Richter, and W. Möller, *Thin Solid Films* **445**, 48

- (2003).
- [226] D. Smith, N. G. Adams, and T. M. Miller, *J. Chem. Phys.* **69**, 308 (1978).
- [227] C. Bittencourt, M. Rutar, P. Umek, A. Mrzel, K. Vozel, D. Arçon, K. Henzler, P. Krüger, and P. Guttman, *RSC Adv.* **5**, 23350 (2015).
- [228] I. J. Donnelly and E. K. Rose, *Aust. J. Phys.* **43**, 45 (1990).
- [229] S. Wang, L. Qiao, C. Zhao, X. Zhang, J. Chen, H. Tian, W. Zheng, and Z. Han, *New J. Chem.* **37**, 1616 (2013).
- [230] P. Venezuela, M. Lazzeri, and F. Mauri, *Phys. Rev. B* **84**, 1 (2011).
- [231] A. Eckmann, A. Felten, A. Mishchenko, L. Britnell, R. Krupke, K. S. Novoselov, and C. Casiraghi, *Nano Lett.* **12**, 3925 (2012).
- [232] K. Suzuki, K. Nakamura, H. Ohkubo, and H. Sugai, *Plasma Sources Sci. Technol.* **7**, 13 (1998).
- [233] I. Velchev, W. Hogervorst, and W. Ubachs, *J. Phys. B At. Mol. Opt. Phys.* **32**, L511 (1999).
- [234] M. Stano, S. Matejcik, J. D. Skalny, and T. D. Märk, *J. Phys. B At. Mol. Opt. Phys.* **36**, 261 (2003).
- [235] E. Biémont, Y. Frémat, and P. Quinet, *At. Data Nucl. Data Tables* **71**, 117 (1999).
- [236] I. Shimoyama, Y. Baba, and T. Sekiguchi, *Vacuum* **78**, 563 (2005).
- [237] K. J. Clay, S. P. Speakman, N. A. Morrison, N. Tomozeiu, W. I. Milne, and A. Kapoor, *Diam. Relat. Mater.* **7**, 1100 (1998).
- [238] P. Li, Z. Li, and J. Yang, *J. Phys. Chem. C* **121**, 25949 (2017).
- [239] A. C. Ferrari and D. M. Basko, *Nat. Nanotechnol.* **8**, 235 (2013).
- [240] R. Beams, L. Gustavo Cançado, and L. Novotny, *J. Phys. Condens. Matter* **27**, 083002 (2015).
- [241] M. V. Bracamonte, G. I. Lacconi, S. E. Urreta, and L. E. F. Foa Torres, *J. Phys. Chem. C* **118**, 15455 (2014).
- [242] H. Shu, X. Chen, and F. Ding, *Chem. Sci.* **5**, 4639 (2014).
- [243] Y. W. Tan, H. L. Stormer, P. Kim, K. S. Novoselov, M. L. Cohen, S. G. Louie, X. Wang, L. Zhang, S. Lee, H. Dai, Y. Kobayashi, K. Fukui, M. Fujita, G. Dresselhaus, M. S. Dresselhaus, M. a Pimenta, B. R. a Neves, A. Jorio, Y. Zhang, M. Mailman, P. M. Ajayan, S. K. Nayak, C.-H. H. Park, Y. W. Son, S. P. Lu, S. Piscanec, a C. Ferrari, G. Dobrik, P. Lambin, A. Oberlin, T. Solid, K. Suenaga, S. Iijima, P. Hermet, V. Meunier, L. Henrard, D. Gunlycke, C. T. White, S. Chen, B. I. Yakobson, S. Gradecak, Ç. Ö. Girit, J. C. Meyer, R. Erni, M. D. Rossell, C. Kisielowski, L. Yang, C.-H. H. Park, M. F. Crommie, M. L. Cohen, and S. G. Louie, *Science (80-.)*. **323**, 1705 (2009).
- [244] Y. Hao, Y. Wang, L. Wang, Z. Ni, Z. Wang, R. Wang, C. K. Koo, Z. Shen, and J. T. L. Thong, *Small* **6**, 195 (2010).
- [245] S. Ghosh, K. Ganesan, S. R. Polaki, T. R. Ravindran, N. G. Krishna, M. Kamruddin, and A. K. Tyagi, *J. Raman Spectrosc.* **45**, 642 (2014).
- [246] S. Karlin and P. Colombari, *J. Raman Spectrosc.* **28**, 219 (2005).

- [247] R. N. Tarrant, D. R. McKenzie, and M. M. M. Bilek, *Diam. Relat. Mater.* **13**, 1422 (2004).
- [248] J. N. Rouzaud, A. Oberlin, L. M. Mathieu, and D. Miniralogie, **105**, 75 (2000).
- [249] A. C. Ferrari and J. Robertson, *Philos. Trans. R. Soc. A Math. Phys. Eng. Sci.* **362**, 2477 (2004).
- [250] V. D. Blank, V. N. Denisov, A. N. Kirichenko, B. A. Kulnitskiy, S. Y. Martushov, B. N. Mavrin, and I. A. Perezhugin, *Nanotechnology* **18**, 345601 (2007).
- [251] A. M. Kaushal, A. K. Chakraborti, and A. K. Bansal, *Mol. Pharm.* **5**, 937 (2008).
- [252] N. B. Clothup, *Appl. Spectrosc.* **34**, 1 (1980).
- [253] A. Politano, G. Chiarello, and C. Spinella, *Mater. Sci. Semicond. Process.* **65**, 88 (2017).
- [254] H. Kanzow, A. Ding, J. Nissen, H. Sauer, T. Belz, and R. Schlögl, *Phys. Chem. Chem. Phys.* **2**, 2765 (2000).
- [255] A. Politano and G. Chiarello, *Nanoscale* **6**, 10927 (2014).
- [256] S. Y. Shin, N. D. Kim, J. G. Kim, K. S. Kim, D. Y. Noh, K. S. Kim, and J. W. Chung, *Appl. Phys. Lett.* **99**, 082110 (2011).
- [257] A. J. Papworth, C. J. Kiely, A. P. Burden, S. R. P. Silva, and G. A. J. Amaratunga, *Phys. Rev. B* **62**, 12628 (2000).
- [258] S. R. P. Silvaf, J. Robertson, Rusli, G. A. J. Amaratunga, and J. Schwan, *Philos. Mag. B* **74**, 369 (1996).
- [259] A. L. Hamon, J. Verbeeck, D. Schryvers, J. Benedikt, and R. M. C. M. V. D. Sanden, *J. Mater. Chem.* **14**, 2030 (2004).
- [260] X. Tian and P. K. Chu, *Phys. Lett. Sect. A Gen. At. Solid State Phys.* **277**, 42 (2000).
- [261] K. S. Suraj and S. Mukherjee, *Surf. Coatings Technol.* **196**, 267 (2005).
- [262] A. Jorio, E. H. M. Ferreira, M. V. O. Moutinho, F. Stavale, C. A. Achete, and R. B. Capaz, *Phys. Status Solidi Basic Res.* **247**, 2980 (2010).
- [263] A. C. Ferrari and J. Robertson, *Phys. Rev. B* **61**, 14095 (2000).
- [264] M. Matsuoka, S. Isotani, R. D. Mansano, W. Sucasaire, R. A. C. Pinto, J. C. R. Mittani, K. Ogata, and N. Kuratani, *World J. Nano Sci. Eng.* **02**, 92 (2012).
- [265] A. Barinov, O. B. Malcioğlu, S. Fabris, T. Sun, L. Gregoratti, M. Dalmiglio, and M. Kiskinova, *J. Phys. Chem. C* **113**, 9009 (2009).
- [266] R. Blume, D. Rosenthal, J.-P. Tessonnier, H. Li, A. Knop-Gericke, and R. Schlögl, *ChemCatChem* **7**, 2871 (2015).
- [267] Y. Yamada, J. Kim, S. Matsuo, and S. Sato, *Carbon N. Y.* **70**, 59 (2014).
- [268] F. J. Flores-Ruiz, C. I. Enriquez-Flores, F. Chiñas-Castillo, and F. J. Espinoza-Beltrán, *Appl. Surf. Sci.* **314**, 193 (2014).
- [269] W. J. Gammon, O. Kraft, A. C. Reilly, B. C. Holloway, W. J. Gammon, O. Kraft, A. C. Reilly, and B. C. Holloway, *Carbon N. Y.* **41**, 1917 (2003).
- [270] Y. Zhou, X. Xu, B. Shan, Y. Wen, T. Jiang, J. Lu, S. Zhang, D. P. Wilkinson, J.

- Zhang, and Y. Huang, *Energy Storage Mater.* **1**, 103 (2015).
- [271] Y. F. Lu, S. T. Lo, J. C. Lin, W. Zhang, J. Y. Lu, F. H. Liu, C. M. Tseng, Y. H. Lee, C. Te Liang, and L. J. Li, *ACS Nano* **7**, 6522 (2013).
- [272] T. Schiros, D. Nordlund, L. Pálová, D. Prezzi, L. Zhao, K. S. Kim, U. Wurstbauer, C. Gutiérrez, D. Delongchamp, C. Jaye, D. Fischer, H. Ogasawara, L. G. M. Pettersson, D. R. Reichman, P. Kim, M. S. Hybertsen, and A. N. Pasupathy, *Nano Lett.* **12**, 4025 (2012).
- [273] X. Li, X. Pan, L. Yu, P. Ren, X. Wu, L. Sun, F. Jiao, and X. Bao, *Nat. Commun.* **5**, 1 (2014).
- [274] N. Ketabi, T. De Boer, M. Karakaya, J. Zhu, R. Podila, A. M. Rao, E. Z. Kurmaev, and A. Moewes, *RSC Adv.* **6**, 56721 (2016).
- [275] J. M. Ripalda, I. Montero, and L. Galán, *Diam. Relat. Mater.* **7**, 402 (1998).
- [276] P. Petrov, D. B. Dimitrov, D. Papadimitriou, G. Beshkov, V. Krastev, and C. Georgiev, *Appl. Surf. Sci.* **151**, 233 (1999).
- [277] C. Quirós, P. Prieto, A. Fernández, E. Elizalde, C. Morant, R. Schlögl, O. Spillecke, and J. M. Sanz, *J. Vac. Sci. Technol. A Vacuum, Surfaces, Film.* **18**, 515 (2002).
- [278] A. A. Voevodin, J. G. Jones, J. S. Zabinski, Z. Czigány, and L. Hultman, *J. Appl. Phys.* **92**, 4980 (2002).
- [279] J. Neidhardt, L. Hultman, and Z. Czigány, *Carbon N. Y.* **42**, 2729 (2004).
- [280] Q. Wang, C. Wang, Z. Wang, J. Zhang, and D. He, *Appl. Phys. Lett.* **91**, 21 (2007).
- [281] J. T. Titantah and D. Lamoen, *Diam. Relat. Mater.* **16**, 581 (2007).
- [282] P. Hoffmann and C. Pettenkofer, *Phys. Status Solidi Basic Res.* **248**, 327 (2011).
- [283] Y. Chung, J. C. Lee, and H. J. Shin, *Appl. Phys. Lett.* **86**, 022901 (2005).
- [284] M. I. I. Heggie, T. Trevethan, A. J. J. McKenna, C. D. D. Latham, P. J. J. Young, T. Trevethan, C. D. D. Latham, P. J. J. Young, M. I. I. Heggie, T. Trevethan, A. J. J. McKenna, C. D. D. Latham, and P. J. J. Young, *Carbon N. Y.* **99**, 71 (2015).
- [285] W. J. Chang, *Nanotechnology* **13**, 510 (2002).
- [286] M. A. Cazalilla, N. Lorente, R. D. Muino, J.-P. Gauyacq, D. Teillet-Billy, and P. M. Echenique, *Phys. Rev. B* **58**, 13991 (1998).
- [287] A. Chartier, L. Van Brutzel, B. Pannier, and P. Baranek, *Carbon N. Y.* **91**, 395 (2015).
- [288] K. S. Fancey, *Vacuum* **46**, 695 (1995).
- [289] Y. Wang and J. K. Olthoff, *J. Appl. Phys.* **85**, 6358 (1999).
- [290] Z.-S. Wu, W. Ren, L. Xu, F. Li, and H.-M. Cheng, *ACS Nano* **5**, 5463 (2011).
- [291] G. K. Gueorguiev, J. Neidhardt, S. Stafström, and L. Hultman, *Chem. Phys. Lett.* **410**, 228 (2005).
- [292] Z. Hou, X. Wang, T. Ikeda, K. Terakura, M. Oshima, M. A. Kakimoto, and S. Miyata, *Phys. Rev. B - Condens. Matter Mater. Phys.* **85**, 1 (2012).
- [293] K. Akada, T. O. Terasawa, G. Imamura, S. Obata, and K. Saiki, *Appl. Phys. Lett.*

- 104**, 1 (2014).
- [294] J. Martinez-Asencio, C. J. Ruestes, E. M. Bringa, and M. J. Caturla, *Phys. Chem. Chem. Phys.* **18**, 13897 (2016).
- [295] P. A. Manojkumar, N. G. Krishna, G. Mangamma, and S. K. Albert, *Phys. Chem. Chem. Phys.* **21**, (2019).
- [296] A. Hu, M. Rybachuk, Q. B. Lu, and W. W. Duley, *Appl. Phys. Lett.* **91**, 1 (2007).
- [297] B. Pan, J. Xiao, J. Li, P. Liu, C. Wang, and G. Yang, *Sci. Adv.* **1**, 1 (2015).
- [298] Y. Zhu, T. Yi, B. Zheng, and L. Cao, *Appl. Surf. Sci.* **137**, 83 (1999).
- [299] H. Watanabe, H. Kondo, M. Sekine, M. Hiramatsu, and M. Hori, *Jpn. J. Appl. Phys.* **51**, 01AJ07 (2012).
- [300] G. Sahoo, S. R. Polaki, S. Ghosh, N. G. Krishna, M. Kamruddin, and K. (Ken) Ostrikov, *Energy Storage Mater.* **14**, 297 (2018).
- [301] A. Kozbial, C. Trouba, H. Liu, and L. Li, *Langmuir* **33**, 959 (2017).
- [302] A. Kozbial, Z. Li, C. Conaway, R. McGinley, S. Dhingra, V. Vahdat, F. Zhou, B. D'Urso, H. Liu, and L. Li, *Langmuir* **30**, 8598 (2014).
- [303] A. Kozbial, Z. Li, J. Sun, X. Gong, F. Zhou, Y. Wang, H. Xu, H. Liu, and L. Li, *Carbon N. Y.* **74**, 218 (2014).
- [304] Z. Li, Y. Wang, A. Kozbial, G. Shenoy, F. Zhou, R. McGinley, P. Ireland, B. Morganstein, A. Kunkel, S. P. Surwade, L. Li, and H. Liu, *Nat. Mater.* **12**, 925 (2013).
- [305] F. M. Hassan, V. Chabot, J. Li, B. K. Kim, L. Ricardez-Sandoval, and A. Yu, *J. Mater. Chem. A* **1**, 2904 (2013).
- [306] S. Dutta, A. Bhaumik, and K. C.-W. Wu, *Energy Environ. Sci.* **7**, 3574 (2014).
- [307] E. Frackowiak, Q. Abbas, and F. Béguin, *J. Energy Chem.* **22**, 226 (2013).
- [308] H. Yang, J. Yang, Z. Bo, S. Zhang, J. Yan, and K. Cen, *J. Power Sources* **324**, 309 (2016).
- [309] W. Kang, B. Lin, G. Huang, C. Zhang, W. Hou, Y. Yao, B. Xu, and B. Xing, *J. Mater. Sci. Mater. Electron.* **29**, 3340 (2018).
- [310] M. D. Stoller, C. W. Magnuson, Y. Zhu, S. Murali, J. W. Suk, R. Piner, and R. S. Ruoff, *Energy Environ. Sci.* **4**, 4685 (2011).
- [311] L. L. Zhang, X. Zhao, H. Ji, M. D. Stoller, L. Lai, S. Murali, S. McDonnell, B. Cleveger, R. M. Wallace, and R. S. Ruoff, *Energy Environ. Sci.* **5**, 9618 (2012).
- [312] W. Ren, H. Zhang, C. Guan, and C. Cheng, *Adv. Funct. Mater.* **27**, 1 (2017).
- [313] M. Huang, H. Yan, T. F. Heinz, and J. Hone, *Nano Lett.* **10**, 4074 (2010).
- [314] Q. Wu, Y. Wu, Y. Hao, J. Geng, M. Charlton, S. Chen, Y. Ren, H. Ji, H. Li, D. W. Boukhvalov, R. D. Piner, C. W. Bielawski, and R. S. Ruoff, *Chem. Commun.* **49**, 677 (2013).
- [315] J. Senthilnathan, K. S. Rao, and M. Yoshimura, *J. Mater. Chem. A* **2**, 3332 (2014).
- [316] Z. Lin, Y. Liu, Y. Yao, O. J. Hildreth, Z. Li, K. Moon, C. P. Wong, O. J. Hildreth, Z. Li, K. Moon, and C. P. Wong, *J. Phys. Chem. C* **115**, 7120 (2011).

- [317] G. Sahoo, S. R. Polaki, S. Ghosh, N. G. Krishna, and M. Kamruddin, *J. Power Sources* **401**, 37 (2018).
- [318] I. Tzouvadaki, N. Aliakbarinodehi, D. Dávila Pineda, G. De Micheli, and S. Carrara, *Sensors Actuators, B Chem.* **262**, 395 (2018).

These blank pages are purposefully introduced.